Modification of 2D-Materials by Swift Heavy Ion Irradiation

Dissertation

zur Erlangung des Grades
Doktor der Naturwissenschaft
(Dr. rer. nat.)

vorgelegt der Fakultät für Physik
der Universität Duisburg-Essen

von
Oliver Ochedowski
geb. in Stuttgart

Duisburg, den 22. August 2014

1. Gutachterin: Prof. Dr. Marika Schleberger
2. Gutachterin: Prof. Dr. Janina Maultzsch
3. Gutachter: Prof. Dr. Axel Lorke

Datum der Disputation: 04. Dezember 2014

Abstract

Since the isolation of graphene in 2004, two-dimensional crystals have attracted a lot of attention in a variety of scientific fields. Thus, Andre Geim and Kostya Novoselov were honoured with the Nobel Prize in 2010 for their findings. Ten years later, the interest in materials like graphene and single layer MoS_2 is still growing. In order to actually implement these new materials in the plentitude of applications that are envisaged, new tools are needed. The purpose of this work is to investigate whether swift heavy ions (highly charged ions with typical energies ranging from 100 MeV to GeV) can be used as such a new tool for the modification of the morphology and doping of these materials.

To obtain two-dimensional crystals of the highest quality, the mechanical exfoliation technique is used to prepare graphene and MoS_2 single layers on various substrates. However, as the samples are prepared in ambient the resulting single layers are usually contaminated with adsorbates and water is intercalated between the crystal and the substrate. Furthermore, the presence of the substrate alone results in a significant change of the properties of two-dimensional crystals. Therefore graphene and MoS_2 prepared on different substrates are investigated using non-contact atomic force microscopy and Kelvin probe force microscopy in situ to probe the contribution of adsorbates, intercalated water and the substrate itself under defined conditions.

It has already been shown that graphene is folded upon swift heavy ion impact when irradiated under grazing incidence. In this work, the mechanism of the folding formation is studied and it will be shown that the size of the foldings can be controlled precisely by the energy of the ion, the incidence angle of the ion with respect to the sample surface and the choice of the substrate. In case of single layer MoS_2 an additional modification to the morphology can be observed in form of nanoscale slit pores. The length of these slit pores can be controlled by the incidence angle again and the aspect ratio up to 1:600 (width:length). A mechanism for the formation of the slit pores is formulated: a thermal spike generated by the intense electronic excitation of the swift heavy ion is heating up the substrate on which MoS_2 is attached. The temperature at the surface is exceeding the melting temperature of MoS_2 and results in the formation of the slit pore.

The last part of this thesis deals with the possibility of doping graphene using swift heavy ions. By preparing graphene samples without an intercalated water layer, the folding formation can be prevented. Instead, a surface track is created into the atomically thin carbon layer. This surface track significantly increases the hole charge carrier concentration in graphene and it will be shown that the surface tracks are created by implantation of Si atoms from the substrate due to the swift heavy ion irradiation.

Kurzzusammenfassung

Seit der Isolierung Graphens im Jahre 2004 haben zwei-dimensionale Kristalle größte Aufmerksamkeit in verschiedenen wissenschaftlichen Bereichen erregt. Aus diesem Grunde wurden Andre Geim und Kostya Novoselov 2010 für diese Entdeckung mit dem Nobelpreis geehrt. Zehn Jahre nach der Entdeckung ist das Interesse an Materialien wie Graphen und einlagigem Molybdändisulfid ungebrochen. Aber damit diese neuen Materialien tatsächlichen ihren Weg in eine Vielzahl neuer Applikationen finden, ist es nötig, neue Werkzeuge zur Verfügung zu stellen, um diese Materialien zu bearbeiten. In der vorliegenden Arbeit soll aus diesem Grund untersucht werden, inwiefern schnelle, schwere Ionen (hochgeladene Ionen mit typischen Energien zwischen 100 MeV bis zu GeV) als solch ein Werkzeug benutzt werden können, um eine Modifikation der Morphologie oder Dotierung in diesen Materialen zu induzieren.

Um zwei-dimensionale Kristallite der höchsten Qualität zu erhalten, wird die so genannte mechanische Exfoliationstechnik verwendet, um Graphen und einlagiges MoS_2 auf verschiedenen Trägersubstraten zu erhalten. Da die Proben an Luft präpariert werden, sind die Einzellagen normalerweise durch Adsorbate verunreinigt oder durch Wasser, das zwischen dem Kristall und dem Substrat interkaliert ist. Des Weiteren sorgt der Kontakt zum Substrat alleine schon dafür, dass deutliche Veränderungen der Eigenschaften der zweidimensionalen Kristalle zu Tage treten. Aus diesem Grund werden Graphen und MoS_2 auf verschiedenen Substraten präpariert und mittels non-contact Rasterkraftmikroskopie und Kelvin probe Mikroskopie in situ untersucht, um den Einfluss von Adsorbaten, interkaliertem Wasser und dem Substrat selbst unter definierten Bedingungen zu untersuchen.

Es wurde bereits gezeigt, dass Graphen durch die Bestrahlung mit schnellen, schweren Ionen gefaltet werden kann. In dieser Arbeit wird der Mechanismus, der zu der Faltungsformation führt, näher untersucht und es wird gezeigt, dass die Grösse der Faltung durch die Energie des Ions, den Einfallswinkel und die Substratwahl genau kontrolliert werden kann. Im Fall von einlagigem MoS_2 kann eine zusätzliche Oberflächenmodifikation in Form von Schlitzporen im Nanometerbereich beobachtet werden. Die Länge dieser Schlitzporen kann wiederum durch den Einfallswinkel der hochenergetischen Ionen kontrolliert werden und das Seitenverhältnis der Schlitzporen kann bis zu 1:600 (Breite:Länge) betragen. Ein Mechanismus für die Formierung der Schlitzporen wird postuliert: Ein thermal spike wird durch die intensive elektronische Anregung durch das schnelle, schwere Ion generiert, der das Substrat mit dem MoS_2 lokal aufheizt. Die Temperatur auf der Oberfläche überschreitet dabei die Schmelztemperatur von MoS_2 und führt dadurch zur Bildung von Schlitzporen.

Im letzten Teil dieser Arbeit wird untersucht, inwiefern Graphen durch schnelle, schwere

Ionen dotiert werden kann. Graphen wird hierfür zuerst ohne interkaliertes Wasser präpariert, um die Bildung von Faltungen zu verhindern. An deren Stelle werden Oberflächenspuren in der atomar dünnen Kohlenstoffschicht gebildet. Diese Oberflächenspuren sorgen für eine deutliche Erhöhung der Löcher-Ladungsträgerkonzentration in Graphen und es wird gezeigt, dass die Oberflächenspuren dadurch entstehen, dass Silizium-Atome aus dem Substrat durch das schnelle, schwere Ion in das Graphen implantiert werden.

Contents

1 Introduction

Swift heavy ions (SHI) provide a special way for engineering and nanostructuring on the nanoscale. This is due to their unique properties, namely the nanosized spatial scale, the subpicosecond temporal scale, spatial anisotropy and the extremely intense electronic excitation. The interaction of high energetic ion beams with matter is of substantial interest, from the experimental point of view as well as the theoretical. Swift heavy ions (SHI) typically have energies exceeding 1 MeV/amu and masses above 20 protons. The penetration depth of these projectiles in solids can reach 50 μm depending on the ion and its energy. Along the ion trajectory, phase transitions in a nano spatial scale can be introduced, if the energy of the projectile is higher than a certain threshold. For dielectrics the threshold is usually about 2 to 5 keV/nm and thus achievable with relatively small accelerators. The dominant interaction of SHI with materials leading to these modifications is by inelastic electronic stopping, while damage induced by elastic collision is an order of magnitude lower [1].

In particular swift heavy ion irradiation has been applied to produce nanosized latent tracks, e.g. conducting tracks in diamond like carbon [2] or magnetized tracks in YCo_2 [3, 4]. Ion tracks created in polymers like polyethylen or polycarbonat can be used as an inital point for etching. The irradiated polymer is etched in NaOH and, depending on the polymer material, cylindrical or conical pores are etched with aspect ratios up to 1000:1 and pore sizes between 15 nm and 10 μm [5]. These so-called ion etched membranes are available as commercial products and are used mainly for biomedical applications like cell separation, biosensors, controlled drug release, etc. Furthermore, SHI can be used to induce deformation in embedded nano-clusters as shown for ion implanted Co nanoparticles, which show a transition from spherical to cigar-shape after irradiation [6]. Another recent application is the irradiation therapy of cancer using heavy carbon ions [7]. A more detailed theoretical background of the physical mechanisms for these applications is given in chapter 2.

The motivation behind this thesis is:

- to explore if, and under what conditions, modifications in two-dimensinal materials can be introduced by SHI
- to reveal the energy dissipation pathways which cause these modifications

The just recently emerged material class of two-dimensional materials became a great center of attention when Geim and Novoselov isolated graphene, an atomically thin crystal

of carbon atoms, from a graphite crystal using the mechanical exfoliation technique in 2004 [8, 9]. The mechanical exfoliation can be applied for any so-called van-der-Waals solid with a layered crystal structure. They typically exhibit strong intralayer bonds (covalent or ionic) and weak interlayer van-der-Waals bonds. A great asset of this technique, in which only a scotch tape is needed, is that it can be used to easily prepare two-dimensional crystals in principally every laboratory. As the band structures of these ultimately thin crystals significantly differ from their bulk counterparts, new physical phenoma are expected and have been experimentally measured in many cases. For the most prominent two-dimensional material, graphene, for example record values of the charg carrier mobility, thermal conductivity and mechanical strength have been demonstrated. And although this material is just one atom thick, it has been shown to be impenetrable for even the smallest gaseous molecules [10, 11]. Another class of two-dimensional crystals are the transmetalldichalcogenides of which MoS_2 is the most prominent representative. Strikingly, MoS_2 undergoes a transition from an indirect band gap to a direct band gap semiconductor, if thinned out to a single atomic layer [12, 13]. The most important facts about two-dimensional materials (graphene and single layer MoS_2 in particular) are presented to the reader in the second part of chapter 2. The focus in this thesis is on Graphene and single layer MoS_2, to study the interaction of swift heavy ions with the two most investigated two-dimensional crystals. In addition, they have shown a distinct variation in their physical properties like charge carrier mobility, thermal conductivity and melting temperatures, so that the role of these natural properties for the ion/2D-material interaction can be studied.

As two-dimensional materials principally consist of nothing but a surface, their physical properties are greatly affected by their surroundings. Thus, it can be easily seen that the substrate onto which graphene is deposited may induce doping and/or charge carrier impurities in graphene and that adsorbates/water do have a similar effect. As the substrate and adsorbates influence the swift heavy ion irradiation experiments as well, it is important to have a good understanding of their effect on the properties of graphene. Therefore, in chapter 4 of this thesis, in-situ Kelvin probe force microscopy in combination with atomic force microscopy is employed to study the surface potential and with it the work function of graphene and single layer MoS_2. These measurements have been performed for the first time in-situ in a defined atmosphere, which makes it possible to dissentangle the effects from the substrate, adsorbates and intercalated water layers and study them in detail. In the case of graphene, different substrate materials are investigated, namely $SrTiO_3$, SiC(0001) and muscovite mica. These three materials were chosen because they allow to study graphene on substrates with a large variation in their work function and on hydrophobic as well as hydrophilic substrates. As water is always an issue, if graphene is prepared under ambient conditions, it is crucial to learn in which way water on top of graphene and intercalated water is affecting the electronic properties of graphene and whether it can be removed or not. On the other hand, a single layer MoS_2 is investigated with Kelvin probe on a standard SiO_2 substrate. This substrate was patterned by reactive ion etching to prepare areas with different surface morphology and roughness to study their effect on the work function of MoS_2. To study the effect of contamination introduced by lithographic processes, a gold

contact is patterned on the MoS_2 flake.

One goal of this thesis was to unravel the conditions under which it is possible to drill nanopores into 2D-materials. Nanopores in graphene and single layer MoS_2 might be applied for various applications like detection of DNA [14, 15], gas separation [16], water desalination [17] or drug delivery [18]. In the first part of chapter 5, the effects of swift heavy ion irradiation on the surface morphology of graphene are discussed.

It has already been shown by Akcoeltekin et al. that grazing incidence swift heavy ion irradiation can be used to fold graphene locally and to introduce nanopores in form of foldings in combination with closed bilayer edges into graphene [19]. Whether these formation of foldings is limited to graphene only or can be applied to other two-dimensional materials as well will be studied first. Next, the experimental conditions for the folding formation are investigated in detail. This is done by varying the experimental parameters, namely the SHI energy, the incidence angle and the substrate.

The second part of chapter 5 deals with SHI induced modifications in single layer MoS_2. In contrast to graphene, an additional modification in form of nanoscale rifts is observed here. To explain this behavior, a model based on the Two-Temperature Model (TTM) is proposed. It is based on the hypothesis that the SHI induces a thermal spike in the underlying substrate material which acts like a heat plate for the single layer MoS_2. If the temperature of the substrate exceeds the melting temperature of the MoS_2, the rift is created. This hypothesis is tested by calculating the thermal spike in SiO_2 and the resulting lattice temperatures using a software package by Orkhan Osmani at the Universität Duisburg-Essen.

The motivation behind the final experimental chapter is to explore the applicability of swift heavy ions in the process of doping two-dimensional materials. Dopant implantation has been one of the most important fields of ion physics since Brattain and Bardeen in the Bell labs showed that dopants in a crystal of Ge can act as acceptors or donators of electrons and amplify signals. As ion beams from accelerators are an effective technique to induce dopants into semiconductors, the semiconductor industry relies heavily on them despite the high initial costs [20].

Doping in graphene can be introduced in many different ways. Electronically by applying a back gate voltage in a field defects device or chemically by implantation of foreign atoms, charge transfer from the substrate or adsorbates or even defect engineering [21, 22]. Here, the goal is to use SHI to introduce foreign atoms into the graphene lattice and in chapter 6 it will be investigated whether this is possible.

As it is impossible to implant swift heavy ions themselve into the two-dimensional material, the dopants have to come from somewhere else. The idea here is, that the intense excitation of the SHI may be used to remove atoms from the substrate, which are in turn implanted into vacancies in the graphene lattice. This is tested for graphene on SiC(0001), where not only the doping effect in graphene will be probed by KPFM, but the effect of SHI on the extremely irradiation resistant SiC is studied in detail. In addition to these studies, graphene on SiO_2 field effect devices were manufactured and irradiated with swift heavy ions for the first time.

To conclude this chapter graphene and single layer MoS_2 field effect transistors are tested with respect to their radiation hardness. Swift heavy ions are known to be an appropriate tool to study devices in ionizing environments, which is crucial for appliations in space or fusion reactors. For this experiment multiple devices are irradiated using uranium ions with the highest electronic stopping power avaiable for monoatomic projectiles.

Chapter 7 concludes and summarizes this thesis and gives an outlook for possible applications of the results presented here as well as future experiments.

2 Basics

2.1 Two-dimensional Materials

Two-dimensional (2D) crystals have been theoretically predicted to be thermodynamically unstable over 80 years ago by Landau and Peierls [23, 24]. Because of a divergent contribution of thermal fluctuations in low-dimensional crystals' lattice, the displacement of atoms becomes comparable to interatomic displacements at any finite temperature [25, 26, 27]. And indeed a plentitude of experimental observations further backed up this hypothesis as for example the melting temperature of thin films gradually decreases with decreasing layer thickness and the film becomes unstable, which results in the formation of islands or even decomposition [28, 29]. This is, why in general 2D structures have been exclusively studied as an integral part of three-dimensional (3D) structures. These can be easily obtained by growing atomic monolayers on top of a crystal with similar crystal lattices [28, 29].

The game changer in this scientific field has been the experimental discovery of graphene and other 2D crystals like molybdenum disulfide (MoS_2) and hexagonal boron nitride (hBN) [30, 9]. By using a simple method, the mechanical exfoliation or scotch-tape method, it is possible to obtain atomically thin single crystals of the highest crystalline quality even on non-crystalline substrates [9, 8, 31]. Further, it is possible to prepare suspended membranes [32], liquid suspensions [33] and to grow 2D-materials on metal substrates by chemical vapour deposition (CVD) or plasma-enhanced CVD [OO.14] from which the 2D crystals can be transferred onto a target substrate [34]. In case of graphene, the high crystalline quality obtained from mechanically exfoliated crystals leads to charge carriers travelling up to several microns without scattering [30, 9, 8, 31].

There are two arguments which can be used to reconcile the experimental isolation of 2D crystals with the theory. First, it can be argued that 2D crystallites are quenched in a metastable state as they are extracted from 3D crystals and the strong interatomic bonding ensures that thermal fluctuations do not induce defects or dislocations [26, 27]. Second, the 2D crystal becomes stable by the generation of ripples in the third dimension [32, 35], which has been observed on a lateral scale of 10 nm. With this, thermal vibrations are suppressed and elastic energy is gained which can minimize the total free energy [35, 25].

The question arises how many layers are still 3D and how thin a material has to be, to be considered two-dimensional. Geim et al. proposed to take the electronic structure of the materials into account [25]. In case of graphene/graphite, only single layer and bilayer graphene have a simple electronic spectrum as both are zero band-gap materials

or zero-overlap semimetals. The electronic spectrum from 3-10 layers (so-called few layer) becomes increasingly complicated, several charge carriers appear [30, 36] and conduction and valence band are overlapping [30, 37]. Thicker structures are considered as thin films of graphite [25].

2.1.1 Graphene

The most prominent representative of 2D crystals is graphene, an atomically thin layer of carbon atoms with sp^2 hybridisation. The hexagonal crystalline structure and the unit cell of graphene are shown in fig. 2.1. Each carbon atom is bound to three other carbon atoms via covalent σ-bonding, which leaves one electron to contribute to the delocalized π-bonding system that is responsible for the extraordinary electronic properties of graphene. The unit cell consists of two atoms and therefore, the atomic lattice of graphene is divided into two sublattices. The in-plane lattice parameter in graphene is $a = \sqrt{3}a_0$, with a_0=1.42 $\mathring{A}$ being the nearest neighbour atom [37]. Altough it is not quite right to speak of a "thickness" for the atomically thin graphene sheet, the interlayer spacing of bulk graphite c_0=3.35 $\mathring{A}$ is generally considered as its thickness [38, 37].

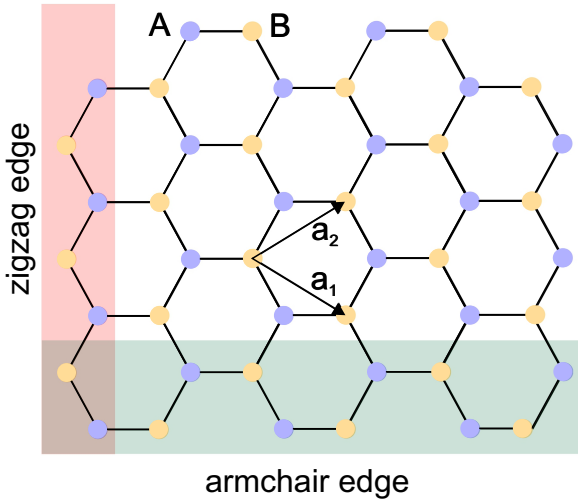

Figure 2.1: Honeycomb lattice structure of graphene, made out of two interpenetrating triangular lattices (a_1 and a_2 are the lattice unit vectors). The different graphene edges, namely zigzag and armchair edge, are marked in red and green, respectively.

Moreover the edges of graphene, which will be important in chapter 3.2, are highlighted in fig. 2.1. By breaking the symmetry at the edge, a major drawback for the application of graphene in electronics - the lack of an intrinsic band gap - can be overcome [39, 40]. The edges of graphene can be either zigzag or armchair oriented and alternate every 30° multiple. Both edges are metallic, but the zigzag edge presents a band of zero energy-modes which is absent in armchair edges [41]. Thus, using these edges to create a band gap in

graphene nanoribbons demands a precise control of edges and width [42]. However, edge disorder is severely decreasing the conductivity of graphene nanoribbons, because of effects like Anderson localization and anomalies in the quantum Hall effect, Coulomb blockade effects or hydrogen passivation [43, 44, 45, 46, 47].

The early work on 2D-materials is focused heavily on graphene due to its extraordinary electronic properties. Its quality can be observed in quantum Hall effect experiments at room temperature [48] or in a pronounced ambipolar field effect as shown in fig. 2.2. Here, the charge carrier concentration in graphene can be continuously tuned by an applied back gate from electron to holes with concentrations of up to 10^{13} cm^{-2}. The mobility μ of charge carriers in graphene on a substrate can exceed 15,000 cm^2/Vs even under ambient conditions [30, 9, 8, 31] and under optimal conditions - suspended graphene membranes, measurement in vacuum, at 5 K - result in mobilities of over 200,000 cm^{2}V/Vs [49] . Further, the mobility of the charge carrier remains constant even at high charge carrier concentration (n>10^{12}cm^{-2}) in electrically as well as chemically doped devices [50, 25].

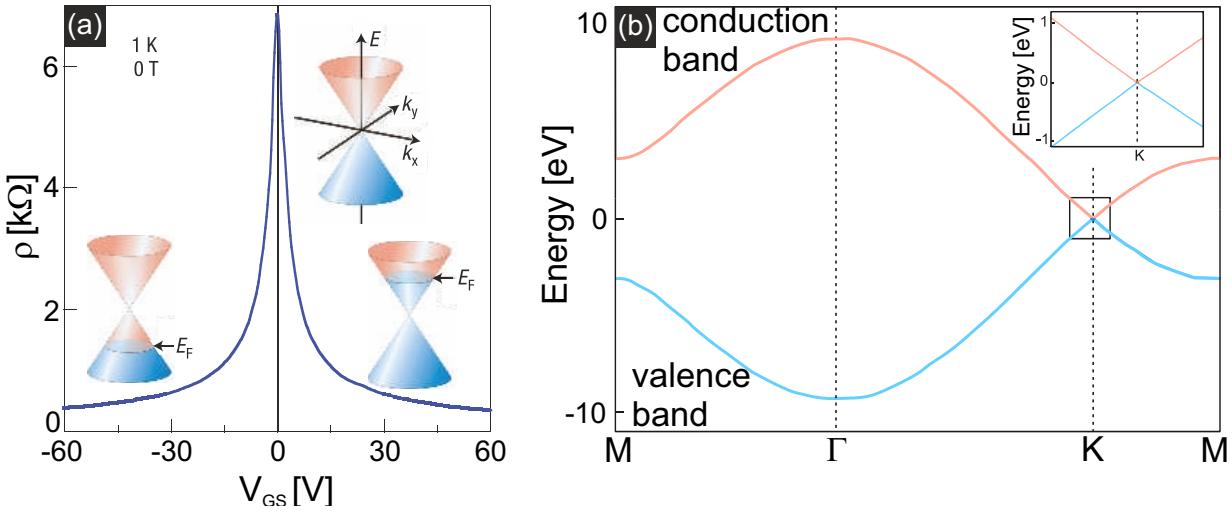

Figure 2.2: (a) Ambipolar electric field effect in graphene and schematic diagram of the band structure. By applying a gate voltage, the Fermi level is shifted above or below the Dirac point to introduce free charge carriers. Image from [25]. (b) The band structure of single layer graphene along $M\Gamma KM$. Inset is a zoom in of the region indicated by the square around the K point. Image adapted from [37].

The band structure of a single layer graphene shown in fig. 2.2 (b) [37]. The first thing to note is, that the valence and conduction bands do not overlap, but touch each other at the K-point of the first Brillouin zone. This makes the density of states vanish at the K-point and graphene is thereby a semimetal with no band gap. Moreover, looking at the area of where the transport is taking place (around the K-point), an unusual linear dispersion for low energies can be observed [51]:

$$E = \hbar v_F \vec{k} \tag{2.1}$$

which is in straight contrast to almost all solid state materials, where the relation $E \sim k^2$ is given for low energies around the K-point. This linear dispersion has direct consequences on the effective mass of charge carriers in graphene as they mimic relativistic particles with the effective speed of light $v_F \approx 10^6$ m/s and are described best by the Dirac equation rather than Schrödinger [25, 52, 53, 54, 55, 56, 57]. These so-called massless Dirac fermions can be seen as electrons that have lost their rest mass m_0 [25].

However, graphene got its nickname "wonder material" not just because of its outstanding electronic properties, but its other physical properties are impressing as well. Graphene is impermeable to gases down to helium atoms [58], it can sustain enormously high densities of electric current, a million times higher than copper [59], and the mechanical strength of graphene exceeds that of steel with an intrinsic strength of 130 GPa and a Youngs modulus of 1 TPa [60, 61]. Graphene is optically transparent with an optical absorption of $\pi a \approx 2.3\%$ [62], with a being the fine-structure constant. Further, graphene can be chemically functionalized via hydrogenation or oxidation to obtain new materials like graphene and graphene oxide, respectively [63, 64, 65, 66].

In order for graphene to play out its advantages it is crucial to find the right substrate materials. The charge carrier mobility for instance can be increased 10-fold, compared to standard graphene/SiO_2 systems, when graphene is encapsulated between hBN layers, resulting in μ values of 100,000 cm^2/Vs, which can even be enhanced to 500,000 cm^2/Vs by using the "dry-peel" transfer allowing ballistic devices [67, 68, 69, 12]. This combination of 2D-materials, which are generally called 2D heterostructures, can be used to specifically adress weaknesses in some materials. The lack of an intrinsic band gap in graphene can be bypassed for example by creating a heterostructure of graphene and single layer MoS_2, a direct band gap semiconductor. A Schottky barrier is formed at the graphene MoS_2 interface and the resulting device exhibits an on/off ratio of up to 100 [70]. The charge carrier device in a graphene/MoS_2 is quite poor with 600 cm^2/Vs, but this again can be circumvented by encapsulating graphene with hBN and MoS_2 where mobilities of up to 60,000 cm^2/Vs have been reported [71]. This underlines the importance of exploring new 2D-materials, which will be briefly discussed in the next section.

2.1.2 Two dimensional materials beyond graphene

In the past nine years of graphene research a plentitude of methods for characterizing, synthesizing, detecting, transferring and manipulating the properties of low dimensional materials have been developed. These methods led to a very quick maturing of research for new 2D-materials which exhibit new and unique properties [13]. The most common class of 2D crystals are the layered van der Waals solids. This is because of their crystalline structure (neutral, single atom thick or polyhedral thick layers of atoms), which exhibits strong covalent or ionic bonds within the layers (energies of 200-6000 meV) and only weakly bound to each other by van der Waals bonding (energies 40-70 meV) [13], allowing researchers to easily exfoliate van der Waals solids into 2D crystals for research.

An attempt to categorize 2D-materials in three different groups has been done by Geim

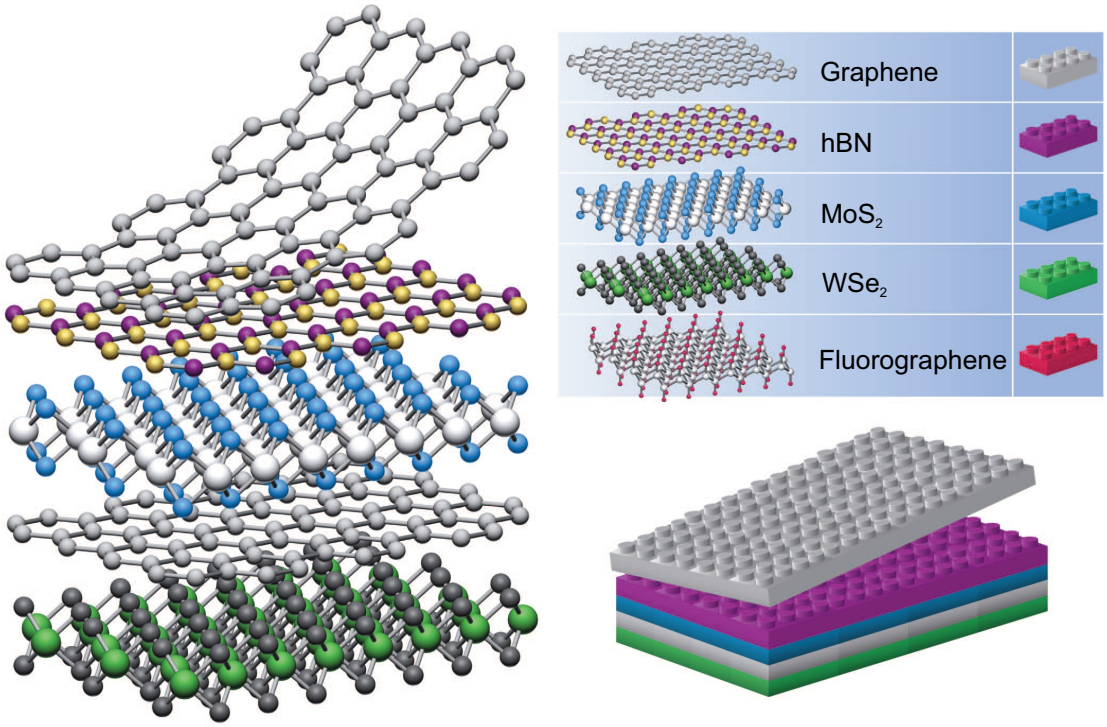

Figure 2.3: Constructing van der Waals heterostructures, concept in analogy to Lego blocks. Image taken from [12].

et al. [12]:

1. **Graphene family** - The first one is the graphene family which consists of graphene derivates like graphane [64], fluorographene [66] and graphene oxide [72] as well as graphene analogoues like "white graphite" hexagonal BN [73], silicene [74, 75] and monolayers of boron carbon nitride [76].

2. **2D chalcogenides** - Next to graphene, the most investigated family is the 2D chalcogenides. This group can be further divided into transmetals, semiconductors, metallic dichalcogenides and layered semiconductors. In general these materials are composed with a stoichiometry of MX_2 (M=Ti,Zr,Hf,V,Nb,Ta,Re;X=S,Se,Te). In this group, MoS_2 is the most studied material and will be further introduced in the next section.

3. **2D oxides** - The last group consists of oxides like monolayers of mica, TiO_2, MoO_3, WO_3, perovskite-like crystals such as BSCOO and $Sr_2Nb_3O_{10}$ and 2D hydroxites [77, 78, 79, 13]. Information about these oxides is very limited up to now, first experiments show that single layers of 2D oxides have lower dielectric constants and larger band-gaps and that they can exhibit charge density waves [9, 77].

These large quantities of available 2D-materials open up the opportunity to design van der Waals heterostructures with a vast pool of potential application. For example, stacking

graphene on top of mica and repeating this numerous times, the resulting van der Waals heterostructures become superficially similar to superconducting CuO [12]. Conceptually this can be seen as playing Lego on an atomic scale, with different construction rules, see fig. 2.3.

However, care has to be taken before using those 2D crystals in air. Monolayers of metallic dichalcogenides for example seem to react with air or liquids. The resulting 2D-material is not the 2D counterpart of the exfoliated 3D crystal. In contrast to this, 2D oxides tend to loose oxygen [12].

2.1.3 Single layers of MoS_2

Until now, of the transmetal dichalcogenides MoS_2 has caught the most attention, because of good availablity and its rich physics related to transport and optical properties [9, 78, 80, 80, 81, 82, 83, 84, 85, 86, 87, 88, 89, 90, 91, 92, 93, 94, 95], [OO.05,OO.11] which have been demonstrated for single and few layer MoS_2. In general the physical structure of MoS_2 is very similar to that of the honeycomb lattice of graphene, shown in fig. 2.4. The difference is, that both sublattices A and B are occupied by either molybdenum or sulfur atoms rather than carbon atoms, which form a trilayer with an height of ∼0.7 nm [96].

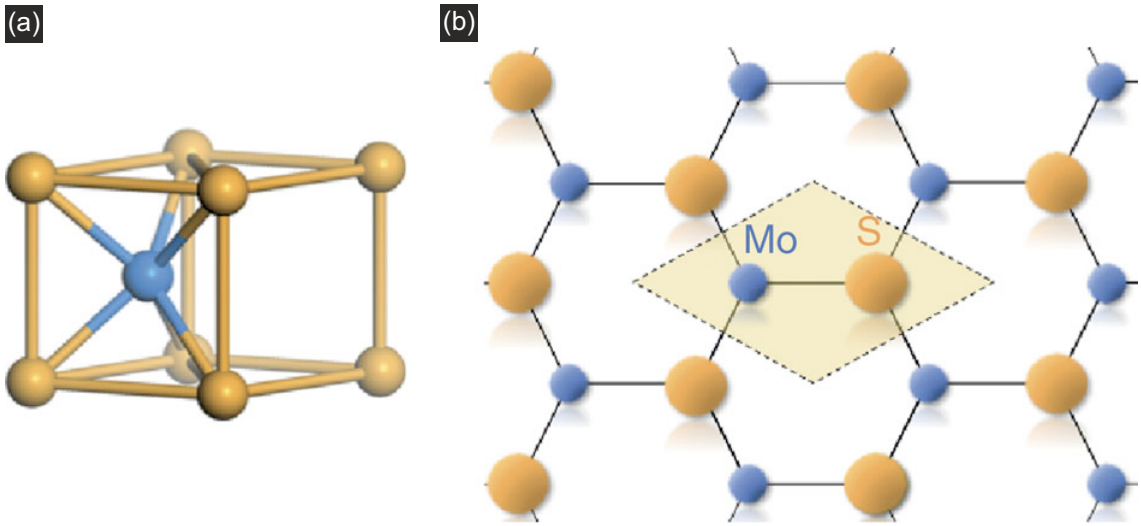

Figure 2.4: (a) Coordination environment of a molybdenum atom (blue sphere) in the MoS_2 structure is shown. Sulphur atoms are coloured golden. (b) Top view of the single layer MoS_2 lattice, which emphasizes the connection to a honeycomb lattice. Shaded region corresponds to one unit cell, with a unit cell parameter of $a = 0.312$ nm. Figure taken from [84].

Bulk MoS_2 is known to be an indirect band-gap semiconductor with a band-gap of 1.29 eV [97] and widely used as a lubricant in industry [98]. The calculated band structures of bulk and single layer MoS_2 are shown in fig. 2.5 (a) and (b) [99]. It can be observed that for

the bulk MoS_2 the extrema of the conduction and valence band do not occur at the K point and thus the indirect band-gap. Due to quantum confinement effects in single layer MoS_2, the indirect band-gap is shifted upward in energy by more than 0.6 eV as confirmed by *ab initio* calculations [99, 100, 101, 102, 103, 104]. This leads to a crossover to a direct band-gap material, which has been experimentally observed by absorption, photoconductivity and photoluminescence spectroscopy [80], shown in fig. 2.5. By thinning out MoS_2 down to one layer, a bright photoluminescence peak at 1.85 eV can be observed, which is not present for thicker layers [SN.2012].

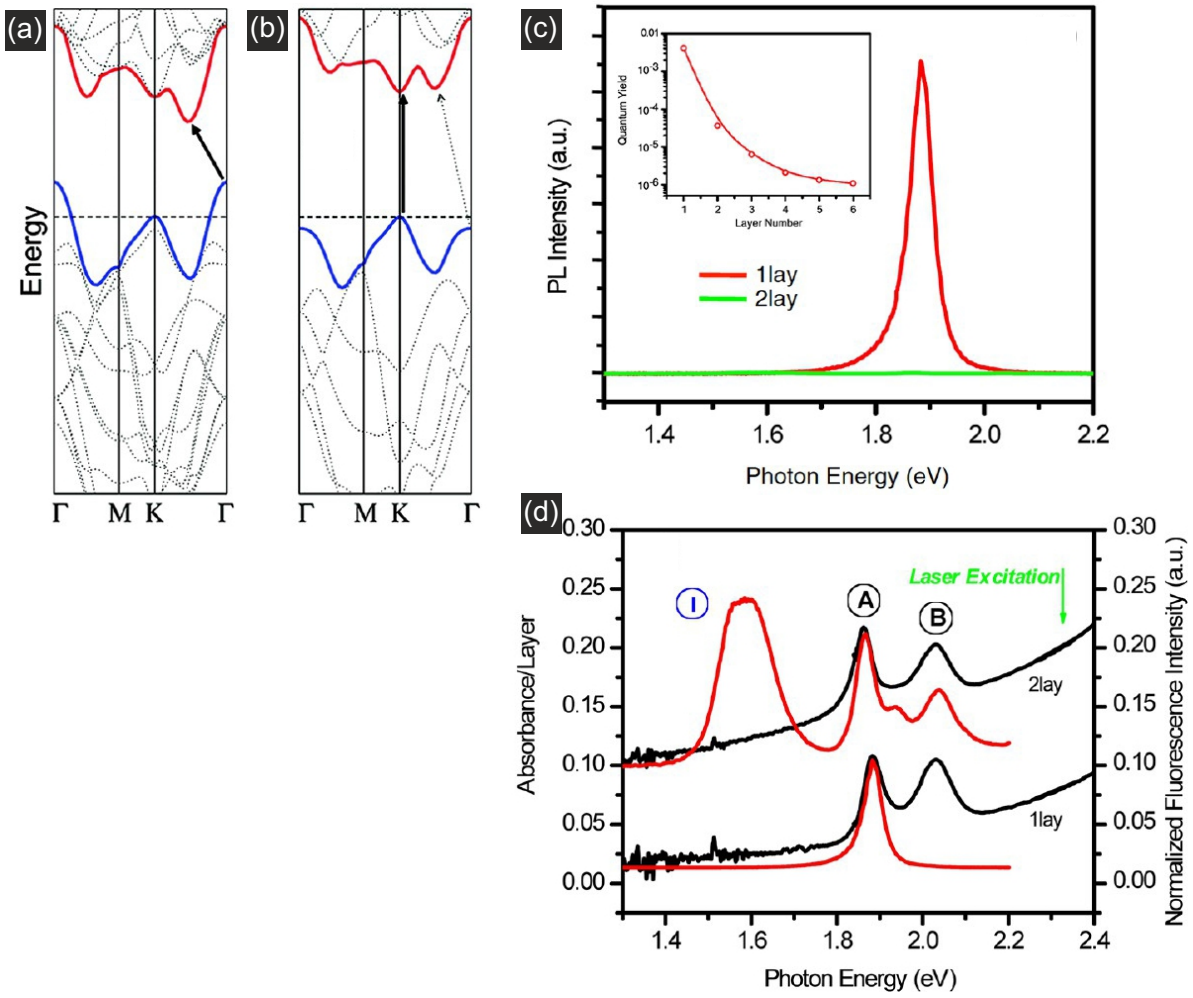

Figure 2.5: Calculated band structure of bulk MoS_2 in (a) and single layer MoS_2 in (b). Solid arrows denote the lowest-energy transition. (c) Photoluminescence spectra of single and bilayer MoS_2. In the inset, the PL quantum yield is plotted. (d) Absorbtion spectra (left axis) and corresponding PL spectra (right axis). Image adapted from [13].

The optical properties of single layer MoS_2 are dominated by excitonic transitions. The

absorption spectra in fig. 2.5 show two distinct absorption peaks, which arise from band-to-band transitions in a 2D system with a direct band-gap, known as A (∼1.9 eV) and B (∼2.1 eV) excitons. These excitons originate from the two highest-lying spin-split valence bands to the lowest conduction bands [99, 80, 105]. The optical properties can be further tuned by strain engineering [106, 107, 108, 109] and doping [86] [OO.03,OO.11].

As with graphene, new phenomena are expected for the edges of single layer MoS_2, where symmetry is broken [110, 111]. In the projection in the plane, transmetaldichalcongenides show a similar hexagonal or honeycomb like lattice structure. However, because there are three different planes, the edge termination can be either zigzag or armchair, chiral or even a mixture of these types [112]. Knowledge about the chemical termination of these edges is crucial in order to determine the local physiochemical properties [13]. For example, metallic edge states have been observed at the edges of single layer MoS_2 and an enhanced catalytic activity has been correlated with the density of edge sites [113, 114, 115, 116].

2.2 Swift heavy ion - matter interaction

2.2.1 Energy loss of ions in solids

Basic knowledge of the ion-matter interaction is crucial for its application in material science, semi-conductor technologies or ion beam analysis [117, 118]. Ions are created by adding electrons to an atom or removing them. These ionized atoms with the charge Q are often accelerated in an electrostatic field by applying a voltage U to kinetic energy of $E = Q \cdot U$. By entering the material, the ion undergoes a variety of collision- and scattering processes, which are depending on the kinetic energy, charge state and kind of target material and come along with an energy loss of the projectile until the ion is stopped after a certain distance [119, 117, 120, 118]. Basically, one can distinguish between two scattering processes.

Firstly, elastic scattering between the atomic nuclei of the collision partners (ion and target atoms). Here, the Coulomb interaction is dominating and the electrons are merely acting in form of screening. This results in changes of the velocity and direction of motion for both collision partners based on the impact and energy conservation [119, 117, 120]. This process is called nuclear stopping or nuclear energy loss in the following. Secondly, inelastic scattering of electrons by one of the collision partners can lead to changes in the electron states, which is called electronic stopping or electron energy loss.

The energy loss of an ion $dE < 0$ per unit of length dx in a bulk material with statistical distributed atoms is defined by the atomic density N_0 and the stopping cross-section S(E):

$$\frac{dE}{dx} = -N_0 S(E) \text{ with } S(E) = \int T d\sigma(T, E) \tag{2.2}$$

T denotes the transferred energy during a single collsion and $d\sigma(T, E)$ denotes the cross-section [117, 118]. Whether elastic scattering, corresponding to nuclear energy loss dE_n with a nuclear cross-section of $d\sigma_n$ and a stopping cross-section $S_n(E)$ or inelastic scattering corresponding to electronic energy loss dE_e with the respective cross-section $d\sigma_e$ and $S_e(E)$ is taking place, is determined by the energy E, atomic number Z_{ion} and mass M_{ion} of the ion as well as atomic number Z_{sol} and mass M_{sol} of the solid. In general, both processes are regarded as statistically independent from each other and therefore we find:

$$d\sigma(T, E) = d\sigma_n(T, E) + d\sigma_e(T, E) \text{ and } S(E) = S_n(E) + S_e(E) \tag{2.3}$$

With this, the energy loss per unit length (or stopping power $S(E) = S_n(E) + S_e(E)$) for a solid made up of i elements is given by:

$$\frac{dE}{dx} = -S(E) = -\sum S^i_{sum}[S^i_n(E) + S^i_e(E)] \tag{2.4}$$

here, the additivity of the stopping cross-sections S^i(E) is used, which can be described by the Bragg rule $S(E) = \sum_i c^i \cdot S^i(E)$ with the relative composition of the bulk material $c^i = S^i_{sum}/S^i_{sum}$ [117].

2.2.2 Swift heavy ions

A major part of this thesis is about the interaction of two dimensional materials - graphene and MoS_2 in particular - with high energetic ions in form of swift heavy ions (SHI). Therefore the focus in this part will be the specific properties of these projectiles, which will be introduced in this section together with possible mechanisms taking place.

The main interaction of SHI with matter occurs in form of electronic excitation and ionization processes (electronic stopping) [121]. This criterion is fulfilled, if the kinetic energy of the ion is around the maximum of the energy loss curve and $S_e \gg S_n$. An exemplary energy loss curve is shown in fig. 2.6, which is calculated using the SRIM 2013 (stopping range in matter) software package [122] and it plots the nuclear and electronic energy loss of Xe ions in graphite with respect to the ion energy. In the low energy region from a few keV to several MeV, the nuclear energy loss S_n is dominating. Typically starting with several tens of MeV energy, the electronic energy loss S_e is dominant and reaches its maximum typically between 300 - 3000 MeV while nuclear stopping is negligible. Nuclear stopping (like sputtering of target atoms) is almost nonexistent and only occurs at the end of the ion trajectory when the energy of the SHI is reduced to a few hundred keV [121]. Particles like protons, alphas and other low-mass projectiles with limited energy loss are excluded by the term "heavy".

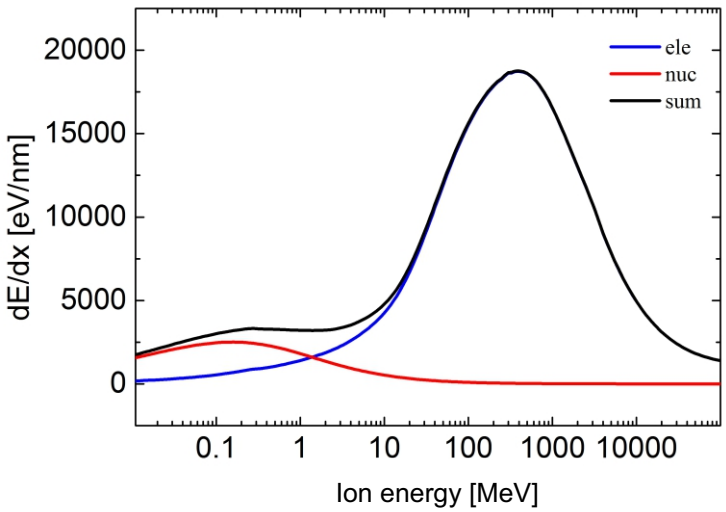

Figure 2.6: Energy loss due to electronic and nuclear stopping of Xe ions in graphite calculated using the SRIM software package [122].

Owing to its high energy, the SHI does not experience changes in direction or velocity and an energy of $S_e \approx (10 - 40)\ \frac{keV}{nm}$ is deposited along its trajectory [117, 123, 124]. This electronic stopping can result in a long, nanometric and permanent modification (ion track) in the target material [125, 126, 127, 128]. The length of this ion track is given by the kinetic energy of the projectile and usually reaches 10 μm to 50 μm.

The area with the highest energy density is located at the core of the ion track with a radius r_c, which can be estimated for non-relativistic ions by the relation $r_c \approx \hbar v_I / 2Eg$,

whereas ν_I is the ion velocity and E_g is the band gap energy [129]. In the early stages, a proportion of S_e leads to a nearly instantaneous primary excitation and ionization of target material along the ion trajectory by Auger-processes ($t = 10^{-19}$ to 10^{-17} s) and plasmons ($t = 10^{-16}$ s) [124, 130]. Electrons with a high kinetic energy are freed, which results in an electronic collision cascade perpendicular to the ion trajectory [123]. The so called δ-electrons deposit their energy far away from the original core of the ion track, leaving the core highly ionized [124]. The electronic energy density in the core region of the ion track is given by

$$\rho \approx \frac{S_e}{2\pi r_c^2}(1 + \frac{1}{1 + 2ln(R_p/r_c)}) \tag{2.5}$$

and amounts to $\approx 50\%$ of S_e [131]. Here R_p is the projected penetration depth of the ion in the solid and r_c the radius of the core track. At first, the area around the ion track core consists of hot, excited electrons and cold, resting lattice atoms (electron-hole-plasma). Starting at $t = 10^{-15}s$ thermalizing effects in the electronic systems are taking place, which lead to energy-dissipation and transfer processes to the lattice atoms [123]. In fig. 2.7 the different processes taking place induced by the SHI excitation of the solid with respect to the time scale are summarized.

Energy transfer mechanisms - Coulomb explosion

In principle there are three different energy transfer mechanisms which are currently discussed for the SHI matter interaction [133, 124]. The fastest process is the so-called Coulomb explosion, described by Fleischer et al. [134]. Here, the removal of the electrons inside the core of the ion track results in an electrostatic repulsion of the positive ions, ejecting them into the surrounding lattice. This is possible, if the electrostatic repulsion is stronger than the mechanical stiffness of the solid atoms and the following criterion is fulfilled:

$$(ne)^2/\epsilon a_0^4 > Y/10 \tag{2.6}$$

whereas Y is the Youngs modulus, a_0 is the average atomic spacing, ϵ the dielectric constant and n is the number of average ionizations (in unit charges) [134]. This relation suggests that Coulomb explosion is preferred in materials with low mechanical strength, low dielectric constant and close interatomic spacing materials. Indicators for this mechanism like electrostatic potentials surrounding the ion track in the fs-regime have been detected by high resolution in-situ electron spectroscopy by the variation of the energy of Auger-electrons [135, 136, 124].

There are however two further restrictions for this mechanism to take place, which are related to the mobility and concentration of current carriers [134]. First, a track formation would be inhibited, if the removed electrons are replaced with electrons from the surroundings before the ionized atoms have been displaced, which happens after t$\approx 10^{-13}$s. With the density of free electrons n_n and the number of ionizations per atomic planes n_a, the radius of the region to be drained is $\pi r^2 a_0 n_n = n_a$. Using the Einstein relation $D = \mu_e kT/e$ (μ_e

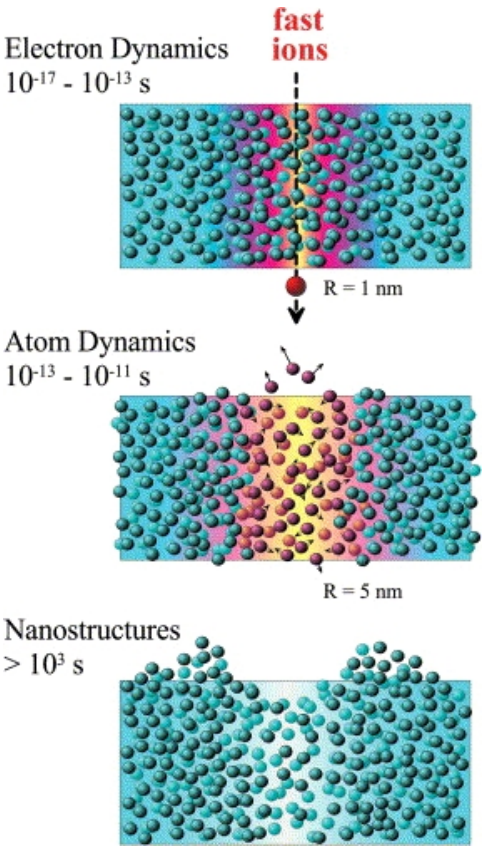

Figure 2.7: Evolution of an ion track with time. The primary excitation and ionization of the SHI induces atomic motion, which results in a permanent modification in the target. The modification can be of structural or chemical nature. At the surface, various modifications like hillocks or craters are formed. Image taken from [132].

as the electron mobility), which is inserted into the time for electrons to diffuse a distance r^2/D, the restriction relation 1 is formed:

$$n_n < en_a/\pi a_0 \mu_e kTt \tag{2.7}$$

Usually this relation is followed by insulators and semi-conductors rather than metals [134]. The second restriction affects the hole mobility. As the core of the ion track is basically a high concentration of holes, they might move away preventing a permanent track creation. Based on the assumption that the holes have to move at least half of r_0 away, the restriction relation 2 is given:

$$\mu_h < r_0^2 e/4tkT \tag{2.8}$$

with μ_h as the hole mobility and r_0 as the track radius. At room temperature, a hole

mobility of at least 10 cm^2/Vs will prevent ion track formation, which excludes a lot of semiconductors like silicon and germanium [134, 137].

The main problem with this model is the theoretical significance, as it is not possible to calculate track lengths/diameters, because of the quantitative data on the important parameters like efficiency of electron capture processes and life time of electrostatic potentials [123].

Energy transfer mechanisms - Non thermal melting

An alternative mechanism to describe the SHI matter interaction is the non thermal melting, in which a collective atomic rearrangement is taking place in the sub-ps time scale after charge neutrality has been restored at the core of the ion tracks [123]. The idea is, that directly after charge neutralization, the interatomic potentials are far away from a state of equilibrium, because the electrons are still excited due to slow recombination processes. This high density of electronic excitations present in the core of the ion track induces nonbinding and repulsive potentials, which will eventually weaken the covalent bondings, finally resulting in bond breaking and atomic rearrangement [138, 139]. Based on a simple quantitative model, Tombrello proposed a critical electronic energy density needed for the breaking of atomic bonds, finding good agreement with inorganic crystalline materials [140].

Energy transfer mechanisms - Electron phonon coupling

The last mechanism which takes place at a time scale of about $t = 10^{-13} - 10^{-12}$s is the electron-phonon-coupling [141]. This model was proposed by Toulemond et al. [142, 141, 143, 144, 145] and Meftah et al. [146, 147] based on the work of Seitz and Koehler [148]. The general idea is to treat the electron propagation within an integrated continuum approximation, which results in the transport being calculated based on the integrated momentum, the electron's kinetic energy. The intense electronic excitation of the SHI projectile is transferred via electron-phonon-collisions into an effective emission of photons - heating the lattice in the core of the ion track [149]. The resulting lattice temperatures can be calculated using the two-temperature-model (TTM) [150, 151, 141], which is based on two coupled heat diffusion equations for the electron and phonon system. The equations of the TTM are given by:

$$\begin{aligned} C_e(T_e)\frac{\partial T_e}{\partial t}(\vec{r},t) &= \nabla\cdot(\kappa_e(T_e)\nabla T_e(\vec{r},t)) \\ &- g\cdot(T_e(\vec{r},t)-T_p(\vec{r},t))+S(\vec{r},t), \qquad (2.9) \\ C_p(T_p)\frac{\partial T_p}{\partial t}(\vec{r},t) &= \nabla\cdot(\kappa_p(T_p)\nabla T_p(\vec{r},t)) \\ &+ g\cdot(T_e(\vec{r},t)-T_p(\vec{r},t)). \qquad (2.10) \end{aligned}$$

Here, $T(\vec{r},t)$ describes the temperature, $C(T)$ and $\kappa(T)$ are the heat capacity and thermal conductivity, respectively. The subscripts e and p refer to electron and phonon quantities.

$S(\vec{r},t)$ denotes the energy deposition of the ion. The transfer of the energy from one system to the other is controlled by the the electron-phonon-coupling parameter g. In general, g depends on the electron distribution function and therefore on the electron density, etc. [145, 152, 153] and thus the specific excitation profile, that is the SHI energy.

The electron-phonon-coupling is a crucial parameter in this equation and can be determined by measuring thermoreflectance [154], optical reflection [155] or evaluating ablation rates [156]. The problem here is however, that these measurements are usually performed for low laser intensities, which are not directly comparable to SHI experiments. There are two ways to approximate the g parameter. The first one is by fitting the experimental data to the TTM calculation [157]. The other assumption describes the changes in all occupied phonon states, in which g can be estimated for high temperatures in the electron system depending on the sound velocity v_s and the electron mean free time between two collisions $\tau_e(T_e)$ [158]:

$$g = \frac{\pi^2 m_e n_e v_s^2}{6\tau_e(T_e)T_e} \tag{2.11}$$

The energy deposition $S(\vec{r},t)$ can be calculated by the following formula:

$$S(\vec{r},t) = bS_eG(t)F(\vec{r}_\perp) \ . \tag{2.12}$$

[159]. $G(t)$ is a Gaussian with a half-width of 1 fs [142] and $F(\vec{r}_\perp)$ is the spatial electron distribution given by Waligorski *et al.* [159], the stopping power S_2 is obtained using the SRIM software package [122].

The intense electronic excitation is expected to result in locally increased temperatures, which may exceed the melting temperature of the material leading to a phase transition and the ion track is created by a so-called thermal spike [143]. Because of the high cooling rates $(10^{-14} - 10^{-13})$ Ks^{-1}, the material cannot recrystallize and the lattice rearrangements of the fluid phase are permanently retained within $(10^{-11} - 10^{-10})$ s [123]. The TTM used for calculations in this thesis has been adapted for processes taking place in close vicinity to the surface, breaking the cylindrical symmetry of the ion track in conventional TTM calculations, by Orkhan Osmani. The used code is based on a fully three dimensional version of the TTM, which was originially used to describe surface tracks in $SrTiO_3$ [157] and was further modified to study effects taking place at the surface in [OO.15].

2.2.3 SHI surface modifications

Depending on the experimental setup (perpendicular or grazing incidence angle irradiation), different surface modifications have been detected. For SHI irradiations under perpendicular incidence angles, a hillock or crater like structure is formed at the impact site [160]. Inside the bulk material a cylindrical ion track is formed with a core and shell track area for SHI irradiated solids, e.g. SiO_2 [161]. In case of glancing incidence irradiation, a so-called surface track is created, which usually consists of a chain of nanosized hillocks or elongated protrusions [162, 160]. Examples for surface modifications after SHI irradiation are shown in fig. 2.8.

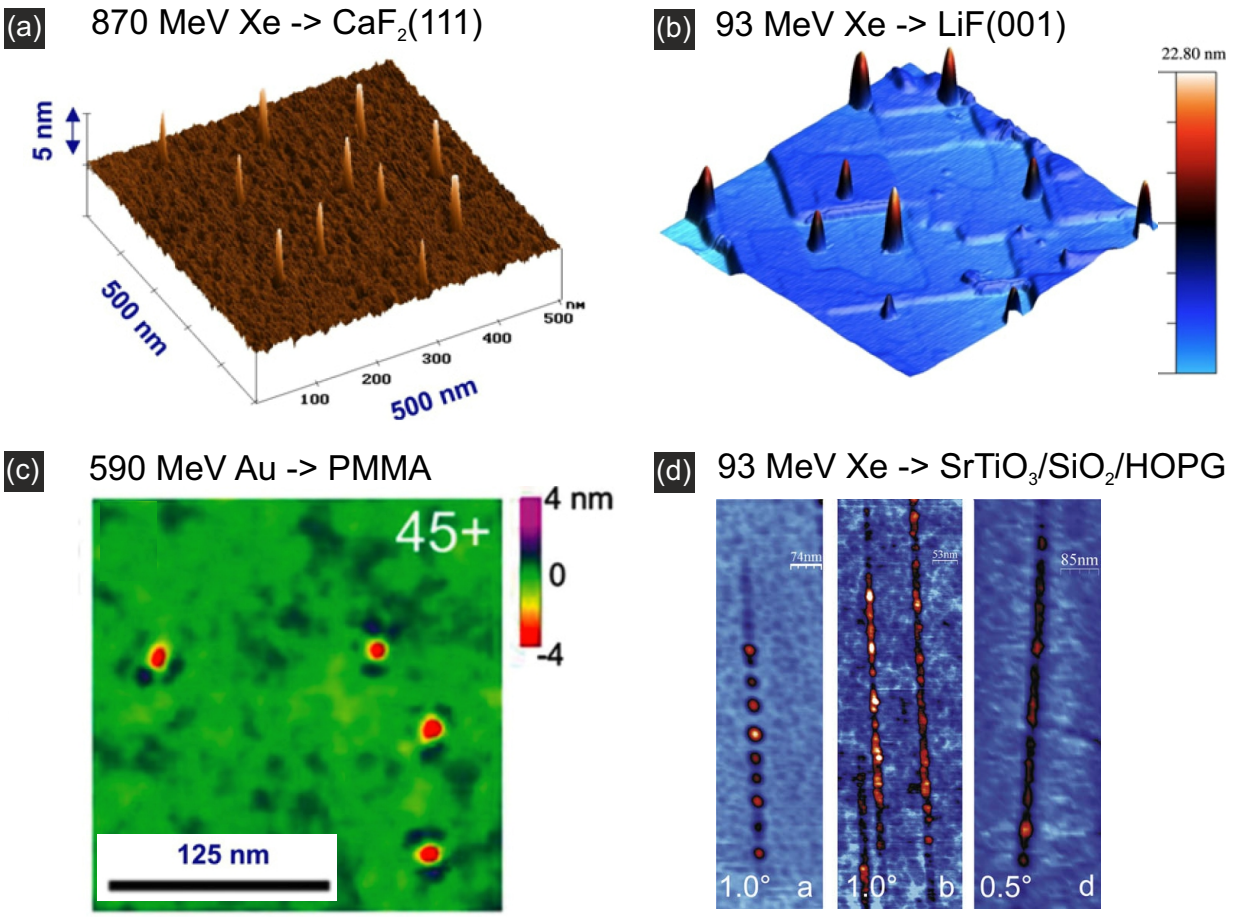

Figure 2.8: (a) AFM topography (contact mode) of $CaF_2(111)$ surface irradiated with 870 MeV Xe ions with a fluence of $5{\cdot}10^9$ ions/cm^2 showing hillock formation after perpendicular incidence irradiation [163]. (b) AFM Topography (tapping mode) of a cleaved LiF single crystal irradiated with 93 MeV Xe ions with a fluence of $5{\cdot}10^8$ ions/cm^2 [121]. (c) AFM topography of craters produced in PMMA by 591 MeV Au ion irradiation [160]. (d) Grazing incidence irradiation with SHI of $SrTiO_3$, SiO_2 and HOPG. Elongated chains of nanosized hillocks are created [164]. All images adapted from the respective publication.

Although the inner structure is unknown as of yet, the surface tracks are commonly understood as the remnants of expanding material due to the primary processes triggered by the SHI. However, which of the processes - Coulomb explosion, non thermal melting or thermal spike - is actually taking place cannot be distinguished with certainty. It is expected, that all three mechanism contribute to track formation on different time scales [123, 133].

In the case of 2D crystals, little is known about the physical triggered mechanisms in these ultimately thin materials by swift heavy ions. As all theoretical models presented

above have been developed for bulk materials, applying them to 2D materials is not trivial and has not been done successfully as of yet. The majority of the work related to irradiation studies of 2D-materials has been performed in the low energy regime (keV) or using electron beams [165, 166, 167, 168, 169, 170, 171, 172]. For the high energy regime (up to 1 MeV) it has been demonstrated using atomistic calculations by Lehtinen et al., that graphene is transparent to high energy ions and that it is stable and hardly permeable for small atoms even with large defects [173, 174]. Therefore it has been proposed to use graphene as a window material for separating a high-vacuum ion beam system from targets [174]. First experimental studies for high energy ions showed however, that the defects induced are not negligible. For grazing incidence irradiation, large foldings can be created [19] while for perpendicular incidence irradiations, the defects exceed single vacancies observed for low energy ions [175, 176]. Interestingly it has been found in these studies that single layer graphene is more sensitive to irradiation defects damage than its bulk counterpart.

The authors from [176] compared track radii of defects induced by 100 MeV Ag irradiation with inelastic thermal spike calculations. As important parameters for the calculation are unknown (in particular the electron-phonon coupling parameter and the thermal conductivity), the thermal spike has been calculated for graphite and therefore the agreement between the experiment and the calculation is not convincing. Whether Coulomb explosion is a possible mechanism in 2D materials can be estimated by the restriction formulas. Because of the very high mobilities measured for graphene devices (suspended and supported graphene sheets), Coulomb explosion in graphene is not expected as even the worst graphene devices show hole mobilities significantly larger than μ_h=10 V/cm^2. This is however not the case for MoS_2 which suggests a comparison between these materials.

The question about the mechanism is further complicated by the fact that graphene is usually supported by a substrate and indirect damage resulting from backscattered particles and sputtered atoms has to be taken into account as well [177].

3 Instruments and Methods

In this chapter, the experimental methods used in this thesis will be introduced to the reader beginning with main imaging and characterization techniques for atomically thin layered materials - namely atomic force microscopy (AFM) in combination with Kelvin probe force microscopy (KPFM) and μ-Raman spectroscopy. After this, the sample preparation techniques are presented, the well known mechanical exfoliation and in addition UHV exfoliation, which is basically applying the mechanical exfoliation in situ. Further, the preparation of graphene and MoS_2 field effect devices by photolithography is presented and the resulting characteristic transport measurements are discussed. At last, the different ion accelerator facilities follow, where the irradiation experiments in this thesis have been performed are introduced.

3.1 Atomic force microscopy

Atomic force microscopes belong with the scannning tunneling microscopes to the group of scanning probe microscopes. They represent ideal tools to deliver spatially resolved data of nanomaterials. They differ from optical and electron microscopes, as the image is formed due to the interaction of a physical probe with a sample and not through light or electrons. The scanning tunneling microscope (STM) was developed first in the early 1980s by Binning and Rohrer [178, 179] which was honoured with the Nobel Prize in Physics in 1986. Shortly after, the first atomic force microscope was developed by Binning, Quate and Gerber [180] and the first atomically resolved AFM image of the Si(111)-(7x7) reconstructed surface was achieved by Giessibl in 1995 [181, 182]. Atomic force microscopy is widely used in the 2D-material community. It enables to image nanoscale deformations, contaminations and defects [166, 183, 184, 185] and it is even possible to achieve atomic resolution under ambient conditions as it has been shown recently [186]. Furthermore, employing various advanced AFM techniques gives access to a manifold of physical properties like conductivity (conductive AFM) [187], elastic and frictional properties (force measurements) [188, 60, 189], surface potential (Kelvin probe force microscopy) [190, 191] and quantum capacitance [192].

3.1.1 Imaging modes

A standard experimental setup of an AFM is shown in fig. 3.1 (a). The probe, which is typically made of silicon with a tip diameter of below 10 nm, is attached to a cantilever that is again connnected to a chip to facilate the handling. During the measurement, the tip is being moved in three dimensions using piezoelectric crystals. A laser is focused on the backside of the cantilever and reflected to a position sensitive photodiode (PSD) in order to detect the tip-surface interaction. Depending on the imaging mode, this can be the bending of the cantilever (contact-mode), amplitude (intermittent contact-mode, or tapping mode) or the frequency shift (non-contact mode). The signal of the photodiode goes to a PID controller, the actual value is compared to the setpoint and a signal is sent out to the z-piezo to adjust the z-position of the tip if necessary. This information is used to assemble an image point by point.

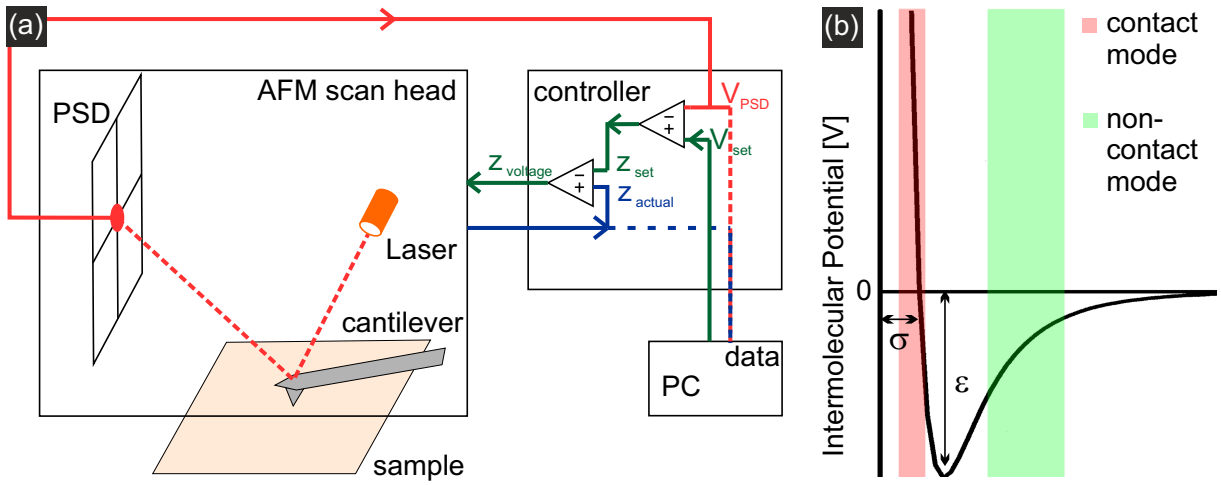

Figure 3.1: (a) Scheme of an experimental AFM setup as described in the text. (b) Lennard Jones Potential, for large distances R the attractive forces are dominating (non-contact mode) while for short distance the repulsive forces are dominant (contact-mode)

The interaction between the tip and the surface, which comprise of the attractive van der Waals forces and Pauli repulsion because of overlapping electron orbitals, can be described by the Lennard-Jones-Potential:

$$V(R) = 4\epsilon((\frac{\sigma}{R})^{12} - (\frac{\sigma}{R})^{6}) \tag{3.1}$$

[193]. Here ϵ is the potentiall well and σ is the zero-crossing of the potential. The minimum of the potential lies on r_0=1.12σ. The Lennard-Jones-Potential is shown in fig. 3.1 (b) and marked therein are the different imaging modes for the AFM. These three imaging modes are briefly introduced in the following:

1. **Contact mode** - Contact mode force microscopy is based on the measurement of the static deflection of the cantilever. The tip is brought into contact with the sample surface (repulsive regime) and the deflection of the cantilever is set to be constant. The deflection corresponds with the normal force on the cantilever, which can be calculated with knowledge about the spring constant [194]. A major drawback in this technique is, that compared to the other imaging modes, very high forces are applied onto the surface, which can result in tearing or folding of 2D-materials [195].

2. **Non-contact mode** - The only AFM technique that is able to provide true atomic resolution imaging is the non-contact (NC) or dynamic force microscopy. The cantilever is excited to oscillate at its mechanical eigenfrequency by a piezoactuator, which is done by a phase-locked-loop. The electrical signal, which is proportional to the cantilever oscillation, is applied to the piezoactuator after amplification and phase-shifting [194]. Due to the tip-surface interaction, the frequency shifts, which is tracked by employing fast frequency demodulation schemes [196]. A constant frequency shift signal is usually used to controll the tip-surface distance.

3. **Tapping mode** - In the dynamic tapping mode, the amplitude of the cantilever instead of the frequency is used as the control parameter. The tip is typically excited near its eigenfrequency to an oscillation between 20 and 100 nm. By approaching the surface, the amplitude is reduced due to an intermittent contact to the surface during each cyle. The advantage of this mode is that while the resolution is mainly limited by the tip shape, comparable to NC imaging, the forces on the sample are greatly reduced compared to contact-mode imaging [197, 198, 194].

3.1.2 Kelvin probe force microscopy

There are two reasons to perform Kelvin probe force microscopy on two-dimensional materials. One is to study the surface potential of these materials, which gives important information on the electronic proporties, and the other is to get correct height informations. In order to obtain correct height information in NC AFM measurements, it is important to compensate electrostatic forces between the AFM tip and the sample surface [199].

Shown in fig. 3.2 is, in which way an electrical force is generated when an AFM tip is brought into close and how this force can be nullified. In fig. 3.2 (a) the tip and the sample are not in contact with each other. The vacuum levels are aligned, while the Fermi levels are not due to the different work functions of the materials. In (b) these materials are electrically connected and the Fermi levels are aligned by electron current flow from the material with the higher work function to the material with the lower work function. This results in a non uniform charge distribution between sample and tip and a contact potential difference V_{CPD} between sample and tip is formed, as the vacuum levels are not the same anymore. The contact potential difference (CPD) between a conducting tip and a sample is defined as:

$$V_{CPD} = \frac{\Phi_{tip} - \Phi_{sample}}{-e}, \tag{3.2}$$

where ϕ denotes the work function for the tip and sample, respectively, and e is the electronic charge. Because of the CPD an electrical force is acting on the tip. In (c) this electrical force is compensated by applying an additional bias voltage V_{bias} with the same magnitude as V_{CPD}. This bias voltage can be simultaneously applied to the AFM tip during AFM imaging using the so-called Kelvin probe force microscopy (KPFM) measurement [200].

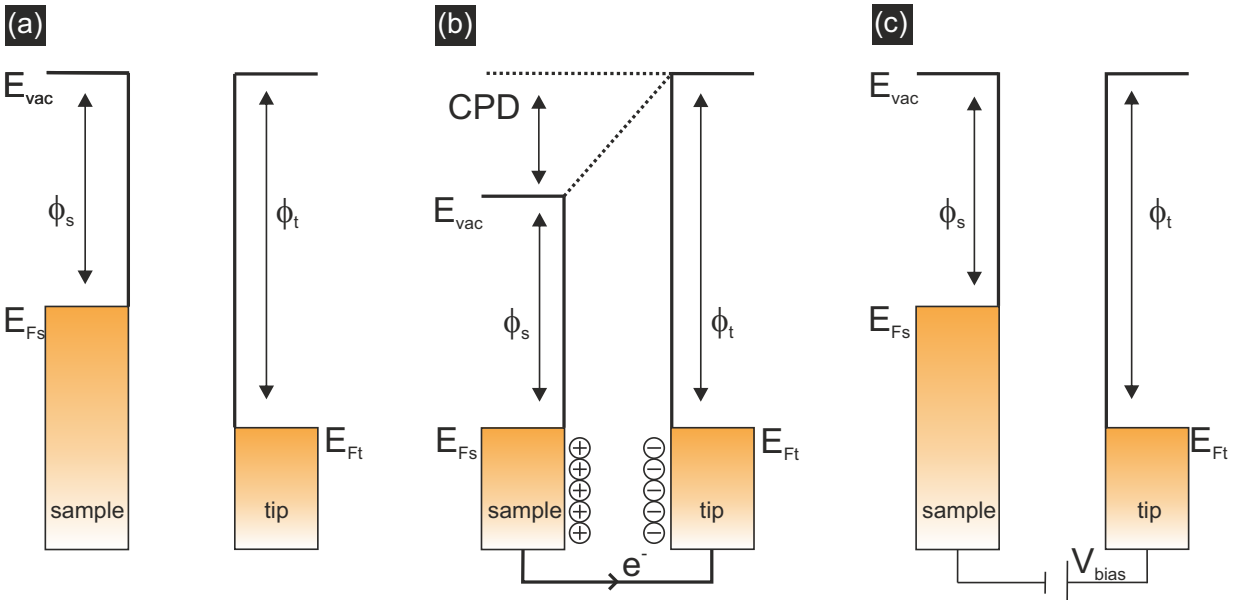

Figure 3.2: Basics of Kelvin probe force microscopy (a) Sample and AFM tip are not in contact and therefore no electrical force is present. (b) Upon electrical contact, the Fermi levels are aligned and a electron current is flowing from the material with the higher work function to the one with the lower work function. (c) By applying an additional V_{bias}, which corresponds to the CPD, the electrical force is compensated.

This technique was first introduced by Nonnenmacher in 1991 [201] and was developed further with the frequency modulated (FM) KPFM, allowing simultaneously topography and surface potential measuring, by Kitamura [202].

The electrostatic force between the AFM tip and the sample depends quadratically on the difference between the sample bias voltage V_{bias} and the contact potential difference (CPD) between tip and sample V_{CPD}. These electrostatic forces can be minimized, if the bias voltage matches the CPD between tip and sample and this voltage corresponds to the surface potential. This is done by using a lock-in amplifier to modulate a bias voltage with a small AC voltage: $V_{bias} = V_{DC} + V_{AC} sin\omega t$. The resulting force between tip and sample goes with $F_{res} = -\frac{1}{2}\frac{\delta C}{\delta z}V^2$ and has three components:

$$F_{DC} = -\frac{\delta C}{\delta z}(\frac{1}{2}(V_{DC} - V_{CPD})^2) \tag{3.3}$$

$$F_\omega = -\frac{\delta C}{\delta z}(V_{DC} - V_{CPD})V_{AC}sin(\omega t) \tag{3.4}$$

$$F_{2\omega} = \frac{\delta C}{\delta z}\frac{V_{AC}^2}{4}(cos(2\omega t) - 1), \tag{3.5}$$

where $\frac{\delta C}{\delta z}$ denotes the gradient of the capacitance between tip and sample [203]. F_{DC} results in a static deflection of the cantilever, F_ω is used to measure the surface potential and $F_{2\omega}$ can be used for capacitance microscopy [200]. Typical values for the applied AC voltage are V_{AC}=0.5-2 V with frequencies in the range of ω=200-2000 Hz.

3.1.3 Quantitative KPFM measurements

If the work function of the AFM tip is known, Kelvin probe force microscopy can be used to directly measure the work function of samples [204]. In general the work function of the tip is unknown as it is not just dependent on the material but on the form of the nanoscale tip as well [205]. An adequate way to calibrate the work function of the AFM tip is using an in situ Ar^+ sputtered Si tip, which exhibits a work function ϕ=4.7 eV [204]. However, the work function of the AFM tip is subject to change, if the tip is deformed by e.g. crashing into the surface or picking up contaminations from the surface. Therefore, the best way to calibrate the tip is by performing the calibration during the measurement, as shown in fig. 3.3.

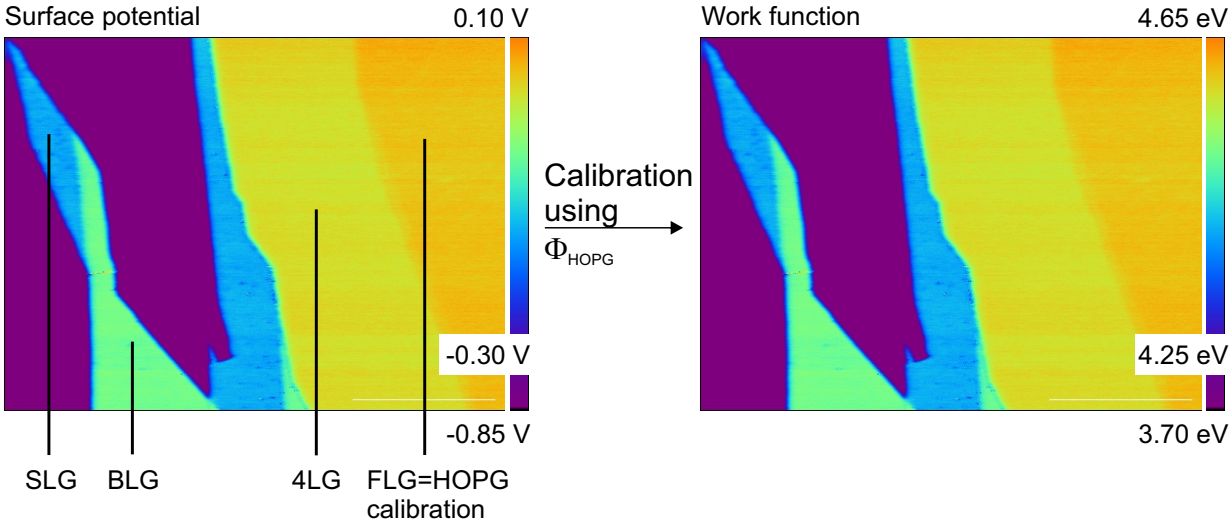

Figure 3.3: Quantitative KPFM measurements are performed by using a reference potential on the sample (in this case few layer graphene). The work function of HOPG (4.65 eV) is assigned to the surface potential of FLG and then the AFM tip is calibrated correctly. Scale bar in this image is 1 μm.

In this thesis two different approaches for the tip calibration have been used. In the case of graphene KPFM measurements, it can be exploited that due to the mechanical exfoliation

technique, which will be discussed later in this chapter, few layer graphene flakes are found easily near the single layer graphene flake. With a layer thickness of ten at least, the work function of few layer graphene corresponds to the work function of HOPG ϕ_{HOPG}=4.65 eV [206, 207, 208], which is a preferred calibration material because of its chemical inertness [204]. In the case of single layer MoS_2 KPFM measurements, bulk MoS_2 is not an optimal calibration material, as the work function is not as defined as HOPG [209, 210]. Therefore a gold contact is patterned via optical lithography on the single layer MoS_2 flake in this work and the tip is calibrated on the gold film, which exhibits a work function of ϕ_{Au}=5.1 eV [211]. Using the relation:

$$\phi_{tip} = \phi_{cal} + \frac{V_{CPD}}{-e} \tag{3.6}$$

the tip can be calibrated and a CPD or surface potential map obtained from the KPFM measurement can be transformed into a KPFM map as shown in fig. 3.3 (b).

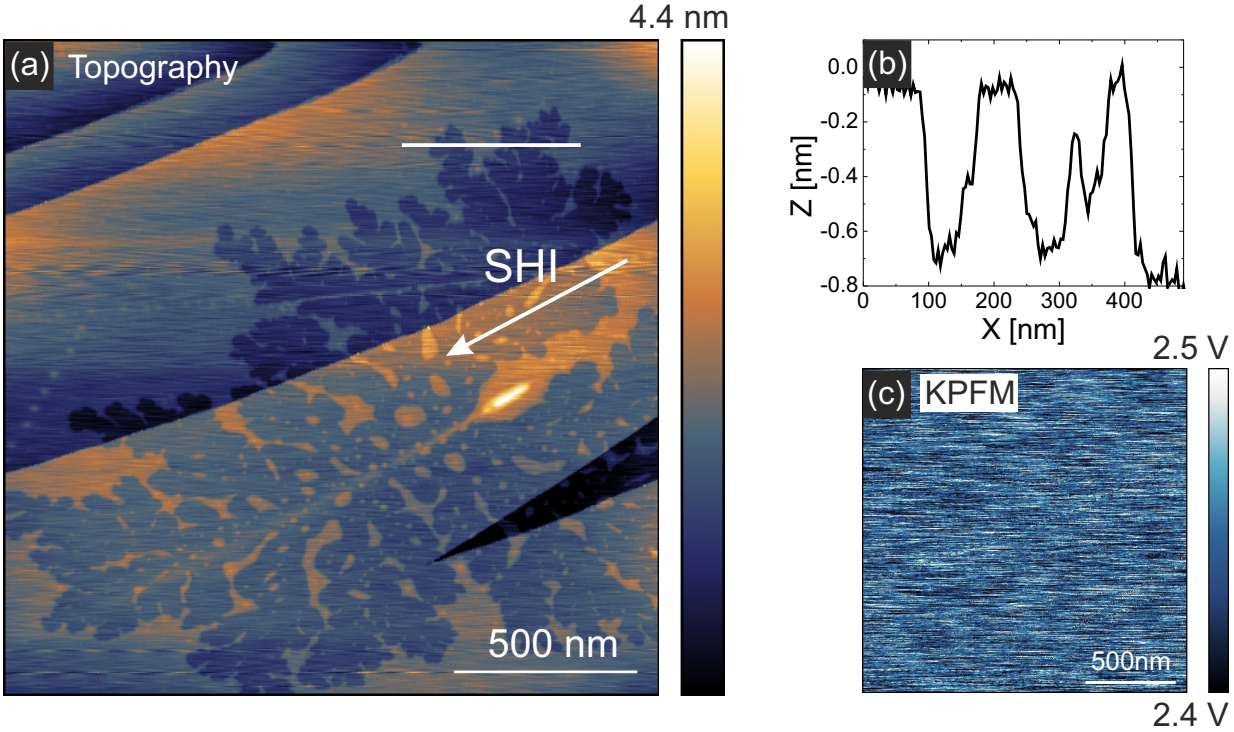

Figure 3.4: Influence of intercalated water on the surface potential. (a) Non-contact AFM topography of a few layer graphene flake on mica. The sample has been irradiated with SHI under grazing incidence angle (91 MeV Xe, θ=1°). After heat treatment, the removal of interfacial water in a fractal shaped area along the ion channel is observed. (b) Line profile which denotes the step height of the water still present at the interface. (c) In the corresponding KPFM image, no contrast can be detected, proving that the interfacial layer has no influence on the surface potential of graphene.

Of course, in general any KPFM data has to be treated with great care due to uncertainties with respect to calibration [204]. Therefore, to ensure that the work function values measured on exfoliated few layer graphene sheets are correct, extra efforts have been taken to rule out that few layer graphene is affected by residual water trapped at the interface due to the exfoliation technique [184]. This procedure was developed in the course of this thesis (based on the results presented in capters 4) and is described in the following:

An exfoliated graphene flake supported on mica was irradiated with swift heavy ions under grazing incidence angle of Θ=1° in order to introduce a small channel of defects into few layer graphene. After irradiation the sample is heated to 180 °C for one hour. This removes the water on top of the FLG and also underneath the FLG. The ion induced channel obviously allows the trapped water to diffuse out from underneath the graphene layers, which is shown in fig. 3.4 (a). The step height where interfacial water has been removed is about 0.6 nm. Looking at the surface potential map of this area in fig. 3.4 (c), no contrast can be detected. The work function values of areas with and without trapped water are identical. This proves that intercalated water does not have an impact on the work function measurement. Having excluded artifacts due to calibration, we must attribute the observed transition to heating-induced changes exclusively.

3.1.4 Experimental AFM setups

In the course of this thesis, two AFM setups have been used, both shown in fig. 3.5. For measurements performed under ambient conditions a Veeco Dimension 3100 AFM was being used (see fig. 3.5 (a)). For in situ measurements and KPFM measurement, RHK system UHV 7500 with the PLL Pro 2 controller has been used (see fig. 3.5 (b)). Standard Si cantilevers have been used as AFM probes, Nanosensors NCHR for the measurements in ambient and Vistaprobe T300 for measurements in situ. In order to sharpen the AFM tip in the in situ experiment, the tip was typically sputtered with 1 keV Ar^+ ions for five minutes.

In order to find the relatively small graphene flakes in the UHV system, first a telemicroscope (Infinity - USA) was installed to the system. In fig. 3.5 (c) an optical image taken with the microscope of a graphene on SiO_2 sample onto which gold contacts have been patterened is shown. As the resolution of the microscope is limited, the gold contacts in the red dotted box can be seen while the graphene flake itself cannot. Because of this, it can take up to a whole day to find the graphene flake in situ. To improve the resolution, a scanning electron microscope has been installed and the resulting image in fig. 3.5 (d) shows a sufficient contrast to locate 2D crystal flakes in situ. In (e) the scan head of the UHV AFM on top of the sample holder is shown. In the sample holder a filament and thermocouple can be integrated to heat the sample and measure the temperature, respectively.

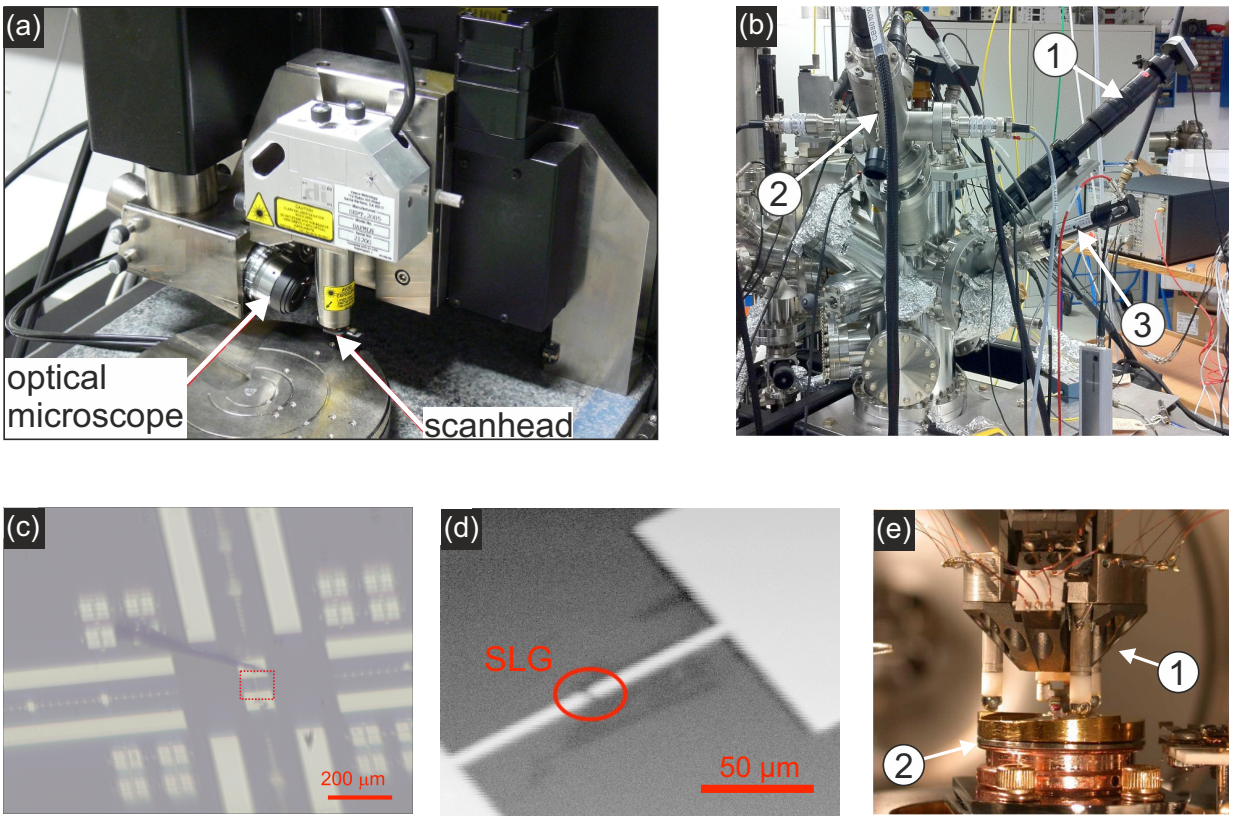

Figure 3.5: Experimental AFM setup. (a) Veeco Dimension 3100 with integrated microscope (b) RHK UHV 7500 system with a telemicroscope (1) and a scanning electron microscope (2 and 3) attached to it. (c) Optical image from the telemicroscope of a graphene field effect device. (d) The same sample imaged with the scanning electron microscope graphene is visible with a faint contrast. (e) Scan head of the RHK 7500 system (1) on top of the sample holder (2).

3.2 Raman spectroscopy

The quickest and most reliable way to identify single layer sheets of van der Waals solids is often Raman spectroscopy. The Raman effect, named in honour of the discoverer Sir Chandrasekhara Venkata Raman in 1928 [212], is an optical process in which light is inelastically scattered. Unlike Rayleigh scattering, where the energy of the emitted photons is unchanged, Raman scattering can create (or annihilate) phonons, therefore the energy of the scattered phonons lost (or gained) energy from vibrations of the atoms. If the energy of the emitted photon is lower than the incidence photon, the process is called Stokes-process, and Anti-Stokes vice versa. Unlike the Stokes process which creates a phonon, the Anti-Stokes process relies on the annihilation of a phonon, therefore the probability/intensity of the Anti-Stokes process will be proportional to the population densiy of the phonons. As a result the Anti-Stokes/Stokes Ratio will strongly depend on the temperature [213].

The Raman spectrum of graphene, single layer MoS_2 and hexagonal BN (hBN) for example clearly vary from thicker layers and their bulk counterparts [214, 215, 216]. In addition to identification of single layer sheets, Raman spectroscopy has been successfully used to characterize defects, doping levels and strain in 2D-materials [217, 218, 219, 220, 221]. By guiding the laser light through a microscope, it is possible to achieve sub micron resolution in the lateral scale. This technique is called μ-Raman spectroscopy.

3.2.1 Raman spectrum of graphene

Historically, Raman spectroscopy has played an important role in characterizing and studying graphitic materials like carbon fibers, graphitic foams, nanographite ribbons, carbon nanotubes, fullerenes and of course graphene [222, 223, 224, 225]. For sp^2 carbon in particular, the Raman spectrum gives information about layer thickness, crystallite size, presence of sp^3 hybridizations, doping, strain, edge structure etc. [226, 227, 228, 229, 230, 231, 213]. The evolution of the Raman spectrum from bulk graphite down to a single layer graphene is shown in fig. 3.6. The two most signature Raman modes are the G-band at $\sim$1580 cm^{-1} and 2D-band at $\sim$2680 cm^{-1} (Note, that the 2D-band is dispersive and this value is given for an excitation wave length of 532 nm).

- The **G-band** is present in all sp^2 carbon systems and is related to the in-plane C-C bond stretching mode giving rise to both the optical in-plane transverse optic (iTO) phonon and the longitudinal (LO) phonon branches. Because of the strong C-C bonds in sp^2 materials and the small mass of C atoms, the Raman frequency of the G-band ω_G is relatively high compared to other materials and only a small pertubation to ω_G is measured [213]. The wave number of the G-band is typically around 1580 cm^{-1}.

- The **2D-band** is present in all sp2 carbons as well in a Raman shift range of 2500-2800 cm^{-1}. The 2D-band is a second-order two-phonon process, which shows a dispersive behaviour towards the laser excitation energy ($\omega_{2D} = \omega_{2D}(E_{Laser})$, which is unusual in Raman scattering. The 2D-band is related to a phonon near the K point in graphene, activated by a double resonance process, responsible for its dispersive nature and a strong dependance on any pertubation to the electronic and/or phonon structure of graphene [222, 213]. This is why the 2D-band is a sensitive probe for e.g. the layer number or the doping of the graphene sheet. The layer number can be determined by comparing the $FWHM_{2D}$ (full width half maximum) of the 2D-band. Single layer graphene has a very narrow peak with a FWHM of $\leq$30 cm^{-1} and the FWHM increases with increasing layer number [232] as shown in fig. 3.6 (a).

Beside the FWHM of the 2D-band, the layer number of up to 8 layers graphene can be determined by a Raman mode on the low frequency side of the G-band. This so-called N mode was first observed by Herziger et al. and is a combination of a Stokes-scattered longitudinal optical phonon and an anti-Stokes scattered rigid-layer compression phonon [233].

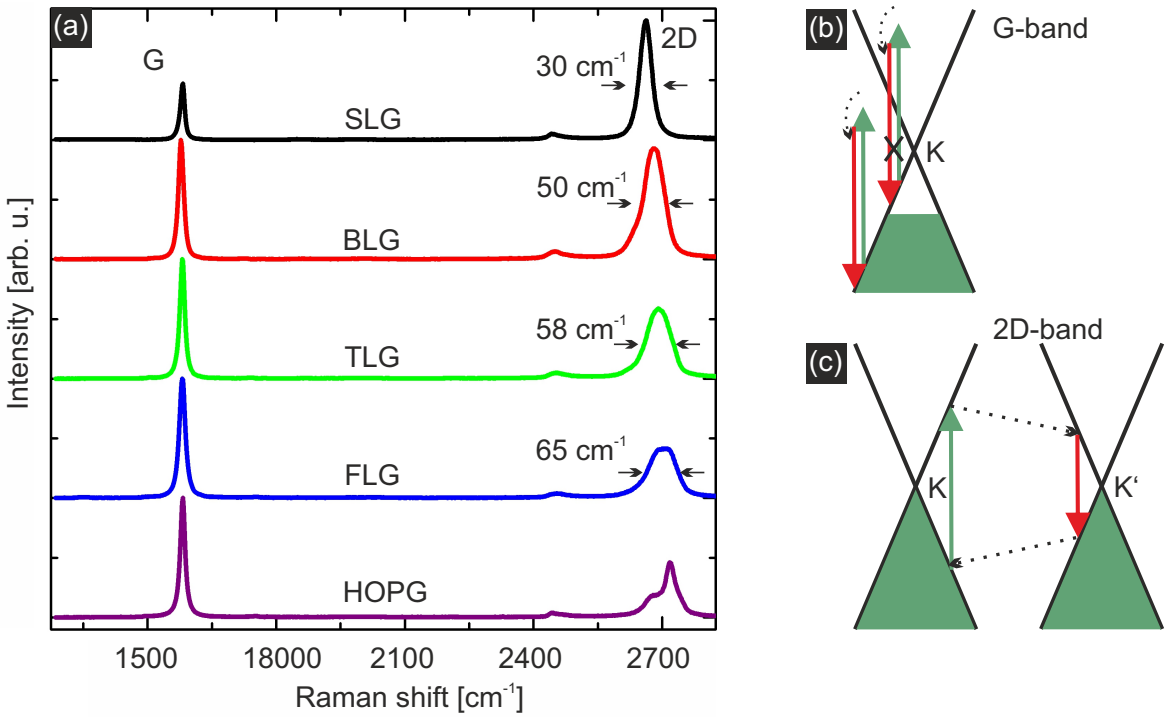

Figure 3.6: Raman spectroscopy of pristine graphene. (a) Evolution of the two prominent G and 2D Raman modes for pristine graphene. The FWHM of the 2D-band is increasing with layer thickness, which allows the identification of single layer graphene. (b) One-phonon process responsible for the G-band. The black lines denote the electron dispersion, the green shaded area the occupied states, green and red arrows the photon absorption and emission, respectively and the dashed arrow corresponds to phonon emission. Some processes can be eliminated by e.g. doping as the one which is crossed out. (c) The 2D-band is generated by two-phonon intervalley scattering. Momentum is conserved by emission of two phonons with opposite wave vectors.

In this thesis, graphene is exposed to high energetic ion irradiation, which results in modifications in form of origami like foldings and defects. As Raman spectroscopy strongly depends on crystal symmetry, it is one of the most sensitive and informative tools to study disorder in sp^2 carbon systems. As an example, an AFM topography of a graphene sheet on a SiO_2 substrate is shown in fig. 3.7 (a), which has been irradiated with Xe^{26+} ions (91 MeV, 50,000 ions/μm^2) perpendicular to the sample surface. The AFM topography exhibits the same features as pristine graphene on SiO_2 and shows no signs of modification or defect creation in the graphene at this resolution. In the Raman spectrum, however, two new bands are appearing due to the ion irradiation, as marked in fig. 3.7 (b). If the symmetery is broken in graphene because of e.g. defects or edges, new spectral features appear in the Raman spectrum at 1345 cm^{-1} and 1626 cm^{-1} which are called the D and

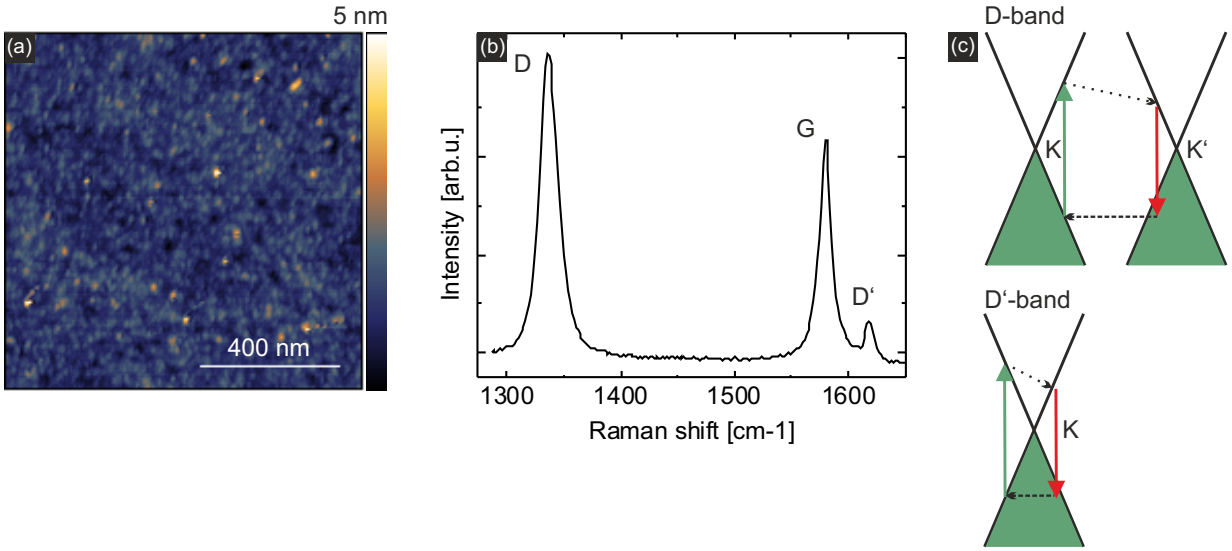

Figure 3.7: Raman spectroscopy of defective graphene. (a) AFM topography of an ion irradiated graphene flake on SiO_2 showing no visible defects. (b) In the Raman spectra, two new modes can be observed, the disorder induced D and D' band. (c) If a defect is present, the wave vector does not have to be zero and intervalley scattering produces the D-band, while intravalley scattering produces the D' band. Black dotted arrows denote phonon emission, while black dashed arrows denote electron scattering.

D'-band, respectively. Like the 2D-band, these bands are dispersive and observed at this position with a 532 nm (2.41 eV) laser.

- The **D-band** is due to the the breathing modes of the six-atom rings and comes from a resonant electron-phonon scattering process around the K and K' point in the first Brillouin zone (intervalley process) [219, 213].
- The **D'-band** is caused by an intravalley process, connecting two points belonging to the same cone around K and K' [219, 213].

3.2.2 Raman spectrum of MoS_2

In this thesis not just graphene as the model 2D-material is investigated but single layers of MoS_2 as well. Out of the four active Raman modes of bulk MoS_2, two strong bands can be detected at around 400 cm^{-1} for all film thicknesses [234, 215, 235], a strong in-plane vibrational mode corresponding to the E^1_{2g} band of the bulk 2H-MoS_2 crystal and the out-of-plane A_{1g} band (see fig. 3.8 (b)).

Shown in fig. 3.8 (a) is the transition of the Raman spectra from bulk to single layer MoS_2. For an increasing layer thickness, the E^1_{2g} vibration shows a softening while the A_{1g} vibration shows a stiffening. Thus, the rate of Raman shift change is twice as large for the

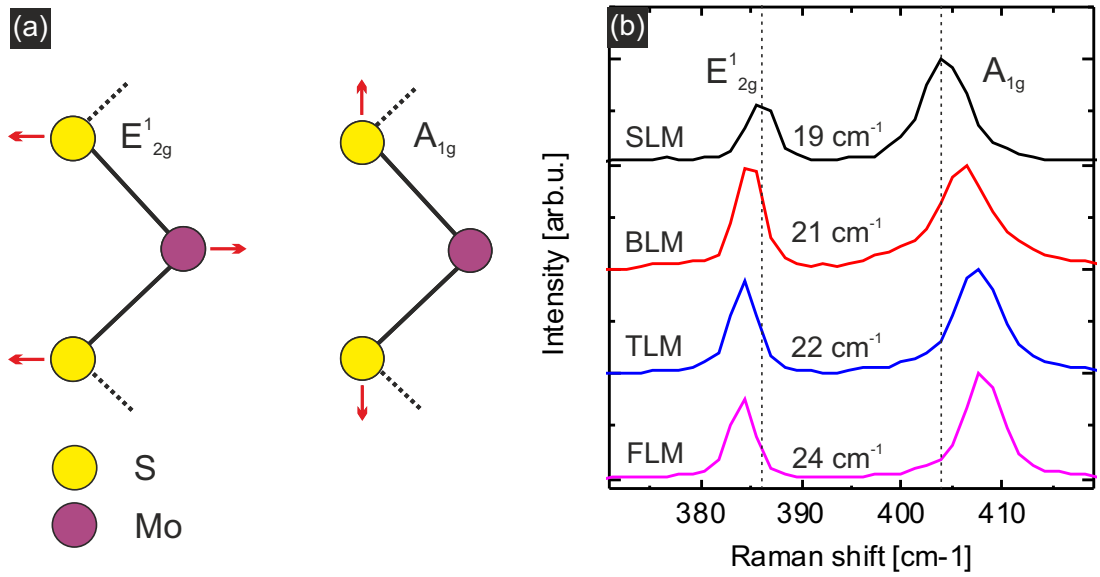

Figure 3.8: Layer thickness determination of MoS_2 by Raman spectrosocopy. (a) Atomic displacements of the two described Raman active modes as viewed along the [1000] direction. (b) Transition of the measured Raman spectrum from single layer to few layer MoS_2. The distance of the E^1_{2g} and A_{1g} mode is increasing with increasing layer thickness.

A_{1g} band than the E^1_{2g} band and starting from four layers, the Raman shifts of both bands are converging to bulk values [215]. This diverging frequency shift can be used for layer number determination as the lowest value of $\Delta\omega$ ~19 cm^{-1} is characteristic for single layer MoS_2, $\Delta\omega$ ~21 cm^{-1} for bilayers and up to $\Delta\omega$ ~25 cm^{-1} for few layer or bulk MoS_2.

3.2.3 Experimental Raman setup

If not noted otherwise, all the Raman spectra presented in this thesis have been obtained using the InVia Raman-microscope from Renishaw (Wotton under Edge, UK) (see fig. 3.9 (a)). It is equipped with a 532 nm (2.33 eV) and a 633 nm (1.96 eV) laser and has a spectral resolution of ~1 cm^{-1}. In order to avoid heating effects in the 2D-materials, the laser power is set to 0.4 mW and 0.2 mW for graphene and MoS_2, respectively [236, 237].

The laser is focused through a microscop on the sample surface, which results in a spot size of the laser of below 1 μm. The microscope is further equipped with a fully encoded motorized stage with a step size of 100 nm. This can be exploited in order to measure so called Raman mappings of a sample by accumulating Raman spectra over a large area.

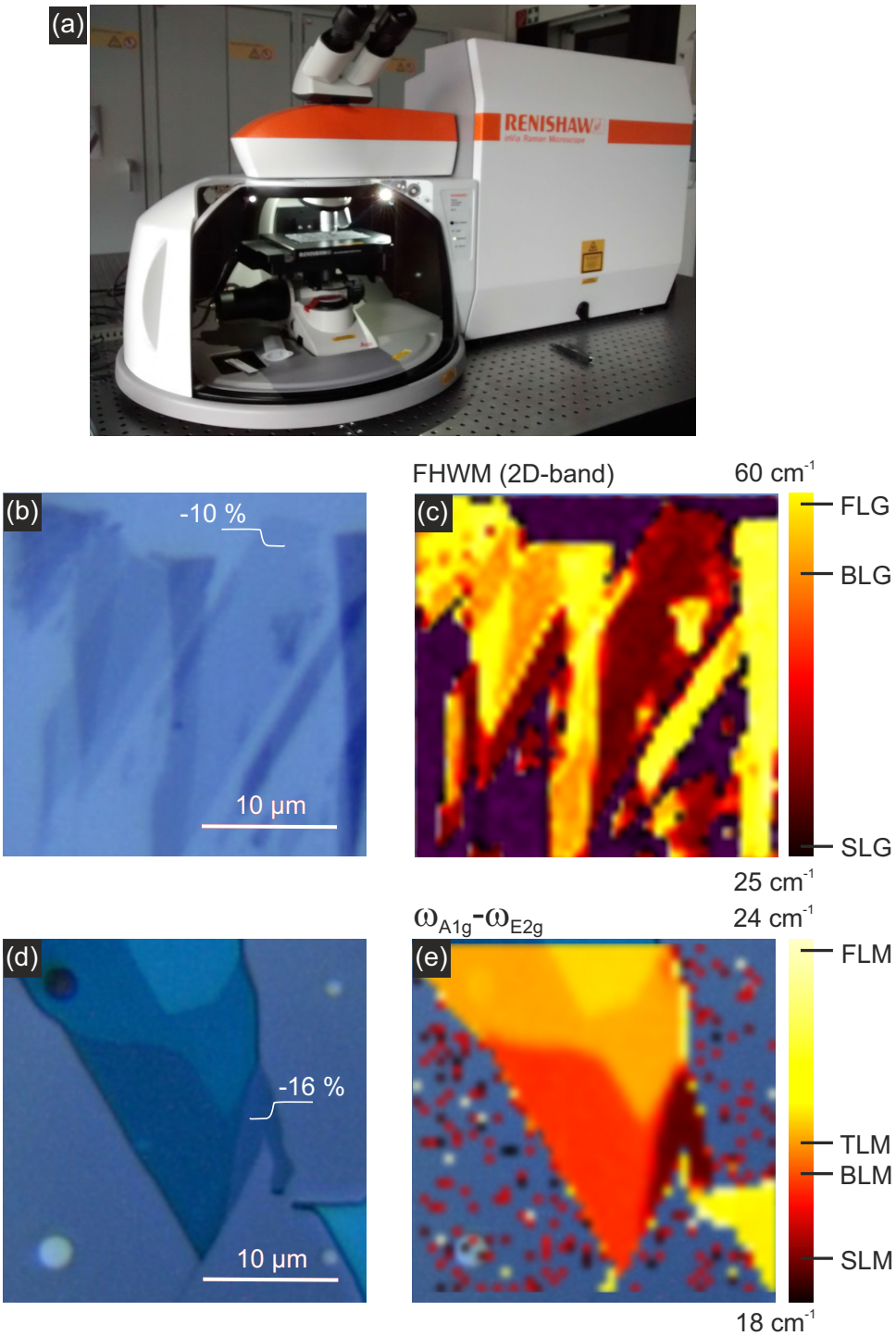

Figure 3.9: (a) Renishaw Raman microscope. (b-c) Optical image of an exfoliated graphene flake on a SiO_2 substrate. The Raman map displays the FWHM of the 2D-band which is increasing with layer thickness. The procentual number denotes the contrast between the SiO_2 and 2D-material surface. (d-e) Optical image of an exfoliated MoS_2 flake, the corresponding Raman map shows the distance between the E^1_{2g} and A_{1g} bands which is increasing with layer thickness.

In general, graphene and single layer MoS_2 flakes are identified by their optical contrast in a standard confocal microscope. However, if the substrate onto which the 2D-materials are prepared or the thickness of the SiO_2 coating on the Si substrate is varied, the contrast of the 2D-material is changing as well [238, 239]. In order to calibrate the optical contrast of the 2D-material, a corresponding Raman mapping of it can be performed. In fig. 3.9 (b-c) an optical image of a graphene flake with varying layer thickness on a SiO_2 (90 nm)/ Si substrate and the corresponding Raman map are overlayed. The Raman map displays the FWHM of the 2D-band which is increasing with layer thickness as already discussed above. Hence, the optical contrast of single layer graphene on this substrate corresponds to -10 % with respect to the SiO_2 surface. The same measurement is performed for MoS_2 in fig 3.9 (d-e), the Raman map however now displays the difference in the frequency of the E^1_{2g} and A_{1g} band. The resulting optical contrast for single layer MoS_2 on a 90 nm SiO_2/Si is -16 %.

3.3 Sample preparation

3.3.1 Mechanical Exfoliation

The samples used in this thesis have all been prepared by using the mechanical exfoliation technique [9]. In this technique a scotch tape is used to peel of some layers of a van der Waals bulk crystal. The three crystals used in this thesis are highly ordered pyrolitic graphite (HOPG - Momentive Performance Materials), MoS_2 and hBN (both from HQ graphene, Groningen - Netherlands). The crystal is further thinned out on the scotch tape and finally the scotch tape is put on the target substrate which is usually a standard 90 nm SiO_2/Si sample (Graphene supermarket, Calverton - United States), shown in fig. 3.10 (a). Typical images of resulting single layer flakes for graphene, MoS_2 and hBN are shown in fig. 3.10 (b-d). Characteristic for exfoliated flakes is, that attached to a single layer or near the single layer, other sheets can be found with different layer numbers with even bulk-like thickness. The typical size of a single layer flake is in the range of 50 μm^2 and even up to 1000 μm^2, which is still far lower than for epitaxial graphene on SiC or chemical vapour deposited (CVD) graphene [11]. However, this size is large enough for most of the basic research experiments and the cristalline quality of the exfoliated flakes is superior.

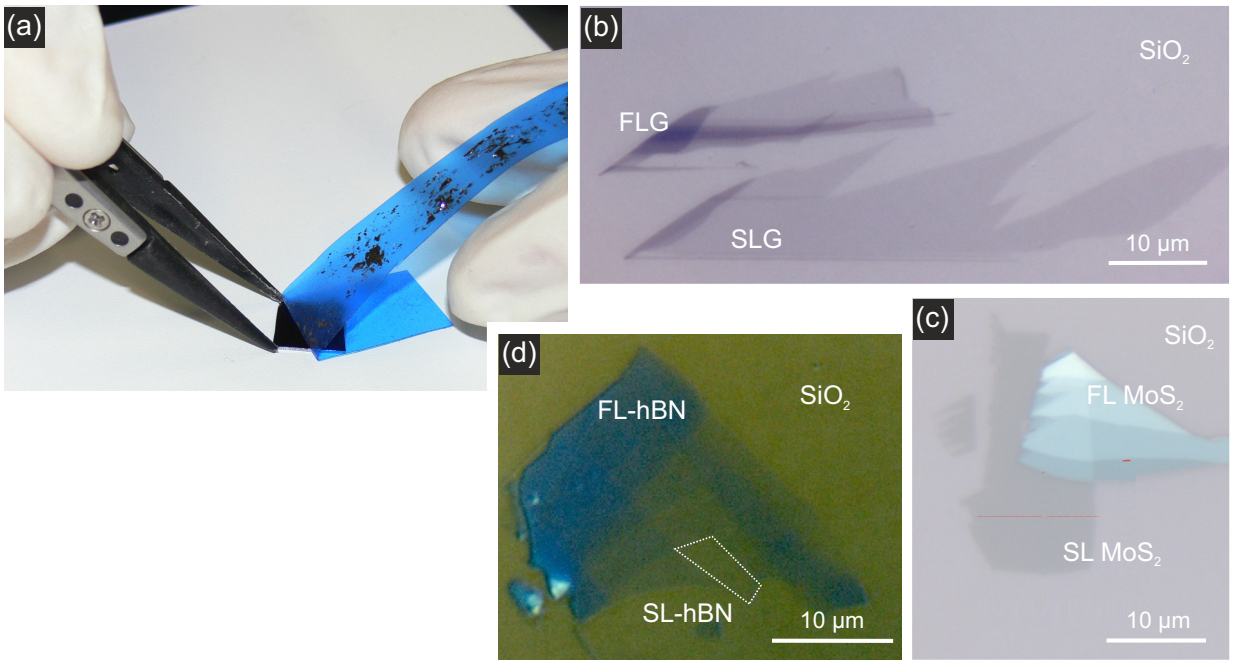

Figure 3.10: Mechanical exfoliation of two-dimensional crystals. (a) Scotch tape with crystals being peeled of. (b) Optical image of an exfoliated graphene flake. (c) Optical Image of a single layer MoS_2 flake. (d) Optical image of a single layer hBN flake.

3.3.2 UHV exfoliation

A major drawback in the exfoliation technique is, that, while the 2D crystal itself is of high quality, it generally encloses an interfacial water layer between the 2D crystal and the substrate because of the exfoliation in ambient and it may even be contaminated with glue residues due to the scotch tape [240]. Therefore a new technique has been developed in this thesis in order to exfoliate graphene under controlled conditions, the UHV exfoliation [OO.05]. For this, the stamp, shown in fig.3.11 (a) has been developed and implemented in an UHV system. Using a two-component epoxy glue, the bulk crystal (in this case graphene) is glued onto the stamp. In situ, with a base pressure of $\sim 3 \cdot 10^{-10}$ mbar, the bulk crystal is brought into contact with the target substrate. The stamp is typically left for several minutes on the substrate before slowly removing it. Besides being able to exfoliate the sample free of water or glue residues, the UHV exfoliation allows to prepare graphene on surfaces which are not stable in ambient. For example, it is possible to prepare graphene on a Si(111)-(7x7) reconstructed surface, as shown in fig. 3.11 (a-c) [OO.05].

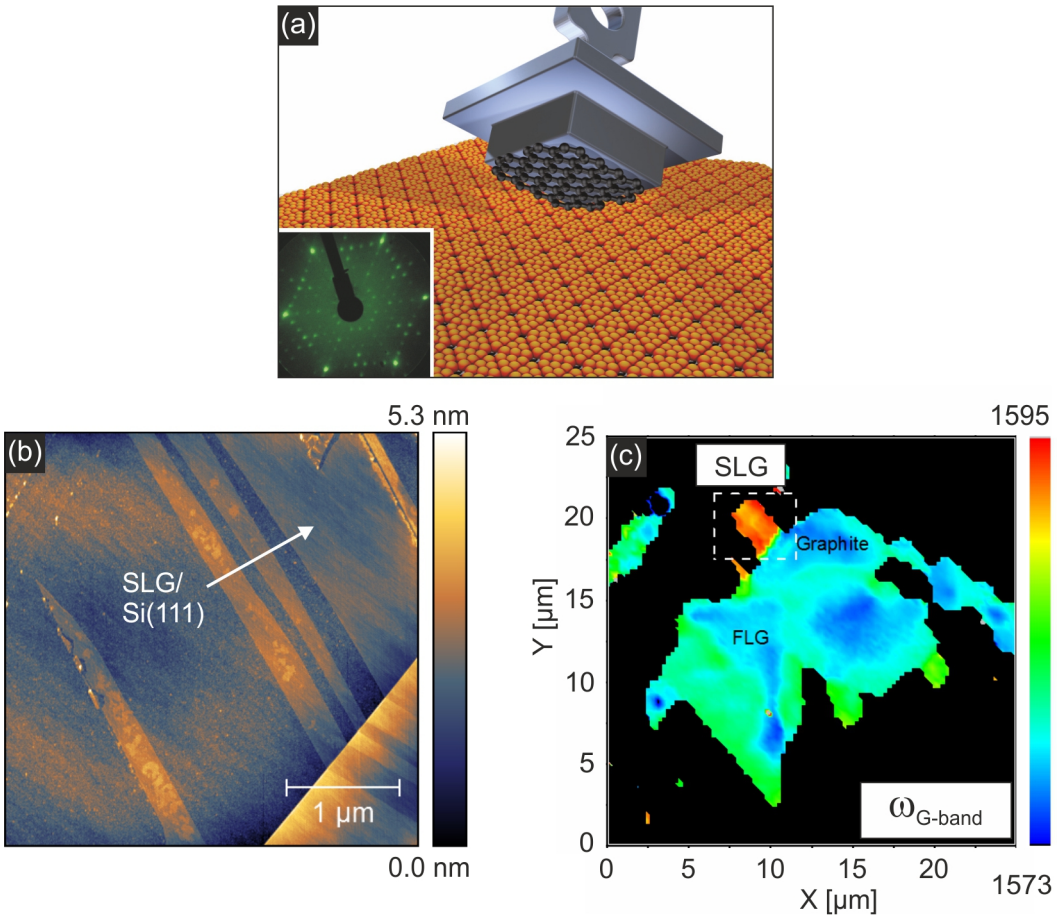

Figure 3.11: UHV exfoliation of graphene on a Si(111)-(7x7) surface. (a) Scheme of the stamp onto which a graphite crystal is glued. The LEED picture shows the well-known (7x7) reconstruction of the Si(111) surface before exfoliation. (b) AFM topography of single layer graphene on Si(111) (c) Raman map of the graphene flake showing a distinct variation of the G-band position for single layer graphene. The Raman spectra presented here were obtained by Nils Scheuschner from the Maultzsch work goup at the TU Berlin. Image adapted from [OO.05]

3.3.3 Photolithography

An integral part of this thesis is to study doping effects due to high energetic ion irradiation in graphene and MoS_2. This can be done using the Kelvin probe technique, which has already been described in chapter 3.1, or by performing transport measurements of 2D-material field effect transistors (FET). A typical 2D-material field effect device is shown in fig. 3.12. Two contacts, one acting as drain and one as source, are placed on the channel material, here the 2D-material. During the transport measurement the charge carrier concentration in the channel is modulated by a back-gate, which is separated from the

channel through a respective dielectric.

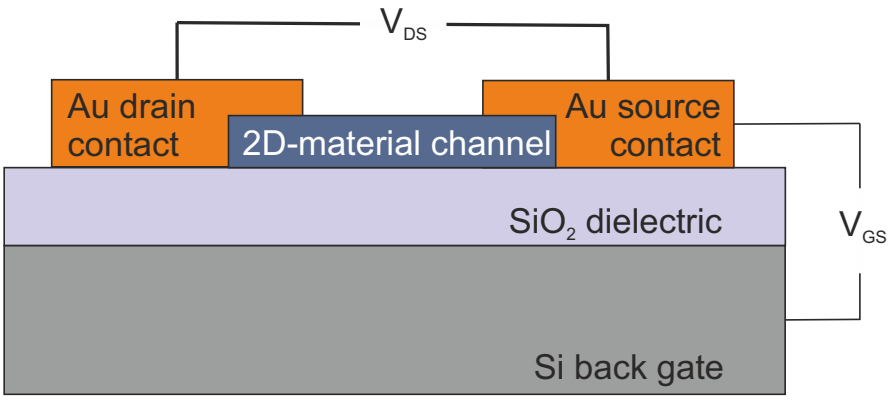

Figure 3.12: Basic field effect device with a back gate and 2D-material as the channel material.

A standard sample obtained by the exfoliation technique consists of 2D-material on top of 90 nm SiO_2, which is again on top of Si. So the channel (graphene or MoS_2), the dielectric (90 nm SiO_2) and the back-gate (Si) are already present. The two missing source and drain contacts are processed onto the 2D-material using the photolithography equipment at the Halbleitertechnik Universität Duisburg-Essen [241]. The accuracy of the patterned contacts is limited to about 1.5 μm due to optical errors and inhomogeneity of the photoresist. Therefore, the 2D-material flakes have to be at least 5x5 μm^2 in size, in order to pattern contacts on them. However, larger flake sizes of 20x10 μm^2 or even more drastically increase the chances of successful contact patterning. Typical channel lengths in our devices are L=6 μm and W=(3-12) μm.

The photolithography process is outlined in fig. 3.13. First, spin coating (7000 rpm/s for 30 s) is used to coat the sample surface with a photoresist (ARP-5350). After this, the resist is baked for 15 min at 95 °C. The photoresist used is a positiv photoresist, which means that by exposing the photoresist to UV-light (365 nm for 2.5 s) it is degenerated and becomes soluable. The sample is not completely exposed to UV-light, but a dark-field mask is used in order to pattern the cold contacts on the 2D-material flake. By putting the sample into the developer AR 300-35 solution (diluted 1:1 with deionized water), the areas which are exposed to light are freed of the coating. Metalcontacts (50 nm Ti and 400 nm Au) are evaporated onto the sample by PVD (physical vapour deposition). After this, the lift-off process is performed by putting the sample into aceton, which removes the remnants of the resist coating and evaporated metal. In the end the sample is boiled in isopropanol to remove Aceton residues. Schematically shown in fig. 3.13 (b-c) is an exfoliated graphene flake prior to processing (a), after developing the resist (b) and after the lift-off (c).

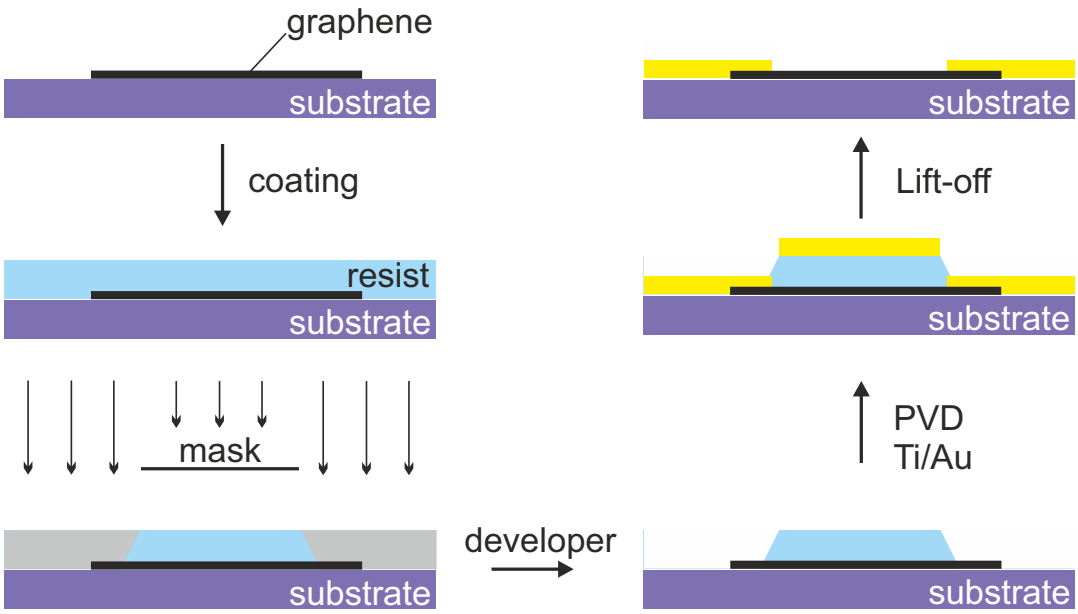

Figure 3.13: Scheme of the photolithography process in which two gold contacts are patterned onto a graphene flake.

3.4 Transport measurements

After graphene and MoS_2 have been prepared by photolithography, they are analyzed with respect to their output characteristics ($I_D(U_{GS})$). The important physical properties which are directly derived from the experiment are the conductivity σ:

$$\sigma = \frac{dI_D}{dU_{DS}} \tag{3.7}$$

and the mobility of the electron and hole charge carriers $\mu_{e,h}$:

$$\mu_{e,h} = \frac{dI_D}{dU_{GS}} \times \frac{L}{WC_iU_{DS}}. \tag{3.8}$$

Here, I_D is the drain current between source and drain contact, U_{GS} is the voltage between the gate and source und U_{DS} is the voltage between source and drain, see fig. 3.12. $C_i = \frac{\epsilon\epsilon_r}{d} = 3.837 \times 10^{-4}$ F/m^2 is the capacitance between the channel and the backgate per unit area, ϵ_r and ϵ are the dielectric constants for the dielectric SiO_2 and air, respectively. Here, the thickness of the dielectric d is 90 nm. However, other SiO_2 thicknesses are used as well (d=50 nm and d=285 nm), which are accounted for in the respective C_i for the calculation of the mobility. Additionally, the charge carrier density $n_{e,h}$ can be derived from this data by:

$$n_{e,h} = \frac{\sigma}{e\mu_{e,h}} \tag{3.9}$$

with the elementary charge e. Note, that μ and σ are measured independently from each other, while n is calculated from these two.

Typical output transfer characteristics (I_D/U_{GS}) for graphene and MoS_2 FET are shown in fig. 3.14 and will be briefly discussed at this point. The ambipolar behaviour of the graphene FET can be observed in fig. 3.14 (a). The point with the lowest current (I_D) or conductivity is called the Dirac point and is located at the gate voltage where the sign of the charge carriers in graphene is changing. For a "perfect" graphene FET - suspended graphene, no defects, contaminations, etc. - the Dirac point would be located at exactly 0 V. As the graphene FETs presented in this work are prepared on a SiO_2 and exposed to ambient conditions during measurement, they always show a p-type doping which results in a Dirac point at positive U_{GS} voltages. This is mainly due to the presence of water and will be discussed in more detail in the result chapter 4. Because of the ambipolar behaviour of graphene FET, two branches are originating from the Dirac point, which correspond to the hole conductivity (left) and electron conductivity (right).

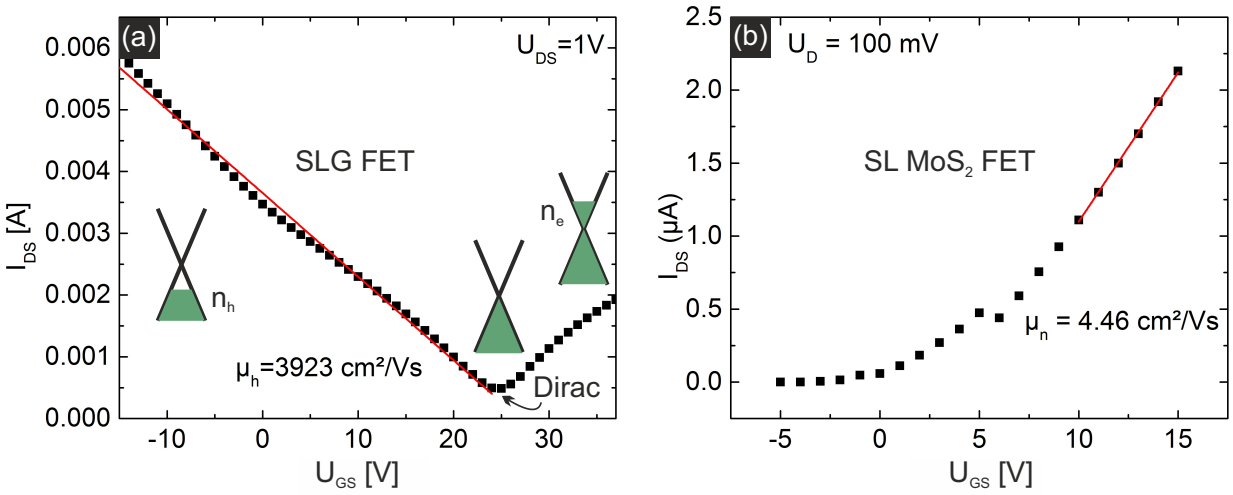

Figure 3.14: Output transfer characteristics of a pristine single layer graphene (a) and single layer MoS_2 field effect device. Both FETs are prepared on a 50 nm SiO_2/Si substrate.

The output characteristic of single layer MoS_2 FET exhibits the typical characterstics of a unipolar field effect device (see fig. 3.14 (b)). Because of the intrinsic band gap of single layer MoS_2, a certain threshold voltage (in this case $\sim$ -1 V) has to be overcome to trigger the electron conductivity in the MoS_2 FET.

Both field effect devices have been prepared on a 50 nm SiO_2/Si substrate and using the relation 3.8 the hole mobility of the graphene FETs shown here in fig. 3.14 is determined to be μ_h=3923 cm^2/Vs and the electron mobility of the MoS_2 is μ_e=4.46 cm^2/Vs. Note, that these numbers vary greatly between different devices and can decrease up to one order of magnitude for other samples manufactured the same way. The reasons for this are mainly the exposure to ambient [242, 243], contaminations due to the processing [244, 245] and

charge impurities because of the SiO_2 substrate [246]. While these values are far off from record mobilities for suspended graphene (μ_h=200,000 cm^2/Vs) and MoS_2 with scandium contacts and a hafnium oxide top gate dielectric (μ_h=1090 cm^2/Vs) [49, 247], they are in good agreement with published data on SiO_2 substrates and thus represent typical values for average devices. As the the primary goals of the 2D-material FET studies in this thesis are the radiation hardness and possible doping effects of the irradiation, these field effect devices are sufficiently suitable.

3.5 SHI irradiation facilities

As already discussed in chapter 1, the energy deposition of swift heavy ions in the target material is dominated by the electronic excitation, which varies with the kinetic energy of the incidence ion. In order to study the threshold for ion modifications in graphene and single layer MoS_2, different ion accelerator facilities have been used, which are shown in fig.3.15.

- The 6 MV EN Tandem Van de Graaff accelerator at the Ruder Boskovic Institute (Zagreb, Croatia) is used for experiments with the lowest kinetic energy from 1 to 30 MeV. In this lower energy regime, the interaction with matter is not limited to electronic excitation. Nuclear collisions are happening as well.

- The majority of the experiments are performed at the IRRSUD beamline of the Grand accelerateur d'ion lourde (GANIL, Caen, France). Typical energies are around 100 MeV and the experimental setup allows to control the incidence angle of the SHI with respect to the sample surface with $\pm 0.2^\circ$ precision. This high precision is needed for the glancing incidence irradiation experiments presented in this thesis.

- At the M branch of the Universal Linear Accelerator (UNILAC) at the GSI (Darmstadt, Germany), SHI with a typical energy of around 1000 MeV are generated. The energy loss of the swift heavy ions can reach up to the maximum of the energy loss curve, which corresponds to the maximum of electronic excitation in the respective material. Glancing incidence irradiation is possible here as well, but the precision is far lower with about $\pm 5^\circ$ deviation because of the experimental setup.

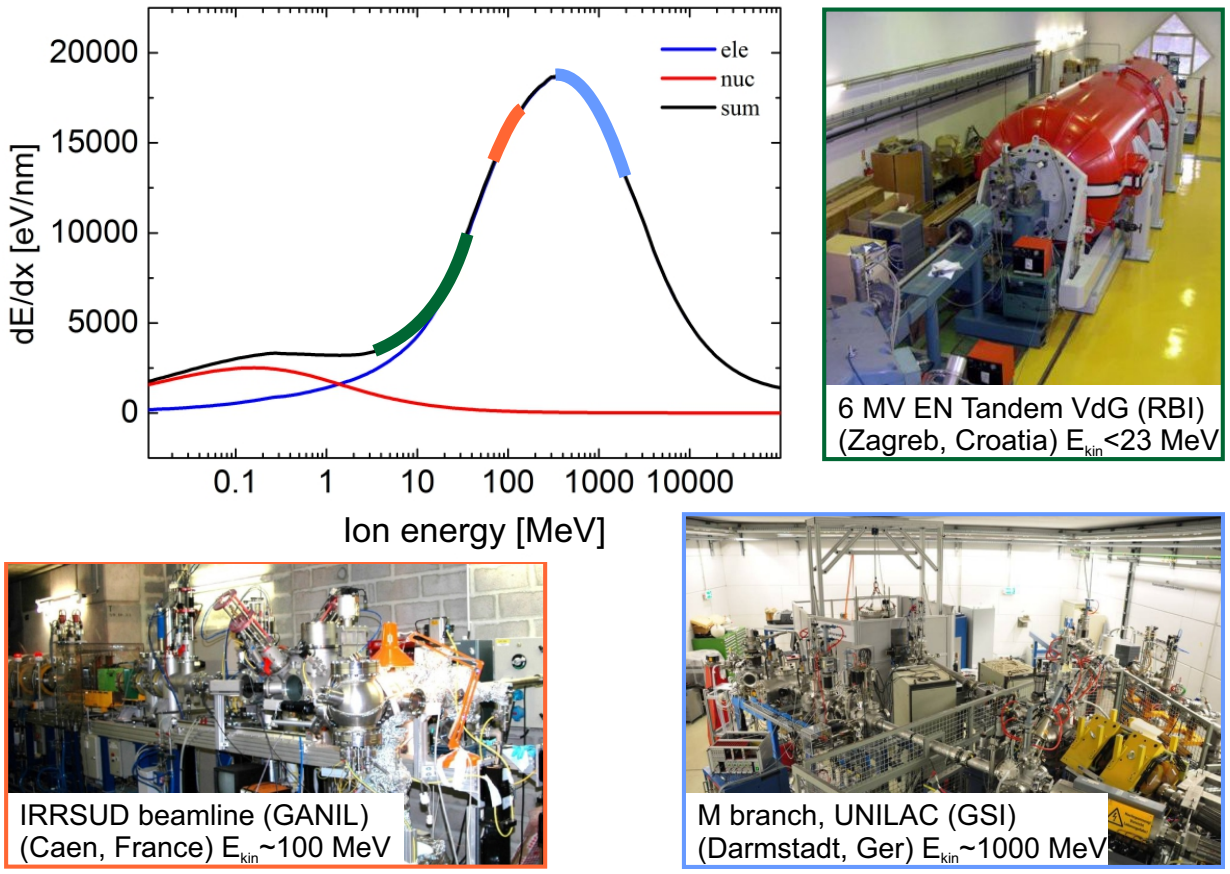

Figure 3.15: Energy loss curve for ions in graphite. The energy regimes of the different ion accelerators used in this thesis are marked in the energy loss curve with the respective colours of the pictures.

4 Charge transfer in atomically thin crystals

The physical properties of two dimensional materials are in general largely influenced by the underlying substrate and the exfoliation of the crystal in ambient conditions. A graphene on SiO_2 field effect transistor measured under ambient conditions for instance shows a charge carrier mobility that is lowered by a factor of 10 compared to suspended graphene measured in situ [248, 249]. This is caused by several reasons. On the one hand, putting graphene on top of a substrate causes graphene to adapt to the surface morphology like a carpet which may induce stress [250, 251]. Additionally charge impurities on the SiO_2 surface give rise to charge inhomogeneity or electron hole puddles in the graphene sheet. Exposure to ambient conditions on the other hand brings these two-dimensional materials in contact with a variety of adsorbates like N_2, O_2 or water, which again affect the performance of two dimensional devices [252, 242, 253, 254]. It is therefore of utmost importance to find the optimal substrate for graphene and to suppress or even exploit effects of adsorbates from ambient.

In the first part of this chapter, single layers of graphene are studied using AFM and KPFM in situ, if not noted otherwise. By varying the substrate it is shown that a charge transfer between two dimensional materials and the substrate is taking place, which can be used to effectively alter the charge carrier concentration in graphene. For example electron as well as hole doping can be induced by the right choice of substrate material. The influence of adsorbates from ambient conditions is explored by heating graphene on various substrates in situ. It is shown that water and adsorbates can be located on top of the graphene sheet as well as at the interface between graphene and the substrate, which can be used to induce p-type doping or to effectively block the charge transfer from the substrate, respectively. In situ heating of graphene cannot be applied for every graphene/substrate system to remove the adsorbates from graphene. In the case of graphene on mica the complete removal of interfacial water layers (IFL) is accompanied by severe defect creation in the graphene sheet.

In the second part, single layers of MoS_2 on standard SiO_2 are investigated in situ in order to determine the intrinsic work function of MoS_2. Furthermore, it will be shown that the work function can be significantly influenced by the substrate and that contaminations due to lithography can introduce contaminations that severly affect the charge homogeneity.

4.1 Graphene on $SrTiO_3$

High-κ dielectrics as substrate material were proposed as a possible way to enhance charge carrier mobility in graphene sheets sticking to a surface. This effect is claimed to take place due to a strong dampening of scattering from charged impurities by the high-κ dielectric [255]. An ideal candidate to study this effect experimentally is the well-known insulator $SrTiO_3$, in which the dielectric constant can be tuned by temperature in a range from 200-300 (room temperature) to $\sim$ 5000 (liquid helium temperature) [256].

For this experiment, graphene was exfoliated from a HOPG crystal (Momentive Performance Materials, Columbus - USA) onto a polished crystalline $SrTiO_3$ (100) surface (Crystek, Berlin - Germany). After exfoliation, single layer graphene flakes were located using optical microscopy. Graphene on $SrTiO_3$ shows a very weak contrast of $\sim$2 % with respect to the $SrTiO_3$ surface [239]. Therefore it is crucial to additionally confirm the layer thickness using μ-Raman spectroscopy. The Raman spectrum of a SLG flake on $SrTiO_3$ directly after exfoliation is shown in fig. 4.1 (black curve).

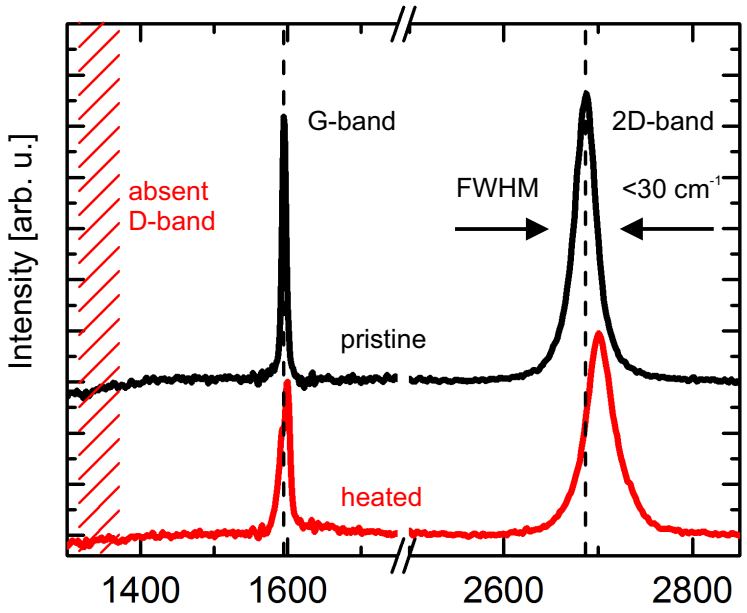

Figure 4.1: μ-Raman spectroscopy measurements of SLG on $SrTiO_3$ (Horiba Labram, λ=514 nm, power below 5 mW). The black curve corresponds to the pristine exfoliated graphene flake, the red curve is taken after heating the sample in situ to 120 °C. The small FWHM of the 2D-band at $\sim$2685 cm^{-1} is used to identify the single layer graphene. No disorder induced D-band is observed for the pristine and the heated SLG flake.

[0]Parts of this section have been published in Kleine Bussmann, O.O. *et al., Nanotechnology 22 (2011)*

The 2D-band at 2685 cm^{-1} with a small FWHM of 27 cm^{-1} can be taken as proof for single layer graphene. The absence of the D-band at ∼1340 cm^{-1} shows the high crystallinity of the graphene flake with no detectable defects [257].

During in situ KPFM measurements graphene on $SrTiO_3$ is heated to about 140 °C. To make sure that this does not introduce defects in the graphene lattice, the sample is measured with Raman spectroscopy before and after in situ heat treatment to 120°C. The Raman spectroscopy of the pristine graphene sample is shown in fig. 4.1 (black line). Directly after the heating process the sample was measured again in ambient, giving the red line in fig. 4.1. Most importantly, no D-band is formed after in situ heating, which prooves that in situ heating does not damage the graphene sheet. By taking a closer look at changes in the position of the G- and 2D-band it can be observed that the G-band only shows a minor shift of ν=2 cm^{-1} while the 2D-band is shifted by ν=15 cm^{-1}. In a simple model, the position of the G- and 2D-band can be used to characterize doping and stress effects in graphene, respectively [217, 258]. Here, the minor shift of the G-band shows that almost no doping effect of the in situ temperature processing can be detected by measuring the sample in ambient. However, the large shift in the 2D-band indicates stress in graphene. To further study this, the sample has to be investigated completely in situ, which will be done in the next part.

n-type doping by charge transfer from the substrate

First, a graphene flake on $SrTiO_3$, which has been exfoliated in ambient and imaged in situ without any heat treatment, is shown. In fig. 4.2 (a) the NC-AFM topography is shown. Graphene sheets with varying layer thickness (SLG, BLG & 4 LG) are marked with different colors. Note, that the crystalline $SrTiO_3$ surface shows a prominent pattern caused by the $SrTiO_3$ terrace steps, which can be observed on the thin graphene sheets as well. This prooves how strong the ultrathin graphene layers are accomodated to the substrate surface. Interestingly, line profile analyses of the two SLG sheets (flake 1 on the left, flake 2 on the right) with respect to the $SrTiO_3$ surface in fig. 4.2 (b) show two different heights for SLG/$SrTiO_3$ with Δz_1= 1.35 nm and Δz_2= 1.10 nm, neither of them being the correct interlayer spacing of graphite of 0.35 nm [259]. It is already known that correct height measurements of graphene are not trivial [260], however using KPFM simultaneously to NC-AFM is supposed to result in correct height values [199] as electrostatic forces are compensated. Therefore it is likely that contaminations from ambient are causing this height difference.

The corresponding KPFM measurements are shown in fig. 4.2 (c). In order to facilitate the discussion, quantitative KPFM is employed in which the work function of the tip is calibrated by the surface potential measurement on "bulk" (>6 LG) graphene (as described in detail in section 3.1). This allows the assignment of work function values to each graphene flake and even the substrate material. The work function of the two SLG sheets differs a lot. The small SLG flake on the left has the same work function as 4 LG with 4.60 eV, the large SLG in the middle shows a large variation on the flake ranging from the work function of BLG 4.55 eV to the values of 4 layers graphene. The high standard deviation of flake 2

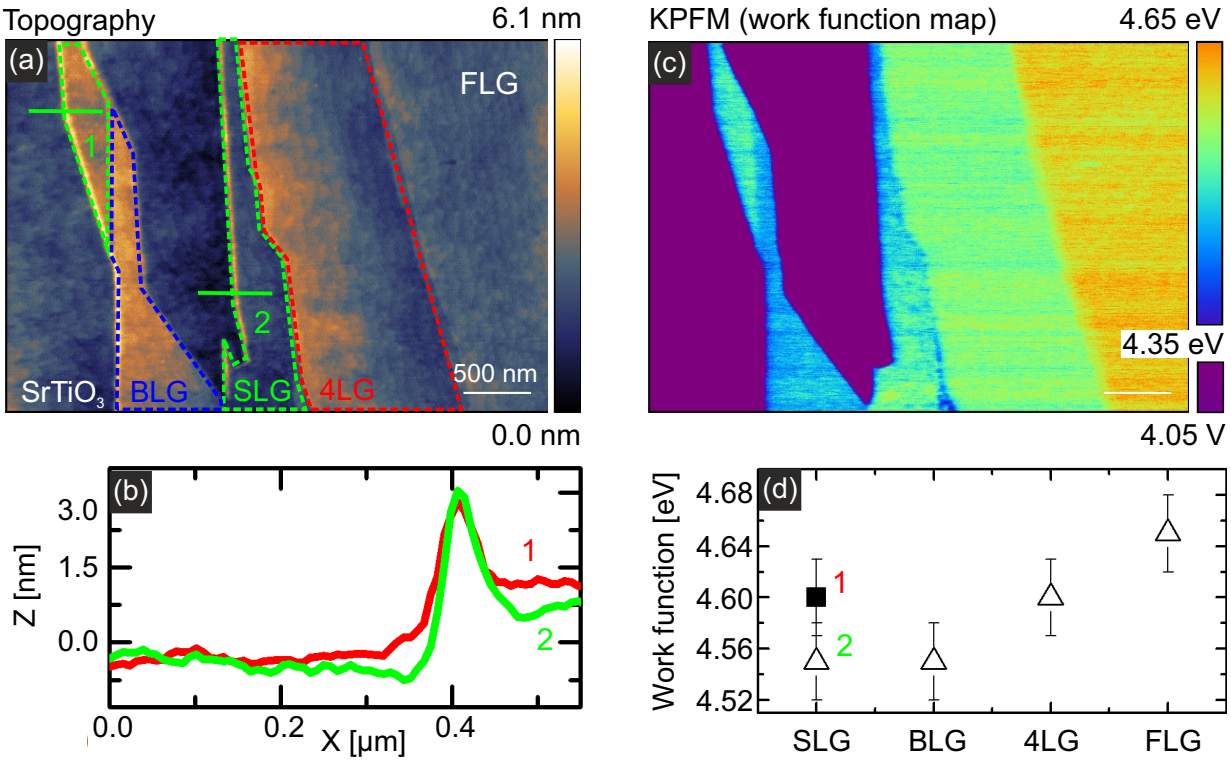

Figure 4.2: Kelvin Probe measurement of pristine graphene exfoliated on $SrTiO_3$. (a) NC-AFM topography, different graphene layer thicknesses are marked using colours. Terrace steps present on the $SrTiO_3$ can be observed on the graphene sheets as well. (b) Line profiles of SLG flake 1 and flake 2, showing heights of over 1 nm for pristine graphene sheets. (c) Corresponding KPFM work function map revealing different work function values for SLG caused from preparation in ambient conditions. (d) Work function values for different graphene layer thicknesses.

$\Delta\Phi_2$=49 meV compared to the flake 1 $\Delta\Phi_2$=22 meV corresponds to an increased charge inhomogeneity, which is detrimental for the performance of graphene devices [261, 262].

To investigate how large the influence of ambient contaminations on these findings are, the sample was heated up to 140 °C for three hours. After cooling down the sample for over 12 hours, the same graphene flake was measured again using NC-AFM and KPFM. The topography in fig. 4.3 (a) reveals the same morphology of the heated graphene flake compared to the pristine one. However, by analyzing the line profiles, a similar decreased height for both SLG flakes of about 0.58 and 0.78 nm can be observed, which can be attributed to the removal of ambient contaminations. The fact that these two SLG sheets still show different and increased height informations is most likely caused by the $SrTiO_3$ terraces, which are oriented along the graphene edge. The removal of contaminations is even more clearly detectable in the quantitative KPFM map shown in fig. 4.2 (c). The work function of the graphene layers has decreased to 4.25 eV, 4.44 eV and 4.60 eV for SLG,

BLG and 4LG respectively. Note, that the work functions of both SLG flakes have the same value now and the charge inhomogeneity of the SLG flake 2 is significantly lowered to 20 meV.

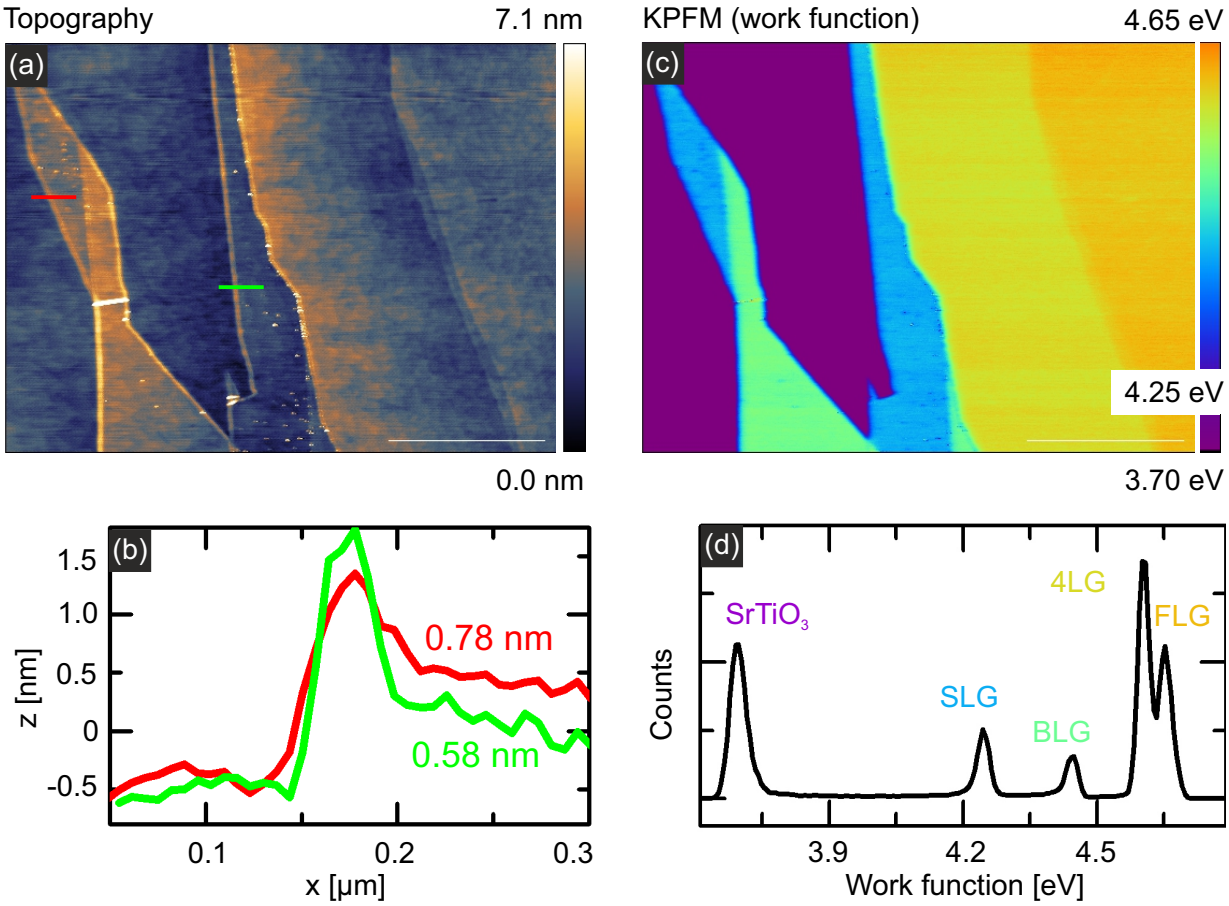

Figure 4.3: Kelvin Probe measurement of in situ heat treated graphene on $SrTiO_3$. (a) NC-AFM topography with the corresponding KPFM work function map (c) revealing a monotonous increase of the work function values with layer thickness. (b) Line profiles of the lines marked in (a) showing the decreased height for SLG/$SrTiO_3$ after annealing. (d) Work function histogram of (c). Scale bars in the images are 1 μm.

4.2 Conclusion

To sum up the results until now, it has been found that contaminations due to preparation of the graphene samples in ambient can alter the electronic properties of graphene. The contaminations present on the pristine flake cannot be identified directly in the AFM topography as they are most likely present as a continuous film on top of graphene or

at the interface between graphene and the substrate. The unusual heights of the SLG flake 1 on $SrTiO_3$ with 1.35 nm and flake 2 with 1.10 nm already indicate the presence of continuous adsorbate layers. The height difference between pristine and heated SLG matches the height of two molecular water layers found in literature quite well [184].

In contrast to the in situ findings, the Raman measurements in ambient show no signs of doping after UHV heat treatment. This is quite surprising as Raman spectroscopy is well-known to be a very powerful tool to monitor charge dopants in graphene [217]. The shift of the 2D-band can be explained by an increased uniaxial strain. This is propably induced by the removal of adsorbates at the SLG/$SrTiO_3$ interface, which results in a higher adhesion between graphene and the $SrTiO_3$ surface. The reason why this higher adhesion can be observed with Raman spectroscopy but the heavy n-type doping is not, is that by exposing the graphene sample to air humidity the graphene flake will be immediately covered by adsorbates and water again, which is known to cause p-type doping by a redox reaction of water [263]. As the adsorbates cannot penetrate the graphene sheet, the interface between graphene and the substrate stays adsorbate free and the higher adhesion can be detected by Raman spectroscopy.

The ambient contaminations have a large impact on the work function of graphene. The work function of pristine SLG sheets can be either of the same value as the work function of BLG (flake 2) or 4 LG (flake 1). Futhermore a non-uniform distribution of adsorbates can lead to a high charge inhomogeneity in the SLG flake. By heating graphene on $SrTiO_3$ in situ, the contaminants can be removed and the effect of the substrate charge transfer from the $SrTiO_3$ can be investigated. The work function value of SLG is lowered from 4.6 eV (almost undoped graphene) to 4.4 eV (n-doped). The reason for this charge transfer is not understood in total yet, however interfacial dipoles, chemical bonds and band structure effects have been discussed. In a simple model, the difference in work function between graphene and its substrate leads to a interfacial dipol, which is related to the well-known pillow effect of adsorbed molecules on surfaces. It can be described by Pauli repulsion between electrons from graphene and the substrate that cause charge redistribution at the interface compared to the free surface [264, 265, 266].

4.3 Graphene on SiC

Although graphene can be effectively doped by the $SrTiO_3$ substrate, it has been shown that the high-κ dielectric advantage in form of reduced charge carrier scattering is only existent for low temperatures [267, 256]. This mobility enhancement is completely washed out in ambient by a strong surface-optical-phonon scattering which leaves intermediate-κ dielectrics such as SiC(0001) the optimal choice for mobility enhancement. This is not the only reason why SiC is an interesting choice as a substrate material for graphene. By heating SiC to temperatures over 1450 °C, silicon is evaporating from the surface and carbon left behind is reorganizing itself to graphene [268]. This epitaxially grown graphene on the SiC is highly crystalline, shows n-type doping and it is possible to grow graphene nanoribbons on SiC [269].

In this chapter, it will be investigated whether the doping behaviour of exfoliated graphene differs from epitaxial graphene on SiC and it will be further studied how local water layers influence the work function of graphene. For this experiment, graphene was exfoliated from a HOPG crystal (Momentive Performance Materials, Columbus - USA) onto a 6H-SiC (0001) substrate (Pam-Xiamen, Xiamen - China) in ambient conditions without prior treatment of the substrate. Single- and bilayer graphene flakes were identified using Raman spectroscopy. Before introducing the samples to UHV conditions, the sample was measured in ambient conditions with AFM to check for graphene flakes with isolated water layers to study the effect of local water layers on the surface potential.

4.3.1 Intercalated, local water layers

A sample with varying graphene layer thicknesses and isolated water layers is shown in fig. 4.4 (a) and (b). The NC-AFM topography reveals a water layer height of typically 0.5 nm for the interfacial water layers (IWL). In the corresponding KPFM map, graphene on top of these water layers shows a clear contrast in the work function compared to the graphene flakes directly in contact with SiC. The work function is increased by 40 meV and a similar effect can be observed for BLG and FLG. For water observed on BLG and FLG the exact location remains unclear. Whether the water is located at the interface between graphene and the substrate, intercalated between the graphene layers or even adsorbed on top, cannot be distinguished by KPFM.

In order to remove the IWL, the sample was heated in situ to 180 °C for 1 hour. This procedure allows the removal of IWL between graphene and the SiC substrate, but it is not sufficent to completely remove water layers underneath BLG and FLG as can be seen in the NC-AFM topography image in fig. 4.4 (d). No IWL is present at the interface between SLG and SiC, but the BLG on top of the SLG shows almost complete water intercalation. This can be observed in the corresponding KPFM work function map (fig. 4.4 (e)) as well, as the the water-free SLG shows a constant work function of 4.50 eV (n-type doping) while BLG with 4.60 eV shows a second contrast which is increased by 0.04 eV. The plot in 4.4 (c)

[0]Parts of this section have been published in Ochedowski *et al., Applied Physics Letters 102 (2013)*

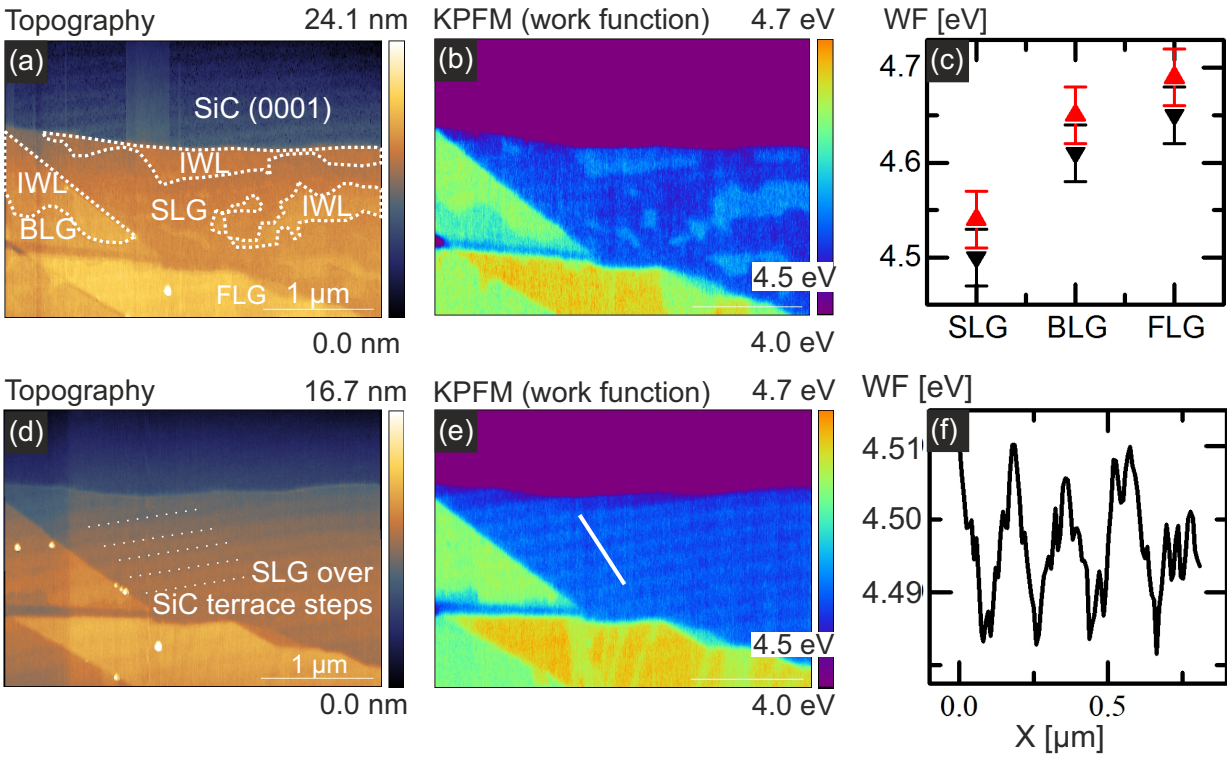

Figure 4.4: In situ measurements of exfoliated graphene on SiC (0001) before and after annealing. (a) NC-AFM topography, local IWL are marked with white dotted lines. (b) Corresponding KPFM image, the IWL can be clearly distinguished in the work function map. (c) Work function of graphene in direct contact with the SiC surface (black, filled triangles) and graphene on top of IWL (red, hollow triangles). (d) The same graphene flake after in situ annealing to 180 °C. (e) Corresponding KPFM image, IWL vanished after annealing and the work function of graphene shows a modulation following the SiC terrace steps. (f) Line profile over the line marked in (e). Image adadpted from [OO.07]

sums up the work function for the different graphene layers and the influence of IWL.

The exfoliated graphene on SiC shows a similar n-type doping as epitaxially grown graphene on SiC. The work function difference between SLG and BLG is similar as well, being 0.10 eV for exfoliated and 0.13 eV for epitaxially grown graphene on SiC [270]. Note that the interface between graphene and SiC is completely different. While exfoliated graphene is n-type doped by a thin oxid layer on the SiC surface, the doping of epitaxial graphene originates from the C-rich buffer layer, which is formed during the epitaxial growth [270].

Looking at the work function data for local water layers a decrease in charge carrier concentration from $n_e = 3.6 \cdot 10^{11}$ e/cm^2 for clean graphene to only $n_e = 1 \cdot 10^{11}$ e/cm^2 for areas with intercalated water underneath graphene is observed. This is a clear indication that water molecules are blocking the charge transfer between the substrate and graphene.

However the exact mechanism behind this effect is still unknown. It is possible that water bilayers act as a tunneling barrier which affects the charge transfer. It has been proposed to use this effect to locally gate the graphene sheets, which might be challenging due to the limited stability of the IWL when heated [271].

4.3.2 Adsorbed water layer

Graphene and graphite are known to be hydrophobic materials [272, 273]. This is why local water layers are in general considered to be trapped between graphene and the substrate rather than being adsorbed on top of graphene. However water on top of graphene will most likely influence the electronic properties of graphene as well as the adsorbtion of other molecules onto graphene which is crucial for sensor applications.

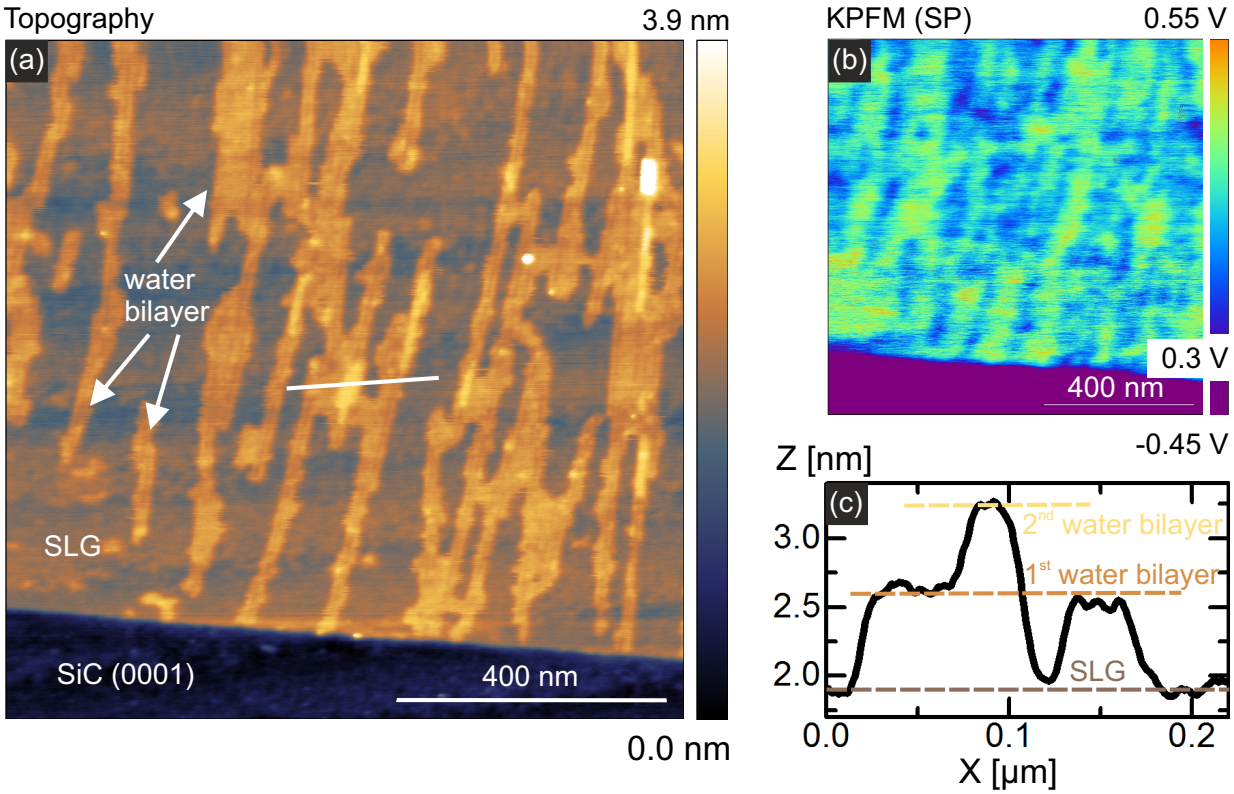

Figure 4.5: Water adsorbed on exfoliated graphene on SiC (0001). (a) Storing graphene under ambient conditions for 12 months results in water adsorbtion on top of the graphene sheet. NC-AFM topography shows a preferred orientation of these water layers of approximately 90° with respect to the graphene edge. (b) Corresponding KPFM image, the surface potential is decreased where water is adsorbed. (c) Line profile of the line marked in the topography revealing bilayer heights of 0.6 nm for the water layers.

In order to study the water on top of graphene, a graphene on SiC sample was stored under ambient conditions for over 12 months. After this time, the sample was introduced to the UHV system and NC-AFM in combination with KPFM was performed as can be seen in fig. 4.5 (a). While the water layers observed previously at the interface between graphene and SiC are oriented by the SiC terrace steps, the adsorbed water layers show an orientation of 90 ± 10 ° with respect to the graphene edge. This indicates water molecules on top of graphene orient themselves rather along the crystallographic lattice of the hydrophobic graphene than SiC. A line profile analysis in fig. 4.5 (c) reveals that these water layers exhibit a height of 0.6 nm and 1.2 nm, which correspond to a single bilayer of water and two bilayers, respectively. [184]. The effect of the adsorbed water layers on the surface potential is shown in fig. 4.5 (b). The surface potential, which corresponds to a change in the work function, is decreased for areas where water bilayers are adsorbed on graphene, which strongly affects the charge inhomogeneity of graphene. In contrast to the IWL, adsorbed water can be removed by mild heat treatment to 60 °C.

4.3.3 Conclusion

In conclusion, exfoliated graphene on SiC(0001) shows n-type doping comparable to epitaxial graphene on SiC. Due to the exfoliation method in ambient conditions, local water layers can be trapped at the interface between graphene and SiC, which considerably influences the doping level and charge inhomogeneity of graphene. The charge transfer between SiC and graphene is locally blocked and reduced by the intercalated water layers.

4.4 Graphene on muscovite mica

The preceding in situ studies of graphene on $SrTiO_3$ and SiC(0001) revealed that graphene free of water exhibits n-type doping. This finding is in strong contrast to Kelvin measurements in ambient conditions where graphene generally shows p-type doping. The in situ studies prior to heat treatment showed, that this behaviour is related to adsorbates from ambient conditions like water, oxygen, nitrogen, etc. For graphene on SiO_2 a combination of air humidity and oxygen molecules have been shown to be the dominant factor in the p-type doping [274, 275, 276, 277]. The question remains, if there is a substrate that is able to induce p-type doping in graphene even without adsorbates from ambient conditions.

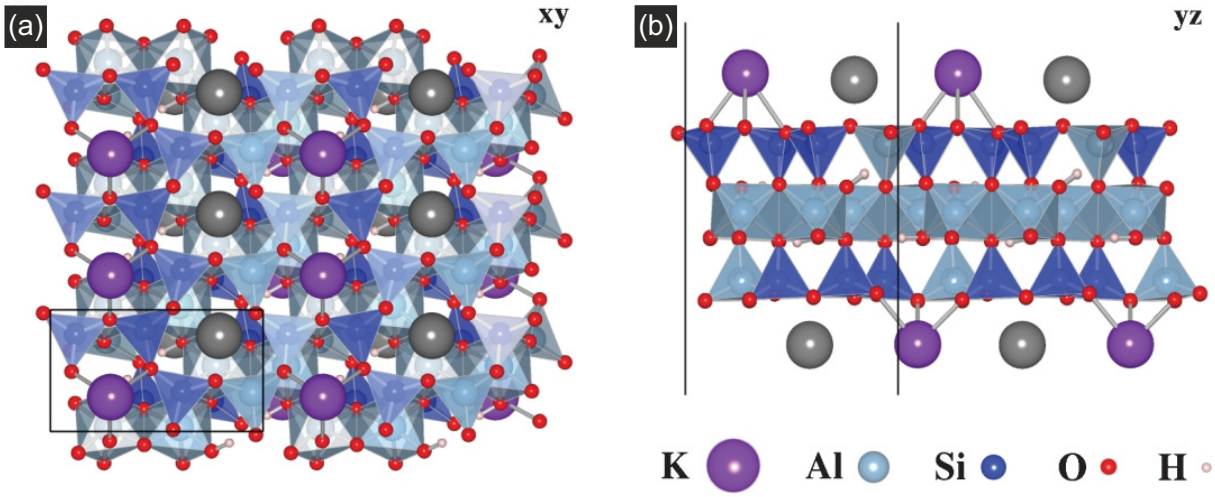

Figure 4.6: Electroneutral surface structure of muscovite mica in [001] projection and [100] projection with a uniform potassium distribution. Grey spheres mark possible positions of additional potassium ions in electropositive surface. Image taken from ref. [278]

Another graphene substrate which has been investigated in detail under ambient conditions is muscovite mica [279]. Belonging to the group of phyllosilicate minerals, mica consists of a two dimensional sheet structure. The chemical formula of muscovite mica is $KAl_2(Si_3,Al)O_{10}(OH)_2$ [278]. The surface structure of muscovite mica is depticted in fig. 4.6. In each muscovite layer, two tetrahedral silicate layers enclose a layer of octahedrally coordinated Al^{3+} ions. Within tetrahedral units aluminum is randomly substituted with silicon with a ratio of 1:3. The resulting negative charge is countered by potassium ions which are present in a 12-fold oxygen coordination. Typically muscovite mica is prepared by cleaving, which results in a non-uniform distribution of potassium ions [278]. After cleaving the reactive ionic surface tends to adsorb impurities to compensate excessive charges, finally resulting in a neutral mica surface. Using surface potential measurements

[0]Parts of this section have been published in Ochedowski *et al., Scientific Reports 4 (2014)*

Qi et al. have shown that it can take several hours of exposure to ambient conditions for an air cleaved mica surface to neutralize [280]. A similar behaviour is observed for in situ cleaving of mica where surface charges of up to 2 magnitude orders higher have been detected [281].

The most notable advantage muscovite mica has as a supporting material for graphene in comparison to standard substrates like SiO_2 is its ultraflat nature. Cleaving mica in a dry N_2 atmosphere and exfoliation of graphene on top of it results in a surface roughness of only 23.1 pm (RMS) [282]. However, exfoliating graphene in ambient results in an inevitable intercalation of water layers [283, 284, 285, 271, 286, 287], which could prove detrimental for electronic devices. Raman spectroscopy, Kelvin probe force microscopy (KPFM) and scanning tunneling spectroscopy performed in ambient conditions revealed a *p*-type doping from the substrate, that is effectively blocked by the intercalated water layers [271]. It was suggested by Shim et al. to actually use water to modulate the electronic properties of graphene [271], but in practice controlling water islands locally would be extremely difficult to realize. Therefore one is confronted with the problem to remove the intercalated water.

In this chapter, it will be investigated whether the observed p-type doping of graphene on mica is due to the measurement in ambient conditions or due to the surface structure of muscovite mica. Rudenko et al. found by using DFT calculations that a potassium depleted mica surface is able to p-type dope graphene [278]. The samples are prepared by exfoliating graphene from a HOPG crystal (Momentive Performance Materials - USA) in ambient conditions (room humidity typically 40%) onto a freshly cleaved muscovite mica substrate (MaTeck - Germany). Single layer graphene flakes were located using optical microscopy and were unambigiously identified with Raman spectroscopy using a Horiba Labram (λ=633 nm, P<1 mW).

4.4.1 p-type doping from the substrate

Shown in fig. 4.7 (a) is a typical non-contact AFM topography of a pristine graphene flake on mica after introduction to UHV conditions ($p_{\text{base}} = 1 \times 10^{-10}$ mbar). The zoom-in topography image in (b) shows that the single layer graphene (SLG) flake is decorated with small islands. The red line profile in fig. 4.7 (b) denotes the height of the SLG on mica which is about 0.4 nm. While this value corresponds well to the nominal interlayer spacing of graphite, we observe that the measured heights frequently vary between 0.4 nm and 0.9 nm. This is in agreement with values reported for SLG on mica varying between -0.8 nm and 1.0 nm [288, 271]. By exfoliating graphene on mica in ambient conditions, water layers will be trapped at the interface between graphene and mica which results in increased step heights measured by AFM [284, 184]. These interfacial water layers, IWL called in the following, have been found in different thicknesses from one to three IWL. The small islands which are up to 1.2 nm in height (see black line profile in fig. 4.7(b)) are attributed to water on top of graphene and they can easily be identified in the surface potential map as well (see figure fig. 4.7(c)). Here, the water islands decrease the surface potential of graphene by up to 200 mV.

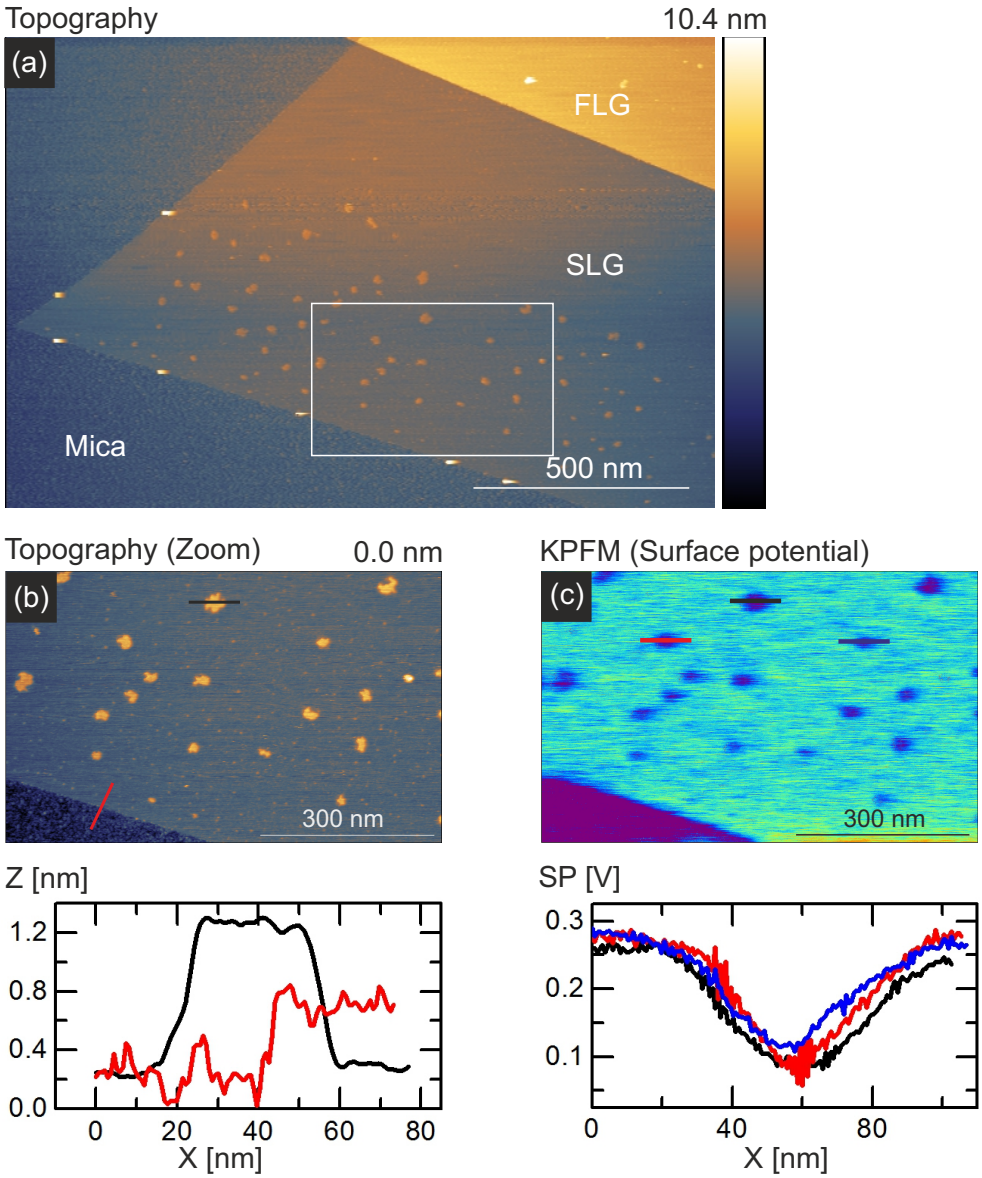

Figure 4.7: Pristine condition of exfoliated graphene on mica. (a) Non-contact AFM topography of pristine graphene. Single layers are decorated with water islands. (b) Zoom-in on the white box marked in (a). The red line denotes the step height of the graphene flake, the black line profile denotes the height of a water island. (c) Surface potential map corresponding to the topography in (b). Water islands decrease the surface potential by up to 200 mV. Image adapted from ref. [OO.16]

Next we tried to apply a thermal treatment to remove the intercalated water film. To this end, several heating steps were performed at different temperatures and exposure times. The pristine SLG flake in fig. 4.8 (a) with the continuous IWL exhibits a work function of

4.83 eV, which is lowered to 4.66 eV in areas where water islands are adsorbed on top of it as seen in fig. 4.7 (c). Heating this sample to about 180 °C for 1 hour can be used to remove the adsorbed water islands but not the interfacial water as can be seen in fig. 4.8 (b). As the intercalated water cannot penetrate the graphene sheet, only small areas at the edge of graphene are freed from water. Because grain boundaries and defect sites are very rare in exfoliated graphene sheets, no effective alternative desorption pathways exist. The work function map shows a similar work function distribution, the work function is decreasing with increasing layer number. However, the work function of graphene in direct contact with mica is about 0.17 eV higher compared to graphene lying on the interfacial water layer.

The last image in fig. 4.8 shows results that were obtained after heating the sample to about 600 °C for 19 hrs. The area where the intercalated water layer has been removed has increased (dark blue areas in fig. 4.8(c)), but in large areas of the graphene flake intercalated water can still be clearly seen (light blue areas in fig. 4.8 (c)). The work function has changed significantly over the whole flake: From 4.8 eV (greenish area in fig. 4.8 (b)) to 3.93 eV (bluish area in fig. 4.8 (c)) where the water has been removed, and from 4.65 eV to 4.28 eV in the areas where the water could not be removed. In addition, new characteristic features have appeared (marked with "nanoblisters" in fig. 4.8) with typical diameters of about 10 nm and heights of 0.3 to 1.5 nm. Note that these features are quite different from the water islands found before heating (fig. 4.7), because they are much higher and are located underneath the graphene and not on top of the graphene sheet. We repeated the experiment with other flakes and found that the observed changes are indeed characteristic but with small deviations with respect to absolute values.

At this point we want to stress that the observed change in work function upon excessive heating is not only surprisingly pronounced, it also represents a transition from p- to n-type doped graphene. Such a transition has never been observed for graphene on mica before.

4.4.2 Effect of exposure to ambient

To test whether the original state of the system with respect to work function can be restored, a sample has been exposed to ambient conditions for three days after it had undergone the same treatment as described above. The results of this experiment are summarized in fig. 4.9. The work function of SLG in its pristine condition 5.09 eV (p-type) decreases to 3.90 eV (n-type) after in situ heat processing. The same transition can be observed for bilayer graphene (BLG), where the work function is decreasing from 4.88 eV to 4.35 eV. After the in situ heat processing the sample was exposed to ambient conditions for three days. The work function map in fig. 4.9 (c) shows a KPFM measurement after this exposure to ambient conditions. Again the SLG and BLG sheets exhibit p-type doping with a work function of 4.82 eV and 4.78 eV, respectively. Thus, the initial values are almost completely restored, which can be attributed to the presence of water and oxygen in ambient conditions.

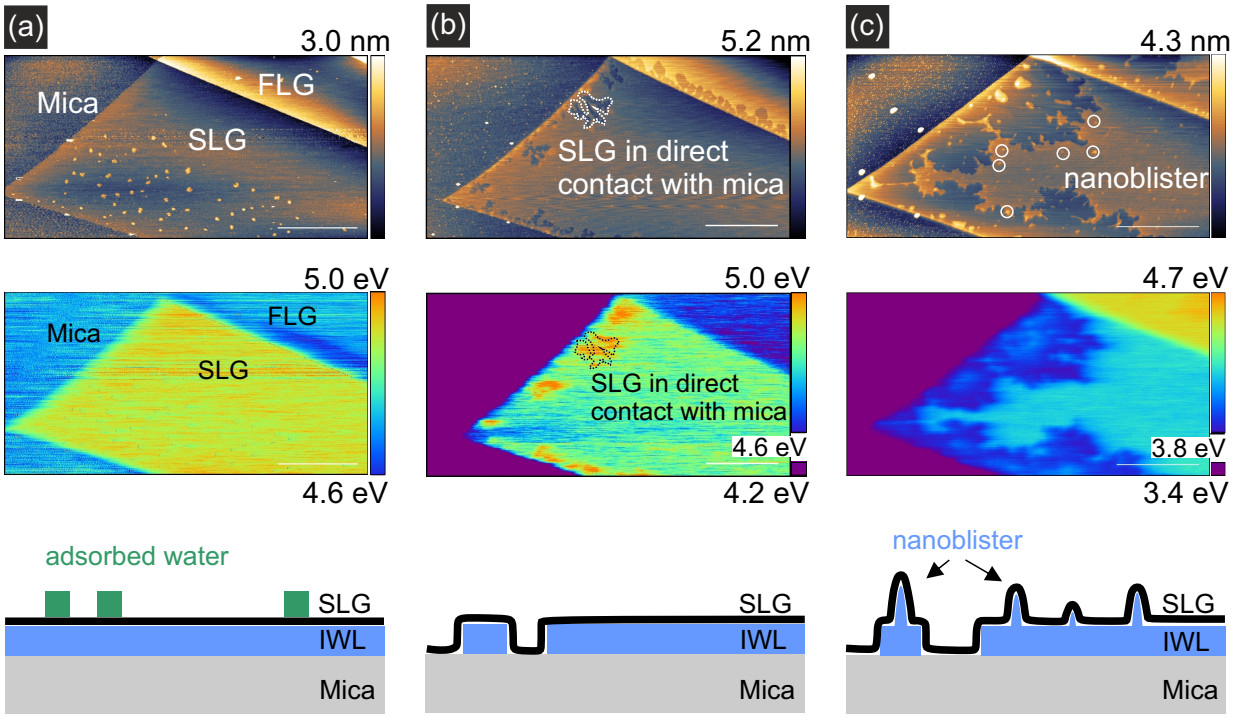

Figure 4.8: Temperature dependent work function of graphene on mica. (a) Topography and work function map of pristine graphene at room temperature without any thermal processing. The work function decreases with increasing layer thickness. The sketch illustrates that a continuous IWL is located beneath graphene while adsorbed water islands are located on top of it. (b) Heating the sample to 180 ° for 1 hour leads to the removal of water islands and the IWL is not completely continuous anymore. Graphene is partly in direct contact with the substrate. The work function is still decreasing with increasing layer thickness. (c) Topography and work function map after heating the sample to 600 ° for 19 hours. The size of the IWL is further decreased and nanoblisters beneath the graphene flake are formed. A contrast inversion in the work function map can be observed, i.e. the work function is now decreasing with layer thickness. Scale bar in all images is 400 nm. Image adapted from ref. [OO.16]

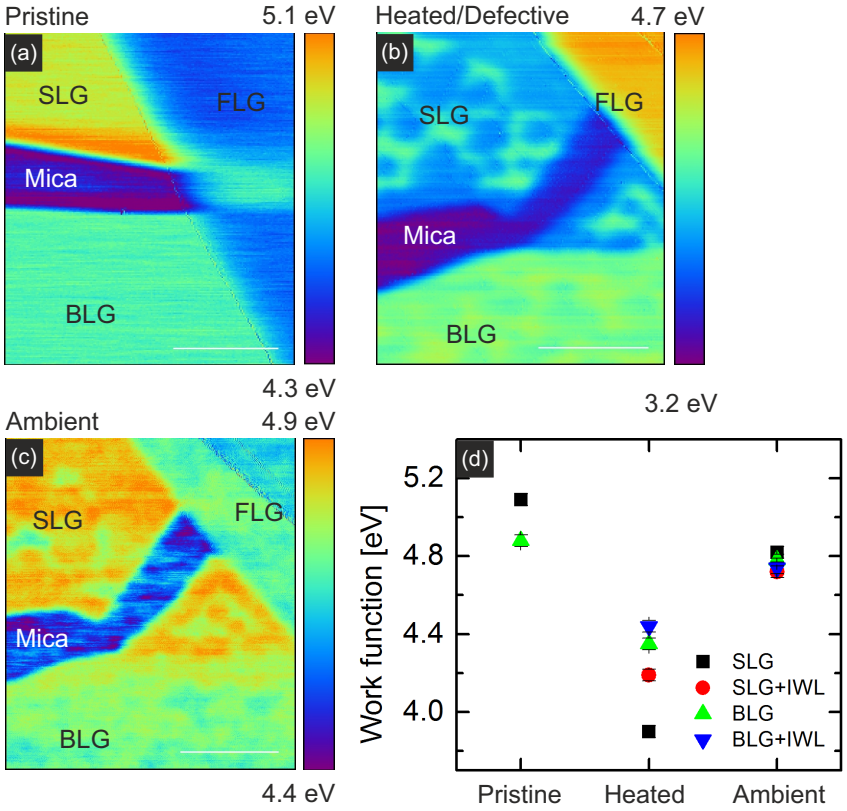

Figure 4.9: (a) Work function map of pristine single, bilayer and few layer graphene on mica. (b) Heat treatment results in an inversed work function map. (c) Work function map after three days of exposure to ambient conditions. The work function is inversed again, qualitatively restoring the work function distribution to its pristine condition. (d) Summary of the work function measurements from (a-c). Scale bar in all images is 400 nm. Image adapted from ref. [OO.16]

4.4.3 Nanoblisters inducing defects in graphene

To find the origin of the observed contrast inversion in the surface potential, a heat treated sample was investigated additionally in ambient conditions using AFM (tapping mode) and Raman spectroscopy.

In fig. 4.10 (a), an ambient AFM topography of a similar treated - heating to 600 °C in UHV - mica supported graphene flake is shown. The few layer part of the graphene flake is covered with nanoblisters that are up to 15 nm in height and about 400 nm in diameter. Additionally, round plateau-like structures of similar diameter with a constant height of about 1 nm are observed. These flat plateaus could very well be the remnants of ruptured nanoblisters. Shown in fig. 4.10 (b) are the Raman spectra of SLG graphene before (black line) and after (red line) heat processing. In its pristine condition the Raman spectra consists of the well known first order non resonant G mode at 1588 cm^{-1} and the resonant $2D$ mode at 2645 cm^{-1}. With a full width half maximum (FWHM) of 24 cm^{-1}

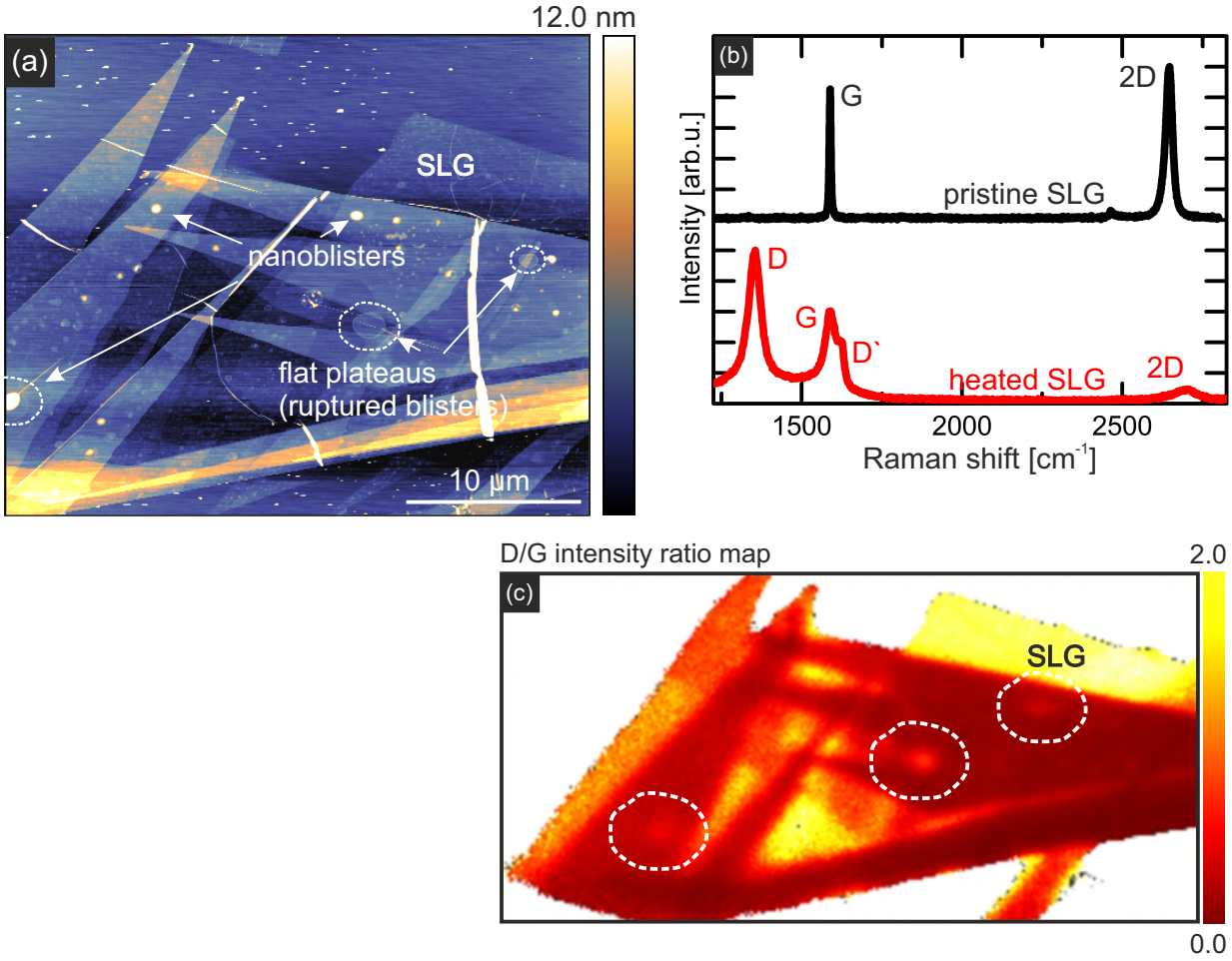

Figure 4.10: Defect analysis using Raman spectroscopy. (a) AFM topography of a graphene flake after in situ heat treatment. Nanoblisters and areas with flat plateaus (ruptured blisters) are marked in the image. (b) Raman spectra of pristine and heat treated graphene on mica. A strong, disorder induced D-band is detected after in situ heating. (c) Raman mapping of the I_D/I_G peak intensity ratio of the graphene flake shown in (a). Image adapted from ref. [OO.16]

for the $2D$ mode, this Raman spectrum can be unambigiously assigned to SLG [214].

After heating in UHV two new modes have evolved in the Raman spectrum, the D and D′ mode, which are both induced by disorder [222, 289, 290]; in addition the $2D$ mode is suppressed. The presence of the D and D′ mode indicate a very high defect density. Raman spectroscopy can be used to quantify the amount and even the nature of disorder in graphene as well, namely by determining the I_D/I_G and $I_D/I_{D'}$ intensity ratios. Here, we find $I_D/I_G = 1.7$ and $I_D/I_{D'} = 6.3$, respectively. From comparison with published data we estimate that the defects here are mainly vacancy defects [291] and the mean distance between defect sites is on the order of L_D <5 nm [257, 292, 219]. In an attempt to

correlate the measured morphology with the defect distribution we used Raman mapping. In fig. 4.10 (c) the D/G-peak intensity ratio distribution of the measured sample area can be seen. Due to the very different lateral resolution of the two methods, a one-to-one correlation is not possible. Nevertheless, at many of the locations where large nanoblisters and plateaus (most likely ruptured nanoblisters) were observed in the AFM image, the Raman map does show areas with an increased D/G ratio (marked in fig. 4.10 (c)). This strongly suggests that the formation of nanoblisters is accompagnied by a significant defect formation in graphene.

4.4.4 Conclusion

The experimental evidence presented above suggests that the work function of graphene on mica is governed by different mechanisms, which can be controlled by thermal processing. In the following we will discuss three possible mechanisms induced by heating: removal of adsorbates, substrate changes and defect formation.

As already discussed in the previous sections, any kind of adsorbate is expected to have a large influence on the properties of graphene. Here, we are dealing with different adsorbates, namely water (from the humidity always present in ambient conditions) and air (O_2, N_2, etc.). Their effect on (non-defective) SLG has been investigated by several groups [274, 293, 294, 275, 295]. Hitherto, only p-type doping of graphene on mica has been reported, but all data has been obtained under ambient conditions [271], where electrophilic adsorbates can be expected to mask the intrinsic properties of graphene as already indicated by the data obtained on SiC and $SrTiO_3$. In general, the adsorbates obviously result in an effective p-type doping as confirmed by our data on mica. It could be shown that it is fundamentally impossible to completely remove the water from in between graphene and mica, but heating to 600 °C ensures that no water is adsorbed on top of graphene and that the intercalated water layer has been successfully removed at least in some areas. Employing locally resolved KPFM data, the difference between areas with the IWL present and areas without the IWL can be easily distinguished. This reveals the different and seemingly adverse effects that water may have on work function measurements: With samples prepared under ambient conditions, intercalated water leads to a decrease of the p-type doping level (see fig. 4.9(c)), while for heated graphene on mica, intercalated water decreases the number of excess electrons, i.e. lowers the n-type doping level (see fig. 4.9(b)). These findings clearly underline the importance of UHV measurements when performing quantitative KPFM studies to determine intrinsic properties of graphene.

The second mechanism that may give rise to changes of the work function of graphene is the charge transfer from the substrate. It has been proposed by Rudenko et al. that the doping level of graphene is very sensitive to the mica surface configuration [278]. From our KPFM data we find that the mica substrate does indeed show a change of its work function from 4.6 to 3.4 eV upon heating (see fig. 4.8), indicating that the mica surface undergoes strong changes towards an electron negative surface. This transition is most likely driven by a depletion of potassium ions on the mica surface [278]. The fact that we observe a

continuous change in the graphene work function upon heating from 5.1 eV (p-type doping) to 3.9 eV (n-type doping), can thus be interpreted in terms of an increasing electron charge transfer from the mica substrate to graphene due to the increasing dehydration of the mica surface.

Apart from direct charge transfer from the mica substrate itself, the heat induced changes of the mica substrate may have an impact on the work function as well. Significant defect formation in graphene can be detected after heating to about 600 °C, where the dehydration of mica sets in [296, 297]. Based on the observations presented above we therefore suggest that the following mechanism is giving rise to defect formation in graphene: when upon excessive heating the crystal water (chemically bound water within the mineral) begins to evaporate from the mica substrate, it cannot permeate through the graphene layer and will thus accumulate and form nanoblisters consisting of trapped water molecules. This is corrobated by the fact that graphene nanoblisters are reportedly accompanied by defect formation [298, 299, 300, 301] [OO.12]. In addition, in the process of the dehydration of mica, O_2 is formed and thus oxidative etching as observed by Yamamoto et al. may play a role for the defect creation formation as well [297, 302].

4.5 Work function of MoS_2 on a SiO_2 substrate

The major drawback when it comes down to actually implementing graphene in devices is the lack of an intrinsic bandgap. This is why other two dimensional crystals are moving more and more into focus. The main advantage of single layers of MoS_2 (SLM) is its direct band gap of 1.9 eV [80]. It allows the facile integration of SLM in electronic devices, which has been demonstrated for highly flexible transistors, optoelectronic devices, small-signal amplifiers, MoS_2 integrated circuits and chemical vapor sensors [89, 95, 303, 304, 94, 305]. However, single layer MoS_2 can be expected to be as sensitive to charge transfer effects from the substrates or contaminations/adsorbates due to the preparation process as graphene, which has been adressed in the previous section. It has been reported that the performance of these devices can greatly vary due to the choice of the contact material, the cleanliness of the SLM surface and a top gated structure with a high κ dielectric [243, 306, 307, 210, 308, 309]. By choosing appropriate substrate materials for MoS_2 devices the work function might be tuned as shown for graphene to e.g. lower the contact resistance and improve their performance. First experiments adressing this issue for MoS_2 have been already reported [310, 311] [OO.03] using Kelvin probe force microscopy (KPFM). However, these measurements were not done on SLM but BLM and higher layer numbers and the measurements were performed in ambient using amplitude modulated KPFM, both having a great impact on the results.

4.5.1 Sample preparation

In this study MoS_2 (HQgraphene, Netherlands) was exfoliated on a prepatterned Si sample that has been covered by a 90 nm SiO_2 layer (graphene supermarket, United States - Calverton, NY). The SiO_2 was patterned by using an inductive coupled plasma reactive ion etching (ICP-RIE) with Cl_2/N_2 chemistry. The etching mask consists of a standard photoresist patterned by optical lithography. Etching was performed at 35 °C using 300 W of ICP and 150 W table power. The chamber pressure was adjusted to $8 \cdot 10^{-3}$ mbar during this procedure. Reactive ion etching was employed to locally alter the surface roughness and introduce defects in the SiO_2 substrate [312, 313]. The resulting etched holes on the SiO_2 surface had a depth of about 40 nm measured by AFM. Immediately after etching, the MoS_2 was exfoliated by mechanical cleavage [30]. Single layer MoS_2 flakes were located using their optical contrast and verified using μ-Raman spectroscopy [314, 215]. For Raman point measurements and mappings, a Renishaw InVia Raman spectrometer (λ=532 nm, P<0.4 mW, spectal resolution $\sim$ 1 cm^{-1}) has been employed. Because SLM is highly flexibel, it is not suspended over the etched hole. Instead the SLM touches the etched SiO_2 surface at the bottom and follows the morphology like a membrane, see scheme in fig. 4.11. While this leaves the SLM heavily strained on the edge of the hole, it allows to experimentally compare the effect of two differently treated substrates (SiO_2 and RIE

[0]Parts of this section have been published in Ochedowski *et al., Beilstein Journal of Nanotechnology 5 (2014)*

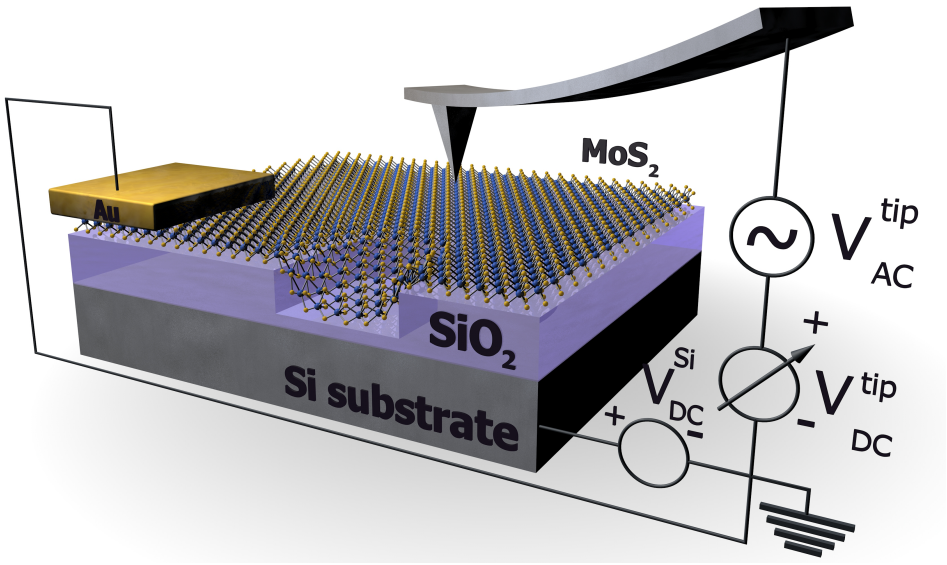

Figure 4.11: Scheme of the experimental setup. MoS_2 exfoliated on top of a prepatterned SiO_2 substrate. A gold contact is deposited on the MoS_2 for the KPFM measurement. Image adapted from [OO.13].

SiO_2) on the same MoS_2 flake.

After identification of SLM areas, a Ti/Au (5 nm/15 nm) contact was patterned on the MoS_2 flake by photolithography, using the photoresist ARP-5350 (Allresist GmbH, Strausberg - Germany) with the developer AR 300-35 (Allresist GmbH, Strausberg - Germany). Acetone was used for the lift-off and at the end the samples were boiled in Isopropyl alcohole. The contact served two purposes. On the one hand, the sample was electrically connected to ground potential, on the other hand, the gold surface was used for calibrating the work function of the AFM tip during KPFM measurements.

4.5.2 Raman spectroscopy characterization

In fig. 4.12 we present an optical image of a sample prepared by the procedure described above together with additional Raman spectroscopy data. The SLM flake can be identified in the optical image in fig. 4.12 (a) by its contrast, which is a transparent green tone. While the majority of the SLM flake is located on pristine SiO_2, a small part of the SLM flake is at the bottom of a hole which was patterned by RIE. To unambiguously identify SLM, Raman spectroscopy was used and the results were compared to literature data [215]. In fig. 4.12 (b) the Raman spectra of SLM on SiO_2 and on SiO_2 (RIE) as well as FLM on SiO_2 is shown. The two prominent peaks, the E_{2g} and A_{1g} peak, correspond to the opposite vibration of the two S atoms with respect to the Mo atom and the out-of-plane vibration of only S atoms in opposite directions, respectively [315, 235]. For SLM on SiO_2 the Raman shifts obtained for the E_{2g} band, ν=386.1 cm^{-1}, and A_{1g} band, ν=403.0 cm^{-1}, are consistent with values reported by other groups. For higher layer numbers the E_{2g} has

been reported to shift to lower wave numbers while the A_{1g} shifts to larger wave numbers, which is again in good agreement with the obtained data.

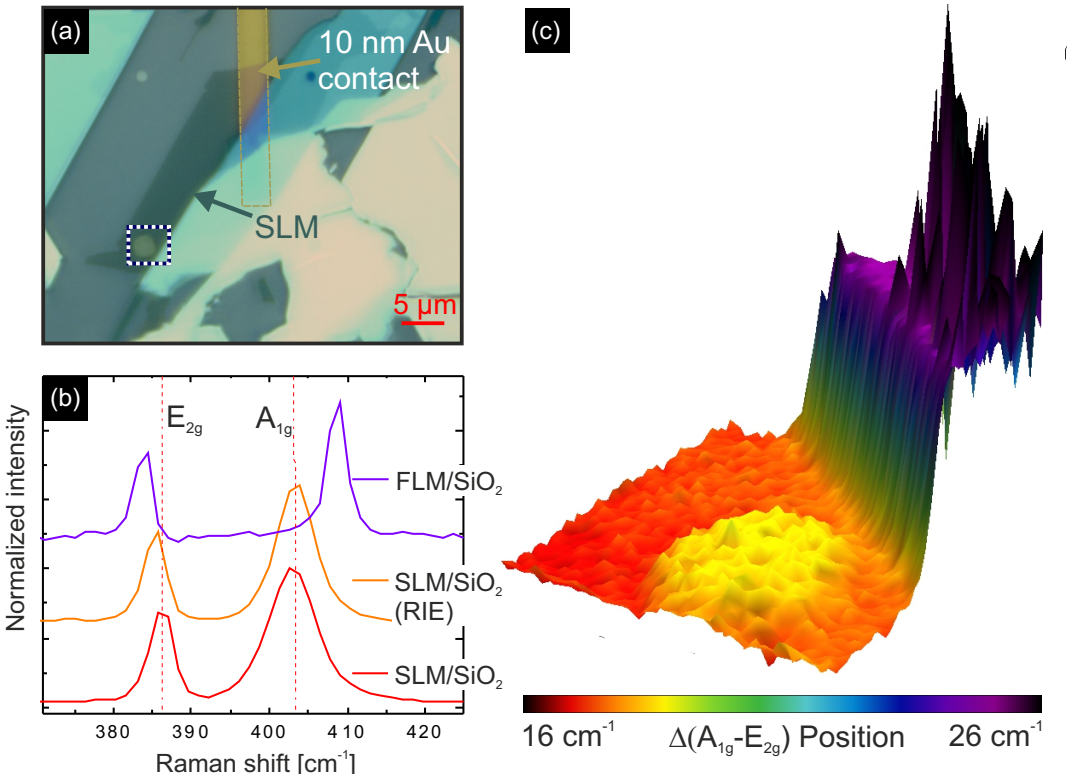

Figure 4.12: Raman spectroscopy of MoS_2. (a) Optical image of the MoS_2 sample on the prepatterned (RIE) SiO_2 substrate. (b) μ-Raman spectroscopy measurements on SLM/SiO_2, SLM/SiO_2 (RIE) and FLM/SiO_2. (b) Raman mapping over the area marked in the blue box in (a). The difference between A_{1g} and E_{2g} mode position is plotted, revealing a shift of the Raman modes for SLM on the RIE SiO_2 substrate. Image adapted from [OO.13].

However, the SLM on RIE SiO_2 shows a different behaviour compared to SLM on pristine SiO_2. The E_{2g} is slightly downshifted to ν=385.2 cm^{-1} and the A_{1g} shows a minor shift to ν=403.4 cm^{-1}. Shifts of the E_{2g} and A_{1g} modes of SLM can have multiple reasons. Uniaxial tensile strain has been observed to cause a splitting in the E_{2g} mode and a shift to lower wave numbers for the resulting E^- and E^+ modes by 4.5 and 1 cm^{-1}/% [221, 316]. While the A_{1g} mode shows no distinct sensitivity to uniaxial strain, a charge carrier dependency has been observed [317]. Electron doping of $1.8{\cdot}10^{13}$/cm^2 leads to a linewidth broadening of 6 cm^{-1} and the phonon frequency decreases by 4 cm^{-1}. As our data shows a shift in both Raman active modes, we suggest that the RIE SiO_2 surface causes a slight strain and maybe local doping by charge transfer in the MoS_2 flake. The Raman mapping shown in (c) corresponds to the evaluation of point spectra performed in the green box marked in (a). Plotted is the difference of the E_{2g} an A_{1g} mode positions. While the difference

between SLM and FLM on SiO_2 is significant with $\triangle$=8.2 cm^{-1}, the difference between SLM on SiO_2 and on RIE SiO_2 is relatively small with $\triangle$=1.3 cm^{-1}. As can be seen in the Raman mapping, the difference in the SLM induced by the substrate is constant over the whole flake and not just present in single point measurements.

4.5.3 In situ KPFM and screening length

For the NC-AFM and KPFM measurements the sample was introduced to the UHV system. Prior to the data collection, the sample was heated in situ to 200 °C for 30 min to remove adsorbates from ambient conditions. In fig. 4.13 (a) and (c) the NC-AFM topography and the corresponding work function map are shown, respectively. On the right side the Ti/Au contact can be seen, which is about 20 nm high and shows a distinct contrast in the surface potential in comparison to the MoS_2 layers. In fig. 4.13 (d) a work function histogram of SLM, FLM and the gold surface of the Ti/Au contact is given. As no graphite/few layer graphene flakes are present on the sample, quantitative work function values were obtained by calibrating the tip on the gold surface by using the known work function of gold Φ_{Au}=5.10 eV [318, 319]. With the relation Φ=5.10 eV-$e \cdot (CPD_{Au} - CPD_{nMoS_2})$ the work function of SLM Φ_{SLM}=4.49±0.03 eV and FLM Φ_{FLM}=4.59±0.03 eV can be assigned. The given error bar consists of the experimental error of our system. Not included in this error is band bending, which occurs when doing KPFM measurements on a semi-conductor surface and a false estimation of the work function of the patterned gold contact.

Besides graphite [OO.08] (see section 3), gold is a common material to calibrate the work function of the AFM tip [319], but while the work function Φ_{Au}=5.10 eV is often used, other work function values in the range from 4.74 eV to 5.54 eV have been reported as well [320, 321]. Surface roughness, homogeneity and humidity can have an effect on the measured work function of metal surfaces as Guo et al. recently demonstrated [322]. The presented data is measured in situ after annealing and we are therefore confident that humidity can be neglected. It has to be pointed out that an error in the work function calibration does not affect the work function values of SLM, BLM and FLM with respect to each other. While the surface potential on the Au contact in fig. 4.13 appears uniform, strong local variations can be observed on the MoS_2 flake. We attribute these features, marked in fig.4.13 (a) with green circles, to contaminations due to the patterning process. The height of these contaminations varies between 1 nm up to 20 nm. These contaminations have a noticeable effect on the work function of SLM, as Φ_{SLM} can be lowered by up to 0.15 eV. As the work function of these contaminations is clearly different from that of the Au contact, the contaminations are most likely resist residues, which have not been completely removed. Such contaminations may act as scattering centers or charge puddles, which are likely to be detrimental to the performance of SLM devices [323].

In the next step, the work function of BLM and the screening length of MoS_2 are determined. For this, the SLM/BLM/FLM area in fig. 4.13 has been measured again in more detail and the work function is analyzed by line profiles. Shown in fig. 4.14 (a), (b) and (c) are the NC-AFM topography, work function map and the corresponding line profiles,

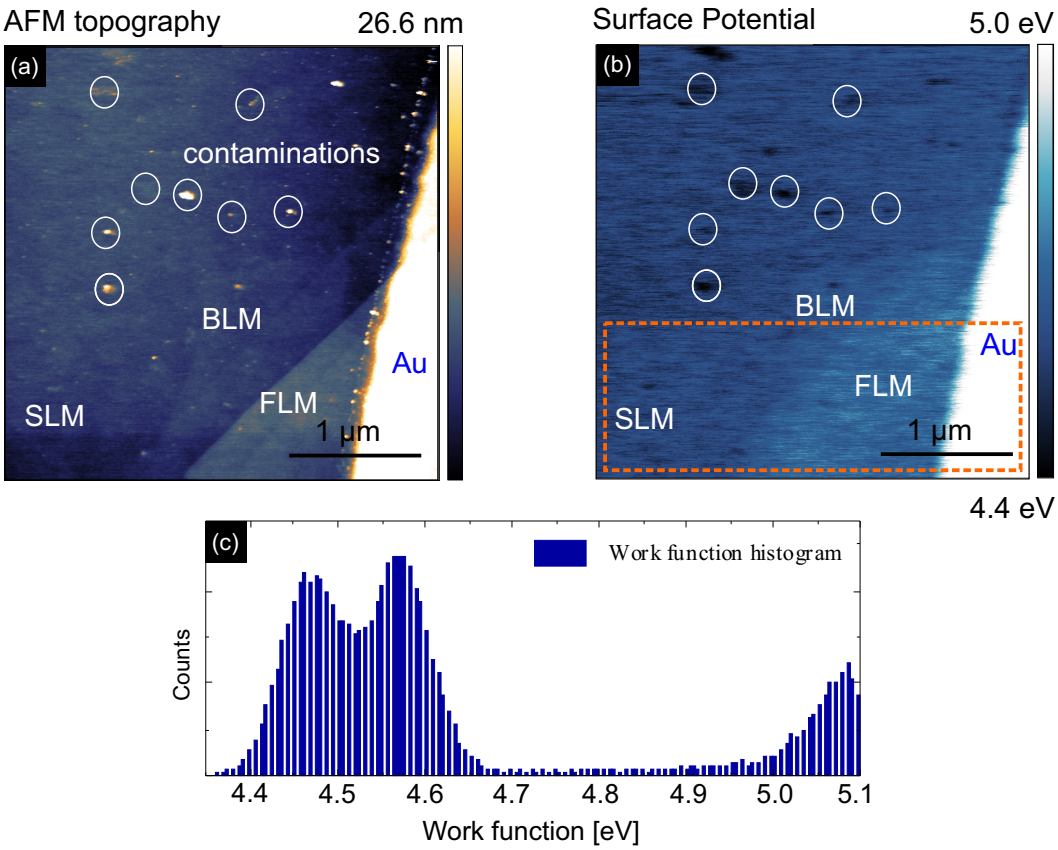

Figure 4.13: In situ KPFM on single layer MoS_2. (a) NC-AFM image of a MoS_2 flake with a gold contact on top of it. Topography reveals areas with contaminations due to the photolithography process. (b) Corresponding KPFM surface potential map. The surface potential is increasing with increasing layer thickness. (c) Surface potential histogram of the orange box marked in (b). Image adapted from [OO.13].

respectively. The measured height for BLM is 0.92 nm +/- 0.10 nm, which is slightly higher than the interlayer spacing of a bulk MoS_2 crystal [324]. For FLM we get two different heights, one is 2.96 nm ($\sim$ 5 layers) and 7.89 nm ($\sim$ 12-13 layers). In the work function map in (b), three contrasts can be observed - SLM, BLM and FLM. As the work function for FLM=2.96 nm and the other FLM with 7.89 nm is not changing, it can be concluded that the screening length of MoS_2 is at least $\sim$ 2.96 nm, which is in good agreement with previous findings for annealed MoS_2 [311].

Li et al. compared the screening length of pristine MoS_2 flakes on SiO_2 with annealed MoS_2 flakes and found a decrease from approximately 5 nm down to 2.5 nm for annealed MoS_2. Measurements here yield a screening length between 1.6 nm and 2.96 nm, which is much lower than the value for pristine MoS_2. Therefore it can be said that the investigated MoS_2 is not affected by ambient adsorbates. In fig. 4.14 (c) line profile analysis is employed

to quantify the work function of SLM and BLM. The work function of SLM is determined to be the same as using the histogram analysis in fig. 4.13 with Φ_{SLM}=4.49±0.03 eV. The work function of BLM is increased with respect to SLM by about 0.05 eV to Φ_{BLM}=4.54±0.03 eV. Again, contaminations on BLM appear to decrease the work function as can be seen in fig. 4.14 (b).

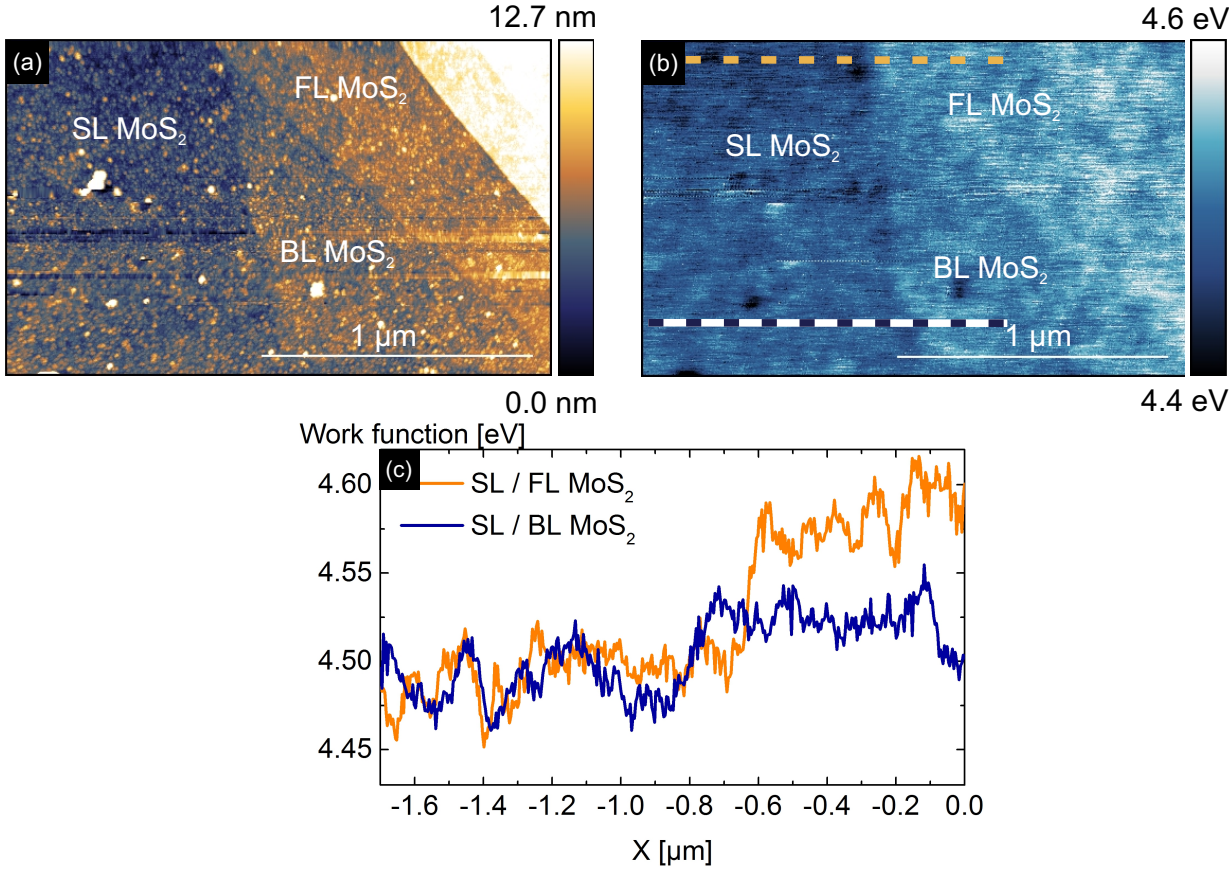

Figure 4.14: Screening length of MoS_2 on SiO_2. (a) NC-AFM topography of an area consisting of single, bilayer and few layer MoS_2. (b) The corresponding work function map to the topography. (c) Line profile measurements of the dashed lines marked in (b). Image adapted from [OO.13].

4.5.4 Substrate effects on the work function of single layer MoS_2

To study the effect of the substrate on the work function of SLM, the work function of SLM on SiO_2 with SLM in the RIE SiO_2 holes are compared in fig. 4.15. The work function map in fig. 4.15 (b) shows an increased work function over the etched hole of about $\triangle$ Φ=0.04 eV. This shift is caused by the charge transfer from the etched substrate, which leads to an effective doping that has been proven to have a large impact on the optical properties of

SLM [325]. The etched SiO_2 substrate has an effect on the surface potential distribution as well. By comparing histogram data of SLM on SiO_2 and RIE SiO_2 (see inset in fig. 4.15 (c)), a decreased surface potential fluctuation by 0.02 eV for SLM on the etched SiO_2 is found. The potential fluctuation is related to charge impurities, which are detrimental for the performance of 2D devices, and KPFM is an efficient way to probe it [326].

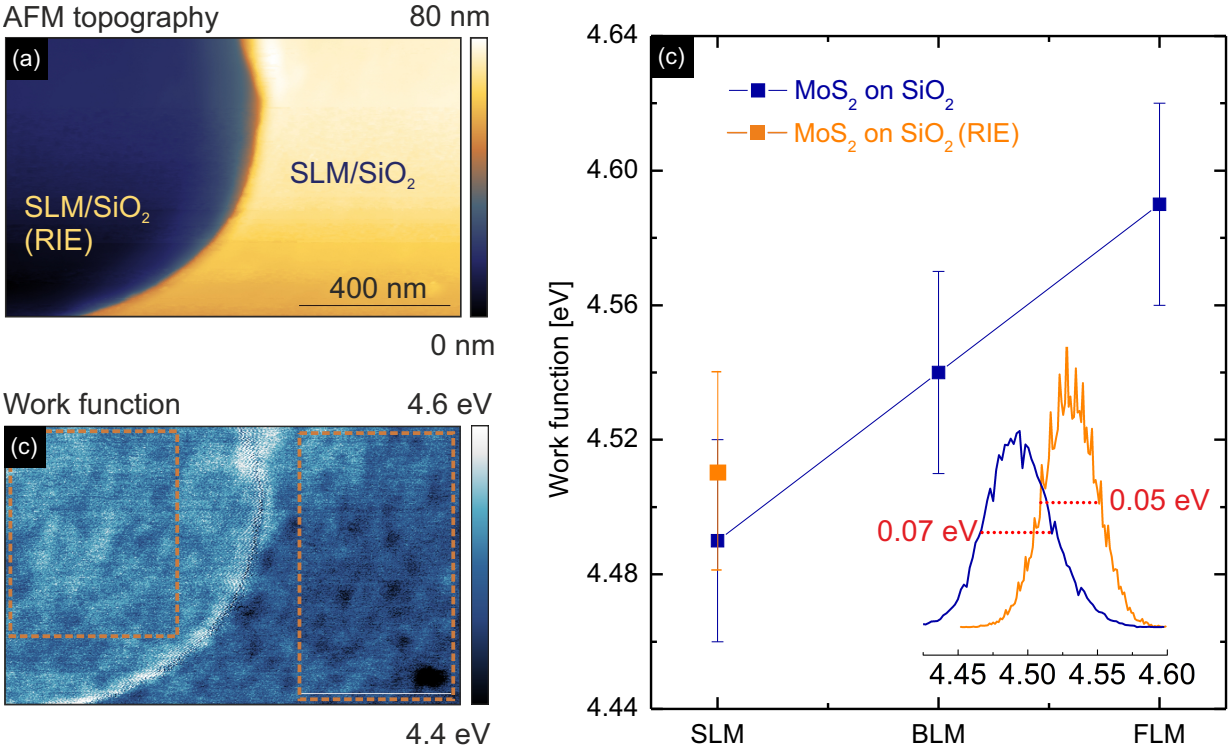

Figure 4.15: Substrate effects on the work function of SLM. (a) NC-AFM topography of a SLM flake partially over pristine SiO_2 and partially over RIE SiO_2. (b) Corresponding work function map shows an increase in the work function over the etched area. (c) Layer dependent work function of MoS_2. The inset shows the work function histogram evaluation of the areas marked in the orange, dashed boxes in (b). The FWHM of SLM on RIE SiO_2 is decreased by 0.02 eV. Image adapted from [OO.13].

Further, a less pronounced potential fluctuation indicates a higher charge homogeneity. Charge inhomogeneity has been shown to play a crucial role in the oxidative reactivity of graphene [302]. At the edge of the etched hole, where SLM is heavily bent and thus strained, a strong increase in the work function by another $\Delta\ \Phi$=0.05 eV compared to SLM on the RIE SiO_2 substrate caused by stress can be observed. It has been shown by Castellanos-Gomez et al. that heavy strain in SLM has a large impact on the band gap of SLM [327]. However, KPFM only measures the contact potential difference (from which the work function is derived). For insulating materials there is no straightforward relation between the contact potential difference and the band-gap. Therefore, these results are not

directly comparable. The plot in fig. 4.15 (c) sums up the findings with respect to the work function of MoS_2. The work function of FLM in ambient has been determined previously by amplitude modulated KPFM. The reported values of Φ=5.25 eV [310] are significantly higher than the values found here. This difference is clearly due to the contaminations, which are absent in our measurements. Our data should instead be compared to the values determined by other non-locally resolved means like ultraviolet photoelectron spectroscopy [328, 329, 330, 209]. The excellent agreement again underlines the importance of UHV measurements, if intrinsic properties are to be probed.

4.5.5 Conclusion

In conclusion in situ Kelvin probe force microscopy measurements on single layers of MoS_2 on a SiO_2 substrate were performed in situ for the first time. Work functions for SLM Φ_{SLM}=4.49 eV, BLM Φ_{BLM}=4.54 eV and FLM Φ_{FLM}=4.59 eV have been experimentally determined. The observed screening length between 1.6 nm and 2.96 nm indicates a clean MoS_2 flake in this experiment. Furthermore, the effect of the substrate on the work function of MoS_2 was investigated by partly etching the SiO_2 substrate. Raman spectroscopy measurements suggest substrate effects like strain, which increase the work function of SLM of $\triangle$ Φ=0.04 eV on etched SiO_2. The next step would be to investigate completely free standing MoS_2 flakes without a substrate in order to probe the intrinsic charge homogeneity and work function of SLM.

5 Interaction of Swift Heavy Ions with 2D-Materials

Although graphene, MoS_2 and 2D-materials in general are highly interesting from a scientific point of view, many potential applications need further modification of these materials. In graphene for example, it has been shown that defect engineering [331, 332, 333, 334], changes in the morphology [335, 336] or chemical functionalization [337, 338, 339, 340, 341] can drastically alter its physical properties. In this chapter it will be elaborated in which way irradiation with swift heavy ions (SHI - ions with energies that are typically around the maximum energy loss) can be used to modify 2D-materials. The unique interaction of SHI with matter has been already applied in material research to e.g. create ion-tracks and nanostructures in materials, tracks on insulator surfaces or study the radiation hardness of electrical devices [342, 162][OO.08]. Still, looking at 2D-materials, the experimental and theoretical studies of the interaction with SHI are still sparse.

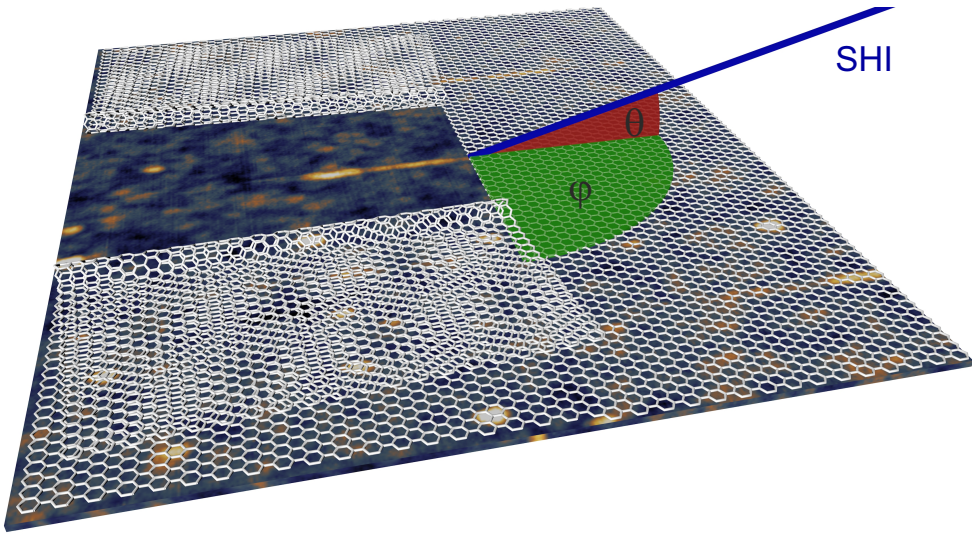

Figure 5.1: Scheme of SHI impact onto a graphene/SiO_2 surface. Depicted are the angle of incidence with respect to the surface (θ), and the azimuthal angle (ϕ), which defines the orinetation of the in beam with respect to one of the low-indexed directions of a graphene flake, i.e. an armchair or zigzag edge.

It has been shown for graphene that SHI irradiation under glancing incidence angle can cause foldings in this material [19]. Akcöltekin et al. proposed a two step model for the formation of foldings in graphene. In the first step the SHI irradiation causes an extended line of defects in form of a transition from hexagonal carbon rings to a defective graphene lattice like e.g. pentagonal and heptagonal. Subsequent to these defects, the hillocks, which are formed by the SHI interaction with the substrate surface, are pushing through graphene, which is then unzipped along the ion trajectory. This hypothesis will be further elaborated in the following, with a focus on two materials - graphene and single layers of MoS_2. In fig. 5.1 a SHI impact under glancing incidence angle onto a graphene/SiO_2 surface is sketched. Note that the two important angles in this study are marked in fig. 5.1; θ which denotes the angle of incidence of the ion with respect to the sample surface and ϕ for the angle between the incidence ion and a typical crystallographic edge in the 2D-crystal.

5.1 Foldings in Exfoliated 2D-Materials

In this section it will be compared in which way atomically thin materials respond to SHI irradiation under glancing incidence. For this single- and bilayers of graphene, MoS_2 and hexagonal BN have been exfoliated on 90 nm SiO_2 substrate in ambient (RH ∼40%). These materials were chosen in order to compare the behaviour of different material classes to SHI irradiation. Graphene is known to be a semi-metal with extraordinary charge carrier mobilities [10], single layer MoS_2 is a direct band gap semiconductor [99] and hBN is a dielectric [343]. As the main interaction of SHI with matter is the excitation of the electron system, these materials are chosen in order to study a possibe influence of the conductance of the SHI modifications.

The samples were irradiated at the IRRSUD beamline (GANIL, Caen - France) with 106 MeV U^{28+} and 91 MeV Xe^{26+} ions. The results of this experiment are shown in fig. 5.2. The first thing to note is, that all single layers exhibit foldings upon SHI irradiation. Although the length and shape of the foldings in single layers graphene/MoS_2/hBN cannot be directly compared with each other, as important parameters like ion energy and angle of incidence are not identical, the comparison between irradiated single and bilayers on the respective material reveal differences. In single layer graphene (fig. 5.2 (a)) every incident ion causes one folding with a typical length of 149 ± 24 nm while bilayers only fold in about 50% of the cases with a decreased length of 84 ± 22 nm. In the bilayer graphene areas, where a SHI did not create a folding, a surface track created in the SiO_2 under graphene can be observed. In hBN (fig. 5.2 (b)) single layers as well as bilayers fold with an efficiency of 1 upon SHI impact. The length of foldings in SL hBN is with 163 ± 51 nm almost the same as in bilayer hBN with 149 ± 23 nm. In contrast to graphene and hBN, foldings in MoS_2 do not come alone but are accompagnied by nanoscale rifts with a typical width of below 10 nm. Furthermore, no foldings are observed in bilayer MoS_2, only rifts are introduced.

[0]Parts of this section have been published in Ochedowski *et al., Nuclear Instruments and Methods B accepted (2014)*

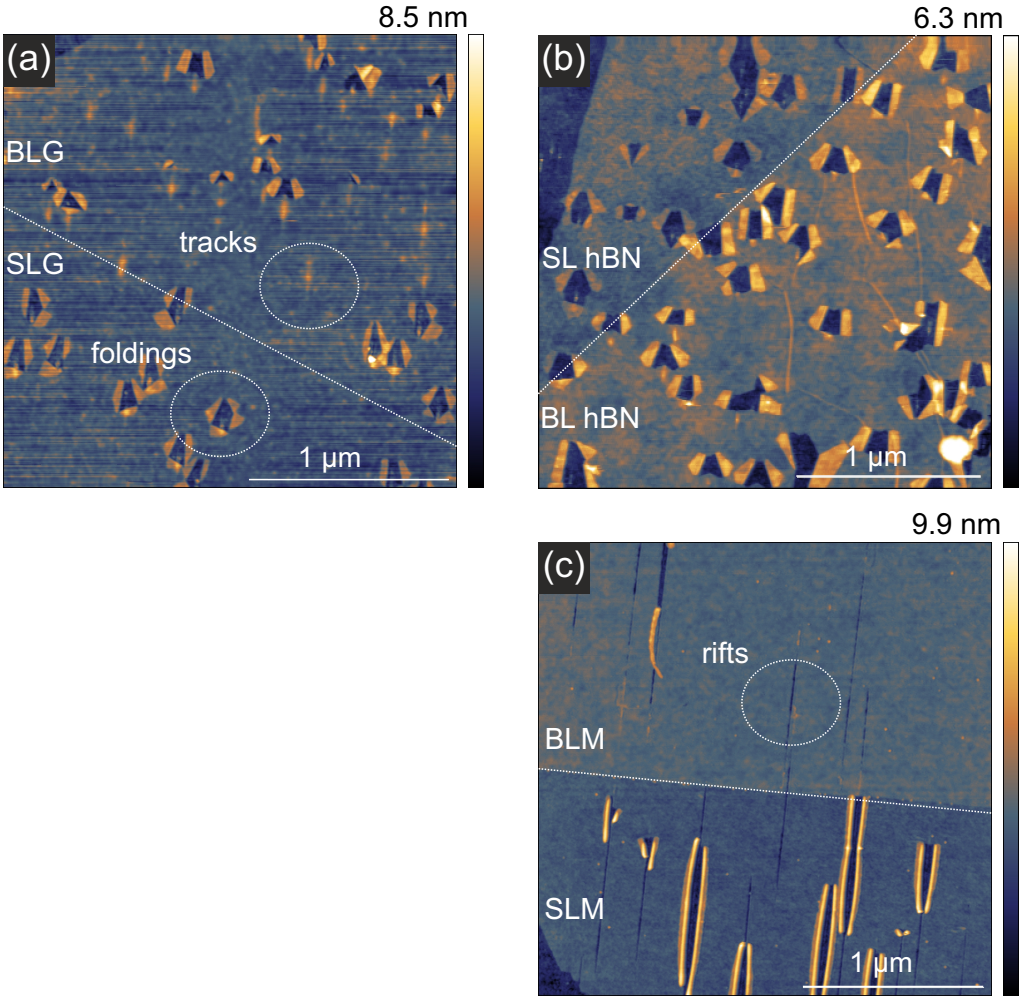

Figure 5.2: SHI irradiation of 2D-materials under glancing incidence angle. (a) SHI irradiation (θ=1.3°, 106 MeV U, 5 ions/μm^2) of graphene. Single layer fold upon every ion impact while in bilayer graphene about every second ion causes a folding. (b) SHI irradiation (θ=1.5°, 106 MeV U, 6 ions/μm^2) of hBN. Single and bilayers of hBN show foldings, one for every incident ion. (c) SHI irradiation ($\theta \leq 1°$, 91 MeV Xe, $\leq$6 ions/μm^2) of MoS_2. Single layers show a combination of nanoscale rifts and foldings while bilayer show no foldings at all. Image adapted from [OO.18]

Based on these experimental results, two important findings can be derived. First, while the foldings in graphene and hBN are similar, foldings in MoS_2 are accompagnied by rifts and no foldings can be observed in bilayer MoS_2. This suggests that an entirely different process might take place after SHI irradiation. Second, foldings in graphene become shorter and scarcer with increasing layer number while foldings in hBN bilayer still are created by each SHI impact and exhibit almost the same size. This finding suggests that the conductance of the material is indeed a parameter, which has to be considered in the folding

process. In a simple modell the energy in the excited electron system in graphene (semi-metal) can dissipate more quickly than in hBN (insulator), which results in a decreased direct damage in graphene by the SHI. In the following chapters the formation of foldings in graphene as well as rifts in MoS_2 will be investigated in more detail.

5.2 Foldings in Graphene

Folding is an every-day technique, which is often used to modify material properties such as mechanical strength. In the case of 2D-materials folding has attracted quite a lot of attention, as it might offer the chance to additionally tune electronic properties [344]. For example, it has been shown that graphene folds locally strenghten the material [345], and at the point where graphene is bend a closed bilayer edge (CBE) is formed. In these CBE the covalent bonds are bent, which changes the local chemical reactivity and transport properties [346]. Because of this a strong magnetophotoelectric effect [347] as well as bandgap openings [348, 349] and enhanced spin-orbit interaction [350] are expected in graphene foldings. Furthermore, it has been shown that graphene origami boxes could serve as a container for hydrogen storage [351] for which then an electric field can be used to unfold graphene and release the hydrogen. Therefore methods for folding graphene in a controlled manner are in high demand.

In graphene, folding has so far been achieved by ultrasound sonification [352], the use of chemicals [353], by using the tip of an atomic force microscope [OO.09], femtosecond laser ablation [354] and swift heavy ion irradiation (SHI) [19]. While most of those methods create foldings in a more or less random way with respect to size and orientation of the folding, only the latter offers the advantage of a great degree of control. This however is a prerequisite to prepare specific graphene nanostructures by folding. Therefore, understanding the mechanism of folding by SHI irradiation to achieve perfect control of this technique is crucial.

In this section, the ion induced folding process of exfoliated graphene is analyzed in detail. The heterosystem is divided in three parts - graphene, interfacial layer, substrate - and it will be shown in the following that each part plays a significant role for the folding. By designing specific experiments focusing on one part at a time and excluding the influence of the others as far as possible, it is possible to disentangle their respective contributions. The results show that by tuning the system components accordingly, folding of graphene by SHI can be reliably controlled. These findings represent an important step for the establishment of SHI irradiation as a tool for the production of well-defined graphene nanostructures, which can most likely be applied for other nanostructuring 2D-materials as well.

5.2.1 Angle dependence of foldings in graphene

The first and most important prerequisite for a folding formation in graphene is using a grazing incidence irradiation setup. Altough irradiation under perpendicular incidence can be used to induce defects as has been shown for singly charged ions [257], highly charged ions

[355] and swift heavy ions [OO.08], no foldings are introduced with perpendicular incidence angle. So the question arises which incidence angle is needed for folding formation. In order to study this a set of SiO_2 supported graphene samples have been irradiated with a 106 MeV U beam and a constant fluence of $5{\cdot}10^4$ ions/μm^2 and varying incidence angles.

The result of this experiment is shown in fig. 5.3. For the 90° irradiation in fig. 5.3 (a) no distinct ion modifications can be observed using AFM and the surface roughness measured on the graphene sheet with 0.65 nm RMS is about the same as for pristine graphene. For the 60° irradiation (fig. 5.3 (b)) modificiations in graphene in form of nanoscale holes with diameters of under 10 nm can be detected. The zoom-in reveals even smaller holes in the graphene sheet with a diameter below 5 nm. However, because of tip convolution effects the actual size of the holes cannot be specified without further knowledge of the conditions of the AFM tip during the measurement [356, 357]. The fact that the amount of holes does not correspond well with the ion fluence (factor 10 discrepancy) can be attributed to the AFM measurement setup as well. If the created holes are in the range of 1 or 2 nm, the relatively large surface roughness of 0.77 nm RMS will make it impossible to detect these features with an AFM tip of at least 10 nm in diameter.

Starting at 45° (fig. 5.3 (c)) foldings can be observed in the AFM topography. The length of the foldings varies between 5 nm and 30 nm. Most likely these larger foldings are created by multiple SHI impacts as the ion fluence far exceeds the number of foldings in the graphene sheet. The high ion fluence in the irradiation experiments with 30° and 15° yields graphene with a very high surface roughness of 2.03 nm RMS and 2.87 nm RMS respectively. This results in a nanoporous graphene sheet and amorphous carbon, which is shown in fig. 5.3 (d+e). All these samples have been measured with Raman spectroscopy as well (see fig. 5.3 (f)). With decreasing incidence angle and constant fluence the amount of disorder (which corresponds to the I_D/I_G peak intensity ratio) is continously increasing. For the 15° irradiation the amount of disorder is so high that the I_D/I_G is decreasing again (which is an indication of amorphization) and the characteristic 2D mode for graphene is hardly detectable anymore.

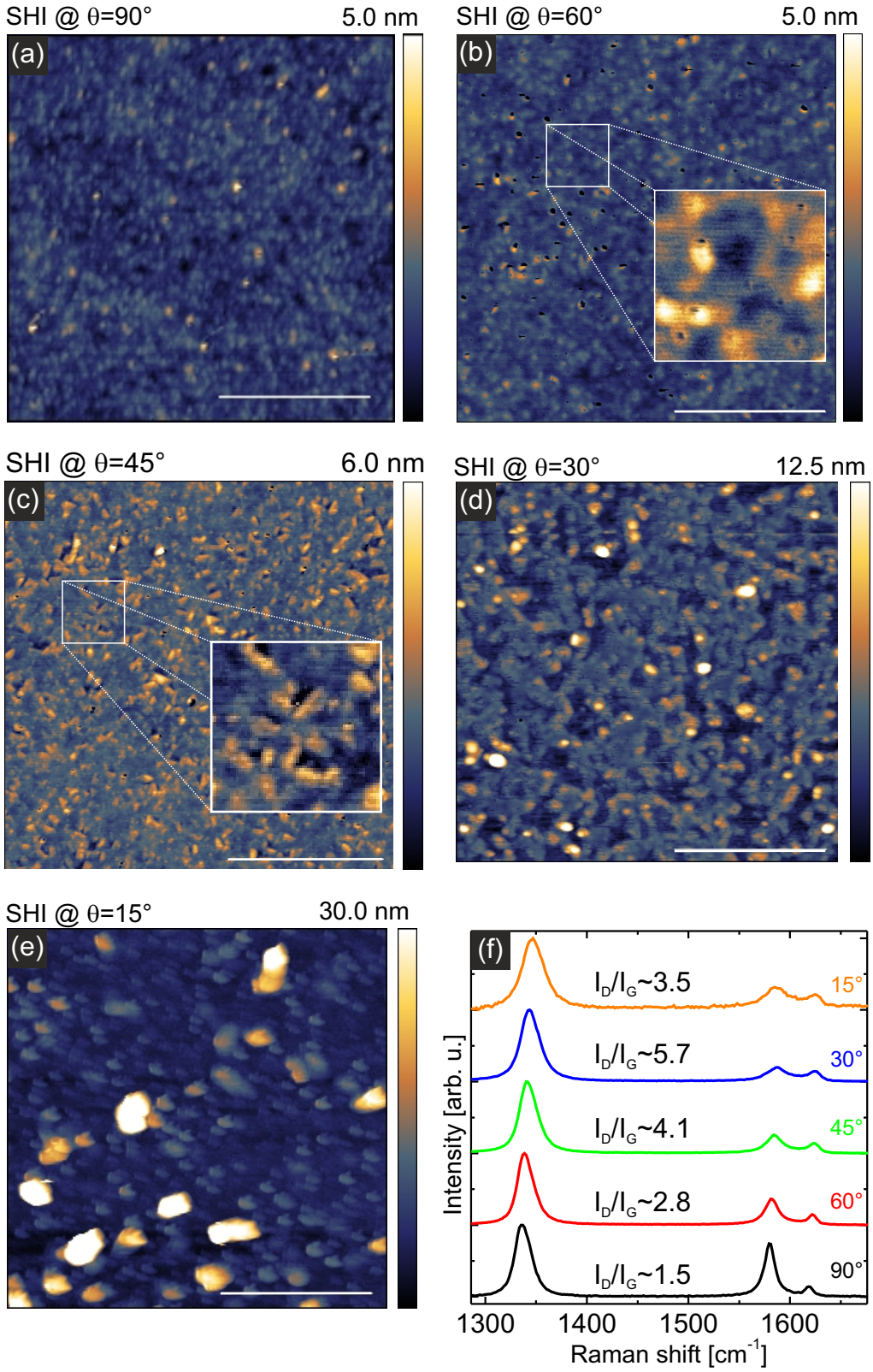

Figure 5.3: Angle dependent threshold for folding formation. Graphene on SiO_2 irradiated with $5{\cdot}10^4$ ions/μm^2 with 106 MeV U. The scale bar in all images is 400 nm. Different incidence angles θ are applied (a) θ=90° (b) θ=60° (c) θ=45° (d) θ=30° (e) θ=15°. Foldings can be observed starting at θ=45°, for smaller θ the fluence is too high to identify single foldings. (f) Raman spectra taken on the graphene flakes shown in (a-e) display the increasing defect formation.

These Raman measurements already suggest that with decreasing incidence angle, the size of the modifications is getting bigger. To study single ion impacts in graphene on SiO_2, additional samples were irradiated with a much lower fluence of ≤ 15 ions/μm^2. In fig. 5.4 (a-c) three AFM images are shown in which graphene has been irradiated under θ=5.9°, θ=2.8° and θ=0.1°. For all three graphene flakes foldings can be observed, the length of the foldings varies drastically however. For θ=5.9° the length of the foldings is 46 ± 7 nm. This value increases to 91 ± 16 nm for θ=2.8° and can be as high as 996 ± 691 nm for ultragrazing incidence angles like θ=0.1°. It has to be mentioned that these experiments have been performed using different SHI projectiles. The influence of the ion is discussed later and is of only minor impact on the findings here.

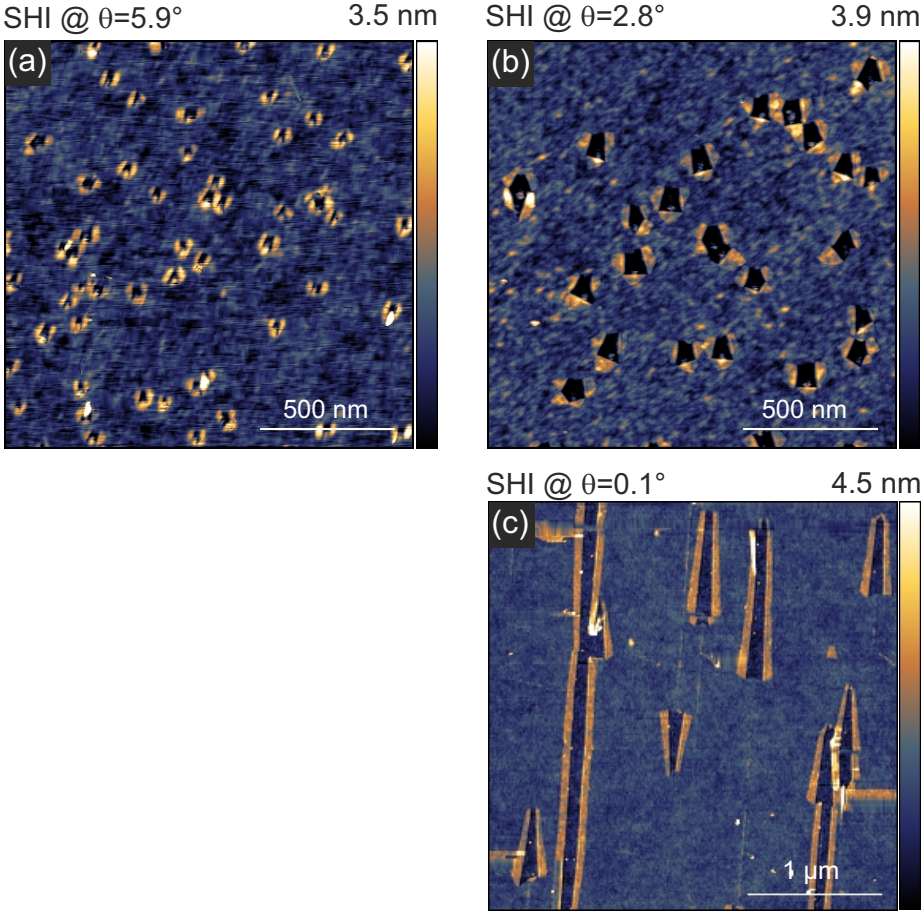

Figure 5.4: Evolution of folding length with respect to θ. (a) Graphene foldings on SiO_2 with an average length of 46 nm (106 MeV U, θ=5.9°) (b) Graphene foldings on SiO_2 with an average length of 91 nm (106 MeV U, θ=2.8°) (c) Graphene foldings on SiO_2 with an average length of 996 nm (91 MeV Xe, θ=0.1°)

In summary, the irradiation of graphene under different incidence angles leads to different kinds of modifications. While 90° irradiation results in defects only observable with Raman

spectroscopy, the irradiation at 60° leads to the creation of nano sized pores. Foldings are created starting from 45° onwards and increase in size from below 10 nm to ≈1μm. This makes the incidence angle of the ion an important parameter for adjusting the length of the folded area as well as the closed bilayer edge structure.

5.2.2 Influence of the Substrate

In the previous chapter the influence of the supporting substrate on properties of graphene like work function, doping and behaviour towards heat treatment has been discussed in detail. The question arises whether the substrate is contributing to the folding formation as well. For this study graphene was irradiated on different substrates, which were chosen because of their response towards SHI irradiation under grazing incidence angle. While SiO_2 is just showing a small chain of amorphous hillocks, which are up to 1.5 nm in height, $SrTiO_3$ shows a chain of distinct nanosize hillocks (up to 7 nm in height) [162, 358] and PMMA shows very prominent SHI induced modifications up to 6 nm high [160]. In contrast to this, suspended graphene without any substrate at all is investigated as well as graphene on SiC, a material which is supposed to show no modifications in case of low fluence SHI irradiation [359].

Suspended graphene can be most easily prepared by exfoliating a graphene flake on a prepatterned SiO_2 substrate. The sample has been patterned with 3 μm (diameter) holes that are 8 μm in depth by photolithography and consecutive dry etching. A typical flake on a patterned substrate is shown in the optical image in fig. 5.5 (a). The red box marks the area where the AFM image in (b) has been taken, which is partly suspended graphene and partly SiO_2 supported graphene. The sample has been irradiated with 91 MeV Xe ions (θ=0.1°) and the resulting foldings on the SiO_2 substrate are in average 996 nm long (typical folding in fig. 5.5 (d)). At first glance no foldings or modifications at all can be observed in the suspended graphene sheet in (b). However, the zoom-in shows that nanoscale slit pores can be observed on suspended graphene. The length of these slit pores is about one tenth of the length of the foldings on the SiO_2 substrate. The Raman spectrum in fig. 5.5 shows a similar behaviour, the spectrum of irradiated suspended graphene resembles pristine graphene, while a distinct disorder induced D mode can be observed for SiO_2 supported graphene.

It takes quite an effort to image suspended graphene with AFM in tapping mode as the oscillating tip comes into contact with the graphene membrane, which is deformed due to the applied force. This results in a suboptimal topography image with only little information. To investigate the SHI modification with highest resolution, transmission electron microscopy (TEM) measurements were performed by Ossi Lehtinen from the Universität Ulm (work group Kaiser). For the TEM measurements, graphene has to be prepared on a special sample holder, a TEM grid. This has been done by a collaboration partner, Andrey Turchanin from the Universität Bielefeld (work group Gölzhäuser). Graphene is grown on a copper foil and transfered using PMMA on a lacey carbon film TEM grid (Quantifoil Micro Tools GmbH - Germany, Grosslöbich), which is shown in the optical image in fig. 5.6 (a).

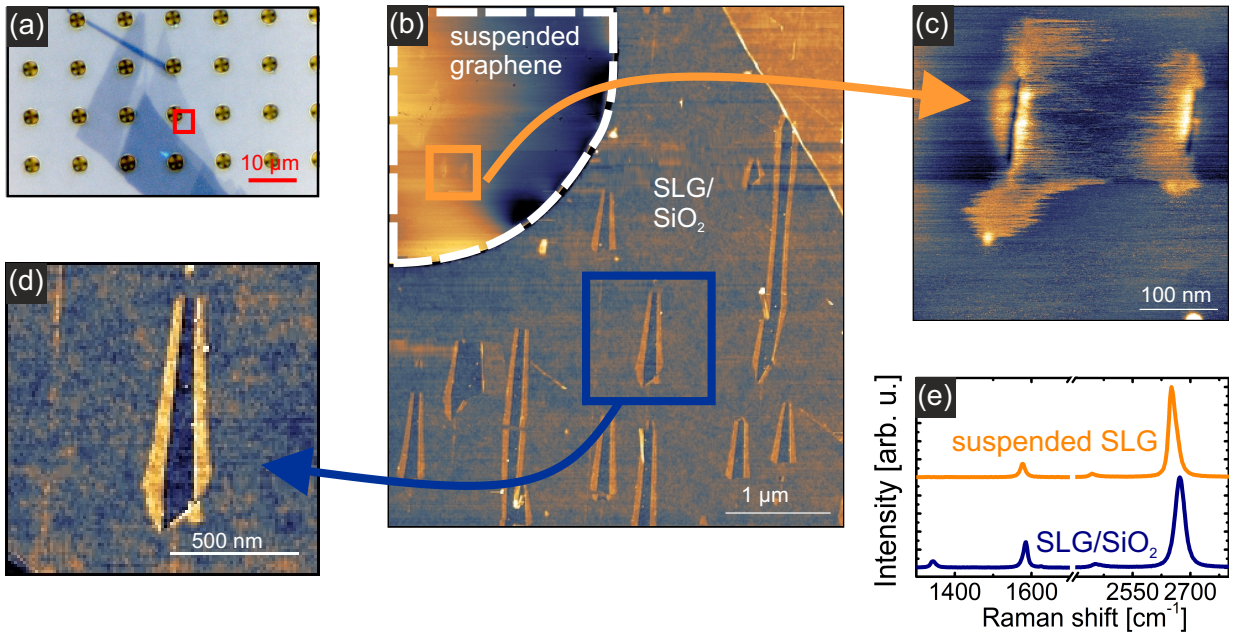

Figure 5.5: Comparison between substrate supported and suspended graphene. (a) Optical image of graphene exfoliated on a patterned SiO_2 substrate. (b) AFM topography of the irradiated graphene flake (91 MeV Xe, θ=0.1°) marked with the red box in the optical image. (c) Nanoscale rifts in the suspended graphene sheet. The length is about one tenth of the length on the substrate. (d) Zoom-in on a typical folding. (e) Raman spectra taken on the suspended graphene sheet and on the supported graphene sheet. A distinct D-band at 1350 cm^{-1} can only be observed on the SiO_2 supported graphene.

The suspended graphene sheets are located on top of the holes with a diameter of 2-3 μm, which is sufficiently large for the TEM measurement. The glancing indidence irradiation does not just affect the graphene sheet but the lacey carbon film as well, as can be seen in fig. 5.6 (b+c), where the lacey carbon film is shown before and after the irradiation with 91 MeV Xe ions. Additionally Raman spectroscopy is performed on the suspended graphene sheet (see fig. 5.6 (d)) to check whether the irradiation of graphene has been successful.

To compare the AFM and TEM measurements, both images are shown with the same scale bar in fig. 5.6 (e+f). Most notably, the slit pores, which appeared in the AFM images, can be clearly identified as foldings in the TEM measurement. The foldings are sligthly smaller, which can be attributed to a higher incidence angle. Thus, because of convolution effects due to the tip size the nanosized foldings in suspended graphene are measured as slitpores with the AFM. A zoom-in of a folding marked in the orange box in (f) is shown in fig. 5.6 (g). The folded areas are colored in a transparent orange, which shows that no substantial number of carbon atoms is missing: folding back the orange areas will close the nanopore. Furthermore, a lot of contaminations can be seen on the graphene flake which are due to the transfer process and adsorbates/hydrocarbons from air [360].

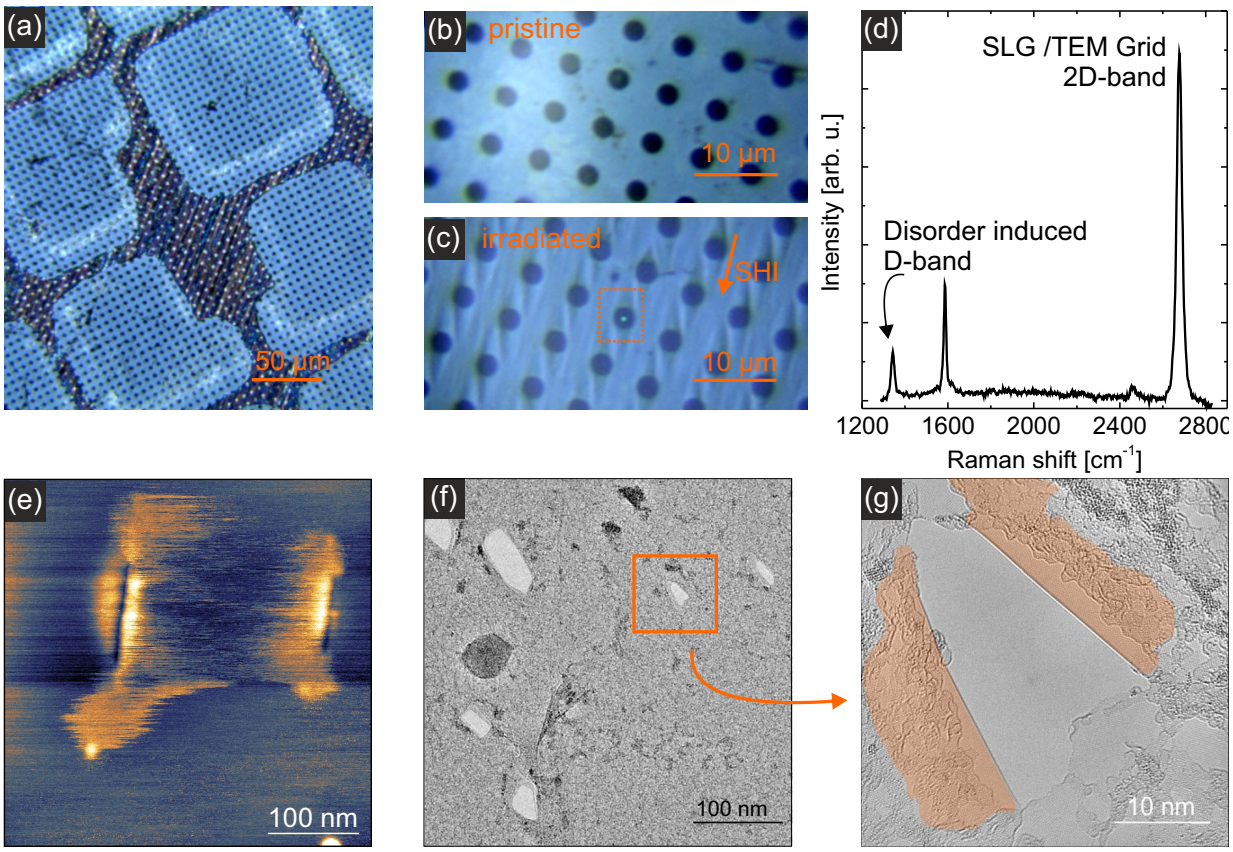

Figure 5.6: SHI modifications in suspended graphene. (a) Optical image of a TEM grid onto which CVD graphene has been transferred. (b) Zoom-in before irradiation (c) Zoom-in after irradiation (d) Raman spectra taken in the orange box in (c) showing defect formation in suspended graphene after SHI irradiation. (e) AFM topography of SHI modifications on suspended graphene (f) TEM measurement of suspended graphene (g) Zoom-in TEM measurement reveals that nanoscale rifts seen in the AFM image are in fact foldings.

Another comparison of suspended graphene with substrate supported graphene is shown in fig. 5.7. Here, the incidence angle has been kept almost constant at θ=1.3°, just the PMMA irradiation incidence angle was slightly off with θ=1.8°. The foldings in suspended graphene are as expected shorter than on any substrate with 24 nm. Graphene on SiO_2 shows foldings with 150 nm lenth in average, which is about 5 times the value of suspended graphene. While SiO_2 shows surface tracks after SHI irradiation, SiC just shows very shallow depressions, which will be discussed in detail in the next chapter. However, the foldings in graphene on SiC are 136 nm in length, which is almost the same length as graphene on SiO_2. For PMMA however, the foldings are expected to be smaller as the incidence angle is higher. But with an average length of 372 nm, the foldings are more than twice as long as foldings on SiO_2, which can be attributed to the large surface track

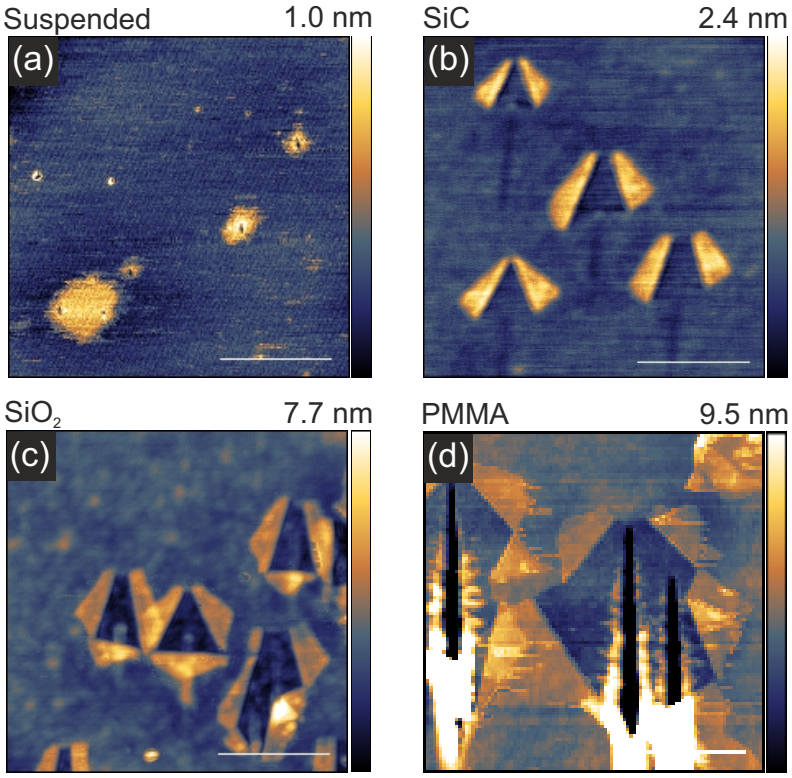

Figure 5.7: Substrate regulated folding length. (a) Foldings in suspended graphene (106 MeV U, θ=1.3°). (b) Foldings in SiC supported graphene (106 MeV U, θ=1.3°). (c) Foldings in SiO_2 supported graphene (106 MeV U, θ=1.3°). (d) Foldings in PMMA supported graphene (106 MeV U, θ=1.8°). All scale bars are 400 nm in length.

created in the PMMA substrate.

A more convenient way to compare the folding length on various substrates is by fitting the angle dependent data on each substrate and suspended graphene with a relation: $L=d/\tan(\theta)$ in which L denotes the folding length and θ the incidence angle with respect to the sample surface. The fitting parameter d denotes the depth of the SHI (measured perpendicular to the surface) at the point where the SHI induced folding at the surface is ending. The same geometrical relation has successfully been applied to describe the surface tracks in dielectrics [358]. A higher d value corresponds to longer surface tracks or graphene foldings and vice versa. In fig. 5.8 data for SiO_2 and PMMA supported graphene as well as suspended graphene has been fitted, finding d values of 0.22 nm for suspended graphene, 4.22 nm for SiO_2 supported graphene and 9.13 nm for PMMA supported graphene. The d value for suspended graphene 0.22 nm is very close to the interlayer spacing of graphite 0.335 nm [259], which is generally considered as the height of graphene. This indicates that the SHI is indeed creating direct damage in the graphene sheet and that e.g. sputtering by substrate atoms is not required.

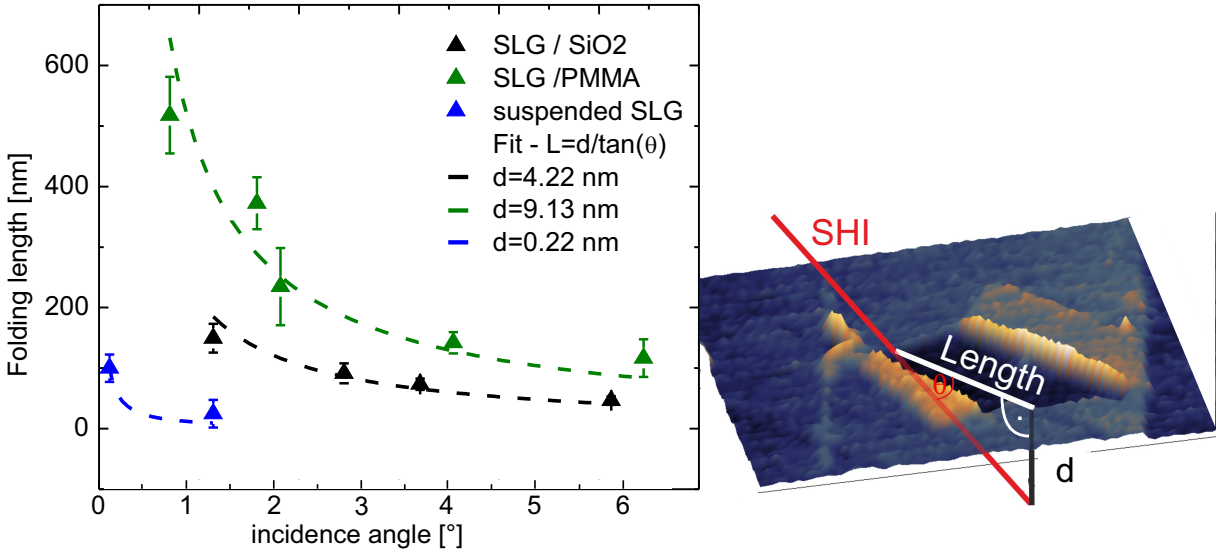

Figure 5.8: Left: Angle dependent folding length in graphene on various substrates (106 MeV U for all samples). Right: Scheme of the $L{=}d/\tan(\theta)$ relation.

In conclusion, foldings in graphene by SHI can be introduced in supported graphene on virtually any substrate and in particular in materials like SiC with almost no distinct surface tracks as well as in PMMA with very prominent surface tracks. The size of the foldings can therefore be tuned in a wide regime by the choice of the substrate material. Suspended graphene exhibits very small foldings, which can be augmented by a factor of ≈20 if PMMA is chosen as the supporting substrate.

5.2.3 Role of the Interfacial Layer

It has been shown in the previous chapter that the interfacial water layer, which is present in between graphene and its supporting substrate material after exfoliation in ambient conditions, is influencing the physical properties significantly. This can lead to e.g. blocking of charge transfer from the substrate to graphene [361, 271], or reduction of the adhesion forces between graphene and the substrate [362]. Since the SHI is penetrating this interfacial layer as well along its trajectory, the interfacial layer has to be considered in the folding process.

In order to study the role of the interfacial layer, graphene on SiO_2 was irradiated in its pristine condition and after heat treatment in a vacuum chamber (base pressure $p{=}10^{-6}$ mbar, 400° C, two hours). This experiment was performed using 23 MeV I (which is sufficient to induce foldings) ions and the results are shown in fig. 5.9. In (a) foldings in the irradiated pristine sample can be observed. For the heat treated sample, no foldings but tracks along the ion trajectory are created upon SHI impact. This presents clear evidence that the interfacial layer is a prerequisite for the folding formation in this system. To

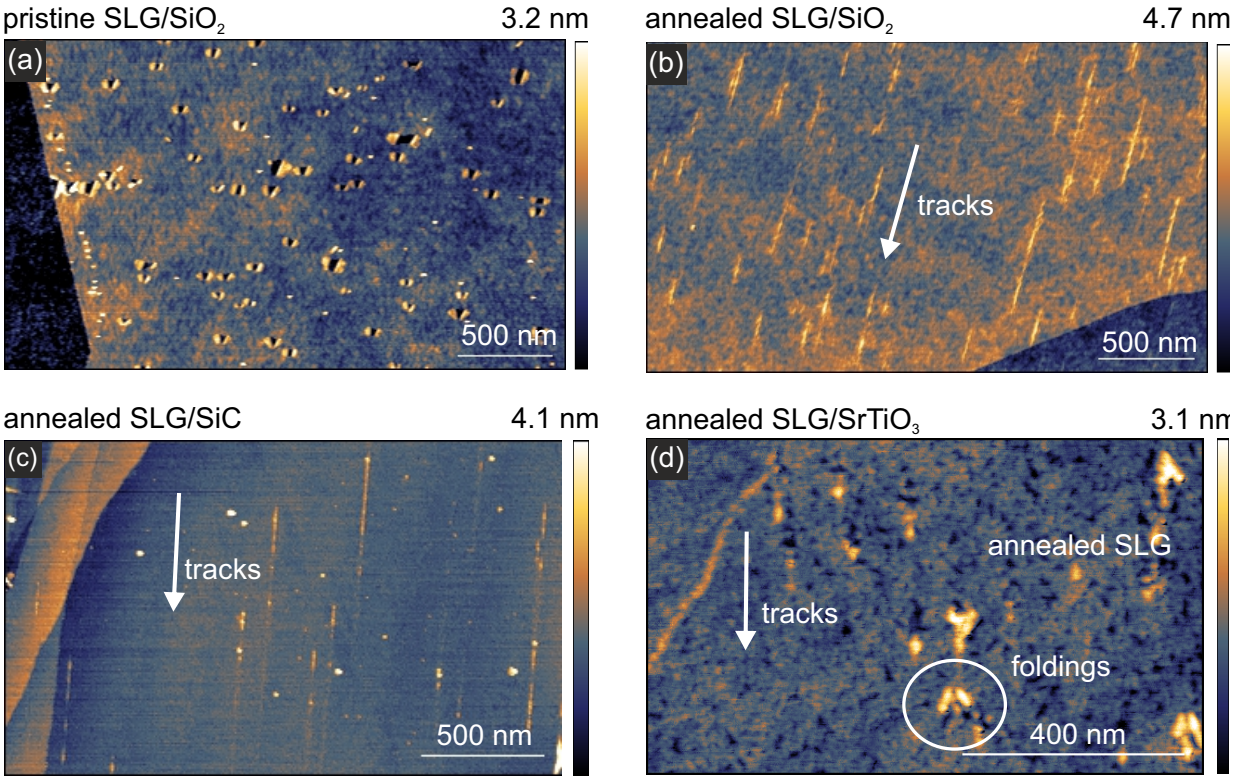

Figure 5.9: Water driven folding formation. (a) Pristine graphene on SiO_2 irradiated with 23 MeV I (b) Vacuum annealed graphene on SiO_2 irradiated with 23 MeV I (c) Vaccum annealed graphene on SiC irradiated with 91 MeV Xe (d) Vacuum annealed graphene on $SrTiO_3$ irradiated with 800 MeV Xe

further investigate whether this finding is true in general or just the case for graphene on SiO_2, similar experiments have been performed on other substrate materials.

One of the chosen substrate materials is SiC(0001), which is known to be very resistant to ion irradiation [359]. In the next chapter of this thesis it will be shown that SHI can be used to modify the surface of SiC, but only on the atomic scale. No surface tracks in form of amourphous chains of hillocks (SiO_2) or periodic chains of hillocks ($SrTiO_3$) are created upon SHI irradiation under glancing incidence angle. Here, only the topmost Si layer sublimates leaving a graphitic surface groove in SiC behind [363]. A graphene on SiC sample was heated in UHV (base pressure p=10^{-9} mbar) for 2 hours to 400 °C. The sample was stored under ambient conditions for several days, before the irradiation took place using a 91 MeV Xe beam. After the irradiation, AFM measurements (fig. 5.9 (c)) show that tracks in graphene comparable to those observed on SiO_2 are created and no foldings are observed.

In contrast to SiO_2 and SiC, SHI irradiation of $SrTiO_3$ results in a very noticeable modifictaion of the surface: a chain of periodic hillocks is created, which can be up to 4 nm high. Additionally, previous measurements of graphene foldings have been performed on

$SrTiO_3$, suggesting that the nanosized hillocks play a major role for the folding formation by pushing through the already weakened graphene sheet [19]. The sample investigated here was heated in situ at the M branch at the GSI (base pressure p=10^{-9} mbar, 600° C, two hours) and directly transferred to the irradiation chamber without exposing the sample to ambient. The sample was irradiated with a 800 MeV Xe beam and the resulting modifications in graphene are shown in fig 5.9 (d). Although about 60% of the SHI impacts result in tracks, the rest is causing foldings in graphene to appear. Note that the incidence angle at the M branch cannot be precisely controlled, which is the reason that the foldings in (d) are very small ($\theta \approx 8°$).

With this it can be said that an interfacial layer contributes significantly to the folding formation in supported graphene by SHI. Without this interfacial layer, no foldings can be created on a SiO_2 and SiC(0001) substrate, since the modification by the SHI in the substrate surface itself is marginal. For substrate materials, where the surface track is very pronounced as for example in $SrTiO_3$, foldings can be introduced even without the interfacial layer. However, the efficiency of folding formation (folding per SHI impact) decreases below one (efficiency of one is typical for single layer graphene) to $\approx$ 0.4 on $SrTiO_3$.

5.2.4 Direct Damage to the Graphene Sheet

After investigating the influence of the substrate material and the interfacial layer in detail, now a possible direct interaction of the SHI with the graphene lattice will be discussed. In order to study this, graphene on SiO_2 samples are irradiated with SHI of different energies and stopping powers. Shown in fig. 5.10 is a graphene sample irradiated with 84 MeV Ta ions (a) and a graphene sample irradiated with 23 MeV I ions (b), both under the same incidence angle of θ=$1.8 \pm 0.2°$. In order to quantitatively compare the SHI projectiles, the respective electronic stopping powers in graphite (energy loss calculated by SRIM [122]) are summarized in fig. 5.10 (c). Comparing the AFM measurements in fig. 5.10 it can be clearly seen that the size of foldings in graphene is dependent on the ion energy. While the foldings with 23 MeV I are just 57 $\pm$ 17 nm in length, folding graphene with 84 MeV Ta ions creates foldings as large as 128 $\pm$ 38 nm. Note, that great care has been taken in determing the accurate incidence angle in this experiment so the large deviation between these two samples cannot be contributed to the incidence angle θ. While the size of the foldings is clearly dependent on the SHI energy, the efficiency of the folding process is not. In both cases the adjusted fluence matches the number of foldings on the sample.

In fig. 5.11 (a-c) it is shown that for stopping powers of 4.5 keV/nm (15 MeV Si) and below, the efficiency of the folding process is close to zero. While for 4.5 keV/nm (15 MeV Si) in fig. 5.11 (a) single, small and one-sided foldings can be observed, yielding an efficiency of $\approx$0.02, this value further decreases for 3.3 keV/nm (6 MeV Si) to $\approx$0.01 (see (b)) and no foldings at all can be observed for the sample irradiated with (1.9 keV/nm) 3 MeV O (see (c)). Prior to irradiation the crystalline quality of the graphene flakes has been checked by Raman spectroscopy and no disorder induced D-peak was observed. However, for all three

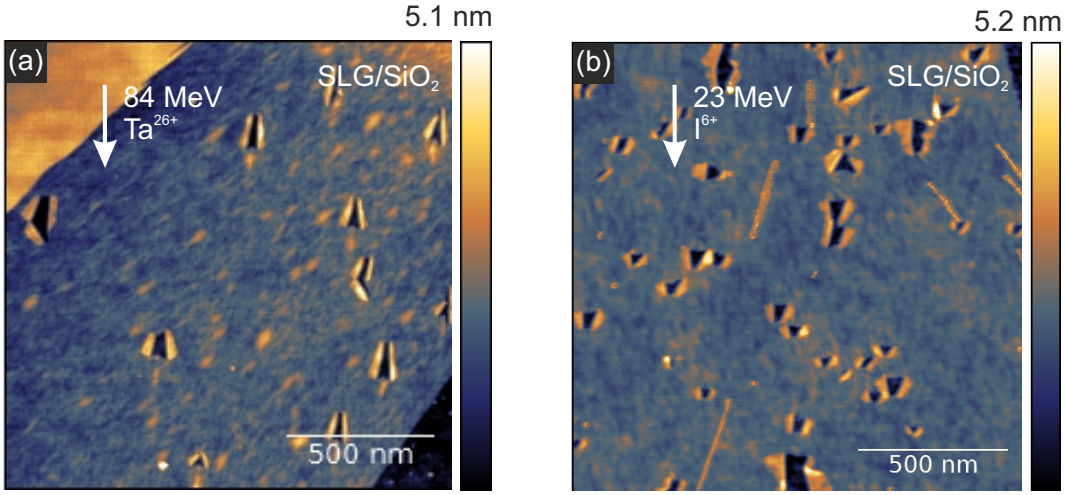

(c)

Swift heavy ion	S_e[keV/nm]	S_n[keV/nm]	Range [µm]
3 MeV O	1.92	0.01	2.5
6 MeV Si	3.28	0.02	3
15 MeV Si	4.30	0.01	5.29
23 MeV I	5.95	0.27	6.15
84 MeV Ta	13.99	0.23	11.09
91 MeV Xe	14.83	0.10	11.41
106 MeV U	16.10	0.36	11.79
800 MeV Xe	17.40	0.16	50.64

Figure 5.10: Energy dependent folding length. (a) AFM topography of SLG on SiO_2 irradiated with 84 MeV Ta, θ=1.8°. (b) SLG on SiO_2 irradiated with 23 MeV I, θ=1.8° resulting in shorter foldings. (c) Electronic and nuclear stopping powers in graphite calculated using the SRIM software package.

irradiated flakes in fig. 5.11 a D-Peak can be detected as shown in (d). This means that altough no foldings are created by ions of these stopping powers, defects in graphene are still created. Because either the size or the nature of these defects prevents an investigation by AFM in tapping mode, further studies are performed using Raman spectroscopy.

Raman spectroscopy is used as a powerful tool when it comes down to quantitatively analyze the amount and nature of defects in graphene. Pioneer work on this topic has been done by Lucchese et al. [257]. They used ion bombardment (90 eV Ar^+, θ=45°) to induce isolated defects with a radius of ∼1 nm, which was checked by corresponding STM measurements on HOPG. Theoretical studies predict about 1-2 sputtered carbon atoms per incidence ion [173, 364]. The average distance between defects L_D can be extracted from the ion fluence σ with $L_D = 1/\sqrt{\sigma}$. Lucchese et al. measured the ratio between the disorder induced D peak and the G peak depending on L_D. While the D peak is sensitive to the defects, the G peak is just related to the relative motion of sp^2 carbon atoms and

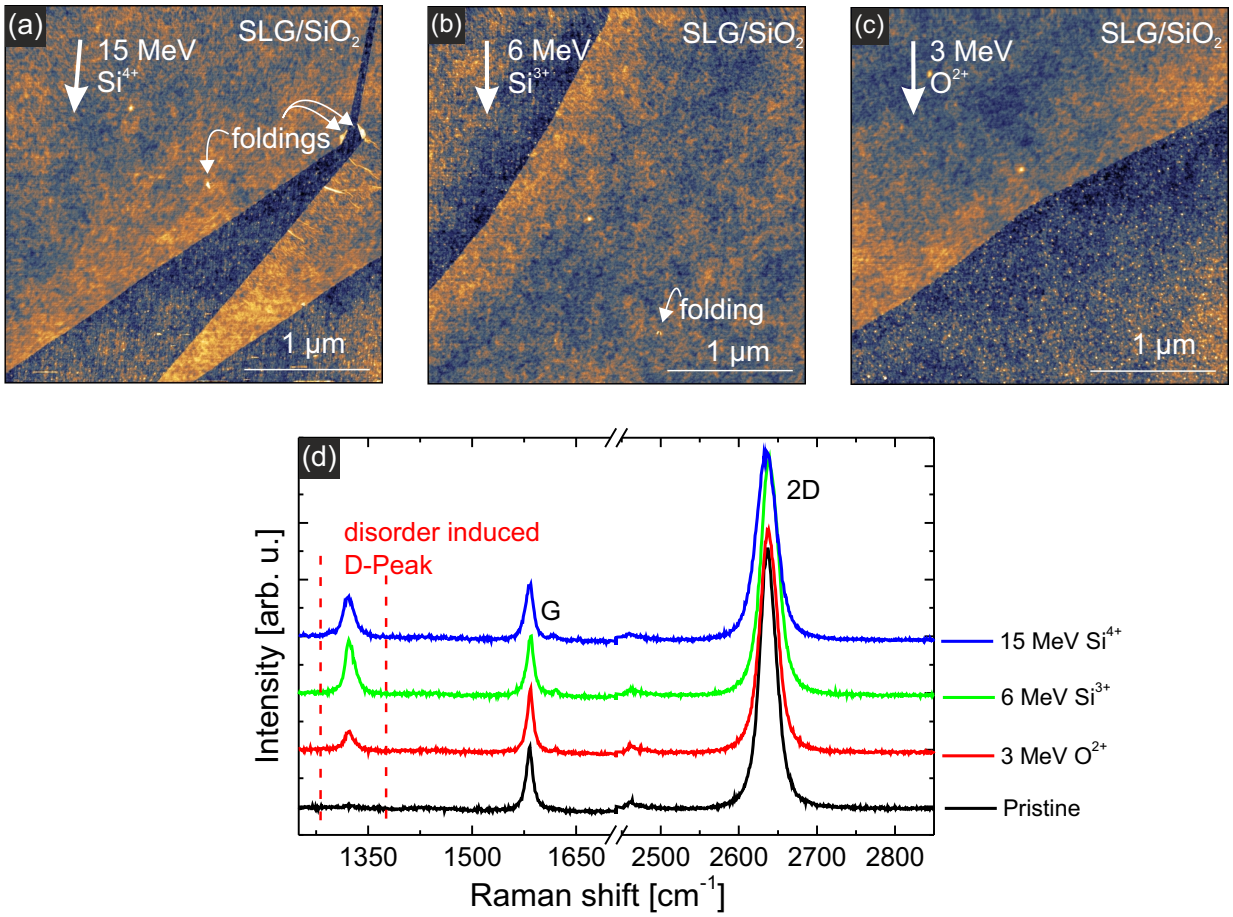

Figure 5.11: Threshold for folding formation. (a-c) Graphene on SiO_2 irradiated with 15 MeV Si, 6 MeV Si and 3 MeV O results in a folding efficiency of nearly 0. (d) Raman spectra taken on the graphene samples shown in (a-c) indicate that nevertheless the irradiation has introduced defects in the graphene lattice.

I_G is assumed to be constant [219]. They found that the I_D/I_G ratio is increasing until L_D reaches 3 nm and is decreasing rapidly towards 0 for lower L_D values. This can be explained by a model which is considering modifications on two length scales denoted as r_A and r_S (see inset fig. 5.12 (a)). The structurally-disordered region which is directly caused by the ion is described by r_S. Because of the total breakdown in the lattice structure itself, this amorphous region contributes less to the D band. In the activated region described by r_A, the lattice structure is preserved. The proximity to the structurally-disordered area causes a mixing of Bloch states near the K and K' valleys of the graphene Brillouin zone, enhancing the D band. The Raman scattering relaxation is given by $l = r_A - r_S$ and found to be 2 nm for the excitation wavelength λ=514 nm. For low defect densities (L_D<2r_A) the area contributing to the scattering process is proportional to I_D/I_G. Increasing the defect density further, the activated regions begin to overlap and the I_D/I_G ratio reaches

a maximum. After this, the graphene sheets starts to be completely covered with the so-called structurally disordered regions, which causes the I_D/I_G ratio to decrease.

Lucchese derived a relation for I_D/I_G which was further simplified by Cancado [219]. With the assumption that defects are the breakdown of the C-C-bonds he could show that in the large defect density regime the following relation holds:

$$\frac{I_D}{I_G} = C_A \frac{r_A^2 - r_S^2}{r_A^2 - 2r_S^2}\left[e^{-\pi r_S^2/L_D^2} - e^{-\pi(r_A^2 - r_S^2/L_D^2}\right] \tag{5.1}$$

C_A corresponds to the maximum possible I_D/I_G ratio within a completely activated sample without any breakdown of hexagonal carbon rings. C_A decreases with increasing laser energy and follows the empirical relation $C_A = AE_L^{-4}$ with A=(160±48) eV^4.

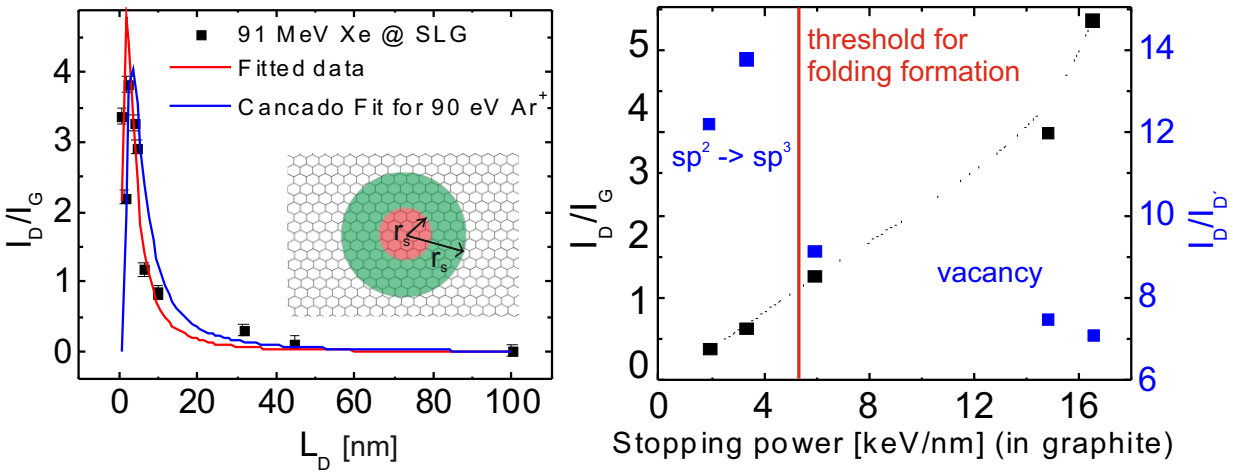

Figure 5.12: (a) Plot of the I_D/I_G peak intensity ratio against the average distance between defects L_D in suspended graphene. The sample has been irradiated with 91 MeV Xe ions and the red line shows the fit (according to formula 5.1) for the experimental data. The blue line depicts the fit found by Cancado et al. for graphene on SiO_2 irradiated with singly charged 90 eV Ar ions. (b) Plot of I_D/I_G and $I_D/I_{D'}$ peak intensity ratios for graphene on SiO_2 irradiated with different ion energies under a constant ion fluence of $5{\cdot}10^4$ ions/μm^2. The red line marks the threshold for the folding formation, the black dotted line is only to guide the eye.

In fig. 5.12 the results of (a) are shown. Graphene is exfoliated on a prepatterned SiO_2 substrate to obtain suspended graphene sheets and irradiated with 91 MeV Xe ions with varying fluences. The samples are investigated with μ-Raman spectroscopy (λ= 532 nm, P=0.4 mW) and the I_D/I_G ratio is plotted against L_D. The error bar is experimentally determined by performing Raman mappings and evaluating the I_D/I_G ratio distribution on more than 200 data points. This data is fitted with the Cancado relation 5.1 and the fitted curve is shown as a red line. The best fit is obtained with r_S=0.35 ± 0.11 nm and

r_A=2.11 ± 0.48 nm. This means that the structurally-disordered area r_S is significantly smaller than the 1 nm obtained with 90 eV Ar ions. Note, that additional defects may be induced in the graphene sheet which do not activate the D band. For example perfect zigzag edges [365, 366], charged impurities [367, 217, 368] and uniaxial and biaxial strain [369, 370] do not contribute to the D band and have to be detected by G and 2D peak shape. The relaxation length $l = r_A - r_S$=1.8 nm is assumed do be independent of the ion according values obtained in literature [257, 219].

The Raman evaluation clearly demonstrates that it is possible to induce direct damage to the graphene sheet even under perpendicular SHI irradiation. However this finding is still not sufficient to explain the threshold for folding formation with respect to the incidence ion energy. For this, graphene on SiO_2 has been irradiated with a constant fluence of $5{\cdot}10^4$ ion/μm^2 with varying ion energies. The plot in fig. 5.12 (b) shows a steady growth of the I_D/I_G ratio with increasing electronic stopping power. This is a clear indication that the electronic excitation is the driving force behind defect formation as the nuclear stopping is hardly varying between these projectiles. Foldings can be observed for stopping powers above the red solid line marked in fig. 5.12 (b). Besides the I_D/I_G ratio, which quantitatively describes the size of the defects, the $I_D/I_{D'}$ ratio can be used to investigate the nature of defects [291]. Eckmann et al. found a maximum for the $I_D/I_{D'}$ ratio (≅13) for defects due to sp^3 hybridisation. Lower $I_D/I_{D'}$ ratios were found for vacancy like defects (≅7) and boundary like defects (≅3.5). Notably the $I_D/I_{D'}$ ratio in fig. 5.12 on the right side of the red line (stopping powers which induce foldings) is between 7 and 9, which corresponds to vacancy like defects. On the left side of the red line (no modifications observed with AFM) an increase of the $I_D/I_{D'}$ ratio to 12-14 can be observed, which corresponds to sp^3 hybridisation. This means that not only the size of the structurally-disordered area but even the nature of defects can be controlled by the SHI energy. This can be explained by the breaking strength of graphene. In terms of stiffness and intrinsic strength, sp^3 defective graphene just shows a 14% lower breaking strength than pristine graphene while vacancy defects significantly lower the breaking strength [371]. This allows the conclusion that the pressure, which the heated interfacial layers and the surface track/sputtered ions apply to the graphene sheet, is not sufficient to fold pristine and sp^3 defective graphene sheets. Only graphene sheets with vacancy defects are adequately weakened to induce foldings. The fact that SHI below the threshold for folding formation still create extended defects is highly interesting for future studies. It has been found by theoretical calculations that modification in graphene lattices can be used to create graphene allotropes which can be exploited to e.g. locally open up a band gap of 1.2 eV [372].

To sum up the findings on the folding process for graphene, there are three conditions to be met to fold exfoliated, supported graphene. First, the SHI has to deposit sufficent energy (in terms of dE/dx) to induce vacancy like defects in the graphene sheet (S_e≥5.9 keV/nm). Second, the graphene flake has to be irradiated under a glancing incidence angle of $\theta \leq 45°$ and third, an interfacial layer of water has to be present in order to achieve an folding efficiency of 1. The size of the foldings can be controlled by three parameters. While the length of the folding is mainly determined by the incidence angle θ and the energy loss

S_e, the width and form of the folding depends on the choice of substrate.

5.3 Twisted Bilayer Graphene and Closed Bilayer Edges

Up to this point, only the size of the nanopores created in graphene by the foldings has been discussed while the folded areas and closed bilayer edges have been disregarded so far. Yet these two structures show very promising properties from a physical point of view. Twisted bilayer graphene for example has been predicted to have flat bands close to the Fermi energy [373], chiral tunneling [374] and large interlayer resistivity strongly dependent on temperature [286].

In fig. 5.13 (a) an AFM topography of a graphene flake irradiated with SHI under glancing incidence (91 MeV Xe, θ=0.8°) is shown. The folded areas in graphene show an average height of 1.1 ± 0.3 nm, which is significantly higher than the expected height of about 0.35 nm for bernal (or AB) stacked bilayer graphene and 0.38 nm for twisted bilayer graphene [375]. Note, that on rare occasions (marked with red and green boxes) the height of the folded bilayer graphene matches the 0.35 nm. In fig. 5.13 (b) a line profile of the white line marked in (a) is shown, where the left folded area exhibits the normal height of a bilayer graphene with 0.3 nm and on the right side, the folding is up to 1.5 nm in height. To further investigate this discrepancy, high resolution TEM imaging (in collaboration with Ossi Lehtinen, Universität Ulm) has been performed on suspended foldings as can be seen in fig. 5.13 (c). Colored in purple is the SLG area, the point where graphene is bent and the closed bilayer edge is formed is marked in red and the edge of the folding is marked with an orange line. Colored in orange are the folded areas that are free of contaminations. Here, the moirée structure can be observed which is due to a lattice mismatch between the first and second layer graphene of ∼5°. Areas on the folded bilayer in grey scale show significant contaminations that might contribute to its unusual height. Another explanation is provided by the observation of Cho et al. They observed that exfoliated graphene on a rough substrate like SiO_2 preserves its rough morphology even after folding it onto an atomically flat substrate like hBN [376]. This finding suggests that folded graphene on SiO_2 is not attaching itself smoothly on the first layer graphene but is rigidly bend and only loosely bound to the first layer.

This twisted bilayer graphene has been intensively studied using Raman spectroscopy finding new peaks like e.g. a new double resonance process at the R' band at 1625 cm^{-1} [375, 377, 336, 286]. Unfortunately, the folded areas created by SHI irradiation are too small to investigate them with Raman spectroscopy where the folded areas have to be at least 600 nm in diameter. Tip enhanced Raman spectroscopy might be able to provide enough lateral resolution for this experiment [378, 379], but the experimental setup using AFM tips is complicated and needs a lot of preparation.

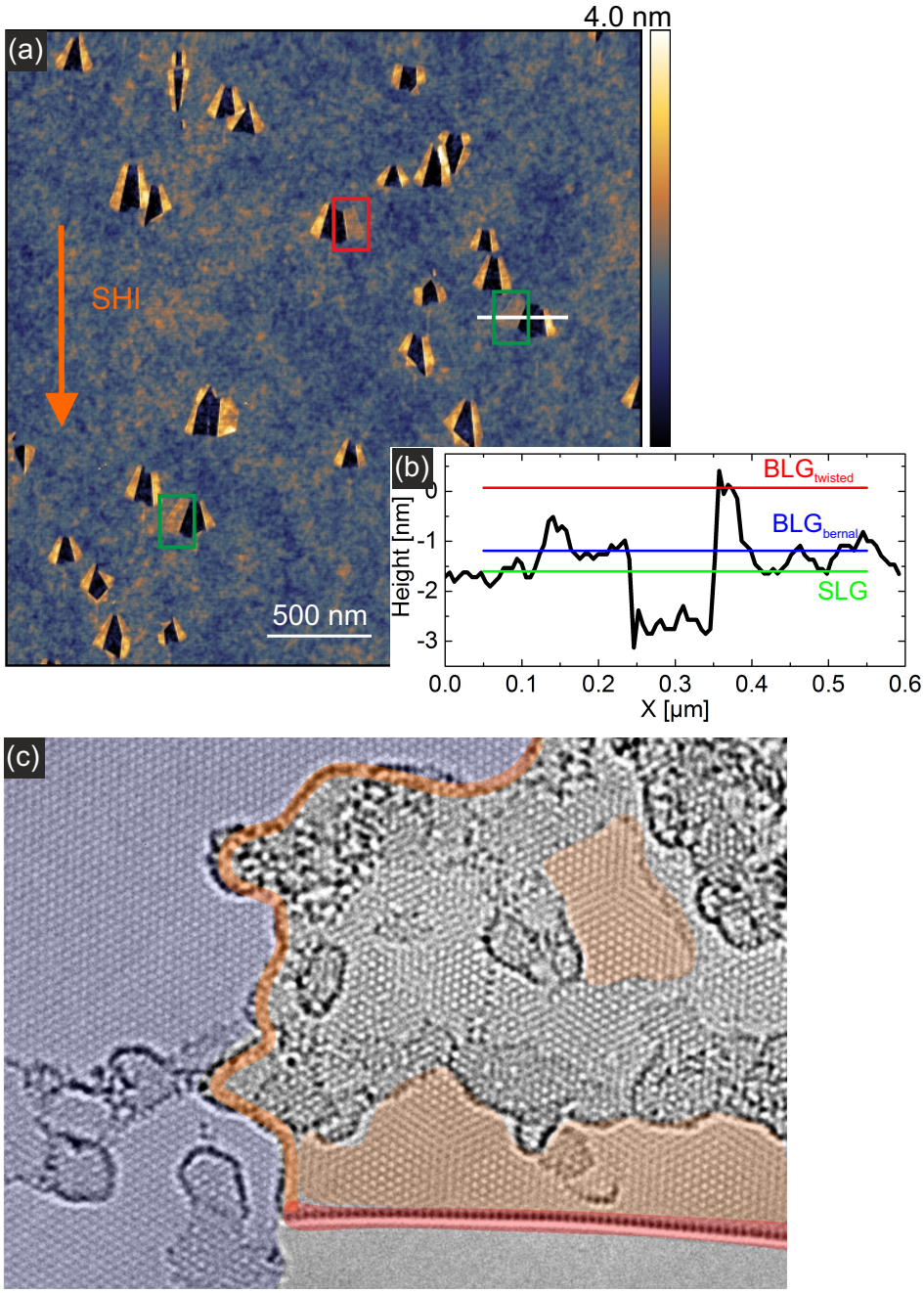

Figure 5.13: (a) Topography of graphene foldings, the orientation of the closed bilayer edge with respect to the ion trajectory varies significantly. (b) Line profile of the line marked in (a), the height of the folding varies between 0.3 to 1.5 nm. (c) TEM image showing moirée structure (orange) for the folded bilayer and the closed bilayer edge (red).

To actually apply these twisted bilayer and closed bilayer edges, it is necessary to control the lattice mismatch or the orientation of the closed bilayer edge, respectively. It is well known that by mechnically exfoliating graphene samples, the angle between the edges usually found to be mulitples of 30°. This indicates that in exfoliated graphene flakes either zigzag or armchair edges are generated [375]. In fig. 5.14 the angle ϕ' of the closed bilayer edge with respect to a graphene edge is measured in dependence of the incidence angle θ of the SHI.

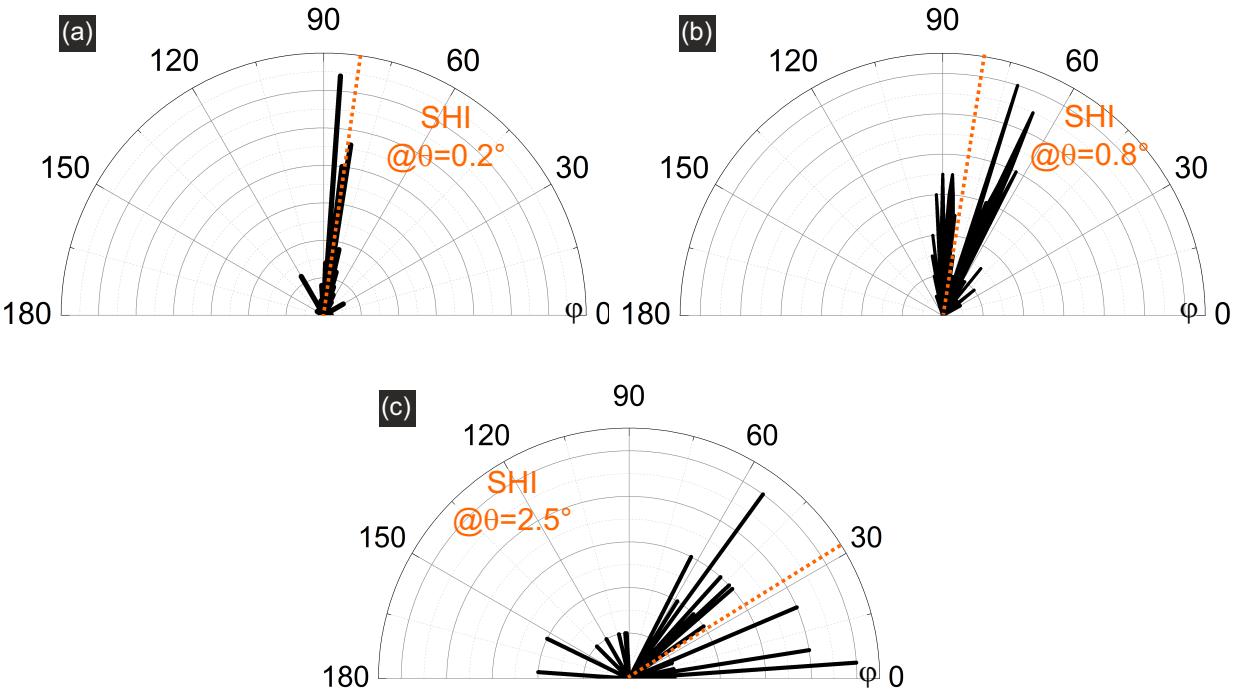

Figure 5.14: Orientation of the closed bilayer edge of graphene on SiO_2 foldings with respect to a graphene edge ϕ'. (a) For ultra grazing incidence angle foldings are mainly oriented along the SHI trajectory. (b) Incidence angles of $\theta \approx 1°$ result in foldings that are close to either zigzag or armchair edges. (c) Even larger incidence angle results in a broad distribution of orientations of the closed bilayer edge.

In this experiment graphene on SiO_2 has been used, the results may vary for different supporting substrates. For ultra glancing incidence angle like θ=0.2° (fig. 5.14 (a)), the orientation of the closed bilayer edges does not show any 30° multiples of the graphene edge, instead ϕ' corresponds almost exactly to the angle of the impinging ions. In (b) the incidence angle is increased to θ=0.8° and the resulting closed bilayer edges show a distribution of ϕ' which is not aligned with the impinging SHI anymore, but more closely to the the graphene zigzag and armchair orientation which are 60° and 90° or vice versa. Irradiating even larger incidence angles like θ=2.5° in fig. 5.14 (c) results in an even larger

distribution of ϕ' in which multiples of 30° seem to be preferred. Note, that the error in the ϕ' measurements in the range of $\pm$ 3∘ mainly because of piezo drift during AFM measurement. In conclusion it can be said that low incidence angles like θ=0.2° and lower favour closed bilayer edge orientation oriented along the SHI trajectory while larger incidence angles favour angles ϕ' which are multiples of 30° and thus oriented along the crystallographic lattice of graphene. So in conclusion, in order to controllably induce foldings with a precise orientation, very low incidence angle of the SHI are necessary.

5.4 Importance of the cristalline quality

It is well known that graphene prepared by mechnical exfoliation exhibits the highest cristalline quality. This is generally not the case for CVD grown graphene, which is currently envisaged for industrial applications of graphene where grain boundaries and defects do affect the properties of graphene [380, 381]. Therefore the question arises in which way the cristallinity of the material plays a role in the folding process. To study this, commercially available CVD graphene transferred onto SiO_2 (Graphenea - Spain, San Sebastian) is compared to carbon nanomembranes (CNM), a polymeric carbon membrane with nm thickness (CNM Technologies - Germany, Bielefeld).

In fig. 5.15 (a) an optical image of CVD graphene grown on Cu foil and transferred onto a SiO_2 substrate is shown [382]. The whole substrate surface is covered with graphene and the spots with a higher contrast which can be observed in (a) are most likely remnants of the transfer process. The inset shows a typical Raman spectrum of this sample, and although a little D-band can be detected, the CVD graphene sheet can be considered of good quality [290]. This sample has been irradiated with 91 MeV Xe ions under glancing incidence angle ($\theta \approx 1°$), which results in the formation of foldings as shown in the AFM topography (see fig. 5.15 (b)). The foldings induced in CVD graphene are comparable to the ones found in exfoliated graphene but they look less uniform. This may be due to the larger surface roughness on CVD graphene (1.5 nm RMS) compared to exfoliated graphene (0.5 nm RMS). In addition wrinkles are present in the CVD graphene sheet, which indicate locally stressed areas [383].

While CVD graphene is almost of the same crystalline quality as exfoliated graphene, carbon nanomembranes can be considered as amorphous [384, 385]. The CNM used in this experiment have been prepared by electron radiation induced cross-linking of self assembled monolayers (aromatic molecules) on a copper foil substrate. The resulting CNM have a thickness of 1 nm which is similar to graphene. In fig. 5.15 (c) an optical image of a CNM transferred to SiO_2 is shown. The Raman spectrum shown in the inset further underlines the amorphous nature of the CNM, as no peaks can be detected [384]. This CNM has been irradiated with 857 MeV U ions ($\theta \leq 1°$) and the resulting modifications can be observed in fig. 5.15 (d). The SHI modifications in CNM differ significantly from graphene as it begins with a nanoscale rift and can end in foldings, which are even less uniform than foldings in

[0]The CNM experiment was planned and performed by Hanna Bukowska, Universität Duisburg-Essen

CVD graphene and appear to be broken and discontinued in a lot of cases. All in all, this demonstrates that the cristalline quality is an important parameter, if uniform foldings are to be introduced into an atomically thin material.

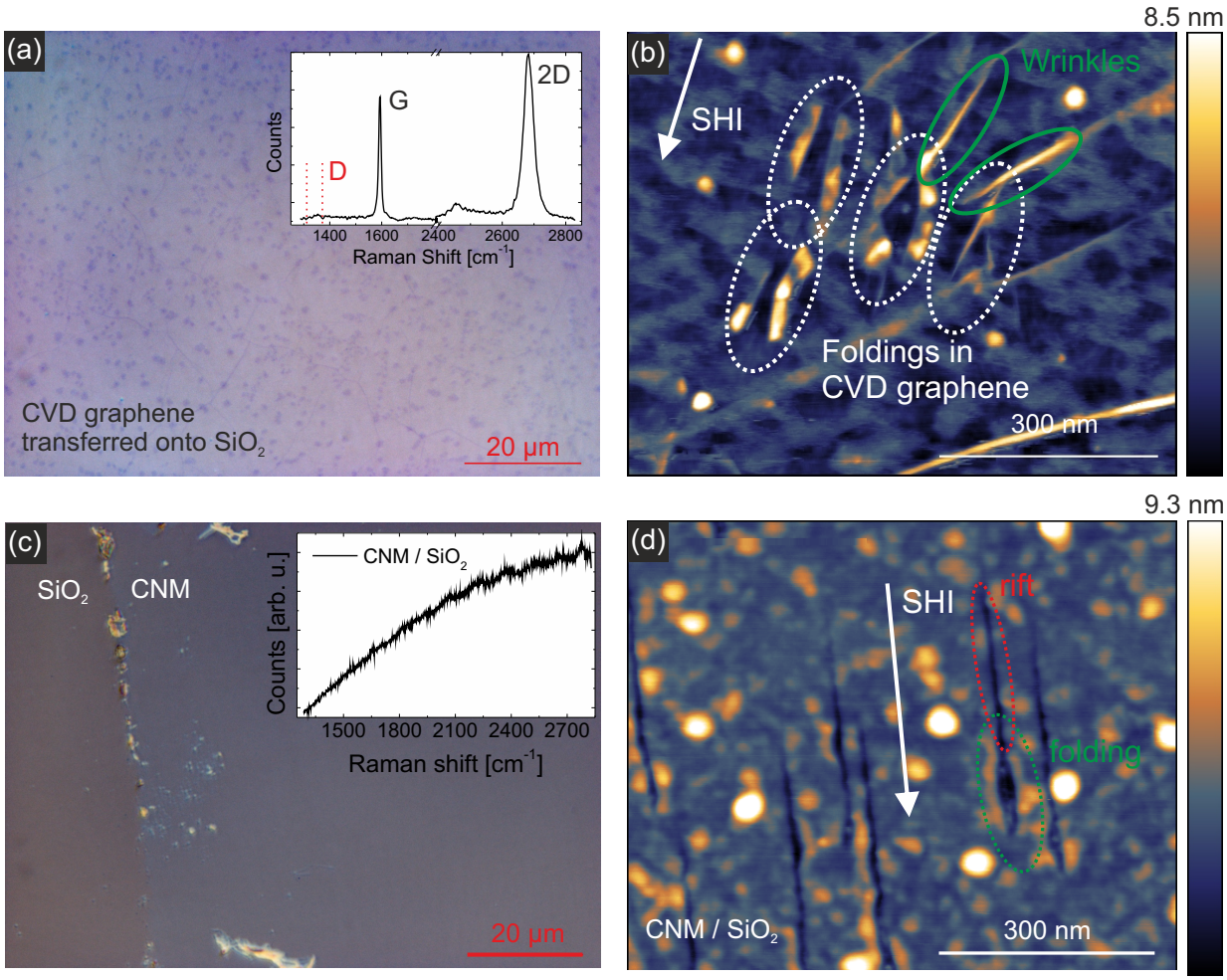

Figure 5.15: (a) Optical image of CVD graphene transferred onto a SiO_2 wafer, inset showing a Raman spectrum where the D-band is only faintly detectable. (b) AFM topography after 91 MeV Xe irradiation, showing foldings upon SHI impact. (c) Optical image of a CNM transferred onto a SiO_2 wafer, inset showing a Raman spectrum revealing its amorphous nature. (d) AFM topography of the CNM after irradiation with 857 MeV U ions (θ=2°). Upon SHI impact, nanoscale rifts and partial foldings are created.

5.5 SHI modifications in MoS_2

It has already been shown in the introduction of this chapter, that the formation of foldings is not limited to graphene but can be observed on other 2D-materials like hexagonal BN and MoS_2 as well. However, in contrast to hBN, the SHI irradiation of MoS_2 results in a new kind of modification - nanoscale rifts. In the course of this thesis, over 50 single layers MoS_2 have been irradiated with SHI and it has been found that both rifts and modifications can be introduced into SLM. This is shown in fig. 5.16.

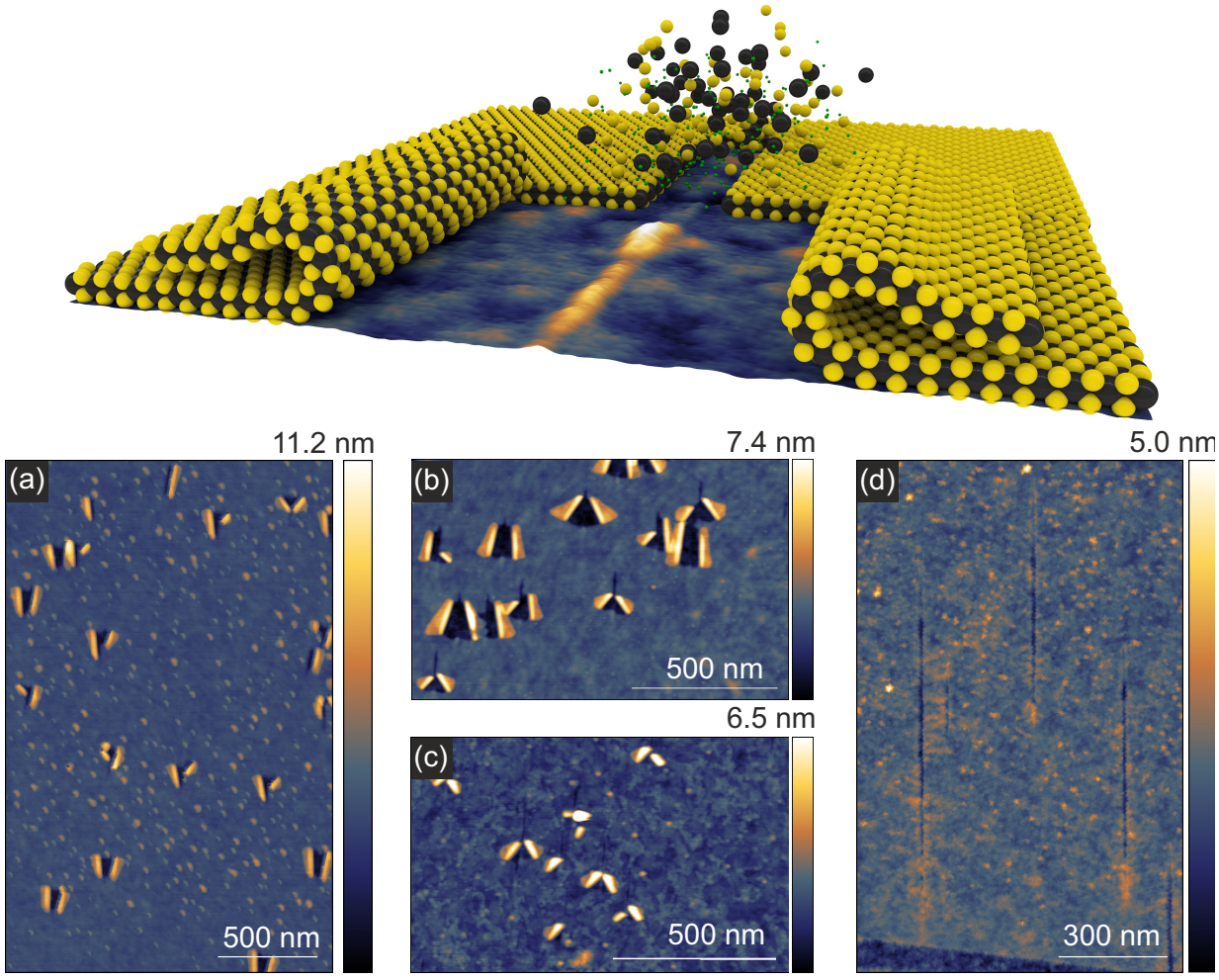

Figure 5.16: Schematic view of SHI modifications (91 MeV Xe, $\theta \leq 5°$) in single layer MoS_2. These modifications can be foldings (a), foldings with small rifts (b), rifts with small foldings (c) and only rifts in (d).

The samples in this chapter have all been exfoliated on standard 90 nm SiO_2/Si substrates under ambient conditions and were measured using tapping mode AFM microscopy after the irradiation experiment if not mentioned otherwise. In fig. 5.16 the samples have been irradiated using 91 MeV Xe ions under a grazing incidence angle of $\phi \leq 5°$, which can result

in the formation of ≈ 100 % foldings (a) or 100 % rifts as shown in (d). Furthermore, a combination of first rift formation and subsequent folding can be observed as well. The ratio between rift and folding is not fixed and can vary continously between zero and one. This ratio is not related to the incidence angle ϕ of the impinging ion, which is demonstrated in fig. 5.16 (b) and (c). Here, AFM images of two SLM flakes on the same sample and therefore with the exact same incidence angle are shown. The SLM flake in (b) shows a ratio of 0.2±0.2 (length of rifts / length of SHI modification) while the SLM flake in (c) has a ratio of 0.8±0.2. Note that the overall length of both modifications in (b) and (c) is the same, i.e. 275 nm. These findings stress that the transition from rift to folding modification does neither depend on the impinging SHI nor the incidence angle of the SHI. In order to actually use foldings or rifts in SLM for potential applications, it is necessary to introduce these modifications in a controlled way, which will be the main topic in the next section. An explanation for the rift creation will be given in section 5.6.

5.5.1 Foldings in MoS_2

After investigating a variety of irradiated single layer MoS_2 flakes, it can be said that flakes with modifications consisting of only foldings and next to no rifts have one thing in common: The angle ϕ between the SHI trajectory and a crystalline border (marked by the edge of the MoS_2 flake) is typically a multiple of 30°. Two examples of this behaviour are shown in fig. 5.17 (a) and (b) in which the the angle ϕ is 90° ± 3°. Unfortunately, there are two drawbacks in this analysis, which result in the relatively large error bar. First, as ϕ is determined from AFM topography images, small drift effects due to the piezoelectric positioning system are always present and are difficult to avoid completely. Second, the edges of SLM flakes are not always straight, but can be heavily bend, which is the reason why a lot of SLM cannot be analysed with regards to ϕ in the first place. However, if the incidence angle ϕ is just slightly off as in fig. 5.17 (c) with 62° ± 3° the resulting modifications are mainly rifts. Nevertheless, foldings can be observed on such SLM sheets as well. The reason for small foldings like in the right side of the image is most likely a locally enhanced energy deposition due to an irregularity in the trajectory, e.g. a contamination or some other irregularity. Large foldings on such a sample tend to be heavily bent (and under stress) instead of straight as in (b) and (c). Imaging this folding in situ using non-contact AFM reveals two things. The edges of the foldings are rather fuzzy (see fig. 5.17 (d)) and by analyzing the image carefully it can be seen that the folding is indeed caused by (coincidental) double impact. The first SHI impact already weakend the SLM flake and a second SHI running very close to the first one caused the formation of the folding.

This indicates that the orientation of the SHI trajectory with respect to the MoS_2 is crucial when either foldings or rifts are to be created. This interpretation is further corrabborated by the findings on bilayer MoS_2 as shown in fig. 5.18. In basically every irradiated bilayer MoS_2 rifts are introduced (see fig. 5.18 (a)). However, in one of the samples, where the SHI ion hit the bilayer flake with an exact angle of ϕ=60°, the formation of a folding

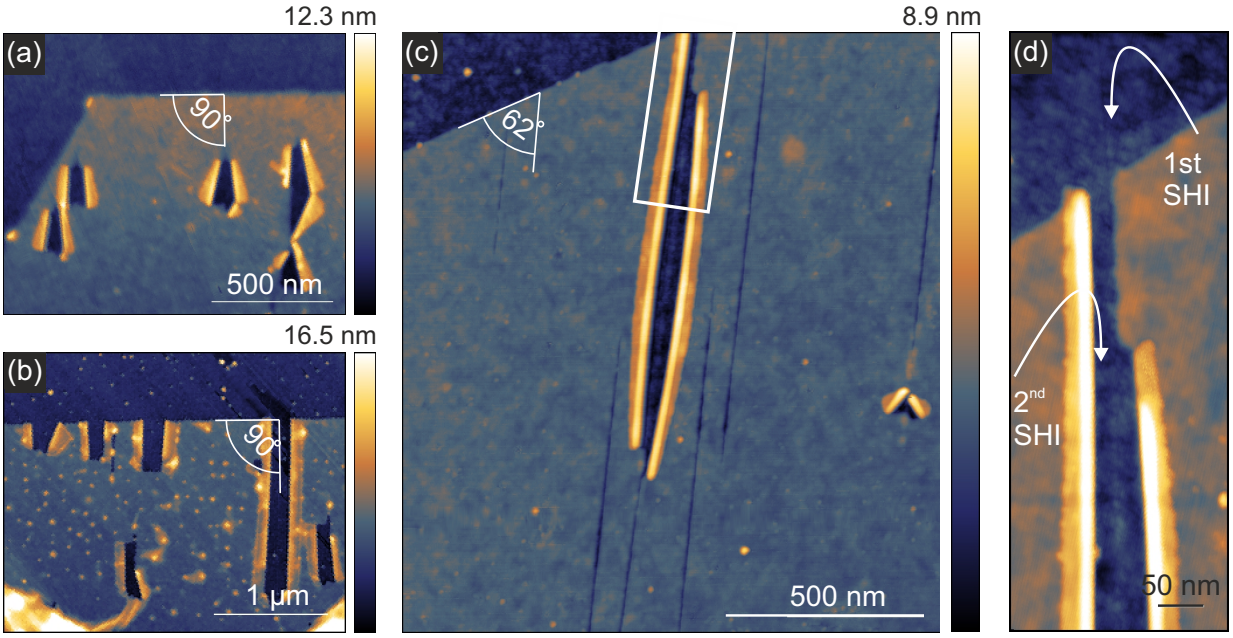

Figure 5.17: Single layer MoS_2 irradiated with 91 MeV Xe ions under grazing incidence angle. (a+b) Impinging SHI trajectory with ϕ=90°±3° with respect to the MoS_2 edge, showing ion modifications of mainly foldings. (c) SHI trajectory with ϕ=62°±3° resulting in primarily rifts. However one large folding is created which is significantly bent. (d) Non-contact AFM topography zoom-in on the white box marked in (c).

can be observed. The foldings have a tendency to bent with a multiple of 30° with respect to the crystallographic MoS_2 edge.

The folding efficiency is significantly lower than in single layer MoS_2 with ≈0.5 (foldings/SHI impact). A lower folding efficiency has been observed for bilayer graphene as well. In the case of graphene, this can be attributed to the fact that bilayer graphene is more resistant to ion irradiation [176] and without vacancy defects no foldings can be introduced as described in the previous chapter. However, this cannot be the case for bilayer MoS_2, because SHI impacts that do not create foldings are still creating rifts which should enable the formation of foldings. Moreover, areas where the SHI impact did not result in a folding look as if the folding process has stopped halfway through. Compared to graphene, MoS_2 is much heavier per unit area as a single layer MoS_2 is actually a trilayer (S-Mo-S). Most likely the pressure exerted from the superheated interfacial water layer (which has been proven to be essential for folding formation in graphene) is the limiting factor here.

In order to test this hypothesis, a commercially available CVD grown MoS_2 on SiO_2 sample (HQ graphene - Groningen, Netherlands) was irradiated 91 MeV Xe ions under grazing incidence angle of θ=0.5°. The idea behind using CVD MoS_2 is, that in contrast to CVD graphene, MoS_2 can be easily grown directly on the SiO_2 surface and no further transfer step is necessary, which prevents the formation of an interfacial water layer[386].

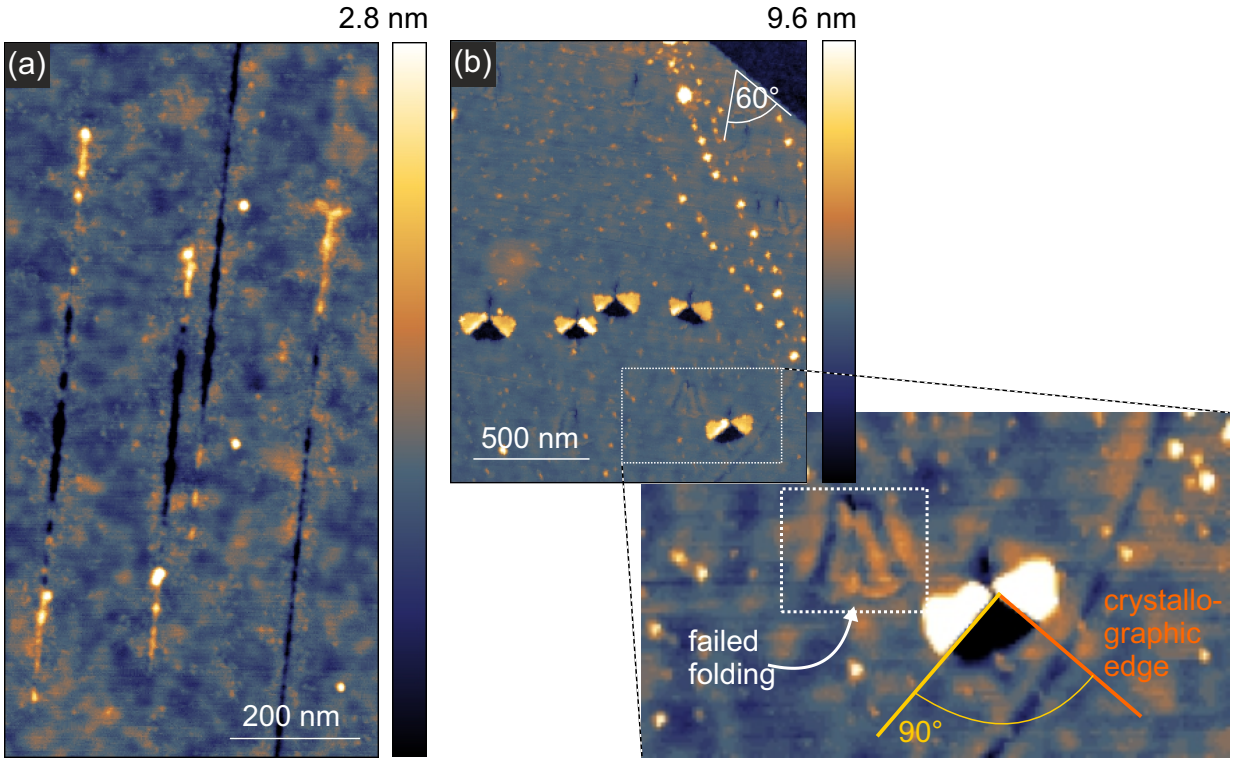

Figure 5.18: SHI irradiation of bilayer MoS_2 (91 MeV Xe, $\theta \leq 2°$). (a) In general, SHI irradiation of BLM leads to the creation of nanoscale rifts. (b) In one rare case, where the impinging SHI has an angle of ϕ=60°, foldings are created. As shown in the inset, the folding efficiency is below one and only closed bilayer edges with an orientation of 30° multiples are created.

In fig. 5.19 (a) a typical optical image of a CVD MoS_2 is shown. The CVD MoS_2 is not completely covering the SiO_2 substrate as it grows in form of single islands with a size of several hundred μm^2 in case of the investigated sample. This can be exploited to study SHI interaction under a variety of different angles ϕ of the ion trajectory with respect to the MoS_2 edge to exclude possible effects due to the crystalline lattice as observed for MoS_2 with intercalated water. The AFM image in fig. 5.19 (b) shows typical modifications that were found after SHI irradiation in every probed CVD MoS_2 (>10). Exclusively rifts can be observed in the CVD MoS_2 flake with a typical length of about 400 nm. These rifts are decorated with adatoms/adsorbates on both sides which is not observed for exfoliated single layer MoS_2. The measured width of the rifts in CVD MoS_2 is 5.2 ± 0.5 nm and therefore almost half as wide as rifts in exfoliated MoS_2 (width=9.2 ± 1.2 nm). This indicates that the intercalated water layer is not just assisting in the folding formation but in the rift creation as well.

The fact that two ion impacts close to each other cause the MoS_2 to fold can be exploited to force foldings in MoS_2 by cross radiation. This technique is applicable for both, single layer and bilayer MoS_2. An example of such a cross irradiation is shown in fig. 5.20. A

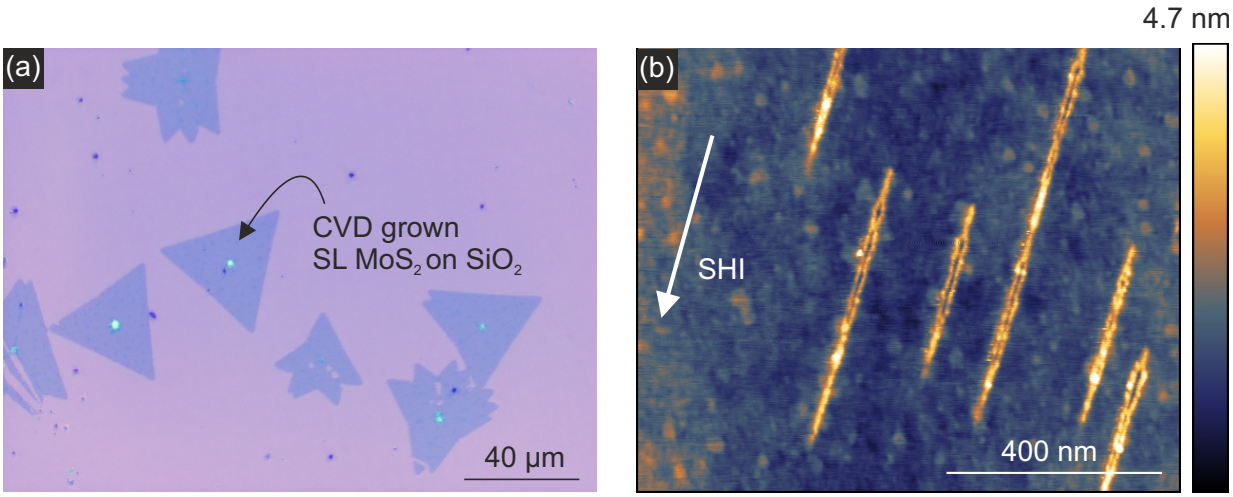

Figure 5.19: SHI irradiation of CVD single layer MoS_2. (a) Optical microscope image of CVD grown MoS_2. (b) AFM topography after SHI irradiation (91 MeV Xe, θ=0.5°). Without an interfacial layer being present, no foldings, but rifts can be observed on the MoS_2 flakes.

bilayer MoS_2 has been irradiated two times with 91 MeV Xe ions under grazing incidence angle of ϕ=1.5°. Between the two irradiations, the azimuthal angle has been rotated by $\Delta\phi$=15°. The MoS_2 folds exactly at the positions, where the two rifts created by the SHI cross each other. Interestingly, two foldings are bend backwards, i.e. against the direction of the ion beam, and one is folded forward. The position of the crossover between the two rifts is determining the direction. If the cross point is at the beginning of the first rift, the folding, which is always present between two rifts, has to be in the direction of the ion trajectory and vice versa. Furthermore, it can be seen that the forward folding has a flat edge, while the backward foldings exhibit the same pronounced edges as observed in single layer MoS_2 (see fig. 5.17). In this case, the closed bilayer may be broken, resulting in an usual open bilayer MoS_2 edge.

In contrast to natural MoS_2 edges, the edges in ultrathin MoS_2 layers created by the SHI are highly reactive. In fig. 5.20 (b-d) typical optical and AFM images after storing irradiated MoS_2 samples under ambient conditions for $\approx$ 12 months are shown. Starting with the optical image in fig. 5.20 (b), it can be seen that the rifts/tracks in few layer MoS_2 are very pronounced and can be detected. The AFM topography in fig. 5.20 (c) shows that storing this sample in ambient conditions results in very pronounced edges in single- and bilayer MoS_2, which have not been present in its pristine condition right after the SHI irradiation. This is shown in more detail in (d), where the same area from (a) is measured again. The edges are heavily decorated indicating their enhanced reactivity with respect to oxidation.

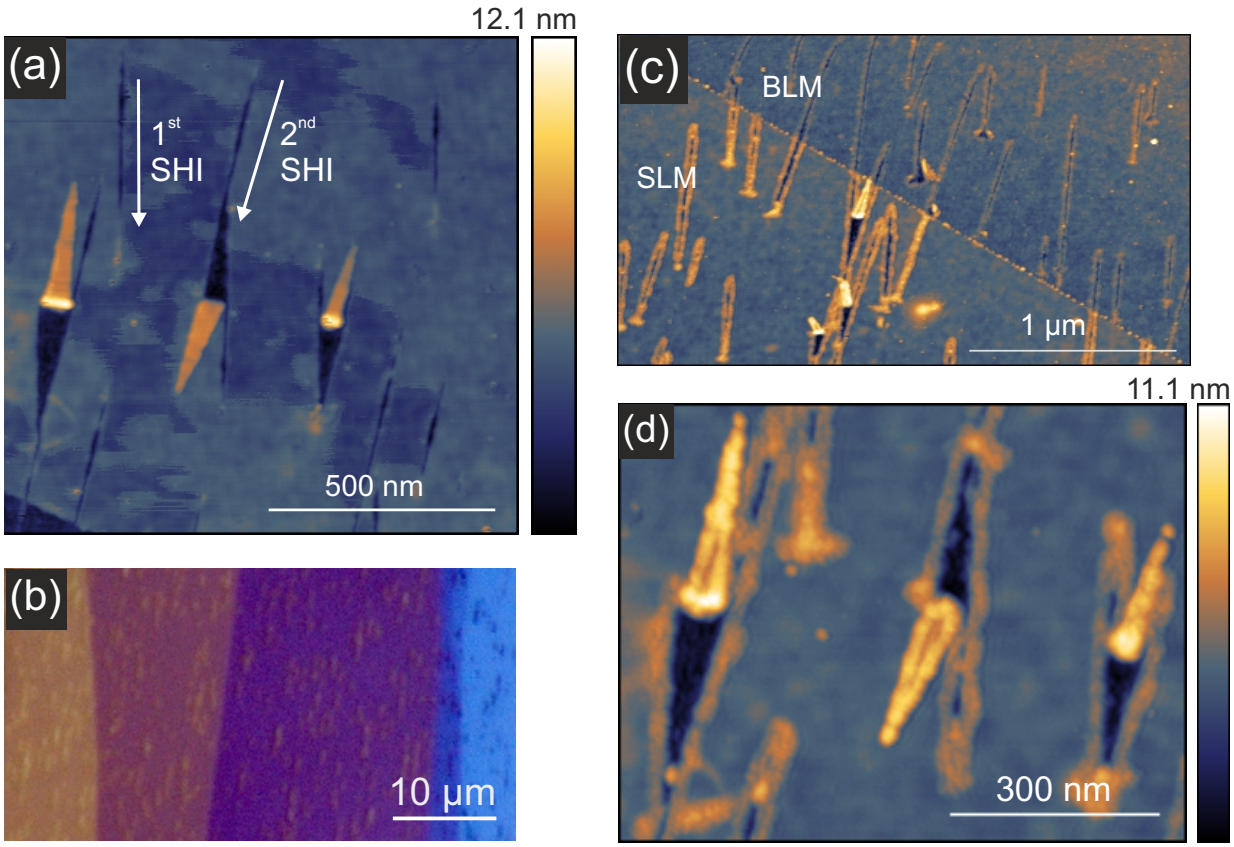

Figure 5.20: Enforced folding and activated edges. (a) Forced folding formation in bilayer MoS_2 by consecutive SHI irradiation with different angles ϕ. Depending on the impact point, the folding can be created in the direction of the ion trajectory or backwards. (b) Optical images of an aged irradiated MoS_2 sample show that tracks can be observed even with optical microscopy. (c) AFM topography of single and bilayer MoS_2 12 months after the irradiation took place. Edges are fuzzy and show an increased height. (d) Bilayer foldings from (a) after 12 months storing under ambient conditions.

That single layer MoS_2 and especially edges in it have an increased catalytic activity has been observed and predicted by several groups [387, 116, 388, 389, 390]. To design MoS_2 where the catalytic properties are optimized is therefore crucial, and it has been found that the number of edge sites is important, as it increases the hopping efficiency of electrons in the vertical direction [391].

5.5.2 Conclusion

To sum up the findings until now, the irradiation of ultrathin MoS_2 layers with SHI under grazing incidence can lead to two different modifications. First, foldings can be introduced in single and bilayer MoS_2 consisting of a closed bilayer stucture which already attracted

a lot of attention in the case of graphene due to their unusual properties. Compared to graphene, the formation of foldings in MoS_2 is not the dominant modification, which is why additional conditions have to be met to introduce these structures in a controlled way. The performed experiments indicate, that besides a sufficiently high energy of the SHI projectile and an interfacial water layer (main parameters for folding formation in graphene, see section above), the azimuthal angle of the ion beam trajectory with respect to a MoS_2 edge has to be a multiple of 30°. In practice, however, irradiating ultrathin MoS_2 with the necessary precision will be hard to achieve. An alternative route to introduce foldings in single- and bilayers MoS_2 is to use cross irradiations. By using e.g. micro beam setups [392] a high accuracy might be achieved in this way. Second, nanoscale rifts with a width of below 10 nm can be created. The easiest way to create these is by simply removing the interfacial water layer. Without the superheated water layer building up pressure underneath the MoS_2, no foldings can be introduced leaving rifts as the only option. These nanoscale rifts might be utilized e.g. as slit pores, opening up a variety of novel applications.

5.6 Mechanism of rift formation

Before nanoscale rifts in MoS_2 can actually be applied, which demands a precise control of both length and width of these structures, the mechanism behind the rift formation has to be understood. The series of images shown in fig. 5.21 shows how the track morphology in MoS_2 evolves with decreasing layer thickness from bulk like MoS_2 down to a single layer. The samples have been irradiated with 91 MeV Xe ions under grazing incidence angle $\theta \leq 1°$ in order to study elongated surface tracks.

In the case of bulk like MoS_2 (measured height over 50 nm) chains of nanosized hillocks protrude from the surface. Their orientation matches the direction of the SHI beam and from the nominal fluence it is safe to assume that each chain corresponds to a single ion trajectory. In most cases, the hillocks are evenly spaced (average distance 60 $\pm$10 nm), their height is up to 8 nm and their average diameter 23.7$\pm$2.3 nm. The length of the surface tracks varies with the angle of incidence. At $\theta \approx 0.5°$ as shown in fig. 5.21 (b) the typical length is about 1040$\pm$275 nm. The striking periodicity disappears almost completely in thin few layer MoS_2 sheets (thickness under 10 nm) - although individual hillocks are still created. The surface track is now a mixture of irregularly formed hillocks/protrusions and rifts, which have already been found in single and bilayer layer MoS_2.

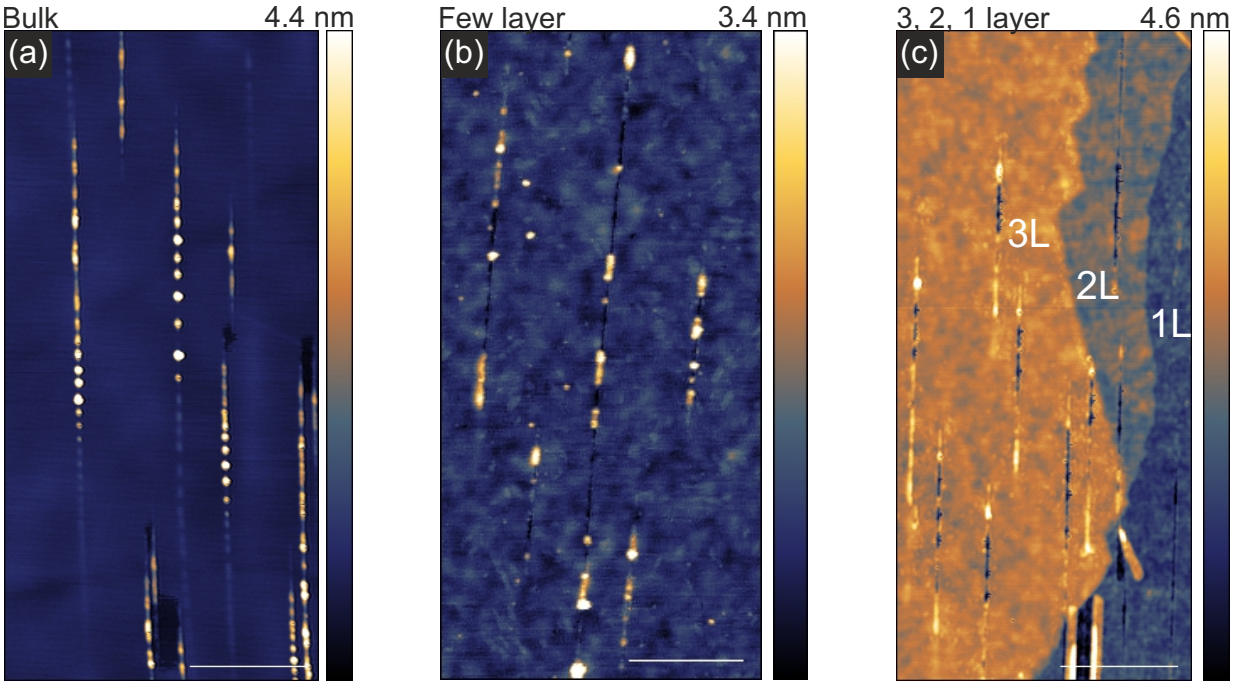

Figure 5.21: Transition of SHI modifications in MoS_2 from bulk to single layer. (a) Bulk MoS_2 shows periodic chains of nanosized hillocks. (b) Few layer (4 layers to $\approx$ 15 layers) shows a combination of hillocks and rifts. (c) For 3 layers MoS_2 and below, rifts are observed. Scale bars in all images are 400 nm.

In even thinner MoS_2 crystallites - three layers and below, the central surface track

consists of a continuous rift. The length of the rift however varies significantly between trilayer (3L), bilayer (2L) and single layer (1L) as shown in fig. 5.21 (c). The surface tracks in trilayer and bilayer MoS_2 are accompagnied by protrusions before and after the central rift. Single layer MoS_2 surface tracks consist in general only of rifts and do not show protrusions. While the surface track length in these three different MoS_2 samples is comparable, the length of the rifts is reduced by ≈25% for bilayer and ≈50% for trilayer. Moreover the morphology of the rifts changes as well. While the rift in single layer is a clean cut with straight edges (see fig. 5.17 (c)), bilayer and trilayer rifts change to chains of "inverted" hillocks. In particular for the trilayer in fig. 5.21 (c) it can be seen that the rift is formed of periodically round pits with a diameter of about 10 nm.

Irradiation induced rifts have never been reported for any crystalline semiconductor. By varying the incidence angle the length can be adjusted to e.g. 708±268 nm and a width of 9.2±1.2 nm for θ=0.5±0.3° . This yields an aspect ratio of about 1:80, which can however be tuned from 1:1 (nanopores) to 1:2000 in case of extreme grazing incidence experiments at the GSI (800 MeV Bi, $\theta \leq 0.05°$). Note, that the rifts occur exclusively due to the passage of the SHI, no subsequent chemical etching has to be performed.

From the length of the rifts with respect to the incidence angle θ the distance perpendicular to the surface d_{eff} up to which the mechanism creating this rift is effective can be deduced. The corresponding experimental data is presented in fig. 5.22 (black squares). The found d_{eff}=4.55 nm is a typical value for semiconductors. Because d_{eff} is larger than the thickness of a single layer MoS_2, it is evident that the process cannot occur exclusively in the single layer MoS_2 but must continue in the substrate as well.

Next, the possible mechanisms taking place in the SHI/SLM interaction will be discussed. The direct collision of a swift heavy ion projectile with the target atoms is neglible in this energy range ($S_e \gg S_n$, see fig. 5.25 e)and other mechanisms relevant for material modifications must thus be related to the electronic excitation. These have already been discussed in chapter 2 and are in particular non-thermal melting (NTM) caused by significant modification of the interatomic potentials, Coulomb explosion (CE) as a consequence of the electrostatic repulsive forces between the atoms in the ionized region, or phase transitions such as melting due to electron-phonon-coupling (EPC). These mechanisms occur on vastly different time scales, ranging from few fs in the case of processes related to non-thermalized electrons up to ps in the case of phase transistions.

Hillock chains (or more general protruding surface tracks) are frequently observed in crystalline insulators [162, 358] and have been observed in graphite as well [393]. The origin of these hillock chains has been successfully attributed to an efficient electron-phonon-coupling, which will be discussed here as a possible mechanism for the rift creation. The surface tracks which are shown in fig. 5.21 (a) in bulk MoS_2 are quite typical for surface tracks in crystalline semiconductors (hillock chains). These chains might as well consist of resolidified MoS_2 due to a phase transition caused by the thermal spike induced by the swift heavy ion excitation and subsequent electron-phonon coupling. For MoS_2 a rather low melting/decomposition temperature of T_{melt}=1458 K has been reported [394, 395]. On the basis of this low melting temperature and the previous observation that the process

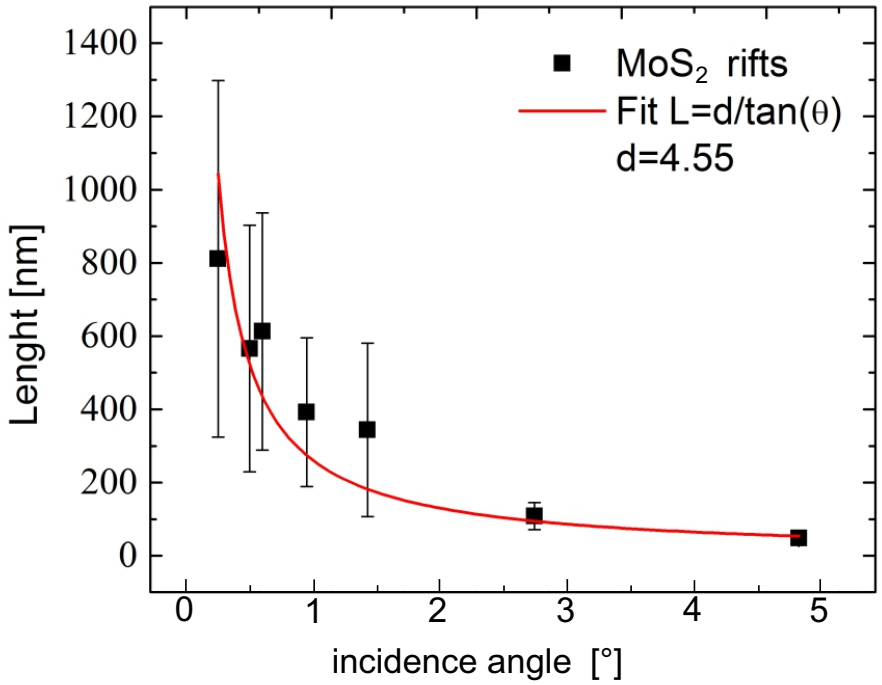

Figure 5.22: Experimental length of rifts in single layer MoS_2 induced by SHI irradiation (91 MeV Xe & 84 MeV Ta) fitted with the $L{=}d/\tan(\theta)$ relation. The parameter d denotes the depth of the projectile at which the surface track formation ends.

cannot take place in the ultrathin MoS_2 only, the following hypothesis for the rift formation is postulated: A thermal spike in SiO_2 results in a super heated surface track on the SiO_2 surface and in areas, where the temperature of the surface track exceeds the melting temperature of MoS_2, nanoscale rifts are formed.

To test if this hypothesis is correct, the lattice temperatures were calculated using the two-temperature model which was already introduced to the reader in chapter 1.2 and will be discussed in more detail in the next chapter. Here, the software package "Two Temperature Model v0.6" written by Orkhan Osmani was used. For simplicity, the MoS_2 was neglected in the calculation and the thermal spike was calculated in SiO_2 only. Later on, we will see that this assumption is justified. In the TTM calculations, the most crucial parameter is g, the electron-phonon coupling parameter, which determines the transfer of energy from the excited electronic system to the lattice. Here, the g parameter for SiO_2 found by Osmani et al. [396] using Monte Carlo simulations has been used. In order to compare our experimental data, which was gathered with incidence angles between 0.25° and 4.84°, the simulation box used to accommodate the ion beam was varied in length between x_{box}=1500 nm and y_{box}=400 nm, respectively, while the width (y_{box}=60 nm) and the depth (z_{box}=20 nm) was kept constant. The simulation box is surrounded by a thermal bath, while van Neumann boundary conditions are used for the surface. Inside the simulation box, the two

equations 2.10 are solved using the finite difference method.The impact point is chosen as x_{impact}=0.5·x_{box}, y_{impact}=0.5·x_{box} and z_{impact}=0.1·x_{box}.

The results of the simulation for the θ=0.95° irradiation with 91 MeV Xe ions 1 ps after the ion impact are shown in fig. 5.23. In (a) a contour plot of the x-y plane can be seen. The area enveloped with a blue contour line marks the point, where the temperature reaches the melting temperature of MoS_2 T_{melt}=1458 K. The track evolves with time and reaches a maximum length of 490 nm after 2 ps. In the same figure in (b), the contour plot in the x-z view is shown. Additionally, a single layer MoS_2 is drawn on top of the simulated data to directly compare the results of the TTM calculation and the experiment. In the experiment, the length of the rift in single layer MoS_2 corresponds to 392 nm, which is significantly smaller than the calculated value. A similar result is observed for other simulations with varying incidence angles.

The most reasonable explanation for this is the unknown sublimation temperature for the single layer MoS_2 sheet. The temperature used has been determined for bulk MoS_2 in thermal equilibrium, in our case however, MoS_2 is thinned out to atomical thickness and the time scale of the heating process is on the order of ps. The thinning of the MoS_2 may have an influence on T_{melt} [397, 398] and considering the very rapid quench rates in the ion track, a much higher melting temperature can be expected. Therefore, the temperature in the simulated data has been accommodated to reproduce the experimental data with a higher consistency. The best fit was found for T_{melt}=1800 K, which corresponds to a length of 360 nm for the 0.95° Xe irradiation.

The assumption, that the direct interaction of the SHI with MoS_2 can be neglected in the simulation can be proven to be correct. Assuming that the SHI directly interacts with the single layer MoS_2, the projected length of the ion at 0.95° is only 42 nm. These 42 nm are marked in fig. 5.23 (b) with a red line, starting at the impact point of the SHI in SiO_2 and drawn contrary to the ion trajectory. It can be easily seen that this area is fully enclosed by the surface track in the SiO_2 and therefore a possible direct interaction of the SHI with single layer MoS_2 is likely to have no influence on the length of the rift.

The plot in fig. 5.24 summarises the results of the angle dependent TTM calculations. The length of the rifts in SLM in the experimental data (black boxes), the TTM data with T_{melt}=1458 K (blue triangle) and the TTM data with T_{melt}=1800 K (green circles) are plotted as a function of the incidence angle θ. The observed lengths in the experiment are in quite good agreement with the simulated data derived from the TTM calculation with T_{sub}=1800 K. This finding strongly suggests that indeed a thermal mechanism is at the origin of rift formation in thin MoS_2 layers. However, non-thermal mechanisms like Coulomb explosion might take place, but to study this additional experiments would have to be performed. In any case, the material obviously can escape freely only from the first two to three layers but is condensing on its way out, if it stems from deeper layers, see fig. 5.21.

At this point the findings can be compared to graphene. In graphene, no rifts have ever been observed after SHI irradiation. Trying to apply the same model - graphene on top of SiO_2 which acts like a heating plate - the sublimation temperature of graphene

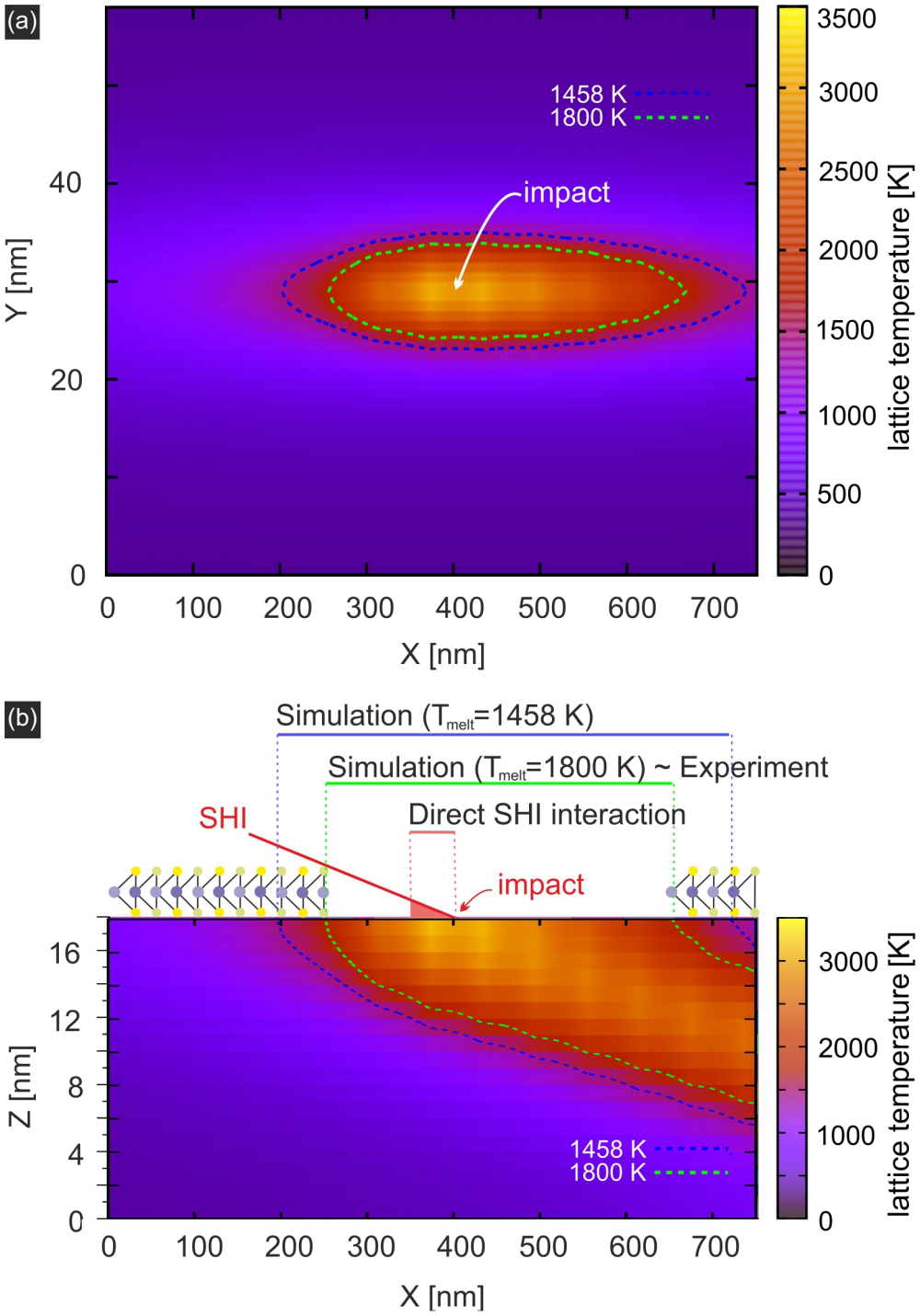

Figure 5.23: Two-temperature model simulation of 91 MeV Xe ions in SiO_2 with an incidence angle of θ=0.95°. (a) View of the x-y plane, the contour line which is marked in blue corresponds to the area on the SiO_2 surface, where the melting temperature of MoS_2 T_{melt}=1458 K is reached. The green contour line marks the area, where the best fit temperature to the experimental data is given (T_{melt}=1800 K). (b) View of the x-z plane, additionally a SLM sheet is drawn on top of the SiO_2 displaying the experimentally determined length of the rift. On top of the x-z view, three lines are drawn, which mark the length of the track for the simulation with 1800 K, 1458 K and the length of the direct interaction of the SHI with single layer MoS_2.

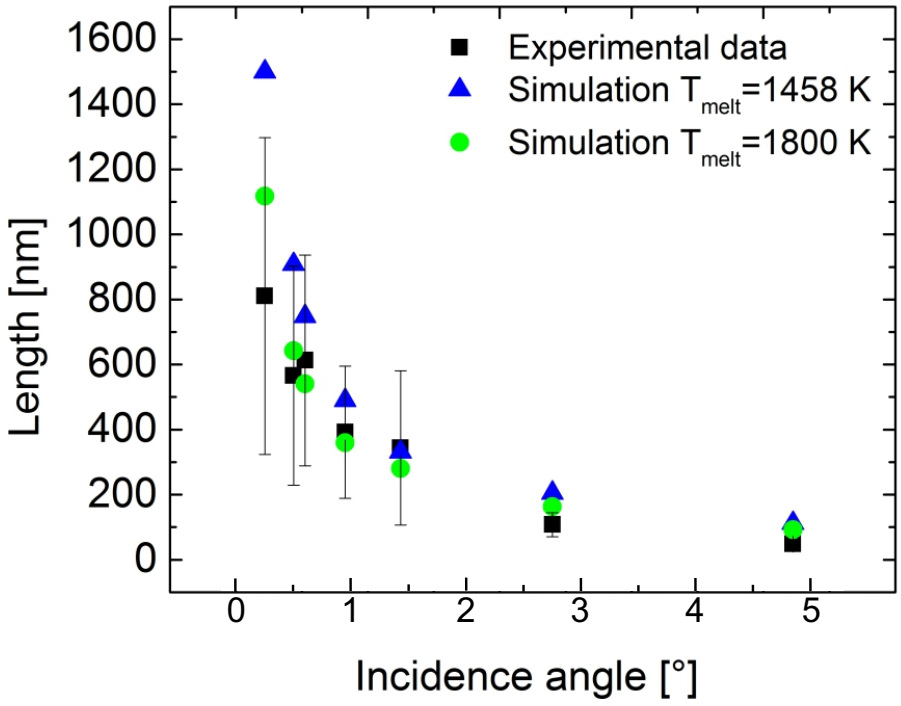

Figure 5.24: Plot of the rift length in single layer MoS_2 as a function of incidence angle θ. Plotted are the experimental data and the results from the TTM calculation for the melting temperature of MoS_2 (T_{melt}=1458 K) and the best fit sublimation temperature T_{melt}=1800 K.

T_{sub} ≥4000 K [399] has to be overcome in the SiO_2. This is however not the case, which therefore supports our hypothesis for MoS_2.

Two important approximations have been made in this mode, the direct interaction of the SHI with SLM has been neglected and the melting temperature of SLM has been assumed higher than the melting temperature of bulk MoS_2. Thus, additional threshold experiments and calculations for rift formation in single layer MoS_2 have been performed. For this, SLM on SiO_2 has been irradiated at the RBI (Croatia) with 23 MeV I, 15 MeV Si, 6 MeV Si and 3 MeV O ions (θ=1±0.5° and 10 ions/μm^2). The results of this experiment are shown in fig. 5.25 (a-d), respectively. The 23 MeV I irradiation in (a) results in a lot of surface tracks, which have a small rift in the center. Whether the surface tracks are created in the SLM sheet or in the SiO_2 cannot be determined at this point. In the 15 MeV Si irradiation in fig. 5.25 (b), these tracks can still be observed, however the rifts in the center are missing. In the 6 MeV and 3 MeV AFM topography images, no surface tracks can be observed. Only one rift can be observed for the 6 MeV irradiation, which is most likely caused by a coincidential impact of two ions near each other, as has already been discussed previously.

Now to investigate, if these findings are in agreement with the thermal spike mechanism, TTM calculations were performed for ions with varying electronic stopping powers (S_e),

which correspond to the projectiles in the experiment. Note, that nuclear stopping can be neglected in this regime, as the dominant interaction is in the electronic stopping regime, as it is shown in fig. 5.25 (f). The angle for the simulation was chosen to be θ=0.95°. This makes it possible to compare the simulation of the very high energy irradiation (S_e=12.35 keV/nm at θ=0.95°) with the lower energy irradiations (S_e=1.77 - 5.5 keV/nm θ=1°). The results are plotted as a function of rift length and stopping power in fig. 5.25 (d). The blue triangles denote the length of the heated zone on the SiO_2, where the melting temperature of 1800 K is reached, which gave the best agreement between calculated and experimentally determined surface track length. Based on this melting temperature for SLM no rift is created in MoS_2 for S_e=5.5 keV/nm (23 MeV I) ions and below. The red triangles are the respective length of the heated zone, where the melting/decomposition temperature of MoS_2 T_{melt}=1458 K is reached. Here, S_e=5.5 keV/nm is enough energy to create a rift. This is clearly more consistent with experiment and suggests that the actual temperature needed might be significantly lower than 1800 K.

In conclusion, it has been shown that if thicker layers of MoS_2 are irradiated with SHI, the modification consists of typical chains of hillocks frequently encountered in bulk insulators. For the 2D allotrop of MoS_2, a completely different morphology is observed. By choosing the right irradiation conditions micrometer long rifts with high aspect ratios can be created by individual ions in single layers MoS_2. The creation of rifts is unique to the 2D-material and has never been observed on the surface of crystalline bulk semiconductors. The formation of the rifts has been attributed to a mechanism, where a thermal spike in the substrate material of the 2D crystal yields temperatures above the sublimation temperature of SLM, thus creating the rift in the SLM sheet above. This mechanism is in good agreement with TTM calculations, which suggest a slightly higher sublimation temperature for MoS_2 of up to 1800 K compared to the 1458 K from literature, which is most likely due to the short time frames in the ps regime in which the thermal spike takes place. As these rifts have a very high aspect ratio and exhibit an increased reactivity, they can be useful as templates or for catalytic purposes. In addition to rifts, also foldings can be created in single layer and bilayer MoS_2 under well-defined conditions.

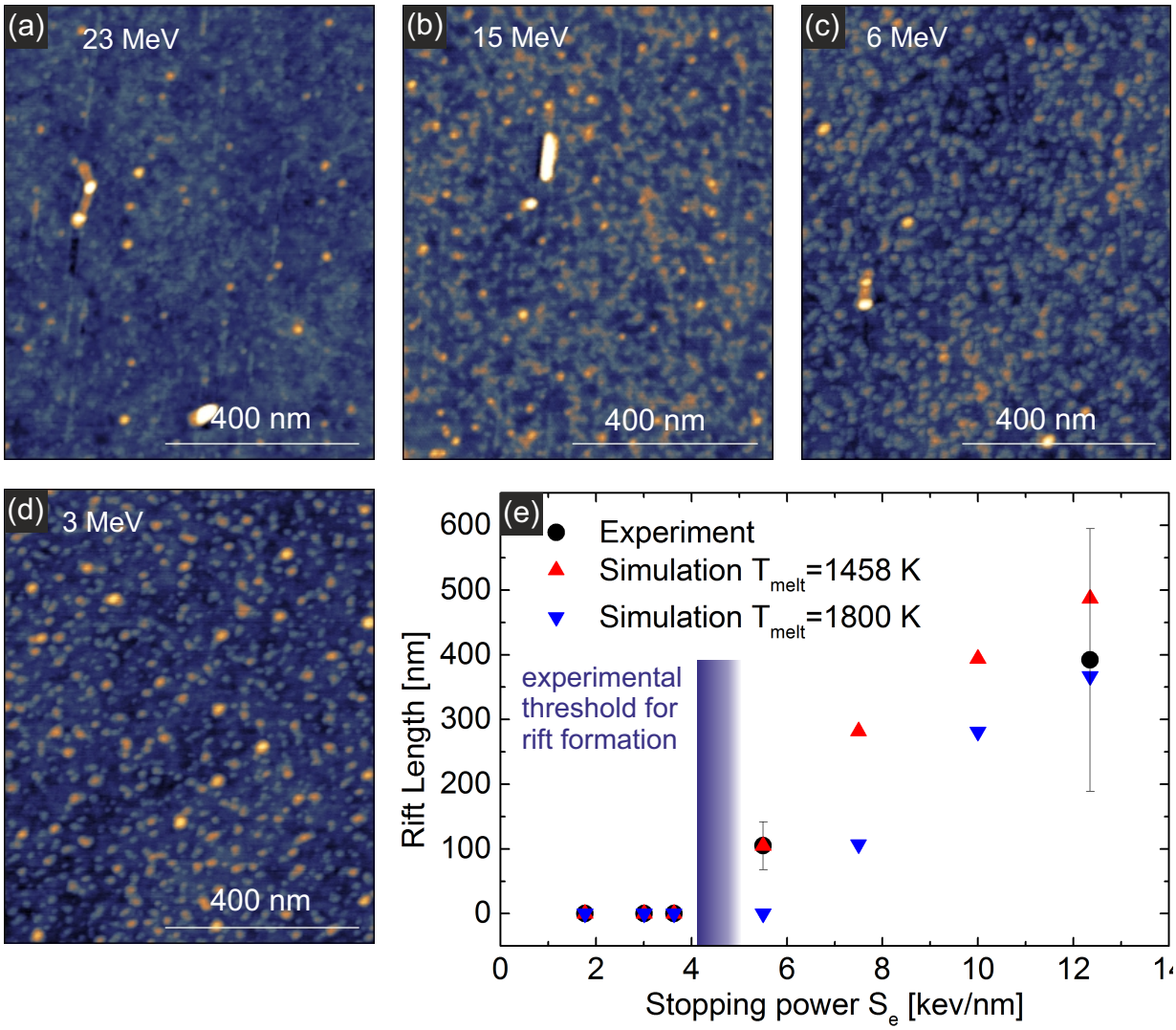

(f)

Swift heavy ion	S_e[keV/nm]	S_n[keV/nm]
	SiO_2	
3 MeV O	1.77	0.01
6 MeV Si	3.01	0.02
15 MeV Si	3.63	0.01
23 MeV I	5.50	0.27
81 MeV Ta	11.82	0,24
91 MeV Xe	12.35	0.10
106 MeV U	13.86	0.36

Figure 5.25: Threshold determination for rift formation in single layer MoS_2. The samples have been irradiated with 23 MeV I, 15 MeV Si, 6 MeV Si and 3 MeV O ions with a fluence of about 10 ions/μm^2 and an incidence angle of θ=1±0.2°. The AFM topography images of these irradiations are shown in (a-d) respectively. (e) TTM calculations for Xe in SiO_2 with varying kinetic energy corresponding to the experiment. The length of the track is calculated within the TTM using the two sublimation temperatures of 1458 K and 1800 K. The blue line marks the threshold for rift formation observed in the experiment. (f) Table of the calculated stopping powers for several projectiles in SiO_2 using the SRIM software package.

6 Doping graphene with swift heavy ions

Modern electronics began with the realization of the bipolar and field effect transistors in the late 1940s [400, 401]. The development of efficient doping techniques of these devices in the 1970s was a technologically important step to realize e.g. microscopic p-n junctions. A common technique to dope bulk materials like silicon is ion implantation. This technique relies on well defined projected ranges due to binary collisions, which result in a controlled electron or hole concentration. In silicon for example, the concentration of charge carriers can be modified between $10^{13}/\mathrm{cm}^2$ and $10^{21}/\mathrm{cm}^2$ [402, 403]. Due to its extraordinary electronic properties, 2D-materials are envisaged to play an important role in future nanoelectronics [25, 10].

In this chapter, it will be investigated whether swift heavy ions can be used to taylor the electronic properties, doping in particular, of 2D-materials. For this, swift heavy ion irradiation under glancing incidence angle of annealed graphene flakes is used to study doping effects of the surface tracks created in this way by Kelvin probe force microscopy. It will be shown that graphene on SiC, which is typically n-type doped by charge transfer effects from the substrate material, shows p-type behaviour after SHI irradiation. This p-type doping is most likely caused by implantation of Si atoms, sublimating from the SiC surface, into the graphene lattice. Additionally, the radiation hardness of 2D-material FETs in form of graphene and single layer MoS_2 is tested with 1.1 GeV U ions offering the maximum electronic stopping power. The results indicate a superior radiation hardness of graphene FETs in comparison to MoS_2. At last, first measurements of swift heavy ion irradiated graphene on MoS_2 field effect devices under glancing incidence irradiation are presented and discussed.

6.1 Manipulation of the work function of graphene on SiC

Before applying graphene in electronic applications, it is crucial to find ways to alter the type and concentration of charge carrier concentration. Because of its two dimensional nature, classical ion implantation is not feasible for graphene and alternative methods are investigated.

Several approaches have been used to achieve doping in graphene. Basically it can be distinguished between electrical doping, which is performed by modulating the charge carrier

[0]Parts of this section have been published in Ochedowski *et al., Applied Physics Letter 102 (2013)*

concentration by an external voltage, or chemical doping, which has various subcategories. One is taking advantage of the substrate charge transfer which has already been been discussed in chapter 3.1. By carefully choosing the right substrate or a special surface preparation technique, the graphene sheet can be doped, which has been shown for insulating and metallic substrates [404, 320] [OO.01,OO.02]. Another chemical doping method is attaching molecules to graphene which may act as electron donators or acceptors like NH_3 or NO_2, respectively [21]. The last one is substitution of carbon atoms in the graphene lattice with atoms like nitrogen (one excessive electron) or boron (lacks one electron) [21, 22].

Ion irradiation and implantation have already been investigated as a potential tool for substitutional chemical doping. For example doping of graphene with keV ions has been theoretically studied [177] and it was shown, that the substrate enhances the chances for successfull indirect implantation. Experimental studies included N^+ irradiation with subsequent NH_3 annealing, which resulted in n-type doping and keV ion implantation in epitaxial graphene on SiC as well as Ni(111), performed by keV N ions at high fluences [405, 406, 407]. Using transmission electron microscopy, single atom substitution in freestanding graphene could be shown, but the samples could not be investigated with respect to changes in charge carrier concentration [408].

In this section, it will be experimentally studied, if swift heavy ion irradiation can be used as a tool for manipulating the charge carrier concentration in graphene as well. In this experiment, the findings from chapter 3.1 and 3.2 will be taken into consideration. To prevent the formation of foldings, the samples are heated in situ to remove the interfacial water layer. After the irradiation, the doping is investigated by using Kelvin probe force microscopy and the changes in the work function of graphene due to the irradiation are evaluated. These measurements are performed in situ to exclude possible doping effects because of chemisorbed adsorbates and water molecules from ambient conditions. Here, the substrate of choice is SiC(0001) (Pam-Xiamen, Xiamen - China), as it is material which is considered as very resistant towards high energetic ion irradiation and the intercalated water film can be completely removed in situ by heating the sample to about 500 °C.

A graphene flake containing graphene sheets of various thicknesses prepared this way is shown in fig. 6.1 (a) with the corresponding work function map in (b). While the interfacial water could be completely removed at the interface between graphene and SiC, remnants of the local water adlayer are still intercalated between graphene layers as marked in fig. 6.1 (b). The water adlayers are visible in the work function map, too, as an additional contrast. The work function of graphene on SiC is increasing with decreasing layer thickness and single layer graphene exhibits a work function of 4.4±0.06 eV and n-type doping as already discussed in chapter 3.1.

After these measurements the samples are transferred in ambient conditions to the IRRSUD beamline at the GANIL for swift heavy ion irradiation. The samples are irradiated with 91 MeV Xe^{23+} ions under a glancing angle of incidence of 0.3° with respect to the sample surface. The ion fluence was adjusted to ∼4 ions/μm^2 to prevent overlapping ion tracks. The samples are measured again in situ and the results are shown in fig. 6.1 (c) and (d). The topography reveals faint surface tracks created in single-, bi- and few-layer graphene,

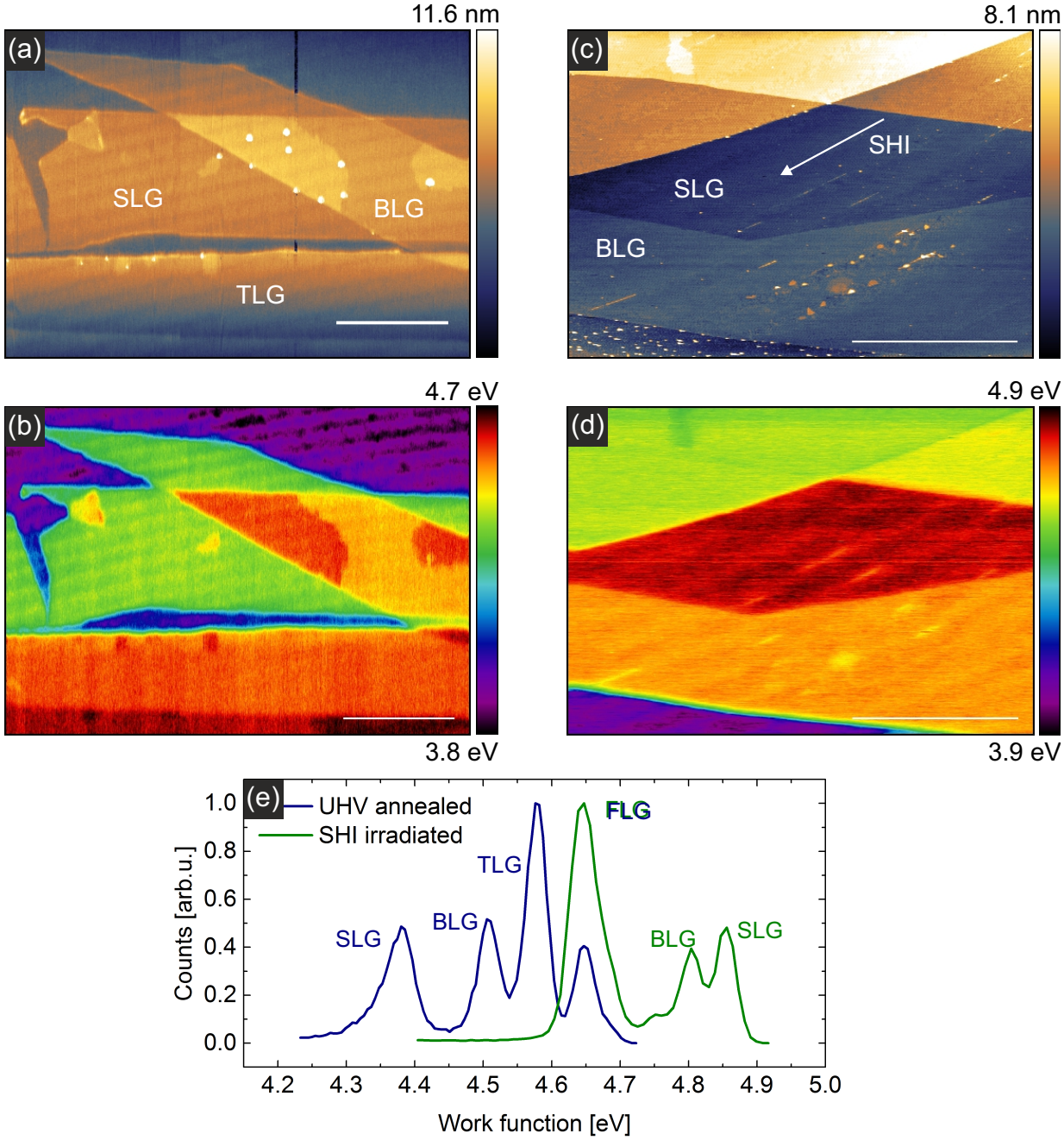

Figure 6.1: (a) Topography of an in situ annealed graphene flake on SiC(0001) with the corresponding work function map in (b). The work function is increasing with the layer number. (c) Topography image of a graphene flake on the same sample after SHI irradiation (91 MeV Xe, θ=1°) with the corresponding work function map in (d). The work function is now decreasing with layer thickness. (e) Histogram evaluation of the work function of graphene before and after SHI irradiation. Scale bars in all images are 1 μm. Image adapted from [OO.07].

which are oriented along the ion trajectory. The average length of these protrusions is 860±290 nm and no defects besides the surface tracks are observed.

The effect of the SHI irradiation on the work function is even more profound. In contrast to the pristine and heated graphene flake, the work function is now decreasing with layer thickness while the work function of SiC is almost unchanged. The plot in fig. 6.1 (e) shows the work function histograms taken from (b) and (d), which display the large shift of the work function from 4.4±0.06 eV to 4.85±0.06 eV. These correspond to an effective transition from n-type to p-type doping for single layer graphene [409].

In fig. 6.2 a zoom-in image of a surface track created by swift heavy ions in graphene on SiC is presented. The topography reveals that the surface tracks consist of a chain of protrusions, which are up to 3 nm in height (average height of 1.25 nm) and have a width of about 10 nm. The work function around the surface track in (b) corresponds to about 4.9 eV. The surface track itself shows a distinct change in the work function as it is lowered by ∼0.07 eV with respect to the surroundings.

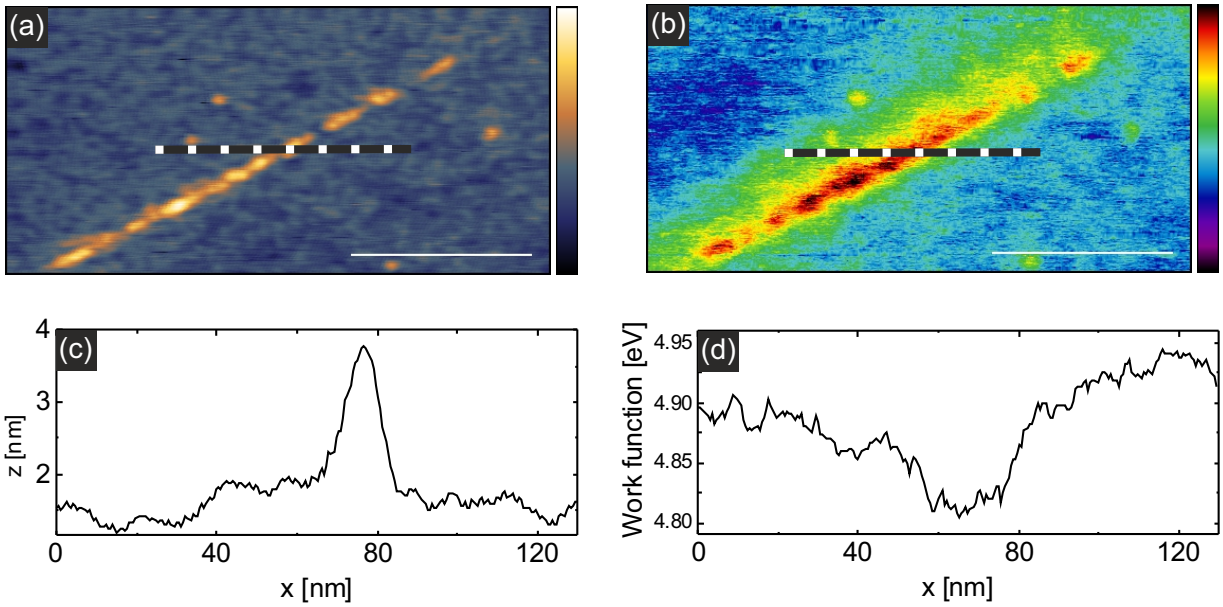

Figure 6.2: (a) Zoom-in image of one of the surface tracks created by the SHI irradiation on graphene/SiC. The corresponding work function map shows an increase of the work function for the surface track area. (c - d) Line profiles corresponding to the lines marked in c and d, respectively. Scale bars in all images are 100 nm. Image adapted from [OO.07].

The fact that the work function is strongly altered in areas with the surface tracks indicates that material properties are modified because of the SHI irradiation. There are two possible explanations for this. Firstly, the SHI ion produces a surface track in the SiC surface and the charge transfer properties are locally altered, which results in a different doping, or secondly, material from the SiC may be implanted into the graphene lattice. To test which one of these assumptions is the case, an additional experiment was performed.

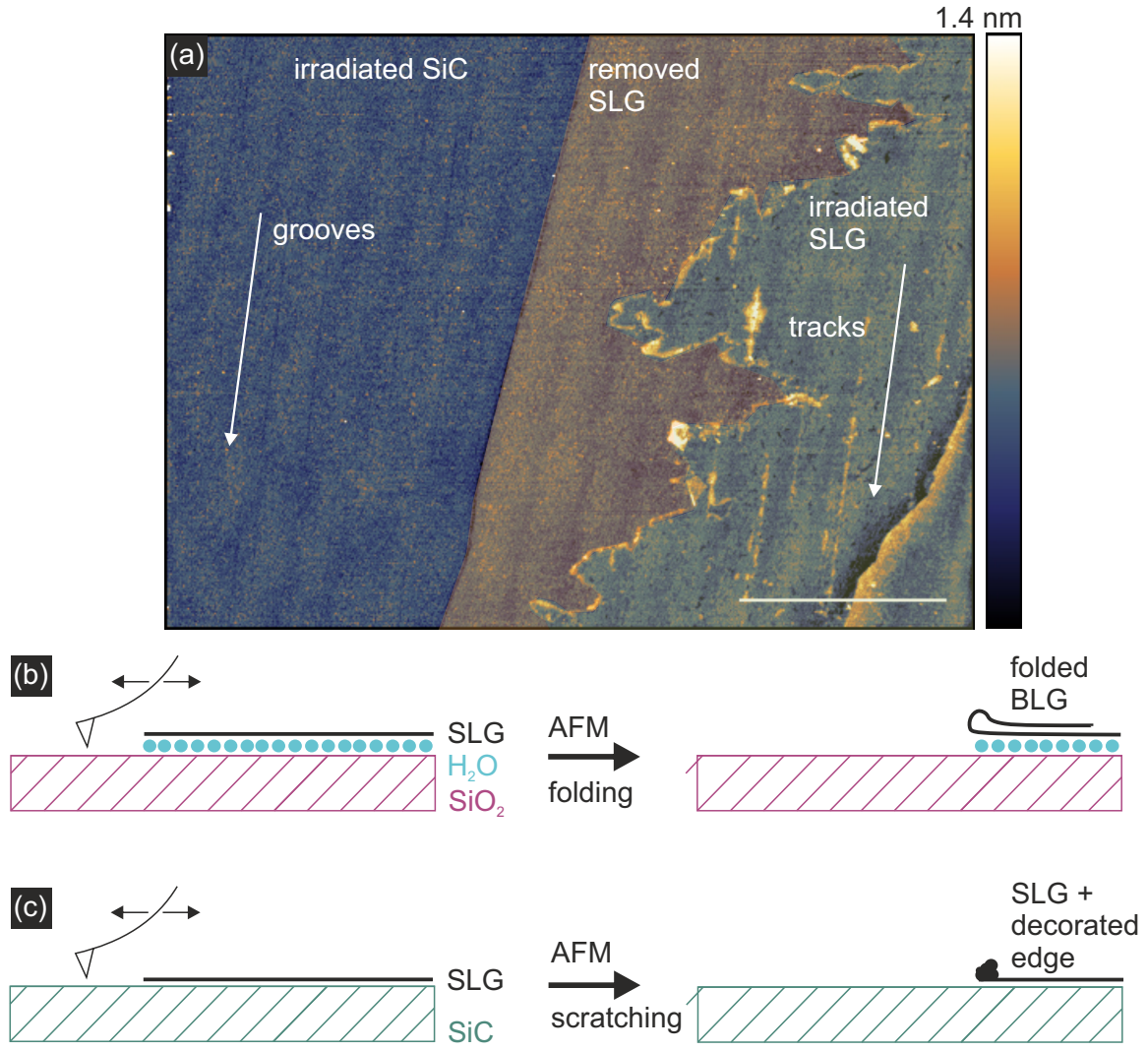

Figure 6.3: (a) Topography image of a graphene flake with surface tracks after removing part of the SLG flake using contact mode AFM (Scale bar 1 μm). On the left, grooves in the SiC surface can be observed. On the right, surface tracks in graphene are shown, which are not visible in the middle area (marked with transparent red), where the graphene flake with the surface tracks has been removed by contact-mode imaging. (b) Contact mode imaging of exfoliated graphene on SiO_2 can lead to folding of the graphene flake. (c) In annealed graphene/SiC samples (no interfacial water present), contact-mode imaging does not result in folding due to the strong adhesion between graphene and the substrate. By applying large forces to the AFM tip, the graphene flake can be scratched away.

The idea is to use contact-mode AFM imaging to fold back the single graphene layer and study whether surface tracks are visible on the exposed SiC surface or not. Folding graphene by contact-mode imaging has already been successfully performed on exfoliated graphene/SiO_2 systems and results in the formation of a folded graphene bilayer as shown in fig. 6.3 (b) [19]. These results could be reproduced on graphene/SiO_2, but using the same scanning parameters on heated graphene/SiC samples did not induce any kind of folding. This is most likely caused by an enhanced graphene - substrate adhesion due to the removal of the interfacial water layer. Therefore higher forces have been applied to the AFM tip, which did result in a removal of graphene on top SiC, but the graphene is not folded but rather scratched away from the substrate, as shown in fig. 6.3 (c).

The AFM topography, imaged using tapping-mode in ambient, after this procedure is shown in fig. 6.3 (a). On the left side, the bare irradiated SiC surface is shown. In contrast to the surface tracks in graphene, which consists of elongated lines of protrusions (see right side of the image), grooves with a depth of about 0.2 nm are observed in the SiC surface. The length of these grooves correspond to the the length of the surface track in single layer graphene on this sample with about 800 nm. In the middle of the image, single layer graphene has been removed by contact mode imaging and it can be observed that no protrusions are created in the SiC surface underneath. This can be taken as proof that the surface tracks are indeed created inside the graphene sheet.

Next, the plot in fig. 6.4 sums up the transition of the work function of graphene on SiC(0001) from its pristine (with interfacial water) state to annealed and finally irradiated with SHI. The values for annealed and irradiated single layer graphene might vary from the ones presented in fig. 6.1, as the values in the plot are averaged values from multiple measurements. The work function values of graphene can be directly related to the charge carrier concentration as it corresponds to a Fermi level shift with respect to the Dirac point in the following way: $n = \frac{1}{\pi} \cdot (\Delta E_F / \hbar \nu_F)^2$. Assuming ν_F=1·10^6 m/s for the Fermi velocity and using the value of undoped single layer graphene of 4.57±0.05 eV reported by Yu et al. [409], it can be deduced that annealed graphene on SiC is n-type doped with a charge carrier concentration of 3.6·10^{11} electrons/cm^2 and irradiated graphene on SiC is p-type doped with a charge carrier concentration of 8.5·10^{12} holes/cm^2. Thus the net transfer of carriers into SLG amounts to 9·10^{12} holes/cm^2.

To exclude the possibility that the doping is not caused by mechanisms unrelated to the irradiation special care has been taken. Because of the transfer to the beamline and the exposure to bad vacuum conditions(p_b=10^{-6} mbar) during the irradiation, the samples may have been contaminated by carbonhydrates or water for example. As already stated in chapter 4.1, the exposure to ambient conditions alone might be enough to result in p-type doping of the graphene layer. Therefore, after the transfer from n-type to p-type doping has been observed, the sample has been annealed in situ and again no change of the work function was observed. Additionally, another sample which underwent the same processing steps but without the irradiation has been investigated, finding again n-type doping after thermal treatment. From this, contaminations can be safely excluded as the origin of the p-type doping after irradiation and the observed hole doping must be related

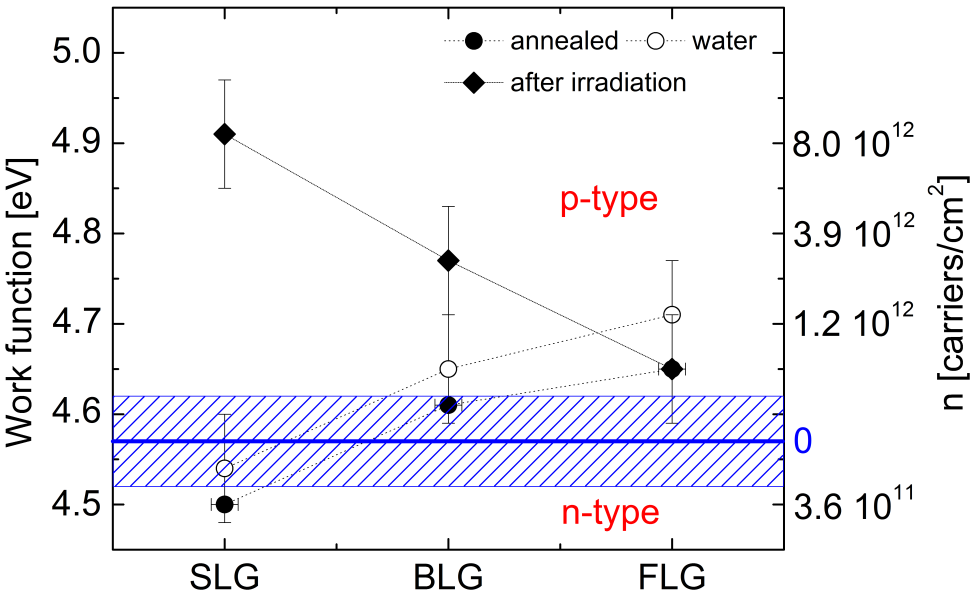

Figure 6.4: Plot summarizing the work function measurements of pristine, annealed and irradiated graphene on SiC(0001). Due to the irradiation graphene transition from n-type to p-type doping. Prior to heating, graphene on top of an intercalated water film has been measured as well. Image adapted from [OO.07].

to the irradiation itself.

Using swift heavy ions, direct implantation of ions can be excluded as well, as their projected depth is about 50 nm [122] and the ion fluence is far too low. A possible explanation is that the conductive graphene with its extraordinary charge carrier mobility is affected by the surface tracks which may act as electron acceptors. Whether this is feasible or not can be estimated by the following: Three tracks per μm^2 with each track being 860 nm long and 10 nm wide correspond to a modified area per μm^2 of $0.26 \cdot 10^5$ nm^2. On the other hand, the induced doping is due to an accumulation of $1 \cdot 10^5$ holes/μm^2. This means that about five to six graphene unit cells would have to contribute one hole each to achieve the observed level of doping. Based on this simple comparison, it is entirely possible that the track region acts as acceptor for electrons, which results in a depletion of electrons over the whole graphene flake.

The remaining question is, how the tracks can act as acceptors. Recalling the results shown in fig. 6.3, it is most likely that material which is being removed during the creation of the surface grooves in the SiC surface is incorporated in the graphene sheet above. It has already been proposed in a theoretical paper by Zhao et al. that indirect implantation of graphene might be possible with keV ions [407]. In this case, swift heavy ions are used, which normally result in the formation of folding [19]. By heating the sample prior to irradiation, however, the folding can be prevented and graphene is able to catch sputtered material as already shown in chapter 3.2. When the SHI induces defects in the graphene lattice along its trajectory, atoms from the substrate material could replace carbon vacancies.

A similar effect has been reported by Wang et al., who studied the deposition of different atoms in graphene vacancies [408]. The constituents of the substrate, which are basically silicon (as carbon is already present in graphene) and oxygen from the native oxide layer covering the SiC surface, are most likely to play a role in this process. Because of the limited spatial resolution in the KPFM measurements, a detailed analysis of the chemical composition is not so simple. Therefore the creation of the grooves in the SiC substrate will be thoroughly investigated in detail in the next section to give further insights into the doping process of graphene.

6.2 Graphitic nanogrooves in SiC

Because of its unusual thermal, mechanical and electronic properties, SiC is an important material used as a biocompatible substrate [410], in nuclear [411] and electronic applications [412]. Just recently, it has attracted even more attention as an excellent material for the epitaxial growth of graphene with very high electronic quality [413, 414, 415, 416, 417] or quasi free-standing graphene by hydrogen intercalation [418, 419]. Additionally, there are a lot of defect related phenomena in SiC like many-body effects in the excitation spectrum of a defect in SiC or defect induced magnetism in neutron irradiation SiC single crystals have been found [420, 421]. Furthermore, it was demonstrated that a Si vacancy in SiC could serve as a quantum system for a single photon source [422].

The primary reason why SiC(0001) was chosen as the substrate for the graphene/SHI doping experiment however is, that it is known for its resistance even in environments with high levels of ionizing particle radiation, for example in fission reactors or in space. In the material science community it is well known that swift heavy ion irradiation can be used to study materials under extreme conditions, which otherwise cannot be achieved [162, 423, 424, 425]. However, corresponding experiments revealed that significant displacement of atoms in SiC can only be obtained by electronic excitation when the energy deposition is above S_e=34 keV/nm, which is not achievable with monoatomic projectiles [359]. Irradiation with SHI projectiles below this value is supposed to only result in isolated point defects. Depending on the fluence, this point defects can accumulate, but this will still not give rise to complete amorphization of the material [426]. Instead, even recrystallization has been observed, which is attributed to competing effects due to nuclear collisions and electronic excitation [426, 427, 428]. All these experiments have been performed using perpendicular incidence irradiation. However, for glancing incidence irradiation, as shown in the previous section, surface modifications using swift heavy ions with far lower energy depositions of $S_e \leq$20 keV/nm can be obtained.

For a detailed analysis of the grooves, more samples were irradiated using swift heavy ions with a similar energy deposition than the ones used in the previous section. The irradiation was again performed at the IRRSUD beamline of the GANIL, one with a stopping power of S_e=17 keV/nm (81 MeV Ta^{24+}, fluence $1{\cdot}10^9$ ions/cm^2) at an angle of θ=1.1° and the other with S_e=22 keV/nm (117 MeV Pb^{31+}, fluence $1{\cdot}10^9$ ions/cm^2) at an angle of θ=0.6-4.2°. The angle θ is measured with respect to the sample surface. The overall error bar for the incidence angle is below 0.2°.

[0]Parts of this section have been published in Ochedowski *et al., Nature Communications 5 (2014)*

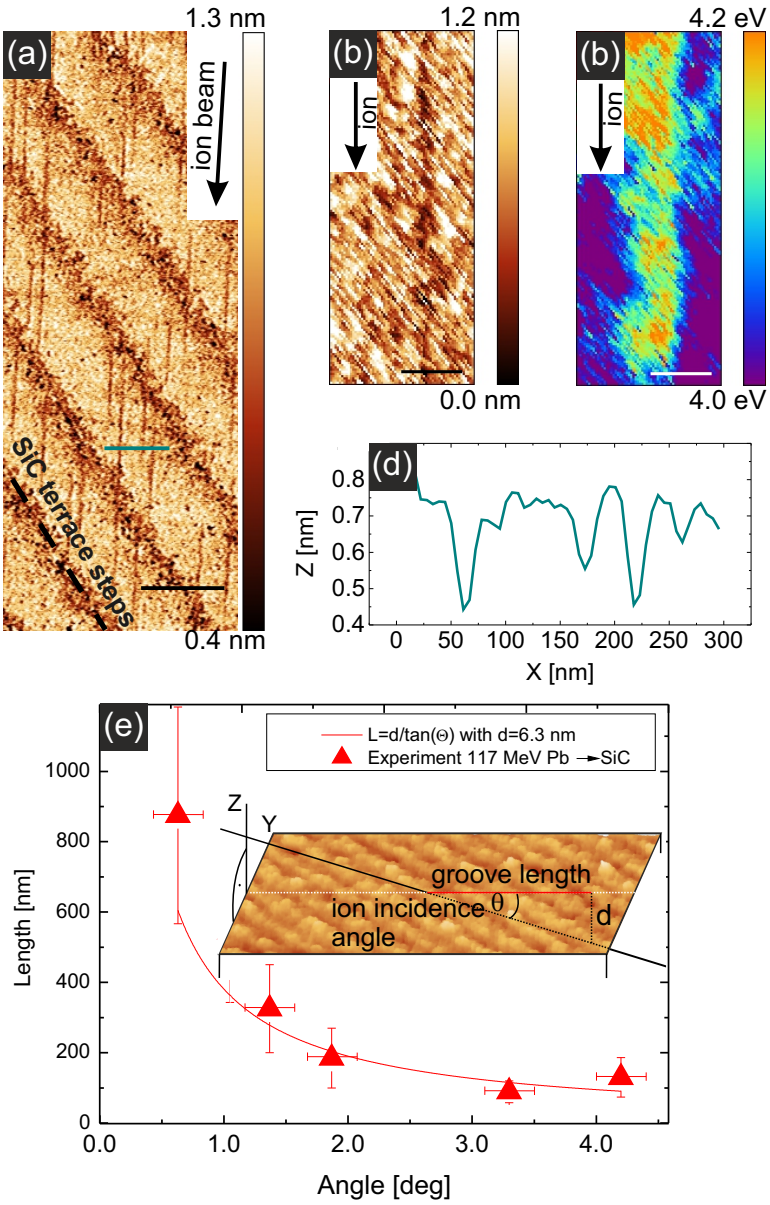

Figure 6.5: (a) Topography (tapping mode) of surface grooves in SiC(0001) irradiated with 81 MeV Ta (θ=1.1°, fluence 10 ions per μm^2, scale bar: 400 nm). (b,c) Topography (NC-mode) and corresponding work function map of a surface groove in SiC irradiated by 81 MeV Ta ions (scale bar: 400 nm). (d) Line profile of the green line marked in (a). (e) Length of the surface grooves with respect to the incidence angle of the SHI. Values measured in ambient, samples are irradiated with 117 MeV Pb ions, the fit corresponds to the relation $L = d/tan(\theta)$. Image adapted from [OO.15].

After the irradiation the samples are investigated using AFM in ambient using tapping mode. As observed for the irradiation with 91 MeV Xe^{23+}, extended but shallow depressions on the surface running along the ion beam direction are created as can be seen in fig. 6.5 (a). The constant width of ∼20 nm and depth of 0.2 nm (see fig. 6.5 (d)) suggest that only the topmost layer of atoms is affected by the SHI irradiation. To get more information of the grooves, the samples were investigated in situ using non-contact AFM and Kelvin probe force microscopy, which is shown in fig. 6.5 (b) and (c). By analyzing a number of samples, it is found that the length of the grooves varies with the angle of incidence θ, the results are shown in fig. 6.5 (e). With decreasing incidence angle of the SHI, the surface grooves significantly increase in length. The statistical deviation in the lengths are mainly due to the beam divergence of ∼0.2° and the statistical nature of the stopping process. The data points in the graph roughly follow the relation $L = d/\tan(\theta)$ (best fit for d yields d=6.3 nm), where L is the length of the surface modification induced by the SHI projectile and d is a constant that corresponds to the maximum depth from which SHI-related damage can still be detected at the surface [157]. Notably, for small angles a distinct deviation can be observed, which will be discussed further below.

As the measured depth of the surface grooves of 0.2 nm is fully compatible with a region of atoms missing at the topmost layer, the main question is which atoms exactly. The KPFM measurements shown in fig. 6.5 were calibrated using exfoliated graphite flakes as described in chapter 2, which results in the work function map. The ion-induced surface grooves can be clearly distinguished in the work function map, as the work function is increased from 4.0 eV (for the SiC surface) to 4.2 eV. This shift upwards means, that the work function of the groove is approaching the value for graphene on SiC with 4.5 eV. This is in full agreement with the topographic data, if we assume that the topmost layer of silicon is removed and the carbon is left behind in the groove. The reason for the shift being too low to actually reach the 4.5 eV of graphene is most likely due to the limited spatial resolution in the KPFM measurement which is 100 nm. The grooves however are much smaller with a width of about 10 nm. The sign of the shift however suggests that the grooves are graphitic in nature.

To exclude the possibility that the grooves are created in the native oxide layer covering the SiC surface rather than the SiC, the irradiated samples were etched with hydrofluoric acid for 10 min. The AFM images before and after irradiation are shown in fig. 6.6. After the etching process, the terrace steps on the SiC appear sharp and straight, proving that the etching was successful. The grooves are still visible even after etching, which can be taken as proof that the grooves are indeed formed in the SiC surface itself and not in the oxide surface layer.

These SHI induced surface grooves clearly differ from other modifications observed in dielectrics like Al_2O_3, $SrTiO_3$, TiO_2, SiO_2, CaF_2 or PMMA when irradiated under similar conditions [162, 429, 430, 160, 164]. In all these surfaces, elongated protrusions (for example chains of hillocks) are formed that follow the ion trajectory. In case of $SrTiO_3$, these have been successfully interpreted as the remnants of a molten zone [162], originating from a rapidly quenched thermal spike [145] induced by the ion. In contrast to this, grooves with

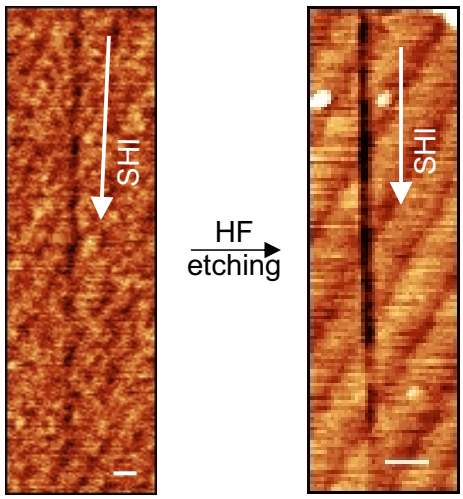

Figure 6.6: Hydrofluoric acid etching of an irradiated SiC(0001) results in the removal of the native SiO_x layer (81 MeV Ta; θ=1.5°, scale bar: 40 nm). The surface grooves are still visible after etching and the terrace steps are more strongly pronounced. Image adapted from [OO.15].

missing material can be observed here instead of protruding molten material. In the next section, it will be presented why SiC behaves so differently.

The AFM topography and KPFM data strongly suggest that the groove is a result of missing silicon atoms. A preferential ejection of Si atoms along the ion trajectory has to be triggered by a temperature rise sufficient to reach the sublimation point of Si in SiC. Exactly this process is used to grow epitaxial graphene on top of SiC. Heating up SiC to T=1400 K, the Si is sublimating and the carbon atoms left are rearranging into graphene [431]. If sublimation is of relevance in this case, it would not be necessary to reach the decomposition temperature of 3,010 K of SiC to form surface grooves, but much lower temperature and thus an energy deposition well below the proposed threshold of S_e=34 keV/nm would suffice. The exact temperature needed in this case is not known as the thermal spike occurs on a time scale of about a few picoseconds. Therefore a higher temperature of T=1900 K than the one used for epitaxial graphene growth (1400 K for a much longer period of time) is used. Note, that this mechanism can only be relevant to the surface and not in the volume, as Si atoms cannot evaporate from a heated zone surrounded by an intact crystal lattice. This is the reason for the constant trench depth observed in our data.

To test whether the origin is indeed connected to the removal of Si, the lattice temperatures are calculated by the two-temperature model. The region where the temperature rise results in a permanent modification is commonly called a "track", which is assumed to manifest itself as a groove on the surface in this case. The code used here is the same as in chapter 3.2, where it has been successfully applied to describe the formation of rifts in single layers of MoS_2. Here, for SiC the TTM calculations have been performed by Orkhan

Osmani, who has written the software. It is a fully three-dimensional version of the TTM, which is necessary to take into account that the process is taking place at the surface and thus breaking the cylindrical symmetry. As already described in chapter 1.2, the electron-phonon coupling strength is a crucial parameter for this calculation and in the case of SiC it has not been determined experimentally yet. An often employed approximation is to treat the electron-phonon coupling parameter g as a constant, which is also been done in the present calculation. Here, the calculated groove length is fitted to the experimental length, shown in fig. 6.5 (e) which gives a g value of $g = 4 \cdot 10^{18}$ $\mathrm{Js^{-1}m^{-1}K^{-1}}$. This value is very close to the value of $g = 6 \cdot 10^{18}$ $\mathrm{Js^{-1}m^{-1}K^{-1}}$, which is basically an estimation based on the band gap of the target material [432].

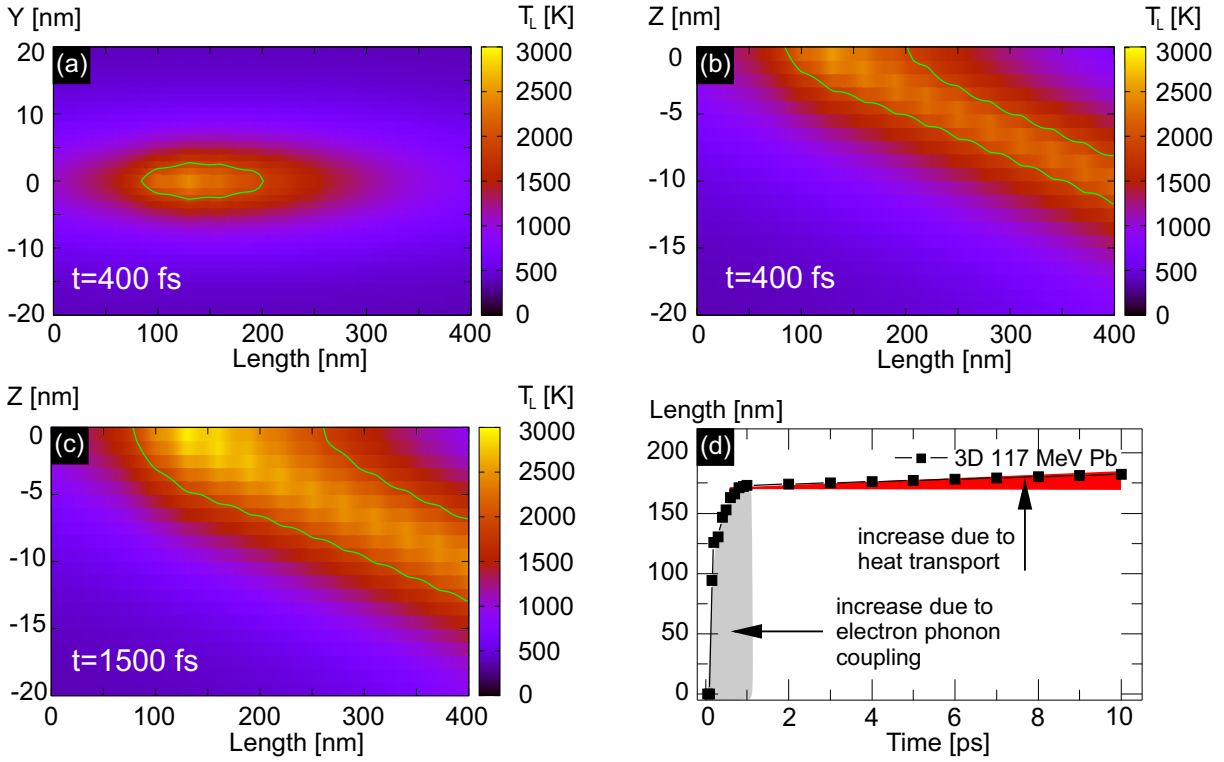

Figure 6.7: Temperature profiles after ion impact. Three-dimensional TTM calculation for SiC(0001) irradiated with 117 Pb (θ=1.9°) at 400 fs. (a) topview (b) sideview and (c) 1.5 ps after the ion impact. (d) Heat is still transported at a time when the temperature gradient between electronic and lattice temperature has already vanished. Image adapted from [OO.15].

The results of the calculations are shown in fig. 6.7. The length of the grooves is determined by the extension of the surface region, which overcomes the sublimation temperature of T_{sub}=1900 K. The impact point of the SHI projectile is chosen to be at x=100 nm, y=0 nm and z=0 nm and z denotes the surface. The presented contour plots are the results for an irradiation with 117 MeV Pb ions at θ=1.9°. The results for 400 fs and 1500 fs after

the ion impact are shown in (a, b) and (c), respectively. The area enclosed by the solid contour line in the surface plane is at $T \geq$1900 K. Yet, the decomposition temperature of SiC is hardly reached and only in a small region.

The track length evolves with time and reaches a length of 174 nm after 900 fs solely because of the electron-phonon coupling. At this time, the electron and lattice temperatures are roughly in equilibrium and almost no heat transport between these two places is taking place. However, as it can be seen in fig. 6.7 (d), the track length is still growing until 6 ps, which is due to energy transported away from the trajectory. Being so close to the surface, this leads to a distinct increase in the groove length of 4% and a maximum length of 180 is achieved. The vicinity of the surface is essential for this extended track length, as the heat is not able to dissipate at the surface except via irradiation, which is rather ineffective compared to the heat transport in bulk material via diffusion. An additional effect can be observed in fig. 6.7 (c). The heated zone is not symmetric anymore but is extended further into the x direction. Thus, the projected track length is increased because of the presence of the surface.

In fig. 6.8 the experimental data and the simulation data for 1900 K long surface grooves are plotted as a function of the SHI incidence angle. In every case, the calculated data is within the error bar of the experiment, which shows a good agreement between experiment and the theory. Additional calculations have been performed by Orkhan Osmani, which are all published in [OO.15] and in the supplementary informations of this publication. There, the 3D TTM model is compared to the 1D TTM model and the threshold for surface groove formation in SiC is determined.

So taking the surface into account in the calculations prooves to be a huge benefit, but in principle both models give a satisfying agreement with the experiment assuming a partial sublimation of silicon. However, the fact that the 3D model still underestimates the length of the tracks may indicate a yet unidentified, additional process. Nuclear stopping can be ruled out in this energy regime and no angular deflection or collision cascades are observed. However, especially at the surface other mechanisms may contribute simply because mechanical constraints are less severe. In the case of Al_2O_3 for example, hillocks can be created using projectiles with an energy below the electronic stopping power threshold for amorphous latent track formation [429]. Here, the authors proposed Coulomb explosion as an alternative mechanism [134, 124]. There are more possibilities like microexplosions and shock waves caused by the thermal spike [433, 434], electronic sputtering [435] or an increased surface damage by coherent displacement of lattice atoms [436]. It would thus be very interesting to compare these TTM results with e.g. molecular dynamics simulations or to measure the kinetic energy and angular distribution of the ejected particles to shed deeper light into which mechanisms are all playing a role in here.

These findings strongly suggest that the doping of graphene on SiC is triggered by the implantation of silicon into the graphene lattice. To be able to use other SHI projectiles for this doping as well, the so-called damage threshold, that is, the minimum energy necessary to induce modifications in the target, has to be determined. For this purpose, the groove lengths for various Pb ion energies with a fixed incidence angle are calculated and shown

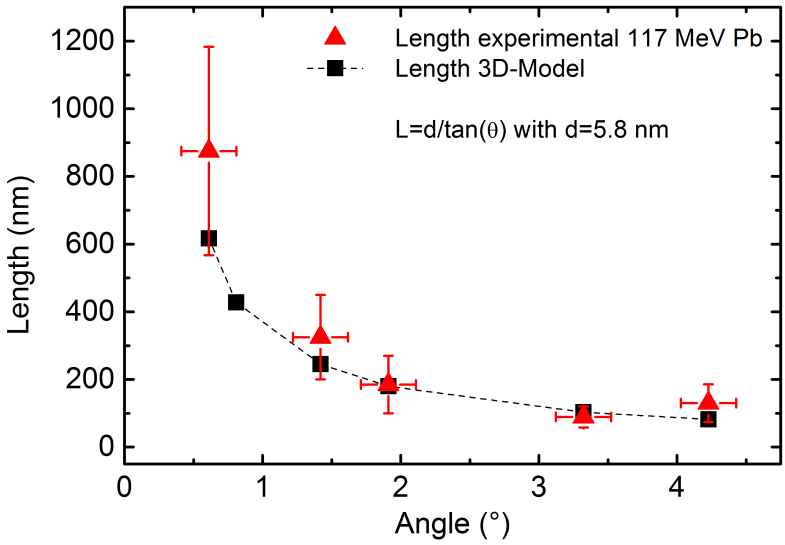

Figure 6.8: Experimental data (red triangles) are compared to the 3D-model (black squares with dashed lines to guide the eye). Calculated data is in every case within the limits of the experimental data. Image adapted from [OO.15].

in fig. 6.8 (b). Starting with 20 MeV, which correspond to a stopping power of 7 keV/nm, the groove grows in length continuously. In order to actually implant the sublimating Si in graphene, vacancies have to be created inside the graphene. Fortunately, the stopping power threshold for vacancy creation in graphene seems to be roughly the same (as determined in chapter 3.2).

6.3 Radiation hardness of graphene and MoS_2

Having proven that it is indeed possible to dope graphene using swift heavy ion irradiation by substrate mediated atom implantation, the question arises how graphene devices respond towards SHI irradiation. As SHI can be used to test whether the electrical devices stay operational in ionizing environments like e.g. outer space, this study has been extended to single layer MoS_2 as well. This allows a comparison of the radiation hardness between the two most common 2D-materials at this time.

For this study, field effect transistors have been prepared from exfoliated graphene and single layer MoS_2 flakes as described in chapter 3. Shown in fig. 6.9 (a) is a scheme of the experimental FET setup, where two Au contacts (drain and source) are patterned on the 2D-material flake and the Si substrate acts as a back gate. The resulting devices have a typical channel length of $L = 6\mu m$ and width $W = 3 - 12\mu m$. The field effect devices were characterized by their output ($I_D(U_{DS})$) and transfer characteristics ($I_D(U_{GS})$) and

[0]Parts of this section have been published in Ochedowski *et al., Journal of Applied Physics 113 (2013)*

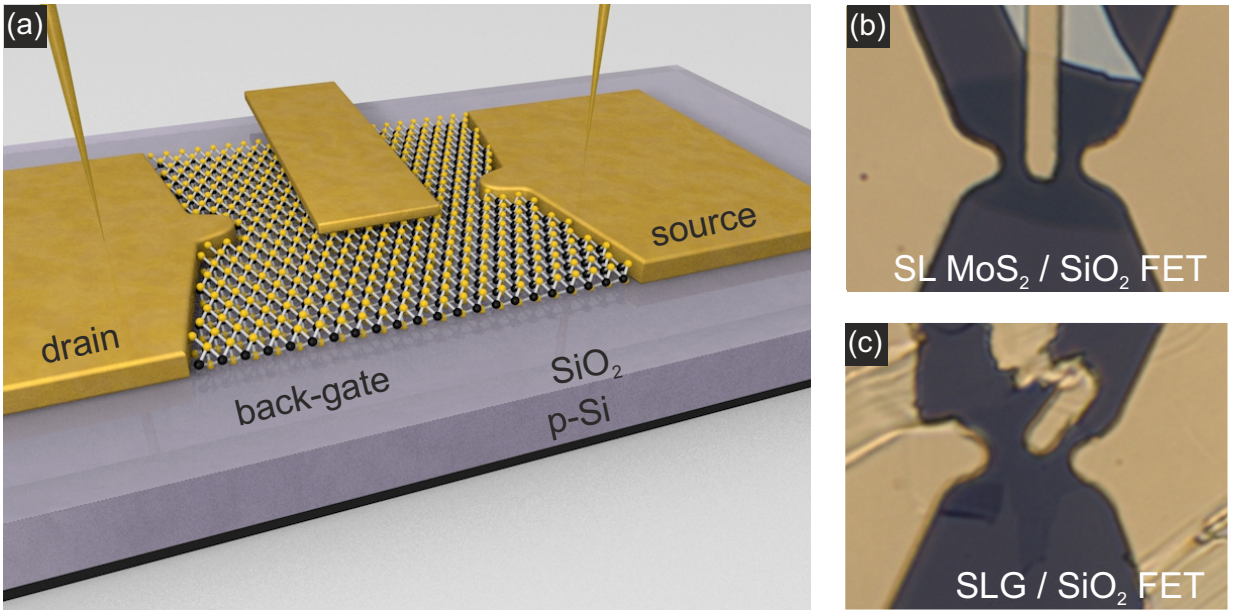

Figure 6.9: (a) Scheme of the experimental setup of the 2D-material field effect devices used for radiation hardness experiments. Optical images of a graphene and single layer MoS_2 FET in (a) and (b), respectively. Image adapted from [OO.08].

the conductivity σ and mobility μ were calculated using the formulas given in chapter 3. In fig. 6.9 (b) and (c) optical images of a single layer MoS_2 and graphene device are presented. The fact that the middle Au contact in (c) is broken has no influence on the experiment, as this contact is not used for the characterization.

After the field effect devices were prepared and characterized, the next step was the irradiation of these devices with 1.14 GeV U ions in the UHV irradiation setup at the M-branch of the swift heavy ion accelerator at the GSI. These projectiles are at the Bragg peak of the stopping power curve, which means electronic excitation is at its maximum. The irradiation was performed under perpendicular incidence angle with respect to the surface plane using three different fluences $4{\cdot}10^{10}$ ions/cm^2, $1.5{\cdot}10^{11}$ ions/cm^2 and $4{\cdot}10^{11}$ ions/cm^2 (corresponding to 400, 1500 and 4000 ions/μm^2). The projected length of these U ions is ∼46 μm [122], it is therefore safe to assume that the projectiles completely pass the drain and source contact as well as the 90 nm SiO_2 layer. Thus, the uranium ions will not be implanted near the surface and will not have any influence in the electronic properties of the electrical devices.

The results of the SHI irradiation on the transfer characteristics of SLM devices are shown in fig. 6.10. The drain source current is plotted as a function of the applied gate voltage. The upper panels show the transfer characteristics before irradiation, which show similar characteristics as SLM on SiO_2 reported in literature. The amplification sets in at gate voltages of about U_{GS}=-4 V (pinch-off) and typical mobility values are $(2.5{\cdot}10^{-4} - 1.7{\cdot}10^{-1})$ cm^2/Vs and charge carrier concentrations of $(9.8 \cdot 10^{11} - 2.5 \cdot 10^{13})$ n$_e$/cm^2.

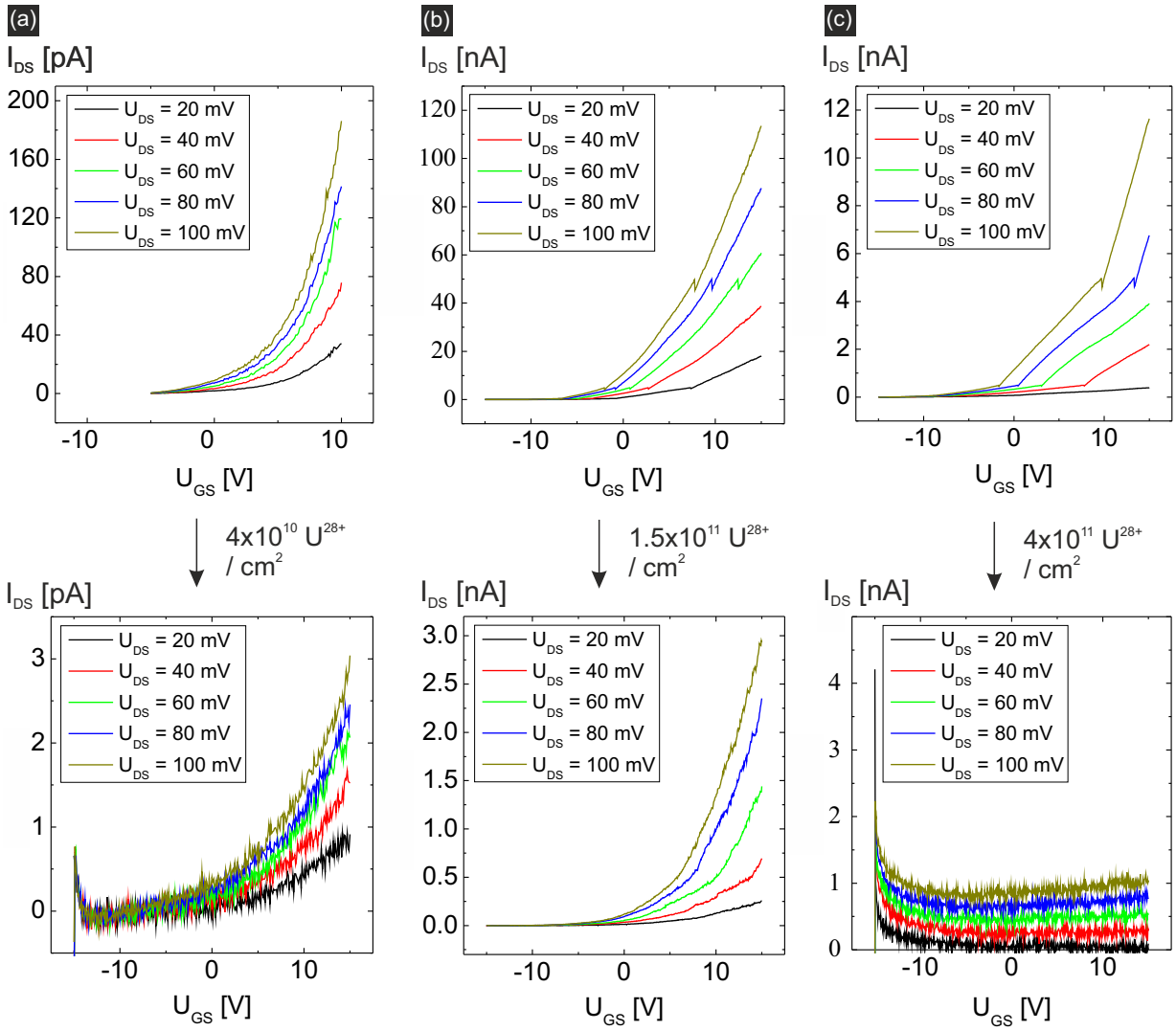

Figure 6.10: Transfer characteristics of single layer MoS_2 field effect devices. Upper panel shows $I_{DS}(U_{GS})$ before the irradiation with 1.1 GeV U with three different fluences of (a) $4{\cdot}10^{10}$ ions/cm^2 (b) $1.5{\cdot}10^{11}$ ions/cm^2 and (c) $4{\cdot}10^{11}$ ions/cm^2. Image adapted from [OO.08].

The lower panels show the resulting transfer characteristics after the irradiation and significant changes can be detected. At low fluences in (a), it can be observed that the drain current is decreased by two orders of magnitude. In the next fluence step in (b), the decrease in the current with respect to the unirradiated SLM FET is similar with a factor of about 1.5. Note, that the SLM FET was of a better quality than the one used in (a) to begin with. This may be a reason for the lower decrease in current even though the ion fluence was higher. For the highest fluence in (c), the SLM FET is no longer operational. To verify this result and exclude the possibility that the dielectric between the channel and the gate is breaking, another device of this type was subjected to a similar

high fluence irradiation. This second SLM FET as well was rendered non-functional after the irradiation.

Atomic force microscopy images in fig. 6.11 (a) of the irradiated SLM flake (lower panel) show many randomly distributed hillocks, which cannot be observed in the pristine flake (upper panel). The height of these varies strongly and depends on the scanning parameters. The ion-induced modifications can be seen more clearly in the corresponding phase image in fig. 6.11 (b) and about 1.62 % of the surface are covered with protrusions.

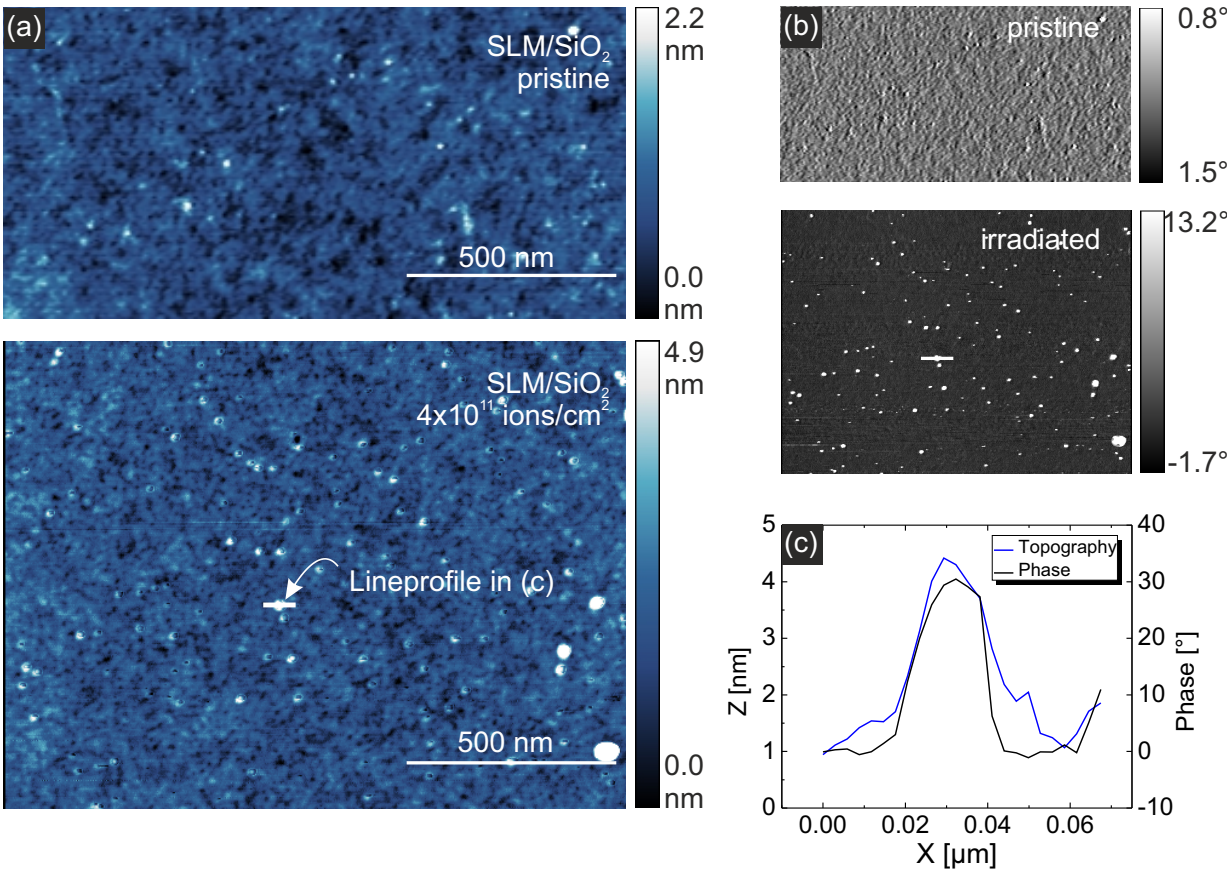

Figure 6.11: (a) AFM topography of pristine (upper panel) and irradiated (lower panel) single layer MoS_2 on SiO_2. The surface is covered with a lot of small protrusions and holes after the irradiation, the former can be clearly identified in the phase image in (b). (c) Lineprofile of the height and phase reveals a height of about 3 nm for a typical protrusion and a diameter of 20 nm. Image adapted from [OO.08].

Next, the data on the irradiated graphene FETs will be presented in fig. 6.12. The results for three SLG devices irradiated with the same fluences as the SLM devices are shown in fig. 6.12 (a-c). Here, the conductivity instead of the current is plotted as a function of the gate voltage. All graphene devices exhibit excess charge carriers resulting in a p-type

doping ranging from $1.3{\cdot}10^{13}$ to $1.4{\cdot}10^{13}$ ions/cm^2. The electron mobility varies between 243 to 390 cm^2/Vs and for the hole mobility values between 595 to 1198 cm^2/Vs are found. After the irradiation (fig. 6.12, blue circles), the graphene device, which was irradiated with the lowest fluence in (a), shows an increase in the mobility for electrons and holes, while the charge carrier density is slightly increased. For the intermediate fluence in (b), the carrier density still increases slightly while the mobility decreases significantly. Most interestingly, even after the irradiation with the highest fluence in (c), the graphene FET stays fully functional in contrast to the SLM FET. The carrier density is again increased and the hole mobility decreased. Another graphene device was irradiated again with the same fluence. This device stayed operational as well.

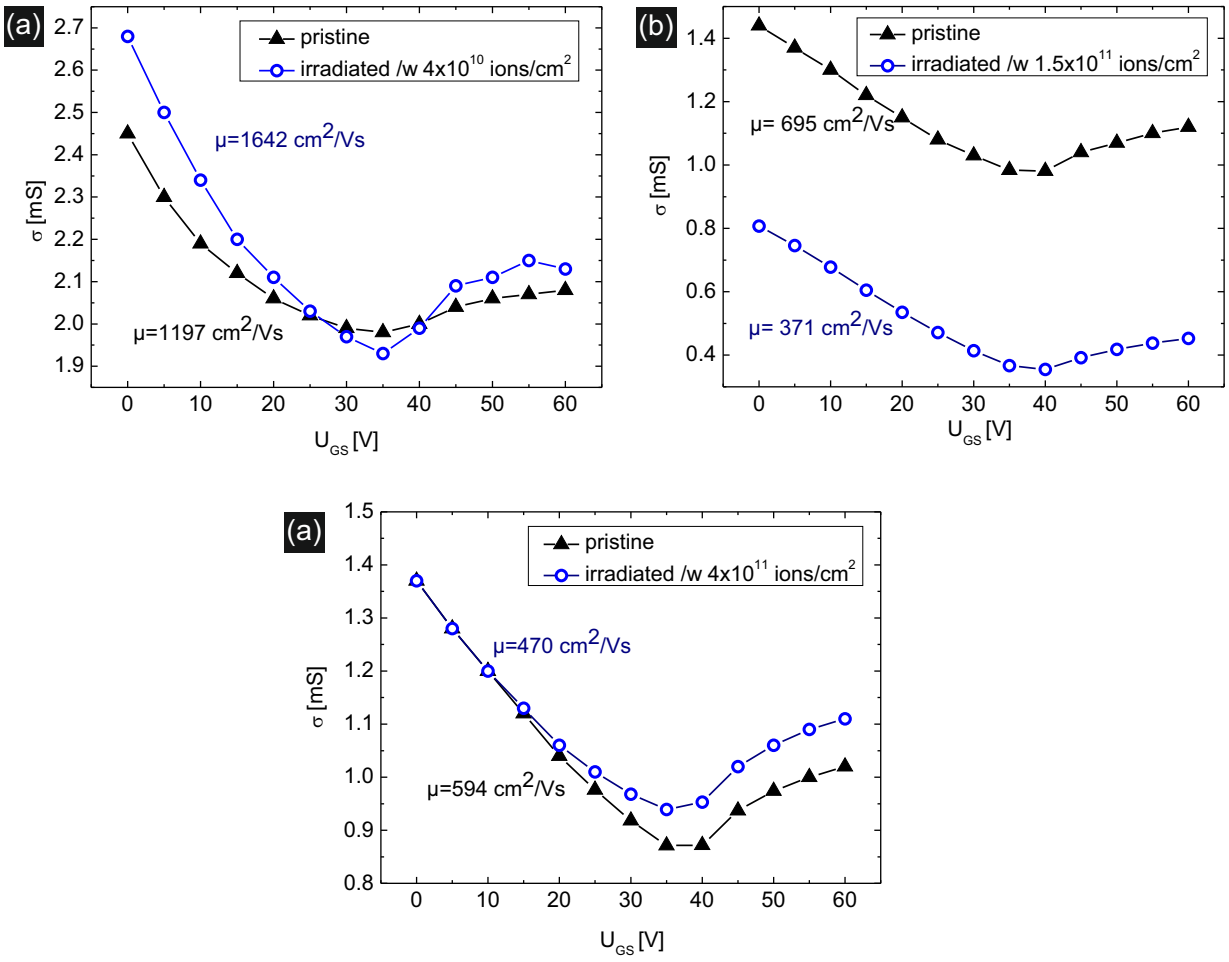

Figure 6.12: Conductivity of three different graphene field effect devices as a function of the back gate voltage. U_{GS} before (black triangles) and after (blue circles) irradiation with (a) $4{\cdot}10^{10}$ ions/cm^2, (b) $1.5{\cdot}10^{11}$ ions/cm^2 and (c) $4{\cdot}10^{11}$ ions/cm^2. Image adapted from [OO.08].

Atomic force microscopy measurements presented in fig. 6.13 of the graphene FET, irra-

diated with the highest fluence show a similar topography in its pristine state compared to the SLM flake in fig. 6.11. However, the irradiated flake in the lower panel in (a) shows a much lower density of protrusions as only about 1.02 % of the surface are covered. That defects induced by perpendicular incidence angle irradiation with SHI are hardly detectable using AFM has already been shown in chapter 5.2 (see fig. 5.3 (a)). However, although this sample has been irradiated with a fluence of only $4{\cdot}10^3$ ions/cm^2, the modifications observed in AFM seem to be far more distinct than the ones observed for the $5{\cdot}10^4$ ions/cm^2 irradiation. This is most likely due to the higher stopping power of S_e=31.52 keV/nm compared to only S_e=15.08 keV/nm for the previous Xe irradiation. In addition to the pits, rather large pits are created. These pits are most likely areas where graphene is in direct contact with the substrate rather than having an intercalated water layer beneath.

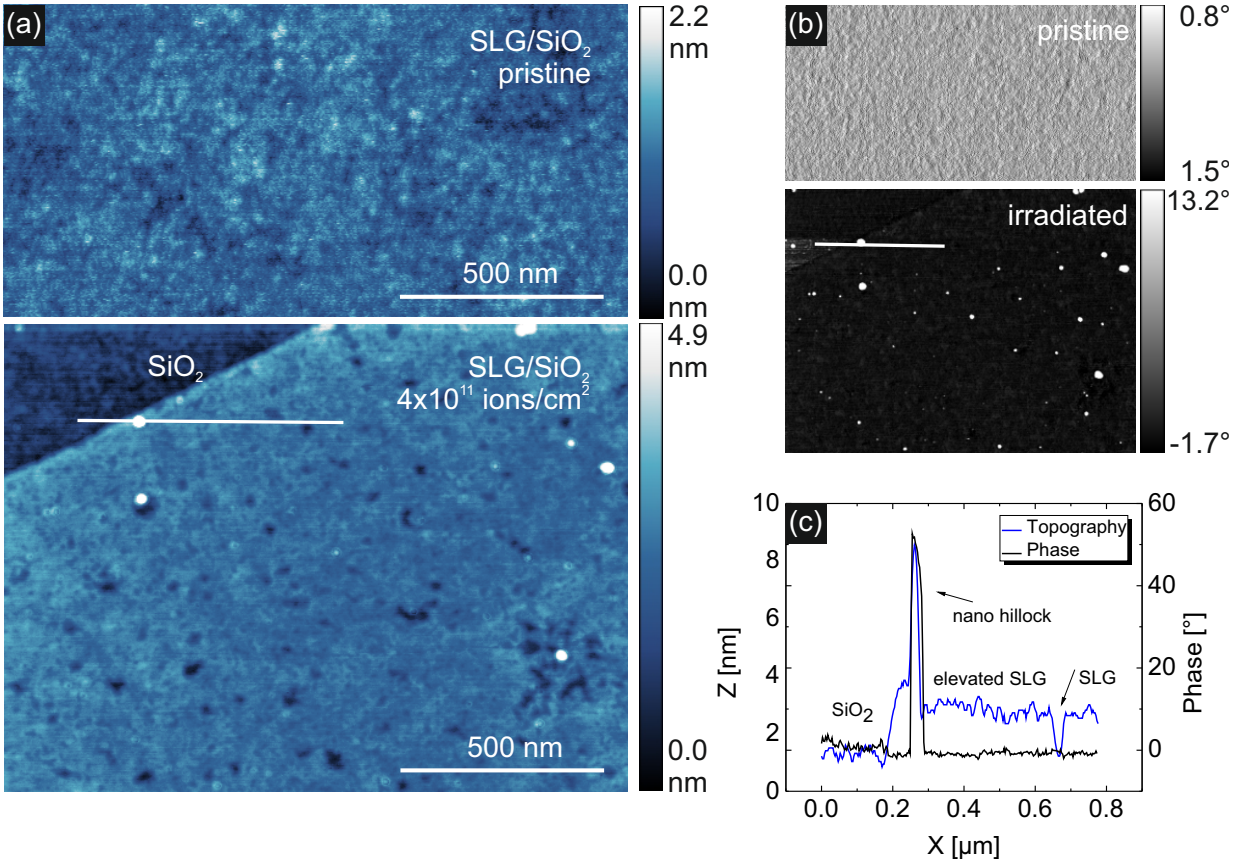

Figure 6.13: (a) AFM topography of pristine (upper panel) and irradiated (lower panel) single layer graphene on SiO_2. The irradiated graphene flake is covered with protrusions, which can be clearly identified in the phase image in (b). (c) shows a lineprofile, marked in the topography and phase image. The height of the hillocks reaches up to 10 nm with a hillock diameter up to 50 nm. The depth of the holes is limited to the apparent thickness of graphene. Image adapted from [OO.08].

All in all, the data above clearly suggests that the irradiation of 2D-material FET can have adverse effects: It can either lead to inferior device performance like for low fluence experiments for SLM FETs and high fluence graphene FETs or even lead to the destruction of the device as shown for high fluence irradiation on SLM or it can be used to improve the device performance as observed for low fluence graphene devices. Based on this data and the previous findings on doping graphene by glancing incidence irradiation, two relevant mechanism are proposed at this point: (1) doping and (2) defect creation. The latter seems to be straightforward as ion irradiation is known to cause structural defects, even in graphene [437, 173, 438, 439, 440, 177, 19]. It has been shown by combined scanning electron microscope/focused ion beam studies, that graphene possesses an enhanced resistance towards sputtering [168]. Here however, it has to be kept in mind that the cross sections for direct collisions of swift heavy ions with target atoms are negligible, so the electronic excitation has to be the origin for defect creation. This is in good agreement with the findings presented here. The SLM FETs are more easily destroyed then the graphene FETs. In the latter, the electronic excitation is spread more efficiently so that the energy density at a given time is too low to create extended defects, while in MoS_2 (being a semiconductor), the electronic energy dissipation will be less rapid and significant damage will occure more easily. Any defect will act as a scattering center and therefore reduce the charge carrier mobility or even result in the FET becoming non-functional.

In the case of graphene, the improvement of the electron and hole mobilities for low fluence irradiation can be taken as a sign for a similar doping mechanism as shown above, for SHI irradiation of graphene on SiC is taking place here. In the case of SLM FETs however, doping by SHI irradiation seems to be only a minor effect. The deterioration of the device performance by defect creation superimposes any possible doping effects. The AFM images in fig. 6.11 clearly show the huge structural changes due to the irradiation.

The experiments show that the performance of graphene FET with average mobility (see fig. 6.12 (a)) increases after low fluence irradiation, indicating either scattering centers being removed and/or charge carried density increase by doping. Assuming point like defect, average distance l between two impacts is proportional to $\sqrt{1/fluence}$, which amounts to 50 nm [292]. Thus, the scattering centers are far enough apart so that the doping is the dominant process.

Furthermore, the graphene FET with below-average mobility (see fig. 6.12 (c)) stays operational even after the high fluence irradiation, which was sufficient to destroy the SLM FET. Surprisingly, the degree of structural damage sustained by graphene seems to be comparable to MoS_2. Both, AFM and Raman spectroscopy data show that graphene is highly defective after the irradiation (see. fig. 6.13 and fig. 6.14). This proves the high radiation hardness of graphene, which was already predicted using atomistic simulations [174].

Transport characteristics of field effect devices are governed by various factors such as environmental adsorbates, unintentional channel doping due to substrate and contact interactions or fabrication steps, as well as oxide thickness, channel width and length [243, 441, 442, 443, 444]. In devices, where the latter is on the order of the depletion

layer width of the source and drain junction, the carrier density does not necessarily remain constant for high gate voltages, and short-channel effects must be considered [445]. In order to investigate these efffects in more detail and to clarify the influence of SHI irradiation induced contributions, further experiments with dedicated devices and under a controlled atmosphere have to be performed.

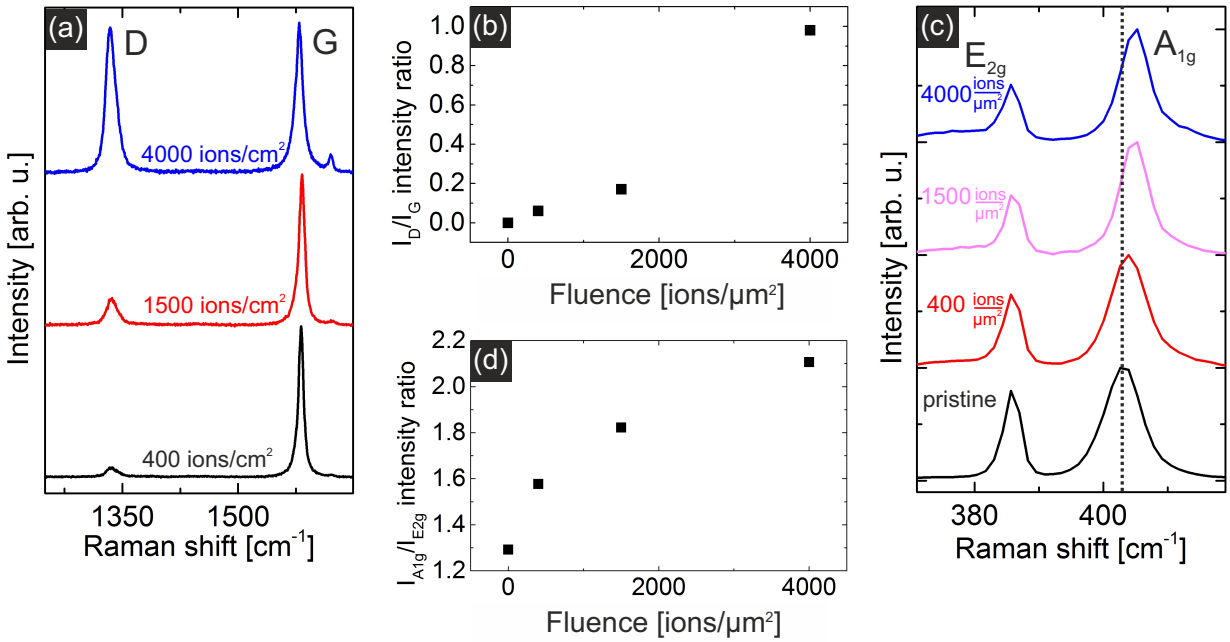

Figure 6.14: Raman spectroscopy studies of irradiated graphene and SLM FETs. (a) Raman spectra of irradiated graphene FET. (b) I_D/I_G intensity ratio plotted as a function of the ion fluence. (c) Raman spectra of irradiated SLM FETs. The A_{1g}-band is shifted to higher wave numbers with increasing defect density. (d) A_{1g}/E_{2g} intensity ratio plotted as a function of the ion fluence.

For further analysis, the samples were investigated by Raman spectroscopy. The origin of the Raman bands has already been introduced to the reader in chapter 3 and the I_D/I_G intensity ratio, which will be used to analyse the defects, has already been successfully applied in chapter 5. In fig. 6.14 (a), Raman spectra of the graphene FETs presented in this section are shown. Due to the SHI irradiation, the signature D-band, given at $\sim$1340 cm^{-1}, is continously increasing with the applied SHI fluence. The I_D/I_G intensity ratio, which is a measure for the average distance between defect sites [257], is plotted as a function of the ion fluence in (b). It increases almost linear with the ion fluence up to a ratio of 1 in the case of the highest fluence irradiation. Comparing this ratio with values obtained for Xe irradiation in chapter 5.2 we find that the fluence needed to achieve a 50% increase in the I_D/I_G ratio is higher by a factor of 12.5. This again shows that the defect size is apparently tunable by the electronic stopping power. In order to quantitatively estimate the amount of displaced/removed carbon atoms, the I_D/I_G ratio has to be compared with

the values from literature obtained for 90 eV Ar ion irradiation [257, 219]. A I_D/I_G ratio of 1 corresponds to about $7.5\pm2.3\cdot10^{11}$ defects/cm^2 assuming the sample has been irradiated with 90 eV Ar. As the sample was irradiated with only $4\cdot10^{11}$ ions/cm^2, defects induced by SHI seem to exceed the single (or even the double) carbon atom displacements typically caused by 90 eV Ar^+ ions.

To test if the defect creation in graphene is caused by the SHI projectile directly, the TRIM code [122] is employed to estimate the amount of sputtered atoms. As input parameter, the displacement energy for carbon atoms in the graphene lattice of 22 eV [289] is used and the sputtering yield is found to be around 0.36 atoms/SHI. As the samples have been irradiated with $4\cdot10^{11}$ ions/cm^2, the sputtered atoms amount to $1.4\cdot10^{11}$ ions/cm^2, which is far lower than the defect concentration found by Raman spectroscopy. Thus, the dominant process of defect creation is not direct sputtering by the projectile but must be related to other mechanisms. As the defect size is strongly dependend on the electronic stopping power, a mechanism like a thermal spike [141] in the substrate or Coulomb explosion [134, 133] is likely to happen.

The Raman spectra of the irradiated MoS_2 FETs are shown in fig. 6.14 (c). While the E_{2g}-band seems to be insensitive to the defects created by SHI irradiation, the A_{1g}-band is shifting to higher wave numbers with increasing fluence. Additionally the A_{1g}/E_{2g} intensity ratio is increasing with defect accumulation as plotted in (d).

The atom displacement energy for MoS_2 of 7 eV [446] is much lower than the one for graphene and therefore the calculated sputtering yield corresponds to 0.6 MoS_2 atoms/ion and 1 S atom/ion. However, for single layer MoS_2 there is no statistical data on the influence of defects on the Raman data. Only the photoluminescence signal has been investigated in this respect [447]. It is likely that the same mechanism for defect formation is taking place here as the one proposed in chapter 5.2. There, a strong local heating of the substrate, due to the SHI excitation and a thermal spike in the substrate, leads to a melting of the SLM sheet on top. For a simple estimation whether this mechanism is potentially applicable here as well, a TTM calculation was performed. Using the melting/decomposition temperature of MoS_2 (T_{melt}=1458 K), the resulting diameter of the modification is 13.33 nm. Using the melting/decomposition temperature which fitted the experimental data better, T_{melt}=1800 K, the resulting modification diameter is 10.62 nm. So in both cases the calculated values are below the typical hillock diameter measured in the AFM topography. This might indicate that the majority of these hillocks are due to more than one SHI impact and thus a larger diameter is measured.

6.4 Transport measurements of irradiated doped graphene field effect transistors

To conclude this chapter, first proofs of principle studies on SHI irradiated 2D-material FETs under glancing incidence angles will be presented. In fig. 6.15, transport measurements of a graphene and a SLM FET are shown, which were both irradiated with SHI under glancing incidence angle of $\phi \sim 1°$. In order to prevent unwanted effects like folding in the 2D-material, the samples were heated under UHV conditions for 2 hours (400 °C for graphene and 200 °C for MoS_2). As a consequence, surface tracks are created in the graphene sheet and rifts in the SLM crystal.

The graphene FET displayed in fig. 6.15 (a) shows a degradation of charge carrier mobility upon ion irradiation, which is most likely caused by defects generation induced by the ions. Especially the hole mobility is severely degraded upon irradiation. This behaviour could enable on/off switching in graphene devices, which is a very important point for graphene electronics.

For the MoS_2 FET SHI irradiation experiment, four contacts are patterned on a single layer MoS_2 flake. The irradiation with swift heavy ions was performed parallel to a pair of contacts as marked in fig. 6.15 (b). The output characteristics of the transport measurement reveal that the current between source and drain is enhanced if measured between the contacts oriented along the ion trajectory compared to the contacts that are oriented perpendicular to the ion trajectory.

[0]The following results have in part been published in the master thesis of K. Marinov, Universität Duisburg-Essen (work group Schleberger)

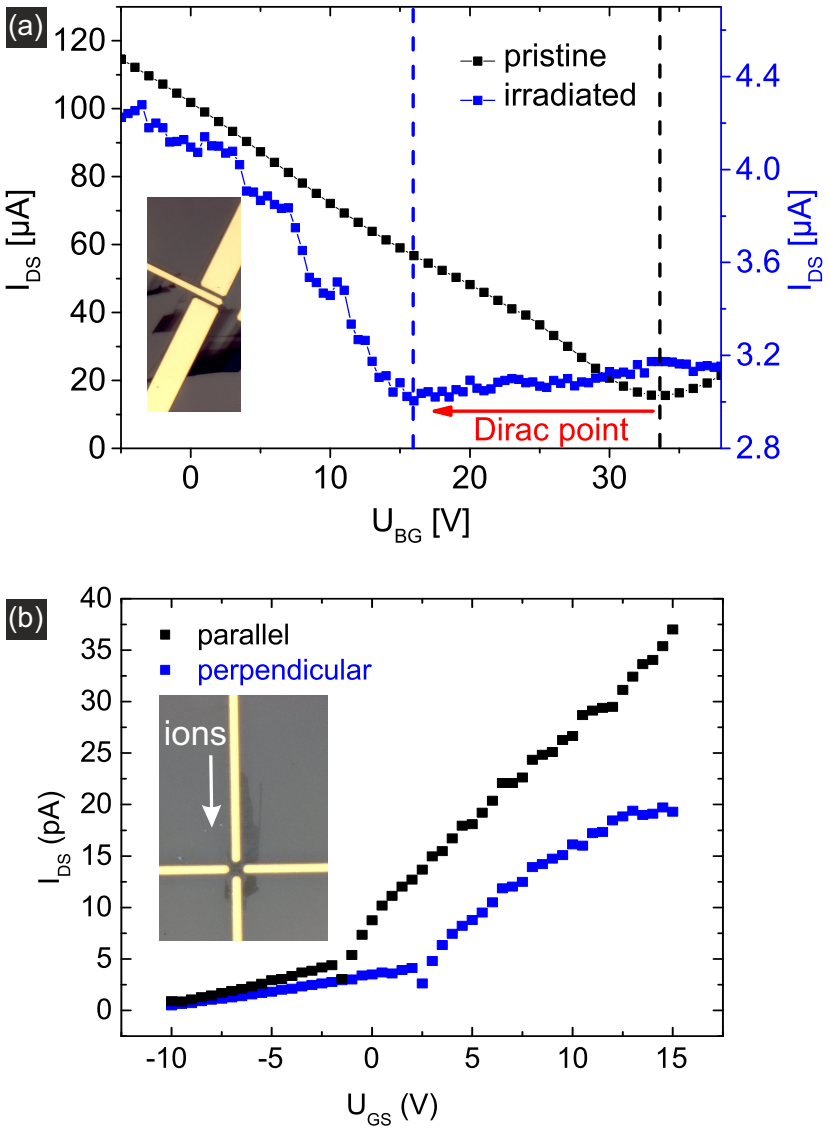

Figure 6.15: (a) Transport measurements of a typical pristine graphene FET (black squares) and an irradiated graphene FET (23 MeV I, grazing incidence 40 ions/μm^2). The irradiated graphene FET shows a shift of the Dirac point towards lower values and the disappearence of hole conductivity. (b) The irradiated SLM FET (23 MeV, grazing incidence 10 ions/μm^2) shows an enhanced conductivity parallel to the trajectory of the SHI induced modifications.

7 Summary & Outlook

As the discussion is already included in the respective chapters, this chapter will just briefly summarize the results and give an outlook of future experiments or potential applications of the findings.

In the first part of this thesis, Kelvin probe force microscopy has been used to study the work function of graphene and single layer MoS_2 under defined conditions (UVH) for the first time. It has been found, that graphene is significantly doped by the underlying substrate material due to the charge transfer effect. In the case of $SrTiO_3$ and SiC(0001), graphene is showing n-type behaviour with work functions of 4.4 eV and 4.5 eV, respectively. In the case of muscovite mica, graphene shows a p-type doping at first with a work function of 4.8 eV. However, by heating the graphene on mica to temperatures over 600 °C, the dehydration of the mica substrate results in the formation of nanoblisters in graphene, which is accompagnied with the formation of defects in graphene. Due to these defects the work function and thus the concentration of hole charge carriers are lowered and a transition to n-type doping can be observed. Further it has been shown that the substrate charge transfer is effectively blocked by water layers, which are trapped at the interface between graphene and the substrate due to the preparation of the samples in ambient. In case of $SrTiO_3$ and SiC, this intercalated water can be easily removed by annealing to $\geq$400 °C, which is not possible for the mica substrate because of the formation of nanoblisters.

For the single layer MoS_2 on SiO_2 system, quantitative Kelvin probe force measurements in situ have been performed for the first time. By patterning the SiO_2 with a reactive ion beam, the surface chemistry of SiO_2 has been locally changed. It has been shown that this local changes in the SiO_2 surface do have a significant effect on the work function of single layer MoS_2, thus proving that the substrate charge transfer effect has to be taken into account for MoS_2 as well. Additionally, it has been shown that contaminations due to photolithography processing have a great impact on the work function and the charge inhomogeneity of single layer MoS_2, which is crucial for the performance of MoS_2 devices.

These findings emphasize that in situ Kelvin probe force microscopy is a powerful tool to characterize two-dimensional materials. Detailed knowledge of the work function, charge carrier concentrations and charge inhomogeneity with a high lateral resolution is required for implementing these materials in applications and optimizing their performance. The next step would be studying the emerging field of stacked 2D-crystals, which do show very promising phenomena already [12]. Very interesting would be to study the effect of defects in single layer MoS_2 with Kelvin probe. For example, the adsorption of oxygen on defect sites has been shown to significantly increase the photoluminescence of MoS_2, which could

be studied in detail [447].

In the second part of this thesis, the effect of swift heavy ion irradiation on the morphology of two-dimensional materials has been studied. This has been done for graphene and single layer MoS_2, as these two materials differ significantly with respect to their charge carrier mobility, mechanical strength and sublimation temperature. For graphene, SHI irradiation perpendicular to the graphene sheet leads to only minor damage in the sheet in the range of 0.5 nm. However, by tilting the sample with respect to the ion beam, the size of the modification can be drastically increased. For θ=60 °C, nanopores in the range of 3 nm can be created. Starting from θ=45 °C, foldings in graphene upon ion impact are observed. These are basically larger nanopores, but the edges of these pores consist of closed bilayer edges, which exhibit new physical properties [347]. The mechanism behind the folding formation has been studied in detail, so the following scenario could be deduced:

First, the SHI pass through the graphene sheet, creating defects directly along the trajectory due to the intense electronic excitation. A thermal spike created in the underlying substrate causes the interface between graphene and the substrate to heat up to temperatures of typically 2000 K. Water present at this interface is thereby superheated and the pressure from this heated water causes the graphene to unzip and fold along the ion trajectory. Three conditions have to be met in order for graphene to fold on SiO_2. The incidence angle has to be below θ=45 °C, the energy loss of the projectile has to be above ∼6 keV/nm and a sufficient amount of water has to be present at the interface. Note, that the given values are only viable for the graphene on SiO_2 system. As the adhesion between graphene and the substrates as well as the temperature created by the thermal spike can vary distinctively, the size of the foldings for all materials under similar irradiation conditions (incidence angles, ion energy) has been shown to greatly vary.

The effect of SHI irradiation on single layer MoS_2 is more diverse. In fact, two different modification types have been observed, foldings similar to graphene and a new modification in form of nanoscale slit pores. It has been shown that the angle between the ion trajectory and the crystallographic lattice of MoS_2 determines, which of the two modifications occurs. Foldings have preferentially been observed, if the angle between the impinging SHI and a crystallographic edge of MoS_2 is a multiple of 30°. To explain the formation of the nanoscale slit pores, a new mechanism of indirect heating by the substrate has been proposed. As a possible direct interaction of the SHI with the atomically thin MoS_2 is far too short to explain the length of the rifts, the main interaction has to take place in the underlying substrate. Therefore, the Two-Temperature Model has been used to calculate the lattice temperature of the SiO_2 surface on which the single layer MoS_2 are prepared. A good agreement of the experiment and the TTM calculations has been found, indicating that because of the short time frame of the SHI induced heating (in the range of a few ps), the temperature required for rift creation might be higher than the melting/decomposition temperature of bulk MoS_2 T_{melt}=1458 K.

These results underline the large potential of using swift heavy ions for tayloring the surface morphology in 2D-materials. Furthermore, it has been shown in two publications that graphene can be used for analyzing ion induced damage in materials [OO.10] or even

the homogeneity of the impinging ion beam [OO.17]. Up to this point, grazing incidence irradiation with SHI is the only way to controllably introduce folded structures in 2D-materials. By using an experimental setup like the micro beam at the RBI in Croatia, these foldings can even be created in a defined region. New phenomena are proposed for these structures and a experiment proposed by Queisser et al. [347] is currently being worked on. A scheme of this experiment is shown in fig. 7.1. Particle-hole pairs are generated in folded graphene under a constant magnetic field. By exciting these particle-hole pairs with incident photons (marked in the figure in red), a charge separation and thus a strong magnetophotoelectric effect is created.

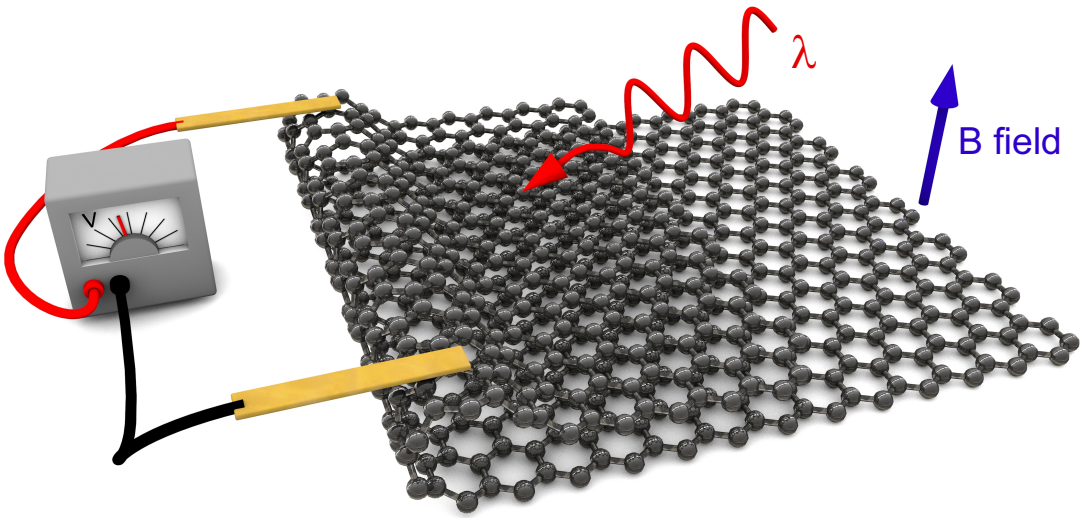

Figure 7.1: Scheme of an experimental setup for studying the magnetophotoelectric effect in folded graphene

While using foldings in actual applications may sound a little exotic, using SHI to create nanopores and slit pores in 2D-materials seems more straightforward in terms of potential applications. A plentitude of applications for nanopores in 2D-materials have been proposed with fundamental implications for the society like water desalination, gas separation or even biomedical applications. However, before 2D-materials can be applied in filters, the issue of stability for these ultrathin membranes has to be resolved. As swift heavy ions can not only be used for creating pores in graphene, but also for the formation of ion track etched pores in polymer membranes, a composite of these two materials might solve this problem. First experiments in this direction have just recently been published [448, 449].

In the last part of this thesis, the applicability of swift heavy ions in the process of doping of 2D-materials has been investigated. It has been shown by Kelvin probe measurements that graphene on SiC(0001) exhibits a transition from n-type to p-type behaviour upon SHI irradiation under grazing incidence angle. This transition is driven by an implantation of substrate atoms due to the intense electronic excitation of the SHI projectile. It has been shown by Two-Temperature Model calculations that Si is partially sublimating from

the SiC surface. To test, if this SHI induced doping is in principle a feasible way to dope 2D-material devices, graphene and MoS_2 field effect transistors have been irradiated with different fluences of SHI. The conclusion has been, that graphene devices are a lot more resistant with respect to defects compared to MoS_2. In a final experiment it has been shown in an actual graphene FET, that irradiation with SHI under grazing incidence angle can indeed result in doping of graphene, which has been observed by a shift of the Dirac point. This opens up the possibility for a plethora of future experiments and applications in order to precisely dope graphene by this new method.

Bibliography

[1] P. Sigmund. *Stopping of heavy ions: A theoretical approach*, volume 204 of *Springer tracts in modern physics*. Springer, Berlin, 2004.

[2] J. Krauser, J.-H. Zollondz, A. Weidinger, and C. Trautmann. Conductivity of nanometer-sized ion tracks in diamond-like carbon films. *J. Appl. Phys.*, 94(3):1959, 2003.

[3] D. Givord et. al. Magnetic properties of amorphous nanocolumns created by heavy ion irradiation of paramagnetic yCo_2 thin films (invited). *J. Appl. Phys.*, 76(10):6661, 1994.

[4] R. Gupta et al. Swift heavy ions for controlled modification of soft magnetic properties of fe 0.85 n 0.15 thin film. *J. Phys.: Condens. Matter*, 22(22):226001, 2010.

[5] P. Apel. Swift ion effects in polymers: industrial applications. *Nucl. Instr. Meth. Phys. Res. B*, 208:11–20, 2003.

[6] C. D'Orléans et al. Anisotropy of co nanoparticles induced by swift heavy ions. *Physical Review B*, 67(2):220101(R), 2003.

[7] D. Schulz-Ertner et al. Results of carbon ion radiotherapy in 152 patients. *International Journal of Radiation Oncology Biology Physics*, 58(2):631–640, 2004.

[8] K. S. Novoselov et al. Two-dimensional gas of massless dirac fermions in graphene. *Nature*, 438(7065):197–200, 2005.

[9] K. S. Novoselov et al. Two-dimensional atomic crystals. *Proc. Natl. Acad. Sci. U.S.A.*, 102(30):10451–10453, 2005.

[10] A. K. Geim. Graphene: Status and prospects. *Science*, 324(5934):1530–1534, 2009.

[11] K. S. Novoselov et al. A roadmap for graphene. *Nature*, 490(7419):192–200, 2012.

[12] A. K. Geim and I. V. Grigorieva. Van der waals heterostructures. *Nature*, 499(7459):419–425, 2013.

[13] S. Z. Butler et al. Progress, challenges, and opportunities in two-dimensional materials beyond graphene. *ACS Nano*, 7(4):2898–2926, 2013.

[14] C. Sathe, X. Zou, J.-P. Leburton, and K. Schulten. Computational investigation of dna detection using graphene nanopores. *ACS Nano*, 5(11):8842–8851, 2011.

[15] J. Lee et al. MoS_2 nanosheet channel and guanine DNA-base charge injection layer for high performance memory transistors. *J. Mater. Chem. C*, 2(27):5411, 2014.

[16] D. Jiang, V. R. Cooper, and S. Dai. Porous graphene as the ultimate membrane for gas separation. *Nano Lett.*, 9(12):4019–4024, 2009.

[17] D. Cohen-Tanugi and J. C. Grossman. Water desalination across nanoporous graphene. *Nano Lett.*, 12(7):3602–3608, 2012.

[18] E. A. Jackson and M. A. Hillmyer. Nanoporous membranes derived from block copolymers: From drug delivery to water filtration. *ACS Nano*, 4(7):3548–3553, 2010.

[19] S. Akcöltekin et al. Unzipping and folding of graphene by swift heavy ions. *Appl. Phys. Lett.*, 98(10):103103, 2011.

[20] D. K. Avasthi and G. K. Mehta. *Swift heavy ions for materials engineering and nanostructuring*, volume v. 145 of *Springer series in materials science*. Springer, Dordrecht [Netherlands], 2011.

[21] H. Liu, Y. Liu, and D. Zhu. Chemical doping of graphene. *J. Mater. Chem.*, 21(10):3335, 2011.

[22] H. Terrones, R. Lv, M. Terrones, and M. S. Dresselhaus. The role of defects and doping in 2d graphene sheets and 1d nanoribbons. *Reports on Progress in Physics*, 75(6):062501, 2012.

[23] R. E. Peierls. Quelques proprietes typiques des corpses solides. *Ann. I. H. Poincare*, 5(5):177, 1935.

[24] L. D. Landau. Zur theorie der phasenumwandlungen ii. *Phys. Z. Sowjetunion*, (11):26–35, 1937.

[25] A. K. Geim and K. S. Novoselov. The rise of graphene. *Nature Mat.*, 6(3):183–191, 2007.

[26] L. D. Landau and E. M. Lifshitz. *Statistical Physics, Part I.* Pargamon, Oxford, 1975.

[27] N. Mermin. Crystalline order in two dimensions. *Phys. Rev.*, 176(1):250–254, 1968.

[28] J. A. Venables, G. D. T. Spiller, and M. Hanbucken. Nucleation and growth of thin films. *Rep. Prog. Phys.*, 47(4):399–459, 1984.

[29] J. W. Evans, P. A. Thiel, and M. C. Bartelt. Morphological evolution during epitaxial thin film growth: Formation of 2d islands and 3d mounds. *Surf. Sci. Rep.*, 61(1-2):1–128, 2006.

[30] K. S. Novoselov. Electric field effect in atomically thin carbon films. *Science*, 306(5696):666–669, 2004.

[31] Y. Zhang, Y.-W. Tan, H.t L. Stormer, and P. Kim. Experimental observation of the quantum hall effect and berry's phase in graphene. *Nature*, 438(7065):201–204, 2005.

[32] J. C. Meyer et al. The structure of suspended graphene sheets. *Nature*, 446(7131):60–63, 2007.

[33] S. Stankovich et al. Graphene-based composite materials. *Nature*, 442(7100):282–286, 2006.

[34] J. W. Suk et al. Transfer of cvd-grown monolayer graphene onto arbitrary substrates. *ACS Nano*, 5(9):6916–6924, 2011.

[35] D. R. Nelson, T. Piran, and S. Weinberg. *Statistical Mechanics of Membranes and Surfaces.* World Scientific, Singapore, 2004.

[36] S. Morozov et al. Two-dimensional electron and hole gases at the surface of graphite. *Phys. Rev. B*, 72(20):201401(R), 2005.

[37] B. Partoens and F. Peeters. From graphene to graphite: Electronic structure around the k point. *Phys. Rev. B*, 74(7):075404, 2006.

[38] S. Trickey, F. Müller-Plathe, G. Diercksen, and J. Boettger. Interplanar binding and lattice relaxation in a graphite dilayer. *Phys. Rev. B.*, 45(8):4460–4468, 1992.

[39] B. Özyilmaz, P. Jarillo-Herrero, and D. Efetov, D. aEfetov. Electronic transport in locally gated graphene nanoconstrictions. *Appl. Phys. Lett.*, 91(19):192107, 2007.

[40] M. Han, B. Özyilmaz, Y. Zhang, and P. Kim. Energy band-gap engineering of graphene nanoribbons. *Phys. Rev. Lett.*, 98(20):206805, 2007.

[41] A. H. Castro Neto, N. M. R. Peres, K. S. Novoselov, and A. K. Geim. The electronic properties of graphene. *Reviews of Modern Physics*, 81(1):109–162, 2009.

[42] A. Zhang et al. Bandgap engineering of zigzag graphene nanoribbons by manipulating edge states via defective boundaries. *Nanotechnology*, 22(43):435702, 2011.

[43] D. A. Areshkin, D. Gunlycke, and C. T. White. Ballistic transport in graphene nanostrips in the presence of disorder: Importance of edge effects. *Nano Lett.*, 7(1):204–210, 2007.

[44] A. Castro Neto, F. Guinea, and N. Peres. Edge and surface states in the quantum hall effect in graphene. *Phys. Rev. B*, 73(20):205408, 2006.

[45] V. Barone, O. Hod, and G. E. Scuseria. Electronic structure and stability of semiconducting graphene nanoribbons. *Nano Lett.*, 6(12):2748–2754, 2006.

[46] F. Sols, F. Guinea, and A. Neto. Coulomb blockade in graphene nanoribbons. *Phys. Rev. Lett.*, 99(16):166803, 2007.

[47] D. Novikov. Transverse field effect in graphene ribbons. *Phys. Rev. Lett.*, 99(5):056802, 2007.

[48] K. S. Novoselov et al. Room-temperature quantum hall effect in graphene. *Science*, 315(5817):1379, 2007.

[49] K. I. Bolotin et al. Ultrahigh electron mobility in suspended graphene. *Solid State Commun.*, 146(9-10):351–355, 2008.

[50] F. Schedin et al. Detection of individual gas molecules adsorbed on graphene. *Nature Mat.*, 6(9):652–655, 2007.

[51] Y. Zheng and T. Ando. Hall conductivity of a two-dimensional graphite system. *Phys. Rev. B*, 65(24):245420, 2002.

[52] G. Semenoff. Condensed-matter simulation of a three-dimensional anomaly. *Phys. Rev. Lett.*, 53(26):2449–2452, 1984.

[53] E. Fradkin. Critical behavior of disordered degenerate semiconductors. ii. spectrum and transport properties in mean-field theory. *Phys. Rev. B.*, 33(5):3263–3268, 1986.

[54] A. Schakel. Relativistic quantum hall effect. *Phys. Rev. D.*, 43(4):1428–1431, 1991.

[55] J. González, F. Guinea, and M. Vozmediano. Unconventional quasiparticle lifetime in graphite. *Phys. Rev. Lett.*, 77(17):3589–3592, 1996.

[56] E. Gorbar, V. Gusynin, V. Miransky, and I. Shovkovy. Magnetic field driven metal-insulator phase transition in planar systems. *Phys. Rev. B*, 66(4):045108, 2002.

[57] M. I. Katsnelson, K. S. Novoselov, and A. K. Geim. Chiral tunnelling and the klein paradox in graphene. *Nat. Phys.*, 2(9):620–625, 2006.

[58] J. S. Bunch et al. Impermeable atomic membranes from graphene sheets. *Nano Lett.*, 8(8):2458–2462, 2008.

[59] J. Moser, A. Barreiro, and A. Bachtold. Current-induced cleaning of graphene. *Appl. Phys. Lett.*, 91(91):163513, 2007.

[60] C. Lee, X. Wei, J. W. Kysar, and J. Hone. Measurement of the elastic properties and intrinsic strength of monolayer graphene. *Science*, 321(5887):385–388, 2008.

[61] F. Liu, P. Ming, and J. Li. Ab initio calculation of ideal strength and phonon instability of graphene under tension. *Phys. Rev. B*, 76(6):064120, 2007.

[62] R. R. Nair et al. Fine structure constant defines visual transparency of graphene. *Science*, 320(5881):1308, 2008.

[63] L. Liu et al. Graphene oxidation: Thickness-dependent etching and strong chemical doping. *Nano Lett.*, 8(7):1965–1970, 2008.

[64] D. C. Elias et al. Control of graphene's properties by reversible hydrogenation: Evidence for graphane. *Science*, 323(5914):610–613, 2009.

[65] K. P. Loh, Q. Bao, P. K. Ang, and J. Yang. The chemistry of graphene. *J. Mater. Chem.*, 20(12):2277, 2010.

[66] R. R. Nair et al. Fluorographene: A two-dimensional counterpart of teflon. *Small*, 6(24):2877–2884, 2010.

[67] L. Wang et al. One-dimensional electrical contact to a two-dimensional material. *Science*, 342(6158):614–617, 2013.

[68] C. R. Dean et al. Boron nitride substrates for high-quality graphene electronics. *Nature Nanotechnol.*, 5(10):722–726, 2010.

[69] A. S. Mayorov et a. Micrometer-scale ballistic transport in encapsulated graphene at room temperature. *Nano Lett.*, 11(6):2396–2399, 2011.

[70] C.-J. Shih et al. Tuning on–off current ratio and field-effect mobility in a MoS_2 –graphene heterostructure via schottky barrier modulation. *ACS Nano*, 8:5790–5798, 2014.

[71] A. V. Kretinin et al. Electronic properties of graphene encapsulated with different two-dimensional atomic crystals. *Nano Lett.*, 14:3270–3276, 2014.

[72] S. Park and R. S. Ruoff. Chemical methods for the production of graphenes. *Nature Nanotechnol.*, 4(4):217–224, 2009.

[73] L. A. Ponomarenko et al. Tunable metal–insulator transition in double-layer graphene heterostructures. *Nature Phys.*, 7(12):958–961, 2011.

[74] B. Aufray et al. Graphene-like silicon nanoribbons on ag(110): A possible formation of silicene. *Appl. Phys. Lett.*, 96(18):183102, 2010.

[75] P. Vogt et al. Silicene: Compelling experimental evidence for graphenelike two-dimensional silicon. *Phys. Rev. Lett.*, 108(15):155501, 2012.

[76] S. Kumar et al. Graphene analogue BCN: Femtosecond nonlinear optical susceptibility and hot carrier dynamics. *Chem. Phys. Lett.*, 499(1-3):152–157, 2010.

[77] R. Mas-Ballesté, C. Gómez-Navarro, J. Gómez-Herrero, and F. Zamora. 2d materials: to graphene and beyond. *Nanoscale*, 3(1):20, 2011.

[78] Q. H. Wang et al. Electronics and optoelectronics of two-dimensional transition metal dichalcogenides. *Nature Nanotechnol.*, 7(11):699–712, 2012.

[79] M. Xu, T. Liang, M. Shi, and H. Chen. Graphene-like two-dimensional materials. *Chemical Reviews*, 113(5):3766–3798, 2013.

[80] K. F. Mak et al. Atomically thin MoS_2: A new direct-gap semiconductor. *Phys. Rev. Lett.*, 105(13):136805, 2010.

[81] T. Korn et al. Low-temperature photocarrier dynamics in monolayer MoS_2. *Appl. Phys. Lett.*, 99(10):102109, 2011.

[82] G. Eda et al. Photoluminescence from chemically exfoliated MoS_2. *Nano Lett.*, 11(12):5111–5116, 2011.

[83] K. F. Mak, K. He, J. Shan, and T. F. Heinz. Control of valley polarization in monolayer MoS_2 by optical helicity. *Nature Nanotechnol.*, 7(8):494–498, 2012.

[84] T. Cao et al. Valley-selective circular dichroism of monolayer molybdenum disulphide. *Nature Commun.*, 3:887, 2012.

[85] H. Zeng et al. Valley polarization in MoS_2 monolayers by optical pumping. *Nature Nanotechnol.*, 7(8):490–493, 2012.

[86] K. F. Mak et al. Tightly bound trions in monolayer MoS_2. *Nature Mater.*, 12(3):207–211, 2012.

[87] J. S. Ross et al. Electrical control of neutral and charged excitons in a monolayer semiconductor. *Nature Commun.*, 4:1474, 2013.

[88] G. Sallen et al. Robust optical emission polarization in MoS_2 monolayers through selective valley excitation. *Phys. Rev. b*, 86(8):081301(R), 2012.

[89] B. Radisavljevic et al. Single-layer MoS_2 transistors. *Nature Nanotechnol.*, 6(3):147–150, 2011.

[90] Y.i Yoon, K. Ganapathi, and S. Salahuddin. How good can monolayer MoS_2 transistors be? *Nano Lett.*, 11(9):3768–3773, 2011.

[91] B. Radisavljevic, M. B.B. Whitwick, and A. Kis. Integrated circuits and logic operations based on single-layer MoS_2. *ACS Nano*, 5(12):9934–9938, 2011.

[92] A. N. Ghatak, S.and Pal and A. Ghosh. Nature of electronic states in atomically thin MoS_2 field-effect transistors. *ACS Nano*, 5(10):7707–7712, 2011.

[93] Z. Yin et al. Single-layer MoS_2 phototransistors. *ACS Nano*, 6(1):74–80, 2012.

[94] B. Radisavljevic, M. B. Whitwick, and A. Kis. Small-signal amplifier based on single-layer MoS_2. *Appl. Phys. Lett.*, 101(4):043103, 2012.

[95] H. Wang et al. Integrated circuits based on bilayer MoS_2 transistors. *Nano Lett.*, 12(9):4674–4680, 2012.

[96] N. Wakabayashi, H. Smith, and R. Nicklow. Lattice dynamics of hexagonal MoS_2 studied by neutron scattering. *Phys. Rev. B*, 12(2):659–663, 1975.

[97] L. Mattheiss. Band structures of transition-metal-dichalcogenide layer compounds. *Phys. Rev. B*, 8(8):3719–3740, 1973.

[98] J.-F. Yang, B. Parakash, J. Hardell, and Q.-F. Fang. Tribological properties of transition metal di-chalcogenide based lubricant coatings. *Frontiers of Materials Science*, 6(2):116–127, 2012.

[99] A. Splendiani et al. Emerging photoluminescence in monolayer MoS_2. *Nano Lett.*, 10(4):1271–1275, 2010.

[100] J. K. Ellis, M. J. Lucero, and G. E. Scuseria. The indirect to direct band gap transition in multilayered MoS_2 as predicted by screened hybrid density functional theory. *Appl. Phys. Lett.*, 99(26):261908, 2011.

[101] T. Cheiwchanchamnangij and W. R. L. Lambrecht. Quasiparticle band structure calculation of monolayer, bilayer, and bulk MoS_2. *Phys. Rev. B*, 85(20):205302, 2012.

[102] A. Kumar and P. K. Ahluwalia. Electronic structure of transition metal dichalcogenides monolayers 1h-mx_2 (m = mo, w; x = s, se, te) from ab-initio theory: new direct band gap semiconductors. *EPJ B*, 85(6), 2012.

[103] H.-P. Komsa and A. V. Krasheninnikov. Effects of confinement and environment on the electronic structure and exciton binding energy of MoS_2 from first principles. *Phys. Rev. B*, 86(24):241201(R), 2012.

[104] H.-P. Komsa and A. V. Krasheninnikov. Two-dimensional transition metal dichalcogenide alloys: Stability and electronic properties. *J Phys. Chem. Lett.*, 3(23):3652–3656, 2012.

[105] B. L. Evans and P. A. Young. Optical absorption and dispersion in molybdenum disulphide. *Proc. R. Soc. A*, 284(1398):402–422, 1965.

[106] E. Scalise et al. Strain-induced semiconductor to metal transition in the two-dimensional honeycomb structure of MoS_2. *Nano Research*, 5(1):43–48, 2012.

[107] W. S. Yun et al. Thickness and strain effects on electronic structures of transition metal dichalcogenides: 2h-MX_2 semiconductors (m = mo, w; x = s, se, te). *Phys. Rev. B*, 85(3):033305, 2012.

[108] J. Feng, X. Qian, C.-W. Huang, and J. Li. Strain-engineered artificial atom as a broad-spectrum solar energy funnel. *Nature Photonics*, 6(12):866–872, 2012.

[109] H. Peelaers and C. G. Van de Walle. Effects of strain on band structure and effective masses in MoS_2. *Phys. Rev. B*, 86(24):241401(R), 2012.

[110] H. R. Gutiérrez et al. Extraordinary room-temperature photoluminescence in triangular WS_2 monolayers. *Nano Lett.*, 13(8):3447–3454, 2013.

[111] A. R. Botello-Méndez, F. López-Urías, M. Terrones, and H. Terrones. Metallic and ferromagnetic edges in molybdenum disulfide nanoribbons. *Nanotechnology*, 20(32):325703, 2009.

[112] D. Le and T. S. Rahman. Joined edges in MoS_2: Metallic and half-metallic wires. *J. Phys.: Condens. Matter*, 25(31):312201, 2013.

[113] S. Helveg et al. Atomic-scale structure of single-layer MoS_2 nanoclusters. *Physical Review Letters*, 84(5):951–954, 2000.

[114] M. Bollinger et al. One-dimensional metallic edge states in MoS_2. *Phys. Rev. Lett.*, 87(19):196803, 2001.

[115] J. V. Lauritsen et al. Size-dependent structure of MoS_2 nanocrystals. *Nature Nanotechnol.*, 2(1):53–58, 2007.

[116] T. F. Jaramillo et al. Identification of active edge sites for electrochemical H_2 evolution from MoS_2 nanocatalysts. *Science*, 317(5834):100–102, 2007.

[117] A. Dittmar. *High energy ion beam analysis of solids*, volume 6 of *Physical research*. Akad.-Verl., Berlin, 1988.

[118] P. Sigmund. *Particle penetration and radiation effects: General aspects and stopping of swift point charges*, volume 151 of *Springer series in solid-state sciences*. Springer, Berlin and New York, 2008.

[119] Heiner Ryssel and Ingolf Ruge. *Ionenimplantation*. Teubner, Stuttgart, 1978.

[120] M. A. Nastasi, J. W. Mayer, and J. K. Hirvonen. *Ion-solid interactions: Fundamentals and applications*. Cambridge solid state science series. Cambridge University Press, Cambridge and New York, 1st pbk. ed edition, 2004.

[121] F. Aumayr et al. Single ion induced surface nanostructures: a comparison between slow highly charged and swift heavy ions. *J. Phys.: Condens. Matter*, 23(39):393001, 2011.

[122] J. F. Ziegler, M. D. Ziegler, and J. P. Biersack. Srim – the stopping and range of ions in matter (2010). *Nucl. Instr. Meth. Phys. Res. B*, 268(11-12):1818–1823, 2010.

[123] S. Klaumünzer. Ion tracks in quartz and vitreous silica. *Nucl. Instr. Meth. Phys. Res. B*, 225(1-2):136–153, 2004.

[124] G. Schiwietz et al. Femtosecond dynamics – snapshots of the early ion-track evolution. *Nucl. Instr. Meth. Phys. Res. B*, 226(4):683–704, 2004.

[125] H. Dammak et al. Tracks in metals by mev fullerenes. *Phys. Rev. Lett.*, 74(7):1135–1138, 1995.

[126] G. Schiwietz, E. Luderer, G. Xiao, and P.L Grande. Energy dissipation of fast heavy ions in matter. *Nucl. Instr. Meth. Phys. Res. B*, 175-177:1–11, 2001.

[127] L. T. Chadderton. Nuclear tracks in solids: registration physics and the compound spike. *Radiation Measurements*, 36(1-6):13–34, 2003.

[128] J. Ackermann, A. Müller, R. Neumann, and Y. Wang. Scanning force microscopy on heavy-ion tracks in muscovite mica: track diameter versus energy loss and loading force. *Appl. Phys. A Mater. Sci. Process.*, 66(7):S1151–S1154, 1998.

[129] A. Mozumder. Track-core radius of charged particles at relativistic speed in condensed media. *J. Chem. Phys.*, 60:1145–1148, 1974.

[130] J. Faïn, M. Monnin, M. Montret, and J. Fain. Spatial energy distribution around heavy-ion path. *Radiat. Res.*, 57(3):379, 1974.

[131] A. Chatterjee and H. J. Schaefer. Microdosimetric structure of heavy ion tracks in tissue. *Radiation and Environmental Biophysics*, 13(3):215–227, 1976.

[132] G Schiwietz et al. Femtosecond dynamics – snapshots of the early ion-track evolution. *Nucl. Instr. Meth. Phys. Res. B*, 225(1-2):4–26, 2004.

[133] E. Bringa and R. Johnson. Coulomb explosion and thermal spikes. *Phys. Rev. Lett.*, 88(16):165501, 2002.

[134] R. L. Fleischer, P. B. Price, and R. M. Walker. Ion explosion spike mechanism for formation of charged-particle tracks in solids. *J. Appl. Phys.*, 36(11):3645, 1965.

[135] G. Schiwietz et al. An experimental determination of electron temperatures in the center of nuclear tracks in amorphous carbon. *Nucl. Instr. Meth. Phys. Res. B*, 146(1-4):131–136, 1998.

[136] G. Schiwietz, G. Xiao, E. Luderer, and P. L. Grande. Auger electrons from ion tracks. *Nucl. Instr. Meth. Phys. Res. B*, 164-165:353–364, 2000.

[137] R. L. Fleischer, P. B. Price, and R. M. Walker. *Nuclear tracks in solids: Principles and applications.* University of California Press, Berkeley, 1975.

[138] P. Stampfli and K. Bennemann. Time dependence of the laser-induced femtosecond lattice instability of si and gaas: Role of longitudinal optical distortions. *Phys. Rev. B*, 49(11):7299–7305, 1994.

[139] P. Stampfli. Electronic excitation and structural stability of solids. *Nucl. Instr. Meth. Phys. Res. B*, 107(1-4):138–145, 1996.

[140] T. A. Tombrello. Predicting latent track dimensions. *Nucl. Instr. Meth. Phys. Res. B*, 94(4):424–428, 1994.

[141] M. Toulemonde, C. Dufour, and E. Paumier. Transient thermal process after a high-energy heavy-ion irradiation of amorphous metals and semiconductors. *Phys. Rev. B.*, 46(22):14362–14369, 1992.

[142] M. Toulemonde et al. Track creation in SiO_2 and $BaFe_{12}O_{19}$ by swift heavy ions: a thermal spike description. *Nucl. Instr. Meth. Phys. Res. B*, 116(1-4):37–42, 1996.

[143] M. Toulemonde, E. Paumier, and C. Dufour. Thermal spike model in the electronic stopping power regime. *Radiat Eff. Defects Solids*, 126(1):201–206, 1993.

[144] Z. G. Wang, C. Dufour, E. Paumier, and M. Toulemonde. The s_e sensitivity of metals under swift-heavy-ion irradiation: a transient thermal process. *J. Phys.: Condens. Matter*, 6(34):6733–6750, 1994.

[145] M. Toulemonde, Ch. Dufour, A. Meftah, and E. Paumier. Transient thermal processes in heavy ion irradiation of crystalline inorganic insulators. *Nucl. Instr. Meth. Phys. Res. B*, 166-167:903–912, 2000.

[146] A. Meftah et al. Track formation in sio$_2$ quartz and the thermal-spike mechanism. *Phys. Rev. B*, 49(18):12457–12463, 1994.

[147] A. Meftah et al. Experimental determination of track cross-section in $Gd_3Ga_5O_{12}$ and comparison to the inelastic thermal spike model applied to several materials. *Nucl. Instr. Meth. Phys. Res. B*, 237(3-4):563–574, 2005.

[148] F. Seitz and J. S. Koehler. Solid state physics-advances in research and applications. 2(2):305–448, 1956.

[149] O. Osmani. *Irradiation effects of swift heavy ions in matter.* Dissertation, 2011.

[150] M. Kaganov, T. Lifshitz, and I. Tanatarov. Relaxation between electrons and the crystalline lattice. *Sov. Phys. JETP*, 4(4):173–178, 1957.

[151] I. Anisimov, B. L. Kapeliovich, and T. L. Perelman. Electron emission from metal surfaces exposed to ultrashort laser pulses. *Zh. Eksp. Teor. Fiz.*, 66(66):776–781, 1974.

[152] B. Rethfeld, A. Kaiser, M. Vicanek, and G. Simon. Ultrafast dynamics of nonequilibrium electrons in metals under femtosecond laser irradiation. *Phys. Rev. B*, 65(21):214303, 2002.

[153] Z. Lin, L. Zhigilei, and V. Celli. Electron-phonon coupling and electron heat capacity of metals under conditions of strong electron-phonon nonequilibrium. *Phys. Rev. B*, 77(7):075133, 2008.

[154] J. L. Hostetler, A. N. Smith, D. M. Czajkowsky, and P. M. Norris. Measurement of the electron-phonon coupling factor dependence on film thickness and grain size in au, cr, and al. *Appl. Opt.*, 38(16):3614, 1999.

[155] R. Groeneveld, R. Sprik, and A. Lagendijk. Ultrafast relaxation of electrons probed by surface plasmons at a thin silver film. *Phys. Rev. Lett.*, 64(7):784–787, 1990.

[156] B. H. Christensen, K. Vestentoft, and P. Balling. Short-pulse ablation rates and the two-temperature model. *Appl. Surf. Sci.*, 253(15):6347–6352, 2007.

[157] M. Karlusić et al. Energy threshold for the creation of nanodots on $SrTiO_3$ by swift heavy ions. *New. J. Phys.*, 12(4):043009, 2010.

[158] M. Toulemonde, Ch. Dufour, Z. Wang, and E. Paumier. Atomic and cluster ion bombardment in the electronic stopping power regime: A thermal spike description. *Nucl. Instr. Meth. Phys. Res. B*, 112(1-4):26–29, 1996.

[159] M.P.R. Waligórski, R. N. Hamm, and R. Katz. The radial distribution of dose around the path of a heavy ion in liquid water. *International Journal of Radiation Applications and Instrumentation. Part D. Nuclear Tracks and Radiation Measurements*, 11(6):309–319, 1986.

[160] R. Papaléo et al. Direct evidence for projectile charge-state dependent crater formation due to fast ions. *Phys. Rev. Lett.*, 101(16):167601, 2008.

[161] P. Kluth et al. Fine structure in swift heavy ion tracks in amorphous SiO_2. *Phys. Rev. Lett.*, 101(17):175503, 2008.

[162] E. Akcöltekin et al. Creation of multiple nanodots by single ions. *Nat. Nanotechnol.*, 2(5):290–294, 2007.

[163] N. Khalfaoui et al. Characterization of swift heavy ion tracks in CaF_2 by scanning force and transmission electron microscopy. *Nucl. Instr. Meth. Phys. Res. B*, 240(4):819–828, 2005.

[164] S. Akcöltekin et al. Patterning of insulating surfaces by electronic excitation. *Nucl. Instr. Meth. Phys. Res. B*, 267(8-9):1386–1389, 2009.

[165] L. Tapasztó et al. Tuning the electronic structure of graphene by ion irradiation. *Phys. Rev. B*, 78(23):233407, 2008.

[166] G. Compagnini et al. Ion irradiation and defect formation in single layer graphene. *Carbon*, 47(14):3201–3207, 2009.

[167] Y.-B. Zhou et al. Ion irradiation induced structural and electrical transition in graphene. *J. Chem. Phys*, 133(23):234703, 2010.

[168] J. J. Lopez, F. Greer, and J. R. Greer. Enhanced resistance of single-layer graphene to ion bombardment. *J. Appl. Phys.*, 107(10):104326, 2010.

[169] G. Buchowicz et al. Correlation between structure and electrical transport in ion-irradiated graphene grown on cu foils. *Appl. Phys. Lett.*, 98(3):032102, 2011.

[170] S. Zhao and J. Xue. Tuning the band gap of bilayer graphene by ion implantation: Insight from computational studies. *Phys. Rev. B*, 86(16):165428, 2012.

[171] S. Standop et al. Ion impacts on graphene/ir(111): Interface channeling, vacancy funnels, and a nanomesh. *Nano Lett*, 13(5):1948–1955, 2013.

[172] W. Li et al. Fabrication of nanopores in a graphene sheet with heavy ions: A molecular dynamics study. *J. Appl. Phys.*, 114(23):234304, 2013.

[173] O. Lehtinen et al. Effects of ion bombardment on a two-dimensional target: Atomistic simulations of graphene irradiation. *Phys. Rev. B*, 81(15):153401, 2010.

[174] E. H. Åhlgren, J. Kotakoski, O. Lehtinen, and A. V. Krasheninnikov. Ion irradiation tolerance of graphene as studied by atomistic simulations. *Appl. Phys. Lett.*, 100(23):233108, 2012.

[175] J. Zeng et al. Swift heavy ions induced irradiation effects in monolayer graphene and highly oriented pyrolytic graphite. *Nucl. Instr. Meth. Phys. Res. B*, 330:18–23, 2014.

[176] S. Kumar et al. Purification/annealing of graphene with 100-MeV ag ion irradiation. *Nanoscale Research Letters*, 9(1):126, 2014.

[177] S. Zhao, J. Xue, and S. Wang, Y.and Yan. Effect of SiO_2 substrate on the irradiation-assisted manipulation of supported graphene: a molecular dynamics study. *Nanotechnology*, 23(28):285703, 2012.

[178] G. Binnig. Tunneling through a controllable vacuum gap. *Appl. Phys. Lett.*, 40(2):178, 1982.

[179] G. Binnig, H. Rohrer, Ch. Gerber, and E. Weibel. Surface studies by scanning tunneling microscopy. *Phys. Rev. Lett.*, 49(1):57–61, 1982.

[180] G. Binnig, C. F. Quate, and Ch. Gerber. Atomic force microscope. *Phys. Rev. Lett.*, 56(9):930–933, 1986.

[181] F. J. Giessibl. Atomic resolution of the silicon (111)-(7x7) surface by atomic force microscopy. *Science*, 267(5194):68–71, 1995.

[182] F. J. Giessibl. Advances in atomic force microscopy. *Rev. Mod. Phys.*, 75(3):949–983, 2003.

[183] J. M. Caridad et al. Effects of particle contamination and substrate interaction on the raman response of unintentionally doped graphene. *J. Appl. Phys.*, 108(8):084321, 2010.

[184] K. Xu, P. Cao, and J. R. Heath. Graphene visualizes the first water adlayers on mica at ambient conditions. *Science*, 329(5996):1188–1191, 2010.

[185] D. S. Wastl et al. Observation of 4 nm pitch stripe domains formed by exposing graphene to ambient air. *ACS Nano*, 7(11):10032–10037, 2013.

[186] D. S. Wastl, A. J. Weymouth, and F. J. Giessibl. Atomically resolved graphitic surfaces in air by atomic force microscopy. *ACS Nano*, 8(5):5233–5239, 2014.

[187] M. Ahmad et al. Local conductance measurement of graphene layer using conductive atomic force microscopy. *J Appl. Phys*, 110(5):054307, 2011.

[188] I. W. Frank, D. M. Tanenbaum, A. M. van der Zande, and P. L. McEuen. Mechanical properties of suspended graphene sheets. *JVST B*, 25(6):2558, 2007.

[189] T. Filleter and R. Bennewitz. Structural and frictional properties of graphene films on sic(0001) studied by atomic force microscopy. *Phys. Rev. B*, 81(15):155412, 2010.

[190] N. J. Lee et al. The interlayer screening effect of graphene sheets investigated by kelvin probe force microscopy. *Appl. Phys. Lett.*, 95(22):222107, 2009.

[191] D. Ziegler et al. Variations in the work function of doped single- and few-layer graphene assessed by kelvin probe force microscopy and density functional theory. *Phys. Rev. B*, 83(23):235434, 2011.

[192] J. Xia, F. Chen, J. Li, and N. Tao. Measurement of the quantum capacitance of graphene. *Nature Nanotechnol.*, 4(8):505–509, 2009.

[193] J. E. Jones. On the determination of molecular fields. ii. from the equation of state of a gas. *Proc. R. Soc. A*, 106(738):463–477, 1924.

[194] E. Meyer, H. J. Hug, and R. Bennewitz. *Scanning Probe Microscopy: The Lab on a Tip*. Advanced Texts in Physics. Springer Berlin Heidelberg, Berlin and Heidelberg, 2004.

[195] A.J.M. Giesbers et al. Nanolithography and manipulation of graphene using an atomic force microscope. *Solid State Commun.*, 147(9-10):366–369, 2008.

[196] T. R. Albrecht, P. Grütter, D. Horne, and D. Rugar. Frequency modulation detection using high-q cantilevers for enhanced force microscope sensitivity. *J. Appl. Phys.*, 69(2):668, 1991.

[197] Q. Zhong, D. Inniss, K. Kjoller, and V. B. Elings. Fractured polymer/silica fiber surface studied by tapping mode atomic force microscopy. *Surf. Sci.*, 290(1-2):L688–L692, 1993.

[198] R. García. Dynamic atomic force microscopy methods. *Surf. Sci. Rep.*, 47(6-8):197–301, 2002.

[199] Sascha Sadewasser and Martha Lux-Steiner. Correct height measurement in noncontact atomic force microscopy. *Phys. Rev. Lett.*, 91(26):266101, 2003.

[200] S. Kalinin and A. Gruverman. *Scanning Probe Microscopy*. Springer New York, New York and NY, 2007.

[201] M. Nonnenmacher, M. P. O'Boyle, and H. K. Wickramasinghe. Kelvin probe force microscopy. *Appl. Phys. Lett.*, 58(25):2921, 1991.

[202] S. Kitamura, K. Suzuki, M. Iwatsuki, and C.B. Mooney. Atomic-scale variations in contact potential difference on au/si(111) (7x7) surface in ultrahigh vacuum. *Appl. Surf. Sci.*, 157(4):222–227, 2000.

[203] W. Melitz, J. Shen, A. C. Kummel, and S. Lee. Kelvin probe force microscopy and its application. *Surf. Sci. Rep.*, 66(1):1–27, 2011.

[204] Ch. Sommerhalter et al. High-sensitivity quantitative kelvin probe microscopy by noncontact ultra-high-vacuum atomic force microscopy. *Appl. Phys. Lett.*, 75(2):286, 1999.

[205] C. Barth et al. AFM tip characterization by kelvin probe force microscopy. *New J. Phys.*, 12(9):093024, 2010.

[206] L. Sun, J. Wang, and E. Bonaccurso. Nanoelectronic properties of a model system and of a conjugated polymer: A study by kelvin probe force microscopy and scanning conductive torsion mode microscopy. *J. Phys. Chem. C*, 114(15):7161–7168, 2010.

[207] P. G. Schroeder, M. W. Nelson, B. A. Parkinson, and R. Schlaf. Investigation of band bending and charging phenomena in frontier orbital alignment measurements of para-quaterphenyl thin films grown on highly oriented pyrolytic graphite and SnS_2. *Surf. Sci.*, 459(3):349–364, 2000.

[208] M. Lorenzoni, A. Giugni, and B. Torre. Oxidative and carbonaceous patterning of si surface in an organic media by scanning probe lithography. *Nanoscale Research Letters*, 8(1):75, 2013.

[209] J.-M. Yun et al. Efficient work-function engineering of solution-processed MoS_2 thin-films for novel hole and electron transport layers leading to high-performance polymer solar cells. *J. Mater. Chem. C*, 1(24):3777, 2013.

[210] M. Fontana et al. Electron-hole transport and photovoltaic effect in gated MoS_2 schottky junctions. *Sci. Rep.*, 3:1634, 2013.

[211] J. Itoh. Microscopic characterization of field emitter array structure and work function by scanning maxwell-stress microscopy. *Journal of Vacuum Science & Technology B: Microelectronics and Nanometer Structures*, 14(3):2105, 1996.

[212] C. V. Raman and K. S. Krishnan. A new type of secondary radiation. *Nature*, 121:501–502, 1928.

[213] A. Jorio. *Raman Spectroscopy in Graphene related systems: Carbon Nanotubes, Nanographite and Graphene*. Wiley-VCH Verlag, Weinheim, 2011.

[214] A. C. Ferrari et al. Raman spectrum of graphene and graphene layers. *Phys. Rev. Lett.*, 97(18):187401, 2006.

[215] C. Lee et al. Anomalous lattice vibrations of single- and few-layer MoS_2. *ACS Nano*, 4(5):2695–2700, 2010.

[216] R. V. Gorbachev et al. Hunting for monolayer boron nitride: Optical and raman signatures. *Small*, 7(4):465–468, 2011.

[217] A. Das et al. Monitoring dopants by raman scattering in an electrochemically top-gated graphene transistor. *Nature Nanotechnol.*, 3(4):210–215, 2008.

[218] M. Mohr, J. Maultzsch, and C. Thomsen. Splitting of the raman 2d band of graphene subjected to strain. *Phys Rev. B*, 82:201409, 2010.

[219] L. G. Cancado et al. Quantifying defects in graphene via raman spectroscopy at different excitation energies. *Nano Lett.*, 11(8):3190–3196, 2011.

[220] F. Otakar et al. Raman 2d-band splitting in graphene: theory and experiment. *ACS Nano*, 5:2231–2239, 2011.

[221] H. J. Conley et al. Bandgap engineering of strained monolayer and bilayer MoS_2. *Nano Lett.*, 13(8):3626–3630, 2013.

[222] J. Maultzsch, S. Reich, and C. Thomsen. Double-resonant raman scattering in graphite: Interference effects, selection rules, and phonon dispersion. *Phys. Rev. B*, 70(15):155403, 2004.

[223] S. Reich and C. Thomsen. Raman spectroscopy of graphite. *Phil. Trans. R. Soc. A*, 362:2271–2288, 2004.

[224] S. Reich, C. Thomsen, and J. Maultzsch. *Carbon nanotubes: basic concepts and physical properties*. John Wiley & Sons, 2008.

[225] S. Ryu et al. Raman spectroscopy of lithographically patterned graphene nanoribbons. *ACS Nano*, 5:4123–4130, 2011.

[226] M. S. Dresselhaus et al. Graphite fibers and filaments. *Springer Series in Material Sciences*, 5(4), 1988.

[227] M. S. Dresselhaus, G. Dresselhaus, and P. C. Eklund. *Science of fullerenes and carbon nanotubes*. Academic Press, San Diego, 1996.

[228] J. Klett et al. High-thermal-conductivity, mesophase-pitch-derived carbon foams: effect of precursor on structure and properties. *Carbon*, 38(7):953–973, 2000.

[229] L. Cançado et al. Anisotropy of the raman spectra of nanographite ribbons. *Phys. Rev. Lett.*, 93(4):047403, 2004.

[230] M. S. Dresselhaus, G. Dresselhaus, R. Saito, and A. Jorio. Raman spectroscopy of carbon nanotubes. *Phys. Rep.*, 409(2):47–99, 2005.

[231] M. S. Dresselhaus et al. Perspectives on carbon nanotubes and graphene raman spectroscopy. *Nano Lett.*, 10(3):751–758, 2010.

[232] J. S. Park et al. G band raman spectra of single, double and triple layer graphene. *Carbon*, 47(5):1303–1310, 2009.

[233] F. Herziger, P. May, and J. Maultzsch. Layer-number determination in graphene by out-of-plane phonons. *Phys. Rev. B*, 85:235447, 2012.

[234] J. Verble and T. Wieting. Lattice mode degeneracy in mos_{2} and other layer compounds. *Phys. Rev. Lett.*, 25(6):362–365, 1970.

[235] H. Li et al. From bulk to monolayer MoS_2: Evolution of raman scattering. *Adv. Funct. Mater.*, 22(7):1385–1390, 2012.

[236] B. Krauss et al. Laser-induced disassembly of a graphene single crystal into a nanocrystalline network. *Phys. Rev. B*, 79(16):165428, 2009.

[237] S. Najmaei, Z. Liu, P. M. Ajayan, and J. Lou. Thermal effects on the characteristic raman spectrum of molybdenum disulfide (MoS_2) of varying thicknesses. *Appl. Phys. Lett.*, 100(1):013106, 2012.

[238] P. Blake et al. Making graphene visible. *Appl. Phys. Lett.*, 91(6):063124, 2007.

[239] S. Akcöltekin et al. Graphene on insulating crystalline substrates. *Nanotechnology*, 20(15):155601, 2009.

[240] W. Xueshen et al. Thermal annealing of exfoliated graphene. *Journal of Nanomaterials*, 2013(5):1–6, 2013.

[241] T. M. Adams and R. A. Layton. *Introductory MEMS*. Springer US, Boston and MA, 2010.

[242] S. Rumyantsev et al. Electrical and noise characteristics of graphene field-effect transistors: ambient effects, noise sources and physical mechanisms. *J. Phys.: Condens. Matter*, 22(39):395302, 2010.

[243] D. J. Late et al. Hysteresis in single-layer MoS_2 field effect transistors. *ACS Nano*, 6(6):5635–5641, 2012.

[244] Y. Dan et al. Intrinsic response of graphene vapor sensors. *Nano Lett.*, 9(4):1472–1475, 2009.

[245] V. Geringer et al. Electrical transport and low-temperature scanning tunneling microscopy of microsoldered graphene. *Appl. Phys. Lett.*, 96(8):082114, 2010.

[246] J.-H. Chen et al. Intrinsic and extrinsic performance limits of graphene devices on SiO_2. *Nature Nanotechnol.*, 3(4):206–209, 2008.

[247] D. Lembke and A. Kis. Breakdown of high-performance monolayer MoS_2 transistors. *ACS Nano*, 6(11):10070–10075, 2012.

[248] X. Du, I. Skachko, A. Barker, and E. Y. Andrei. Approaching ballistic transport in suspended graphene. *Nature Nanotechnol.*, 3(8):491–495, 2008.

[249] X. Hong, K. Zou, and J. Zhu. Quantum scattering time and its implications on scattering sources in graphene. *Phys. Rev. B*, 80(24):241415(R), 2009.

[250] F. Guinea, B. Horovitz, and P. Le Doussal. Gauge fields, ripples and wrinkles in graphene layers. *Solid State Commun.*, 149(27-28):1140–1143, 2009.

[251] M. Neek-Amal and F. M. Peeters. Strain-engineered graphene through a nanostructured substrate. i. deformations. *Phys. Rev. B*, 85(19):195446, 2012.

[252] T. O. Wehling et al. Molecular doping of graphene. *Nano Lett.*, 8(1):173–177, 2008.

[253] Z. H. Ni et al. The effect of vacuum annealing on graphene. *J. Raman Spectrosc.*, 41(5):479–483, 2010.

[254] Y. Yang and R. Murali. Binding mechanisms of molecular oxygen and moisture to graphene. *Appl. Phys. Lett.*, 98(9):093116, 2011.

[255] D. Jena and A. Konar. Enhancement of carrier mobility in semiconductor nanostructures by dielectric engineering. *Phys. Rev. Lett.*, 98(13):136805, 2007.

[256] N. J. G. Couto, B. Sacépé, and A. F. Morpurgo. Transport through graphene on $SrTiO_3$. *Phys. Rev. Lett.*, 107(22):225501, 2011.

[257] M.M. Lucchese et al. Quantifying ion-induced defects and raman relaxation length in graphene. *Carbon*, 48(5):1592–1597, 2010.

[258] Z. H. Ni et al. Uniaxial strain on graphene: Raman spectroscopy study and band-gap opening. *ACS Nano*, 2(11):2301–2305, 2008.

[259] R. Al-Jishi and G. Dresselhaus. Lattice-dynamical model for graphite. *Phy B*, 26(8):4514–4522, 1982.

[260] P. Nemes-Incze, Z. Osváth, K. Kamarás, and L. P. Biró. Anomalies in thickness measurements of graphene and few layer graphite crystals by tapping mode atomic force microscopy. *Carbon*, 46(11):1435–1442, 2008.

[261] Y. Zhang, V. W. Brar, C. Girit, A. Zettl, and M. F. Crommie. Origin of spatial charge inhomogeneity in graphene. *Nature Phys.*, 5(10):722–726, 2009.

[262] R. Jalilian et al. Scanning gate microscopy on graphene: charge inhomogeneity and extrinsic doping. *Nanotechnology*, 22(29):295705, 2011.

[263] C. M. Aguirre et al. The role of the oxygen/water redox couple in suppressing electron conduction in field-effect transistors. *Adv. Mater.*, 21(30):3087–3091, 2009.

[264] J. Gebhardt, F. Viñes, and A. Görling. Influence of the surface dipole layer and pauli repulsion on band energies and doping in graphene adsorbed on metal surfaces. *Phys Rev. B*, 86(19):195431, 2012.

[265] H. Vázquez, Y. J. Dappe, J. Ortega, and F. Flores. Energy level alignment at metal/organic semiconductor interfaces: Pillow effect, induced density of interface states, and charge neutrality level. *J. Chem. Phys*, 126(14):144703, 2007.

[266] H. Coy Diaz, R. Addou, and M. Batzill. Interface properties of cvd grown graphene transferred onto $MoS_2(0001)$. *Nanoscale*, 6(2):1071, 2013.

[267] A. Konar, T. Fang, and D. Jena. Effect of high-k gate dielectrics on charge transport in graphene-based field effect transistors. *Physical Review B*, 82(11):115452, 2010.

[268] K. V. Emtsev et al. Towards wafer-size graphene layers by atmospheric pressure graphitization of silicon carbide. *Nature Mater.*, 8(3):203–207, 2009.

[269] J. Baringhaus et al. Exceptional ballistic transport in epitaxial graphene nanoribbons. *Nature*, 506(7488):349–354, 2014.

[270] T. Filleter, K. V. Emtsev, Th. Seyller, and R. Bennewitz. Local work function measurements of epitaxial graphene. *Appl. Phys. Lett.*, 93(13):133117, 2008.

[271] J. Shim et al. Water-gated charge doping of graphene induced by mica substrates. *Nano Lett.*, 12(2):648–654, 2012.

[272] F. M. Fowkes and W. D. Harkins. The state of monolayers adsorbed at the interface solid—aqueous solution. *J. Am. Chem. Soc.*, 62(12):3377–3386, 1940.

[273] T. Werder et al. On the water−carbon interaction for use in molecular dynamics simulations of graphite and carbon nanotubes. *J. Phys. Chem. B*, 107(6):1345–1352, 2003.

[274] T. O. Wehling, A. I. Lichtenstein, and M. I. Katsnelson. First-principles studies of water adsorption on graphene: The role of the substrate. *Appl. Phys. Lett.*, 93(20):202110, 2008.

[275] S. Ryu et al. Atmospheric oxygen binding and hole doping in deformed graphene on a SiO_2 substrate. *Nano Lett.*, 10(12):4944–4951, 2010.

[276] P. L. Levesque et al. Probing charge transfer at surfaces using graphene transistors. *Nano Lett.*, 11(1):132–137, 2011.

[277] O. Kazakova et al. Epitaxial graphene on sic(0001)): functional electrical microscopy studies and effect of atmosphere. *Nanotechnology*, 24(21):215702, 2013.

[278] A. N. Rudenko, F. J. Keil, M. I. Katsnelson, and A. I. Lichtenstein. Graphene adhesion on mica: Role of surface morphology. *Phys. Rev. B.*, 83(4):045409, 2011.

[279] A. Castellanos-Gomez et al. Atomically thin mica flakes and their application as ultrathin insulating substrates for graphene. *Small*, 7:n/a, 2011.

[280] G. Qi et al. Quantifying surface charge density by using an electric force microscope with a referential structure. *J. Phys. Chem. C*, 113(1):204–207, 2009.

[281] F. Ostendorf et al. How flat is an air-cleaved mica surface? *Nanotechnology*, 19(30):305705, 2008.

[282] C. H. Lui et al. Ultraflat graphene. *Nature*, 462(7271):339–341, 2009.

[283] K. T. He, J. D. Wood, G. P. Doidge, E. Pop, and J. W. Lyding. Scanning tunneling microscopy study and nanomanipulation of graphene-coated water on mica. *Nano Lett.*, 12(6):2665–2672, 2012.

[284] N. Severin, P. Lange, I. M. Sokolov, and J. P. Rabe. Reversible dewetting of a molecularly thin fluid water film in a soft graphene–mica slit pore. *Nano Lett.*, 12(2):774–779, 2012.

[285] S. J. Goncher, L. Zhao, A. N. Pasupathy, and G. W. Flynn. Substrate level control of the local doping in graphene. *Nano Lett*, 13:130315083654001, 2013.

[286] Y. Kim et al. Breakdown of the interlayer coherence in twisted bilayer graphene. *Phys. Rev. Lett.*, 110(9):096602, 2013.

[287] A. Tiberj et al. Reversible optical doping of graphene. *Sci. Rep.*, 3:2355, 2013.

[288] G. Lippert et al. Molecular beam growth of micrometer-size graphene on mica. *Carbon*, 52:40–48, 2013.

[289] C. Thomsen and S. Reich. Double resonant raman scattering in graphite. *Phys. Rev. Lett.*, 85(24):5214–5217, 2000.

[290] M. A. Pimenta et al. Studying disorder in graphite-based systems by raman spectroscopy. *Physical Chemistry Chemical Physics*, 9(11):1276, 2007.

[291] A. Eckmann et al. Probing the nature of defects in graphene by raman spectroscopy. *Nano Lett.*, 12(8):3925–3930, 2012.

[292] E. H. Martins Ferreira et al. Evolution of the raman spectra from single-, few-, and many-layer graphene with increasing disorder. *Phys. Rev. B*, 82(12):125429, 2010.

[293] J. Sabio et al. Electrostatic interactions between graphene layers and their environment. *Phys. Rev. B*, 77(19):195409, 2008.

[294] F. Yavari. Tunable bandgap in graphene by the controlled adsorption of water molecules. *Small*, 6(22):2535–2538, 2010.

[295] P. Cao, J. O. Varghese, K. Xu, and J. R. Heath. Visualizing local doping effects of individual water clusters on gold(111)-supported graphene. *Nano Lett.*, 12(3):1459–1463, 2012.

[296] L. Cartz and B. Tooper. Dehydration of phlogopite micas studied by high-temperature transmission electron microscopy. *J. Appl. Phys.*, 36(9):2783, 1965.

[297] R. Wirth. Dehydration of mica (phengite) by electron bombardment in a transmission electron microscope (tem). *J. Mater. Sci.*, 4(3):327–330, 1985.

[298] M. Lusk and L. Carr. Nanoengineering defect structures on graphene. *Phys. Rev. Lett.*, 100(17):175503, 2008.

[299] S. Goler et al. Self-assembly and electron-beam-induced direct etching of suspended graphene nanostructures. *J. Appl. Phys.*, 110(6):064308, 2011.

[300] J. Lu, A. C. H. Neto, and K. P. Loh. Transforming moiré blisters into geometric graphene nanobubbles. *Nature Commun.*, 3:823, 2012.

[301] C. H. Y. Xuan Lim et al. A hydrothermal anvil made of graphene nanobubbles on diamond. *Nature Commun.*, 4:1556, 2013.

[302] M. Yamamoto, T. L. Einstein, M. S. Fuhrer, and W. G. Cullen. Charge inhomogeneity determines oxidative reactivity of graphene on substrates. *ACS Nano*, 6(9):8335–8341, 2012.

[303] M. Buscema et al. Large and tunable photothermoelectric effect in single-layer MoS_2. *Nano Lett.*, 13(2):358–363, 2013.

[304] J. Pu et al. Highly flexible MoS_2 thin-film transistors with ion gel dielectrics. *Nano Lett*, 12(8):4013–4017, 2012.

[305] F. K. Perkins et al. Chemical vapor sensing with monolayer MoS_2. *Nano Lett.*, 13(2):668–673, 2013.

[306] S. Das, H.-Y. Chen, A. V. Penumatcha, and J. Appenzeller. High performance multilayer MoS_2 transistors with scandium contacts. *Nano Lett*, 13(1):100–105, 2013.

[307] S.-L. Li et al. Thickness-dependent interfacial coulomb scattering in atomically thin field-effect transistors. *Nano Lett.*, 13(8):3546–3552, 2013.

[308] W. Chen et al. Tuning the electronic and chemical properties of monolayer MoS_2 adsorbed on transition metal substrates. *Nano Lett.*, 13(2):509–514, 2013.

[309] W. Bao et al. High mobility ambipolar MoS_2 field-effect transistors: Substrate and dielectric effects. *Appl. Phys. Lett.*, 102(4):042104, 2013.

[310] G. Hao et al. Electrostatic properties of few-layer MoS_2 films. *AIP Adv.*, 3(4):042125, 2013.

[311] Y. Li, C.-Y. Xu, and L. Zhen. Surface potential and interlayer screening effects of few-layer MoS_2 nanoflakes. *Appl. Phys. Lett.*, 102(14):143110, 2013.

[312] M. A. Rad, K. Ibrahim, and K. Mohamed. Atomic force microscopy investigation of surface roughness generated between SiO_2 micro-pits in CHF_3/ar plasma. *Superlattices and Microstructures*, 51(5):597–605, 2012.

[313] C. Gatzert et al. Investigation of reactive ion etching of dielectrics and si in CHF_3/O_2 or CHF_3/ar for photovoltaic applications. *JVST A*, 24(5):1857, 2006.

[314] A. Castellanos-Gomez, N. Agraït, and G. Rubio-Bollinger. Optical identification of atomically thin dichalcogenide crystals. *Appl. Phys. Lett.*, 96(21):213116, 2010.

[315] P. Bertrand. Surface-phonon dispersion of moS_2. *Phys. Rev. B.*, 44(11):5745–5749, 1991.

[316] C. R Zhu et al. Strain tuning of optical emission energy and polarization in monolayer and bilayer MoS_2. *Phys. Rev. B*, 88(12):121301(R), 2013.

[317] B. Chakraborty et al. Symmetry-dependent phonon renormalization in monolayer MoS_2 transistor. *Phys. Rev. B*, 85(16):161403(R), 2012.

[318] H. B. Michaelson. The work function of the elements and its periodicity. *J. Appl. Phys.*, 48(11):4729, 1977.

[319] N. D. Orf, I. D. Baikie, O. Shapira, and Y. Fink. Work function engineering in low-temperature metals. *Appl. Phys. Lett.*, 94(11):113504, 2009.

[320] G. Giovannetti et al. Doping graphene with metal contacts. *Phys. Rev. Lett.*, 101(2):026803, 2008.

[321] A. L. Domanski et al. Kelvin probe force microscopy in nonpolar liquids. *Langmuir*, 28(39):13892–13899, 2012.

[322] L. Q. Guo, X. M. Zhao, Y. Bai, and L. J. Qiao. Water adsorption behavior on metal surfaces and its influence on surface potential studied by in situ spm. *Appl. Surf. Sci.*, 258(22):9087–9091, 2012.

[323] J.-H. Chen et al. Charged-impurity scattering in graphene. *Nature Phys.*, 4(5):377–381, 2008.

[324] A. Molina-Sánchez and L. Wirtz. Phonons in single-layer and few-layer MoS_2 and WS_2. *Phys. Rev. B*, 84(15):155413, 2011.

[325] N. Scheuschner et al. Photoluminescence of freestanding single- and few-layer MoS_2. *Phys. Rev. B*, 89(12):125406, 2014.

[326] K. M. Burson et al. Direct imaging of charged impurity density in common graphene substrates. *Nano Lett.*, 13(8):3576–3580, 2013.

[327] A. Castellanos-Gomez et al. Local strain engineering in atomically thin MoS_2. *Nano Lett.*, 13(11):5361–5366, 2013.

[328] I. T. McGovern, R. H. Williams, and C. H. B. Mee. Electronic properties of cleaved molybdenum disulphide surfaces. *Surf. Sci.*, 46(2):427–440, 1974.

[329] J. McMenamin and W. Spicer. Photoemission studies of layered transition-metal dichalcogenides: MoS_2. *Phys. Rev. B*, 16(12):5474–5487, 1977.

[330] M. Kamaratos and C. A. Papageorgopoulos. Adsorption studies on ar+ -sputtered $moS_2(0001)$. *Surf. Sci.*, 178(1-3):865–871, 1986.

[331] L. D. Carr and M. T. Lusk. Defect engineering: Graphene gets designer defects. *NatuJ. Appl. Phys..*, 5(5):316–317, 2010.

[332] S. Casolo, R. Martinazzo, and G. F. Tantardini. Band engineering in graphene with superlattices of substitutional defects. *J. Phys. Chem. C*, 115(8):3250–3256, 2011.

[333] S. Yadav, Z. Zhu, and C. V. Singh. Defect engineering of graphene for effective hydrogen storage. *International Journal of Hydrogen Energy*, 39(10):4981–4995, 2014.

[334] G. Xie et al. A general route towards defect and pore engineering in graphene. *Small*, 10:2280–2284, 2014.

[335] J. Bai et al. Graphene nanomesh. *Nature Nanotechnol.*, 5(3):190–194, 2010.

[336] C.-C. Lu et al. Twisting bilayer graphene superlattices. *ACS Nano*, 7(3):2587–2594, 2013.

[337] R. Balog et al. Bandgap opening in graphene induced by patterned hydrogen adsorption. *Nature Mater.*, 9(4):315–319, 2010.

[338] T. Kuila et al. Chemical functionalization of graphene and its applications. *Progress in Materials Science*, 57(7):1061–1105, 2012.

[339] M. F. Craciun, I. Khrapach, M. D. Barnes, and S. Russo. Properties and applications of chemically functionalized graphene. *J. Phys.: Condens. Matter*, 25(42):423201, 2013.

[340] L. Zhang et al. Janus graphene from asymmetric two-dimensional chemistry. *Nature Commun.*, 4:1443, 2013.

[341] K. Yang et al. Preparation and functionalization of graphene nanocomposites for biomedical applications. *Nature Protocols*, 8(12):2392–2403, 2013.

[342] M. Toulemonde et al. Track formation and fabrication of nanostructures with MeV-ion beams. *Nucl. Instr. Meth. Phys. Res. B*, 216:1–8, 2004.

[343] F. Forster et al. Dielectric screening of the kohn anomaly of graphene on hexagonal boron nitride. *Phys. Rev. B*, 88(8):085419, 2013.

[344] K. Kim et al. Multiply folded graphene. *Phys. Rev. B*, 83(24):245433, 2011.

[345] Y. Zheng et al. Mechanical properties of grafold: a demonstration of strengthened graphene. *Nanotechnology*, 22(40):405701, 2011.

[346] L. Ortolani et al. Folded graphene membranes: Mapping curvature at the nanoscale. *Nano Lett.*, 12(10):5207–5212, 2012.

[347] F. Queisser and R. Schützhold. Strong magnetophotoelectric effect in folded graphene. *Phys. Rev. Lett.*, 111(4):046601, 2013.

[348] J. Feng, L. Qi, J. Huang, and J. Li. Geometric and electronic structure of graphene bilayer edges. *Phys. Rev. B*, 80(16):165407, 2009.

[349] D. Zhan et al. Low temperature edge dynamics of ab-stacked bilayer graphene: Naturally favored closed zigzag edges. *Sci. Rep.*, 1:12, 2011.

[350] A. T. Costa et al. Origami-based spintronics in graphene. *EPL*, 104(4):47001, 2013.

[351] S. Zhu and T. Li. Hydrogenation-assisted graphene origami and its application in programmable molecular mass uptake, storage, and release. *ACS Nano*, 8(3):2864–2872, 2014.

[352] J. Zhang et al. Free folding of suspended graphene sheets by random mechanical stimulation. *Phys. Rev. Lett.*, 104(16):166805, 2010.

[353] M. J. Allen et al. Chemically induced folding of single and bilayer graphene. *Chem. Commun.*, 41(41):6285, 2009.

[354] J.-H. Yoo et al. Graphene folds by femtosecond laser ablation. *Appl. Phys. Lett.*, 100(23):233124, 2012.

[355] J. Hopster et al. Damage in graphene due to electronic excitation induced by highly charged ions. *2D Materials*, 1(1):011011, 2014.

[356] P. Markiewicz. Simulation of atomic force microscope tip–sample/sample–tip reconstruction. *JVST B*, 13(3):1115, 1995.

[357] D. Tranchida, S. Piccarolo, and Deblieck, R A C. Some experimental issues of AFM tip blind estimation: the effect of noise and resolution. *Meas. Sci. Technol., MST*, 17(10):2630–2636, 2006.

[358] E. Akcöltekin et al. Swift heavy ion irradiation of $SrTiO_3$ under grazing incidence. *New J. Phys.*, 10(5):053007, 2008.

[359] S. J. Zinkle, V. A. Skuratov, and D. T. Hoelzer. On the conflicting roles of ionizing radiation in ceramics. *Nucl. Instr. Meth. Phys. Res. B*, 191(1-4):758–766, 2002.

[360] G. Algara-Siller, O. Lehtinen, A. Turchanin, and U. Kaiser. Dry-cleaning of graphene. *Appl. Phys. Lett.*, 104(15):153115, 2014.

[361] L. D'Urso et al. Water structure and charge transfer phenomena at the liquid–graphene interface. *Phys. Chem. Chem. Phys.*, 14(42):14605, 2012.

[362] Y. Gao et al. The effect of interlayer adhesion on the mechanical behaviors of macroscopic graphene oxide papers. *ACS Nano*, 5(3):2134–2141, 2011.

[363] O. Ochedowski et al. Graphitic nanostripes in silicon carbide surfaces created by swift heavy ion irradiation. *Nature Commun.*, 5:3913, 2014.

[364] O. Lehtinen, J. Kotakoski, A. V. Krasheninnikov, and J. Keinonen. Cutting and controlled modification of graphene with ion beams. *Nanotechnology*, 22(17):175306, 2011.

[365] L. Cancado et al. Influence of the atomic structure on the raman spectra of graphite edges. *Phys. Rev. Lett.*, 93(24):247401, 2004.

[366] C. Casiraghi et al. Raman spectroscopy of graphene edges. *Nano Letters*, 9(4):1433–1441, 2009.

[367] C. Casiraghi et al. Raman fingerprint of charged impurities in graphene. *Appl. Phys. Lett.*, 91(23):233108, 2007.

[368] M. C. Prado et al. Two-dimensional molecular crystals of phosphonic acids on graphene. *ACS Nano*, 5(1):394–398, 2011.

[369] T. Mohiuddin et al. Uniaxial strain in graphene by raman spectroscopy: G peak splitting, grüneisen parameters, and sample orientation. *Phys. Rev. B*, 79(20):205433, 2009.

[370] J. Proctor et al. High-pressure raman spectroscopy of graphene. *Phys. Rev. B*, 80(7):073408, 2009.

[371] A. Zandiatashbar et al. Effect of defects on the intrinsic strength and stiffness of graphene. *Nature Commun.*, 5:3186, 2014.

[372] D. J. Appelhans, L. D. Carr, and M. T. Lusk. Embedded ribbons of graphene allotropes: an extended defect perspective. *New J. Phys.*, 12(12):125006, 2010.

[373] E. Suárez Morell et al. Flat bands in slightly twisted bilayer graphene: Tight-binding calculations. *Phys. Rev. B*, 82(12):121407(R), 2010.

[374] W.-Y. He, Z.-D. Chu, and L. He. Chiral tunneling in a twisted graphene bilayer. *Phys. Rev. Lett.*, 111(6):066803, 2013.

[375] Z. Ni et al. G-band raman double resonance in twisted bilayer graphene: Evidence of band splitting and folding. *Phys. Rev. B*, 80(12):125404, 2009.

[376] D.-H. Cho et al. Effect of surface morphology on friction of graphene on various substrates. *Nanoscale*, 5(7):3063, 2013.

[377] A. Righi et al. Graphene moiré patterns observed by umklapp double-resonance raman scattering. *Phys. Rev. B*, 84(24):241409(R), 2011.

[378] J. Stadler, T. Schmid, and R. Zenobi. Nanoscale chemical imaging of single-layer graphene. *ACS Nano*, 5(10):8442–8448, 2011.

[379] E. Poliani et al. Nanoscale imaging of InN segregation and polymorphism in single vertically aligned InGaN/GaN multi quantum well nanorods by tip-enhanced raman scattering. *Nano Lett.*, 13(7):3205–3212, 2013.

[380] X. Li et al. Large-area synthesis of high-quality and uniform graphene films on copper foils. *Science*, 324(5932):1312–1314, 2009.

[381] P. Y. Huang et al. Grains and grain boundaries in single-layer graphene atomic patchwork quilts. *Nature*, 469(7330):389–392, 2011.

[382] K. S. Kim. Large-scale pattern growth of graphene films for stretchable transparent electrodes. *Nature*, 457(7230):706–710, 2009.

[383] W. Zhu et al. Structure and electronic transport in graphene wrinkles. *Nano Lett.*, 12(7):3431–3436, 2012.

[384] A. Turchanin et al. One nanometer thin carbon nanosheets with tunable conductivity and stiffness. *Adv. Mater.*, 21(12):1233–1237, 2009.

[385] P. Angelova et al. A universal scheme to convert aromatic molecular monolayers into functional carbon nanomembranes. *ACS Nano*, 7(8):6489–6497, 2013.

[386] A. M. van der Zande et al. Grains and grain boundaries in highly crystalline monolayer molybdenum disulphide. *Nature Mater.*, 12(6):554–561, 2013.

[387] B. Hinnemann et al. Biomimetic hydrogen evolution: MoS_2 nanoparticles as catalyst for hydrogen evolution. *J. Am. Chem. Soc.*, 127(15):5308–5309, 2005.

[388] H. I. Karunadasa et al. A molecular MoS_2 edge site mimic for catalytic hydrogen generation. *Science*, 335(6069):698–702, 2012.

[389] M. A Lukowski et al. Enhanced hydrogen evolution catalysis from chemically exfoliated metallic MoS_2 nanosheets. *J. Am. Chem. Soc.*, 135(28):10274–10277, 2013.

[390] D. Le, T. B. Rawal, and T. S. Rahman. Single-layer MoS_2 with sulfur vacancies: Structure and catalytic application. *J. Phys. Chem. C*, 118(10):5346–5351, 2014.

[391] Y. Yu et al. Layer-dependent electrocatalysis of MoS_2 for hydrogen evolution. *Nano Lett.*, 14(2):553–558, 2014.

[392] R. W. Smith, M. Karlušić, and M. Jakšić. Single ion hit detection set-up for the zagreb ion microprobe. *Nucl. Instr. Meth. Phys. Res. B*, 277:140–144, 2012.

[393] J. Liu, R. Neumann, C. Trautmann, and C. Müller. Tracks of swift heavy ions in graphite studied by scanning tunneling microscopy. *Phys. Rev. B.*, 64(18):184115, 2001.

[394] R. Yang et al. Synthesis and characterization of MoS_2 ti composite coatings on Ti6Al4V prepared by laser cladding. *AIP Adv.*, 3(2):022106, 2013.

[395] J. M. Gordon et al. Singular MoS_2, SiO_2 and si nanostructures—synthesis by solar ablation. *J. Mater. Sci.*, 18(4):458, 2008.

[396] O. Osmani, N. Medvedev, M. Schleberger, and B. Rethfeld. Energy dissipation in dielectrics after swift heavy-ion impact: A hybrid model. *Phys. Rev. B*, 84(21):214105, 2011.

[397] K. Lu and Z. H. Jin. Melting and superheating of low-dimensional materials. *Current Opinion in Solid State and Materials Science*, 5(1):39–44, 2001.

[398] K. V. Zakharchenko, Annalisa Fasolino, J. H. Los, and M. I. Katsnelson. Melting of graphene: from two to one dimension. *J. Phys.: Condens. Matter*, 23(20):202202, 2011.

[399] A. I. Savvatimskiy. Measurements of the melting point of graphite and the properties of liquid carbon (a review for 1963–2003). *Carbon*, 43(6):1115–1142, 2005.

[400] W. Shockley, J. Bardeen, and W. H. Brattain. The national academy of sciences: Abstracts of papers presented at 1948 autumn meeting, berkeley, california. *Science*, 108(2816):676–683, 1948.

[401] A. van Dormael et al. Biographies: Herbert f. mataré. *IEEE Annals of the History of Computing*, 31(3):68–73, 2009.

[402] R. Doering and Y. Nishi. *Handbook of semiconductor manufacturing technology*. CRC Press, Boca Raton, 2nd ed edition, 2008.

[403] J. F. Ziegler. *Ion implantation: Science and technology*. Academic Press, Orlando, 1984.

[404] Y. Shi et al. Effective doping of single-layer graphene from underlying SiO_2 substrates. *Phys. Rev. B*, 79(11):115402, 2009.

[405] B. Guo et al. Controllable n-doping of graphene. *Nano Lett.*, 10(12):4975–4980, 2010.

[406] K.-J. Kim et al. Surface property change of graphene using nitrogen ion. *J. Phys.: Condens. Matter*, 22(4):045005, 2010.

[407] W. Zhao et al. Production of nitrogen-doped graphene by low-energy nitrogen implantation. *J Phys. Chem. C*, 116(8):5062–5066, 2012.

[408] H. Wang et al. Doping monolayer graphene with single atom substitutions. *Nano Lett.*, 12(1):141–144, 2012.

[409] Y.-J. Yu et al. Tuning the graphene work function by electric field effect. *Nano Lett.*, 9(10):3430–3434, 2009.

[410] G. Cicero, A. Catellani, and G. Galli. Atomic control of water interaction with biocompatible surfaces: The case of sic(001). *Physical Review Letters*, 93(1):016102, 2004.

[411] Y. Katoh et al. Current status and critical issues for development of SiC composites for fusion applications. *J. Nucl. Mater.*, 367-370:659–671, 2007.

[412] C. R. Eddy and D. K. Gaskill. Silicon carbide as a platform for power electronics. *Science*, 324(5933):1398–1400, 2009.

[413] C. Berger. Electronic confinement and coherence in patterned epitaxial graphene. *Science*, 312(5777):1191–1196, 2006.

[414] K. V. Emtsev, F. Speck, Th. Seyller, and L. Ley. Interaction, growth, and ordering of epitaxial graphene on sic(0001) surfaces: A comparative photoelectron spectroscopy study. *Phys. Rev. B*, 77(15):155303, 2008.

[415] T. Filleter et al. Friction and dissipation in epitaxial graphene films. *Phys. Rev. Lett.*, 102(8):086102, 2009.

[416] J. D. Emery et al. Chemically resolved interface structure of epitaxial graphene on SiC(0001). *Phys. Rev. Lett.*, 111(21):215501, 2013.

[417] S. Hertel et al. Tailoring the graphene/silicon carbide interface for monolithic wafer-scale electronics. *Nature Commun.*, 3:957, 2012.

[418] C. Riedl et al. Quasi-free-standing epitaxial graphene on SiC obtained by hydrogen intercalation. *Phys. Rev. Lett.*, 103(24):246804, 2009.

[419] S. Forti et al. Large-area homogeneous quasifree standing epitaxial graphene on sic(0001): Electronic and structural characterization. *Phys. Rev. B*, 84(12):125449, 2011.

[420] M. Bockstedte. Many-body effects in the excitation spectrum of a defect in SiC. *Phys. Rev. Lett.*, 105(2):026401, 2010.

[421] Y. Liu et al. Defect-induced magnetism in neutron irradiated 6h-SiC single crystals. *Phys. Rev. Lett.*, 106(8):087205, 2011.

[422] P. G. Baranov et al. Silicon vacancy in SiC as a promising quantum system for single-defect and single-photon spectroscopy. *Phys. Rev. B*, 83(12):125203, 2011.

[423] M. Lang et al. Nanoscale manipulation of the properties of solids at high pressure with relativistic heavy ions. *Nature Mater.*, 8(10):793–797, 2009.

[424] M. C. Ridgway et al. Role of thermodynamics in the shape transformation of embedded metal nanoparticles induced by swift heavy-ion irradiation. *Phys. Rev. Lett.*, 106(9):095505, 2011.

[425] M. C. Ridgway et al. Tracks and voids in amorphous ge induced by swift heavy-ion irradiation. *Phys. Rev. Lett.*, 110(24):245502, 2013.

[426] S. Sorieul et al. Optical spectroscopy study of damage induced in 4h-SiC by swift heavy ion irradiation. *J. Phys.: Condens. Matter*, 24(12):125801, 2012.

[427] A. Benyagoub, A. Audren, L. Thomé, and F. Garrido. Athermal crystallization induced by electronic excitations in ion-irradiated silicon carbide. *Appl. Phys. Lett.*, 89(24):241914, 2006.

[428] A. Audren et al. Effects of electronic and nuclear interactions in SiC. *Nucl. Instr. Meth. Phys. Res. B*, 267(6):976–979, 2009.

[429] V. A. Skuratov, S. J. Zinkle, A. E. Efimov, and K. Havancsak. Surface defects in Al_2O_3 and MgO irradiated with high-energy heavy ions. *Surf. Coat. Technol.*, 196(1-3):56–62, 2005.

[430] T. Roll et al. Conductive nanodots on the surface of irradiated CaF_2. *PSS (RRL)*, 2(5):209–211, 2008.

[431] C. Held, T. Seyller, and R. Bennewitz. Quantitative multichannel nc-afm data analysis of graphene growth on sic(0001). *Beilstein Journal of Nanotechnology*, 3:179–185, 2012.

[432] M. Backman et al. Molecular dynamics simulations of swift heavy ion induced defect recovery in SiC. *Comput. Mater. Sci.*, 67:261–265, 2013.

[433] I. V. Vorobyova. Tracks formation on LiF crystal surface due to grazing incidence of 1 MeV/u sn ions. *Nucl. Instr. Meth. Phys. Res. B*, 146(1-4):379–384, 1998.

[434] M.. Ghaly, K. Nordlund, and R. S. Averback. Molecular dynamics investigations of surface damage produced by kiloelectronvolt self-bombardment of solids. *Philosophical Magazine A*, 79(4):795–820, 1999.

[435] W. Assmann, M. Toulemonde, and C. Trautmann. Electronic sputtering with swift heavy ions. In Walter Assmann, editor, *Sputtering by Particle Bombardment*, volume 110 of *Topics in Applied Physics*, pages 401–450. Springer Berlin Heidelberg, Berlin and Heidelberg, 2007.

[436] K. Nordlund, J. Keinonen, M. Ghaly, and R. S. Averback. Coherent displacement of atoms during ion irradiation. *Nature*, 398(6722):49–51, 1999.

[437] E. H. Åhlgren, J. Kotakoski, and A. V. Krasheninnikov. Atomistic simulations of the implantation of low-energy boron and nitrogen ions into graphene. *Phys. Rev. B*, 83(11):115424, 2011.

[438] A. V. Krasheninnikov and K. Nordlund. Ion and electron irradiation-induced effects in nanostructured materials. *J. Appl. Phys.*, 107(7):071301, 2010.

[439] S. Mathew et al. Mega-electron-volt proton irradiation on supported and suspended graphene: A raman spectroscopic layer dependent study. *J. Appl. Phys.*, 110(8):084309, 2011.

[440] I. Deretzis, G. Piccitto, and A. La Magna. Electronic transport signatures of common defects in irradiated graphene-based systems. *Nucl. Instr. Meth. Phys. Res. B*, 282:108–111, 2012.

[441] F. Chen, J. Xia, D. K. Ferry, and N. Tao. Dielectric screening enhanced performance in graphene fet. *Nano Lett.*, 9(7):2571–2574, 2009.

[442] S.-J. Han, Z. Chen, A. A. Bol, and Y. Sun. Channel-length-dependent transport behaviors of graphene field-effect transistors. *IEEE Electron Device Letters*, 32(6):812–814, 2011.

[443] P. Joshi et al. Intrinsic doping and gate hysteresis in graphene field effect devices fabricated on SiO_2 substrates. *J. Phys.: Condens. Matter*, 22(33):334214, 2010.

[444] K. Ganapathi, Y. Yoon, M. Lundstrom, and S. Salahuddin. Ballistic i-v characteristics of short-channel graphene field-effect transistors: Analysis and optimization for analog and rf applications. *IEEE Transactions on Electron Devices*, 60(3):958–964, 2013.

[445] A. Alarcon et al. Pseudosaturation and negative differential conductance in graphene field-effect transistors. *IEEE Transactions on Electron Devices*, 60(3):985–991, 2013.

[446] H.-P. Komsa et al. Two-dimensional transition metal dichalcogenides under electron irradiation: Defect production and doping. *Phys. Rev. Lett.*, 109(3):035503, 2012.

[447] H. Nan et al. Strong photoluminescence enhancement of MoS_2 through defect engineering and oxygen bonding. *ACS Nano*, 8(6):5738–5745, 2014.

[448] S. C. O'Hern et al. Selective molecular transport through intrinsic defects in a single layer of cvd graphene. *ACS Nano*, 6(11):10130–10138, 2012.

[449] M. S. H. Boutilier et al. Implications of permeation through intrinsic defects in graphene on the design of defect-tolerant membranes for gas separation. *ACS Nano*, 8(1):841–849, 2014.

List of own publications

[OO.01] Kleine Bussmann, B., **Ochedowski, O.**, and Schleberger, M. Doping of graphene exfoliated on $SrTiO_3$. *Nanotechnology*, 22(26):265703, 2011.

[OO.02] Bukowska, H., Meinerzhagen, F., Akcöltekin, S., **Ochedowski, O.**, Neubert, M., Buck, V., and Schleberger, M. Raman spectra of graphene exfoliated on insulating crystalline substrates. *New Journal of Physics*, 13(6):063018, 2011.

[OO.03] Kleine Bussmann, B., Marinov, K., **Ochedowski, O.**, Scheuschner, N., Maultzsch, J., and Schleberger, M. Electronic characterization of single-layer MoS_2 sheets exfoliated on $SrTiO_3$. *MRS Proceedings*, 1474, 2012.

[OO.04] **Ochedowski, O.**, Kleine Bussmann, B., and Schleberger, M. Laser cleaning of exfoliated graphene. *MRS Proceedings*, 1455, 2012.

[OO.05] **Ochedowski, O.**, Begall, G., Scheuschner, N., El Kharrazi, M., Maultzsch, J., and Schleberger, M. Graphene on Si(111)7×7. *Nanotechnology*, 23(40):405708, 2012.

[OO.06] Scheuschner, N., **Ochedowski, O.**, Schleberger, M., and Maultzsch, J. Resonant raman profiles and μ-photoluminescence of atomically thin layers of molybdenum disulfide. *physica status solidi (b)*, 249(12):2644–2647, 2012.

[OO.07] **Ochedowski, O.**, Kleine Bussmann, B., Ban d'Etat, B., Lebius, H., and Schleberger, M. Manipulation of the graphene surface potential by ion irradiation. *Applied Physics Letters*, 102:153103, 2013.

[OO.08] **Ochedowski, O.**, Marinov, K., Wilbs, G., Keller, G., Scheuschner, N., Severin, D., Bender, M., Maultzsch, J., Tegude, F. J., and Schleberger, M. Radiation hardness of graphene and MoS_2 field effect devices against swift heavy ion irradiation. *Journal of Applied Physics*, 113(21):214306, 2013.

[OO.09] Temmen, M., **Ochedowski, O.**, Bussmann, B. K., Schleberger, M., Reichling, M., and Bollmann, T. R. J. Routes to rupture and folding of graphene on rough 6H-SiC(0001) and their identification. *Beilstein Journal of Nanotechnology*, 4:625–631, 2013.

[OO.10] **Ochedowski, O.**, Akcöltekin, S., Ban-d'Etat, B., Lebius, H., and Schleberger, M. Detecting swift heavy ion irradiation effects with graphene. *Nuclear Instruments and Methods in Physics Research Section B: Beam Interactions with Materials and Atoms*, 314:18, 2013.

[OO.11] Scheuschner, N., **Ochedowski, O.**, Kaulitz, A.-M., Gillen, R., Schleberger, M., and Maultzsch, J. Photoluminescence of freestanding single- and few-layer MoS_2. *Physical Review B*, 89(12):125406, 2014.

[OO.12] Temmen, M., **Ochedowski, O.**, Schleberger, M., Reichling, M., and Bollmann, T. R. J. Hydration layers trapped between graphene and a hydrophilic substrate. *New Journal of Physics*, 16(5):053039, 2014.

[OO.13] **Ochedowski, O.**, Marinov, K., Scheuschner, N., Poloczek, A., Kleine Bussmann, B., Maultzsch, J., and Schleberger, M. Effect of contaminations and surface preparation on the work function of single layer MoS_2. *Beilstein Journal of Nanotechnology*, 5:291–297, 2014.

[OO.14] Woehrl, N., **Ochedowski, O.**, Gottlieb, S., Shibasaki, K., and Schulz, S. Plasma-enhanced chemical vapor deposition of graphene on copper substrates. *AIP Advances*, 4(4):047128, 2014.

[OO.15] **Ochedowski, O.**, Osmani, O., Schade, M., Kleine Bussmann, B., Ban-d'Etat, B., Lebius, H., and Schleberger, M. Graphitic nanostripes in silicon carbide surfaces created by swift heavy ion irradiation. *Nature Communications*, 5:3913, 2014.

[OO.16] **Ochedowski, O.**, Kleine-Bussman, B., and Schleberger, M. Graphene on Mica - Intercalated Water Trapped for Life. *Scientific Reports*, 4:6003, 2014.

[OO.17] Kozubek, R., **Ochedowski, O.**, Zagoranskiy, I., Karlusic, M., and Schleberger, M. Application of HOPG and CVD graphene as ion beam detectors. *accepted in Nuclear Instruments and Methods in Physics Research Section B: Beam Interactions with Materials and Atoms.*

[OO.18] **Ochedowski, O.**, Bukowska, H., Freire Soler, V. M., Broekers, L., Lebius, H., and Schleberger, M. Folding two dimensional crystals by Swift Heavy Ion Irradiation. *accepted Nuclear Instruments and Methods in Physics Research Section B: Beam Interactions with Materials and Atoms.*

Danksagung

An dieser Stelle möchte ich noch allen Danken, die mir in den letzten Jahren geholfen haben und es mir so ermöglicht haben diese Dissertation zu verfassen. Zuallererst und vor allem möchte ich Prof. Marika Schleberger danken. Sie hat mir die Möglichkeit geboten in Ihrer Arbeitsgruppe in einem sehr spannenden Feld der Wissenschaft auf höchstem Niveau zu forschen und zu promovieren. Insbesondere möchte ich mich hierbei dafür bedanken, dass ihre Tür immer offen ist und sie stets zur Stelle ist, wenn man mal nicht weiterkommt. Vielen Dank Marika.

Direkt dahinter möchte ich Herrn Dr. Andreas Reichert danken. Es war toll im Nano Schülerlabor der Universität Duisburg-Essen arbeiten zu dürfen. Dank seinen Tipps konnte ich mir durch Posterpreise auf Konferenzen ein bisschen Taschengeld verdienen. Und ich möchte mich noch stellvertretend für alle Leser der gebundenen Ausgabe meiner Dissertation bei ihm bedanken, er hat dafür gesorgt, dass die Abbildungen auch ohne Lupe lesbar sein sollten...

Einen besonderen Dank auch an Herrn Prof. Dietrich Wolf. Als damaliger Vorsitzender des Prüfungsausschußes für den Masterstudiengang Physik an der Universität Duisburg-Essen hat er maßgeblich daran beigetragen, daß der Wechsel aus der Biophysik in die Physik für mich reibungslos und erfolgreich verlaufen ist.

Der AG Schleberger mit allen ihren HiWis, Doktoranden, Sekretärin und Techniker möchte ich natürlich auch herzlichen danken. Bei den Doktoranden wären das: Benedict Kleine Bussmann für die gute Zusammenarbeit im UHV AFM Labor, Orkhan Osmani und Mourad El Kharazzi für den exzellenten theoretischen Backup, wenn er nötig war, Johannes Hopster, Roland Kozubek und Philipp Ernst für die Zusammenarbeit in Zusammenhang mit HCI Experimenten, Christian Haake bei Problemen mit der IT, Hanna Bukowska und Florian Meinerzhagen für die Bestrahlung an der GSI und Sevilay Akcöltekin für ihre ganzen Vorarbeiten bezüglich der Faltungen auf Graphen.

Im Verlaufe meiner Promotion hatte ich die Möglichkeit viele Abschlußarbeiten und Projektarbeiten von Studenten zu betreuen, was mir sehr viel Spass gemacht hat und oft auch wichtige Ergebnisse lieferte. Danke also an: Alexander Levisch, Ulrike Hutten, Jinghao Chen, Meike Neubert, Petros Polikronidis, Kolyo Marinov, Genevieve Wilbs, Lukas Madauss, Erik Pollmann, Matthias Grunewald, Lara Bröckers, Matthias Mühlenhoff, Igor

Zagoranskiy und Christoph Mecking. An dieser Stelle auch dank an Viktor Manuel Freire Soler, Gastwissenschaftler aus Spanien in der AG Schleberger, mit dem ich drei Monate intensiv zusammenarbeiten durfte.

Viele der veröffentlichen Publikationen sind aus Arbeiten von mir alleine sondern in Zusammenarbeit mit Kooperationspartern entstanden. An dieser Stelle möchte ich besonderes Nils Scheuschner und Prof. Janina Maultzsch von der TU Berlin danken. Nils habe ich auf der Zaferna Hütte beim Doktorandenseminar des Schwerpunktprojekts Graphen der DFG kennen gelernt (Wir waren die beiden Zuspätkommer die von einer Horde von Kühen verfolgt worden sind). Ich werde es vermissen nach Berlin zu fahren um Raman/PL Messungen zu machen. Zudem möchte ich mich noch bei der Halbleitertechnik in Duisburg bedanken, namentlich Artur Poloczek und Gregor Keller. Durch diese Kooperation wurde es ermöglichst aus diesen kleinen exfoliierten Flocken funktionierende Transistoren zu bauen. Nicolas Wöhrl für die Zusammenarbeit bezüglich Plasma CVD Graphen um nicht mehr von den kleinen Flöckchen abhängig zu sein. Einen Dank auch nach Osnabrück an Herrn Prof. Reichling, Tjeerd Bollmann und Matthias Temmen für die Kooperation im Rahmen des SPP 1459.

Nicht zu vergessen natürlich alle Wissenschaftler an den diversen Ionenbeschleunigern an denen die Experimente durchgeführt worden sind: Henning Lebius und Brigitte Ban d'Etat am GANIL in Frankreich, Markus Bender und Daniel Severin an der GSI in Darmstadt und Marko Karlusic am RBI in Kroatien. An Marko nochmal einen besonderen Dank für das Korrekturlesen von Teilen der Arbeit.

Auch einen lieben Dank an Prof. Horn-von Hoegen, der mir in Zeiten gröer Not einen Platz zur Verfügung gestellt hat, an dem ich in Ruhe meine Dissertation fertig schreiben konnte.

Zu guter letzt noch einen ganz besonderen Dank an meine Eltern und meinen Brudern, die mich stets bedingungslos unterstützt haben.

Erklärung

Hiermit versichere ich, dass ich die vorliegende Arbeit selbstständig verfasst und ohne unzulässige Hilfe Dritter und ohne Benutzung anderer als der angegebenen Hilfsmittel angefertigt habe. Die verwendeten Hilfsmittel und alle wörtlich oder inhaltlich übernommenen Stellen sind unter Angabe der Quelle gekennzeichnet.

Die Arbeit wurde bisher weder im Inland noch im Ausland in gleicher oder ähnlicher Form einer anderen Prüfungsbehörde vorgelegt.

Der Doktorgrad eines Doktors der Naturwissenschaften (Dr. rer. nat.) wird gemäß §1 Satz 2 der Promotionsordnung angestrebt.

Duisburg, den 20. August 2014

Oliver Ochedowski